UNIVERSITAT POLITÈCNICA DE VALÈNCIA

Trabajo Fin de Máster

Máster en Ingeniería Aeronáutica

Curso 2018 - 2019

Finite elements modeling of Compression-After-Impact test for laminated composite thin plates with initial delaminations

---

Universitat Politècnica de València

Escuela Técnica Superior Industrial de Diseño

In cooperation with:

HAW Hamburg University of Applied Sciences

AUTHOR:
Olivares Ferrer, Aurelio José

TUTOR:
García Manrique, Juan Antonio

CO-TUTOR:
Markus Linke

Acknowledgements

I would first like to thank my thesis advisors Prof. Juan Antonio García Manrique of the Mechanical Engineering Dep. (DIMM) at Universitat Politècnica de València and Prof. Markus Linke of the Department of Automotive & Aeronautical Engineering at HAW Hamburg University of Applied Science. They have always had its office door open whenever I ran into a trouble spot or had a question about my research or writing and, they steered me in the right the direction whenever they thought I needed it.

I would like to thank my family and my partner Lucia for all the support received, without which I would not have been able to achieve all my goals so far so successfully.

Abstract

The aim of this project is to create a finite element model to predict the failure mechanisms of thin-walled laminates under Compression-After-Impact testing based on different experimental validation. First, the material properties of the laminate under investigation are estimated from tensile tests and analytical approaches. Then, a controlled low energy impact with a pendulum impact system is carried out in order to induce internal damages (indentation, delamination, matrix cracking, fiber/matrix debonding and fiber breakage). These experiments are followed by ultrasonic scanning of the damaged samples in order to characterize the damaged areas, in particular, at the layer interfaces in the through-thickness direction. This is followed by a set of Compression-After-Impact tests combined with digital imaging correlation using an ARAMIS 3D measuring system (Gom mbH, Braunschweig, Germany). Compression-After-Impact tests are carried out with a frame modified for thin-walled laminates enabling an easier measurement of thin laminates. Finally, all the data collected in the experiments is compared to the finite element simulations built up with the results of Finite Element code Abaqus (Dassault Systèmes SA, Paris, France). Then, through these models the potential interactions between global and local failure mechanisms in Compression-After-Impact testing are analyzed with different interface damage idealizations.

Contents

List of Figures

List of Tables

List of Symbols

CAI	—	—	Compression-After-Impact test
CFRP	—	—	Carbon Fiber Reinforced Polymer
BVID	—	—	Barely Visible Impact Damages
NDT	—	—	Non-Destructive-Testing
VT	—	—	Visual Testing
UT	—	—	Ultrasonic Testing
CT	—	—	X-ray Computed Tomography
RT	—	—	Radiographic Testing
ET	—	—	Electromagnetic Testing
AE	—	—	Acoustic Emission
UD	—	—	Unidirectional
W	—	—	Woven
CLT	—	—	Classical Laminate Theory
x, y, z	$[m]$	—	Laminate global coordinate system
u, v, w	$[m]$	—	Laminate global displacements
$1, 2, 3$	—	—	Ply local coordinate system
E_x	$[Pa]$	—	Elastic modulus in the laminate principal direction
E_y	$[Pa]$	—	Elastic modulus in the laminate transverse direction
G_{xy}	$[Pa]$	—	In-plane shear modulus in the laminate orientation
G_{xz}	$[Pa]$	—	Out-of-plane shear modulus in the laminate principal direction
G_{yz}	$[Pa]$	—	Out-of-plane shear modulus in the laminate transverse direction
ν_{xy}	$[-]$	—	In-plane Poisson's ratio in the laminate orientation
ν_{xz}	$[-]$	—	Out-of-plane Poisson's ratio in the laminate principal direction
ν_{yz}	$[-]$	—	Out-of-plane Poisson's ratio in the laminate transverse direction
ρ	$[kg/m^3]$	—	Density of a ply
E_1	$[Pa]$	—	Elastic modulus in the ply direction
E_2	$[Pa]$	—	Elastic modulus in the ply transverse direction
G_{12}	$[Pa]$	—	In-plane shear modulus in the ply orientation
G_{13}	$[Pa]$	—	Out-of-plane shear modulus in the ply direction
G_{23}	$[Pa]$	—	Out-of-plane shear modulus in the ply transverse direction
ν_{12}	$[-]$	—	In-plane Poisson's ratio in the ply orientation
ν_{13}	$[-]$	—	Out-of-plane Poisson's ratio in the ply direction
ν_{23}	$[-]$	—	Out-of-plane Poisson's ratio in the ply transverse direction
Φ_k	$[^o]$	—	Ply angle in the laminate reference system
ρ_f	$[kg/m^3]$	—	Density of the fiber material
$E_{1,f}$	$[Pa]$	—	Elastic modulus of fiber material in the fiber direction
$E_{2,f}$	$[Pa]$	—	Elastic modulus of fiber material in the transverse direction
$G_{12,f}$	$[Pa]$	—	In-plane shear modulus of fiber material
$G_{13,f}$	$[Pa]$	—	Out-of-plane shear modulus of fiber material in the longitudinal direction
$G_{23,f}$	$[Pa]$	—	Out-of-plane shear modulus of fiber material in the transverse direction
$\nu_{12,f}$	$[-]$	—	In-plane Poisson's ratio of fiber material

$\nu_{13,f}$	$[-]$	—	Out-of-plane Poisson's ratio of fiber material in the longitudinal direction
$\nu_{23,f}$	$[-]$	—	Out-of-plane Poisson's ratio of fiber material in the transverse direction
$\sigma_{f,F}$	$[Pa]$	—	Failure stress of the fiber material in the fiber direction
$\varepsilon_{f,F}$	$[-]$	—	Failure strain of the fiber material in the fiber direction
ρ_m	$[kg/m^3]$	—	Density of the matrix material
E_m	$[Pa]$	—	Elastic modulus of matrix material
G_m	$[Pa]$	—	Shear modulus of matrix material
ν_m	$[-]$	—	Poisson's ratio of matrix material
$V_{f,UD}$	$[-]$	—	Fiber volume ratio of unidirectional plies
$V_{f,W}$	$[-]$	—	Fiber volume ratio of woven plies
M	$[Pa]$	—	Elastic constant of ply material for Halpin-Tsai model
M_f	$[Pa]$	—	Elastic constant of fiber material for Halpin-Tsai model
M_m	$[Pa]$	—	Elastic constant of matrix material for Halpin-Tsai model
η	$[-]$	—	Parameter of Halpin-Tsai model
ξ	$[-]$	—	Correlation parameter of Halpin-Tsai model
σ_x	$[Pa]$	—	Stress in the laminate principal direction
σ_y	$[Pa]$	—	Stress in the laminate transverse direction
σ_z	$[Pa]$	—	Stress in the laminate through-thickness direction
τ_{xy}	$[Pa]$	—	In-plane shear stress in the laminate orientation
τ_{xz}	$[Pa]$	—	Out-of-plane shear stress in the laminate principal direction
τ_{yz}	$[Pa]$	—	Out-of-plane shear stress in the laminate transverse direction
ε_x	$[-]$	—	Strain in the laminate principal direction
ε_y	$[-]$	—	Strain in the laminate transverse direction
ε_z	$[-]$	—	Strain in the laminate through-thickness direction
γ_{xy}	$[-]$	—	In-plane shear strain in the laminate orientation
γ_{xz}	$[-]$	—	Out-of-plane shear strain in the laminate principal direction
γ_{yz}	$[-]$	—	Out-of-plane shear strain in the laminate transverse direction
σ_1	$[Pa]$	—	Stress in the ply principal direction
σ_2	$[Pa]$	—	Stress in the ply transverse direction
τ_{12}	$[Pa]$	—	In-plane shear stress in the ply orientation
τ_{13}	$[Pa]$	—	Out-of-plane shear stress in the ply principal direction
τ_{23}	$[Pa]$	—	Out-of-plane shear stress in the ply transverse direction
ε_1	$[-]$	—	Strain in the ply principal direction
ε_2	$[-]$	—	Strain in the ply transverse direction
ε_3	$[-]$	—	Strain in the ply through-thickness direction
γ_{12}	$[-]$	—	In-plane shear strain in the ply orientation
γ_{13}	$[-]$	—	Out-of-plane shear strain in the ply principal direction
γ_{23}	$[-]$	—	Out-of-plane shear strain in the ply transverse direction
K_x, K_y, K_{xy}	$[m^{-1}]$	—	Middle surface curvatures of laminates
$\{\varepsilon^0\}$	$[-]$	—	Deformations of the middle surface
$\{\overline{\sigma}\}$	$[Pa]$	—	Stresses in the ply reference system
$\{\sigma\}$	$[Pa]$	—	Stresses in the laminate reference system
$[Q]_k$	$[Pa]$	—	Stiffness matrix of ply k in the laminate reference system
$[\overline{Q}]_k$	$[Pa]$	—	Stiffness matrix of ply k in the ply reference system
$[T]_k$	$[-]$	—	Rotational matrix of ply k
$[R]$	$[-]$	—	Reuter matrix
N_x	$[N/m]$	—	Membrane axial force in x direction
N_y	$[N/m]$	—	Membrane axial force in y direction
N_{xy}	$[N/m]$	—	Membrane shear force in xy plane
M_x	$[N]$	—	Flexural momentum in x direction
M_y	$[N]$	—	Flexural momentum in y direction

M_{xy}	$[N]$	—	Torsional momentum in xy plane
$\{N\}$	$[N/m]$	—	Membrane forces
$\{M\}$	$[N]$	—	Momentums
$[A],[B],[D]$	—	—	Stiffness matrices of the laminate
α	$[-]$	—	Hashin damage model parameter
X_T	$[Pa]$	—	Ply tensile strength in the fiber direction
X_C	$[Pa]$	—	Ply compression strength in the fiber direction
Y_T	$[Pa]$	—	Ply tensile strength in the transverse direction
Y_C	$[Pa]$	—	Ply compression strength in the transverse direction
S_T	$[Pa]$	—	Ply tensile strength in the transverse direction
S_L	$[Pa]$	—	Ply compression strength in the transverse direction
G^C_{ft}	$[N/m]$	—	Ply tensile fracture energy in the fiber direction
G^C_{fc}	$[N/m]$	—	Ply compression fracture energy in the fiber direction
G^C_{mt}	$[N/m]$	—	Ply tensile fracture energy in the transverse direction
G^C_{mc}	$[N/m]$	—	Ply compression fracture energy in the transverse direction
η^C_{ft}	$-]$	—	Ply tensile viscous regularization in the fiber direction
η^C_{fc}	$[-]$	—	Ply compression viscous regularization in the fiber direction
η^C_{mt}	$[-]$	—	Ply tensile viscous regularization in the transverse direction
η^C_{mc}	$[-]$	—	Ply compression viscous regularization in the transverse direction
E_{nn}	$[Pa/m]$	—	Cohesive tensile stiffness
E_{ss}	$[Pa/m]$	—	Cohesive shear stiffness in the s direction
E_{tt}	$[Pa/m]$	—	Cohesive shear stiffness in the t direction
t^0_n	$[Pa]$	—	Cohesive tensile strength
t^0_s	$[Pa]$	—	Cohesive shear strength in the s direction
t^0_t	$[Pa]$	—	Cohesive shear strength in the t direction
η_{BK}	$[-]$	—	Cohesive exponent parameter for B-K model
G^C_n	$[Pa \cdot m]$	—	Cohesive tensile fracture energy in the normal direction
G^C_s	$[Pa \cdot m]$	—	Cohesive shear fracture energy in the s direction
G^C_t	$[Pa \cdot m]$	—	Cohesive shear fracture energy in the t direction
μ^C_{BK}	$[-]$	—	Cohesive viscous regularization
J_A	$[kg \cdot m^2]$	—	Mass moment of inertia
E_{imp}	$[J]$	—	Impact energy
ω	$[^o/s]$	—	Angular velocity
σ_{CAI}	$[Pa]$	—	Failure stress of the CAI test

Chapter 1

Introduction

1.1 Initial situation

Nowadays, the aeronautical and aerospace industry is using composite materials not only in the non-structural parts like fairings, but also in many critical parts of the primary structure and control elements. This trend aims to have a 50% of the airframe structural mass made of CFRP in the Aribus A350 fleets according to [1]. Composite materials used in these critical structures, such as wing box, airframe, ailerons, flaps and struts, have to combine excellent mechanical properties as high specific stiffness and strength. One of the composite material which best meets these requirements is the Carbon Fiber-Reinforced Polymer (CFRP) but, the low impact strength is one of its main drawbacks.

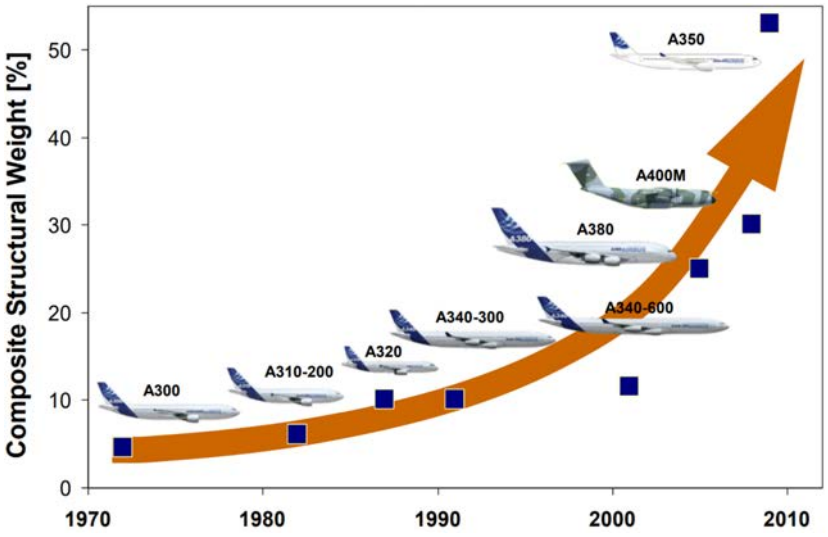

Figure 1.1: Airbus composite structural weight progression during the last 40 years [1].

Coming back to the greater use of composite materials in aerospace structures, they are more exposed to impacts mainly due to foreign object debris (like tool drops or runway debris) and damages due to ground services equipment [2]. Also, impacts by forgotten objects inside the components, like tools and/or bolts and nuts loose. Most of these impacts are classified as low energy impacts and given the low impact strength of CFRP, internal damage might be caused. These internal damages may lie in many forms as indentation, delamination, matrix cracking and fiber/matrix debonding and fiber breakage [3], some of them showed in Figure 1.2. Often, leading to high reduction in strength, stiffness and integrity of composite structures.

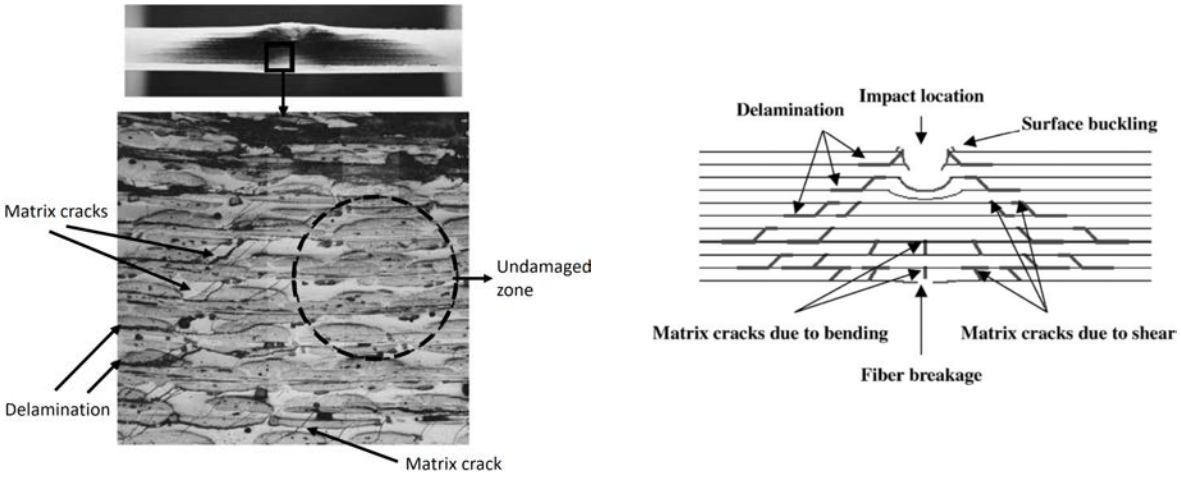

Figure 1.2: Typical damages at low-energy impact in a composite laminated [4].

These damages caused by low energy impacts are most of the time barely visible impact damages (BVID) or even invisible without the assistant of special devices. Then, the development of detection techniques of these internal damages has become one the main issues in the aerospace and aeronautical industry. This damaged area is hard to detect, but it is possible to do so through several passive and active Non-Destructive-Testing (NDT) techniques. These techniques have been developed over several years of experience to monitor these internal damages in components and structures. The most widely used are based on Visual Testing (VT), Ultrasonic Testing (UT), Thermography testing, Radiographic Testing (RT), Electromagnetic Testing (ET), Acoustic Emission (AE), Acousto-Ultrasonic testing and Shearography Testing [5].

A procedure has been established to study the influence of the damages induced by low energy impact on composites plates through a set of experimental tests. The main goal is to evaluate the residual strength after a low energy impact. The experimental procedure consists of the following phases:

1. Impact test on an undamaged specimen at a controlled low energy in a drop tower.
2. Damage characterization by means of the proper NDT technology.
3. Compression After Impact (CAI) test is carried out to check the remaining strength in the composite plate with internal damage.

This procedure is the most widely used in the aeronautical and aerospace industry to evaluate these characteristics of the laminate. Moreover, it is used to evaluate the effectiveness of the repair method carried out in the plate. In this way, the residual strength can be compared with the undamaged and damaged plate.

(a) Impact test frame. (b) Ultrasonic C-Scan image. (c) CAI test frame.

Figure 1.3: Experimental procedure for CAI test [6].

If these damages are not monitored and repaired, an unexpected catastrophic failure in the whole structure may result. This is why in the aeronautical industry an internal damaged area thershold has been established to determine when to repair the component. The most traditional repairing method of CFRP laminates and the only one that is certificated in the aeronautical industry, is to remove the damaged area and replace it.However, this technique adds weight to the structure and, also, it takes a lot of time for it to carry it out. So, an effort is being done to find more efficient strategies. One of these other methods is the re-infiltration with low viscosity resin [7]. This technique needs to know in advance the geometry of the internal damage. In this way, with a drilling strategy that connect every cavity, the repair could be done with just one injection point and one or more vents. Similarly, *Hautier, M. et al.* [8] propose this infiltration method.

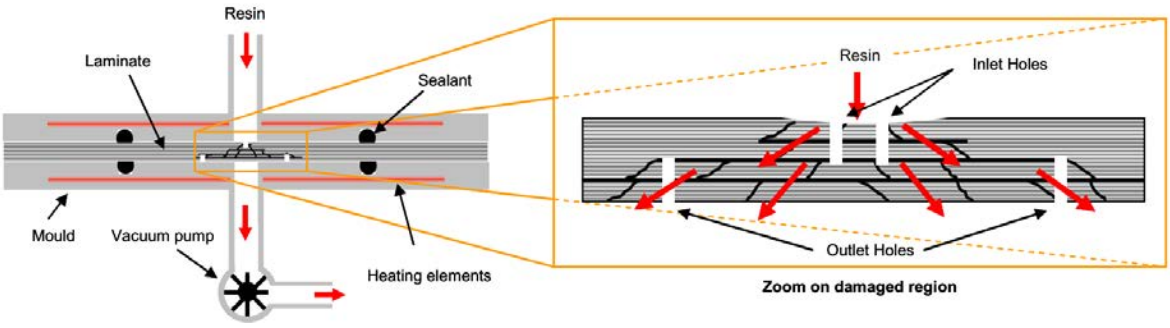

Figure 1.4: Principle of infiltration method [8].

Several studies consider the repair specimens under CAI tests in order to quantify the quality of it. Besides, some of them combine the repair with fatigue tests like [9] and [10]. However, the effect of fatigue and repairs are not an objective to evaluate in this thesis. They are topics to consider in future studies.

1.2 Problem definition and physics

There are many factors intervening in the failure load of a standard CAI test, which is meant for thick composite laminated, such as layers materials failure and local damaged area due to the impact with matrix cracking, fiber ruptures and delaminations. But, when the same test is carried out with thin plates, an extra difficulty is added. Unlike in thick plates the failure due to the local damage take place before reaching the buckling load of the plate, in thin plates the failure take place with a post-buckled shape.

Matrix cracking, fiber ruptures and delaminations are the typical damages observed in experimental tests where the impact does not penetrate the target. After the impact, the laminate gets a matrix cracking pattern through the thickness. They can be classified as tensile cracks or shear cracks. On the one hand, tensile cracks are formed when in-plane normal stresses exceed the transverse tensile strength of the layer. On the other hand, shear cracks are formed at an angle from the mid-surface, close to the normal direction of the laminate, where the transverse shear stresses are quite large.

When the impact take place on thick laminates, the plate bending is small and the contact stresses are quite high in the surface impacted. This induces matrix crackings and fiber breakage in the surface of the first layer and the matrix cracking progress in a conical pattern through the thickness as can be seen in Figure 1.6. However, for thin laminates, the bending is larger and, in consequence, the bending stresses are the most significant in the opposite surface of the impact. These are tensile stresses and also start with matrix cracking and fiber breakage in the opposite ply to the impact. Then, the matrix cracking grows through the layers in a invert conical pattern

(a) Shear crack. (b) Tensile crack.

Figure 1.5: Types of matrix cracks due to impacts on composites [3].

as can be seen also in Figure 1.6.

(a) Conical pattern in thick laminates. (b) Reversed conical pattern in thin laminates.

Figure 1.6: Matrix cracking patterns in laminated composites [3].

These matrix cracks induce delaminations at ply interfaces which are the debonding between adjacent layers. This type of damage seriously reduce the strength of the laminate and also could affect its stiffness. Delaminations only occurs in interfaces located between layers with different orientations. Some research actually pointed out that adjacent layers with the same orientation have not a real interface between them, and they behave as a single layer with greater thickness. The usual shape of these delaminated areas is similar to a oblong or a peanut where its axis is oriented in the fibers direction. But, delamination shapes are considerably irregular.

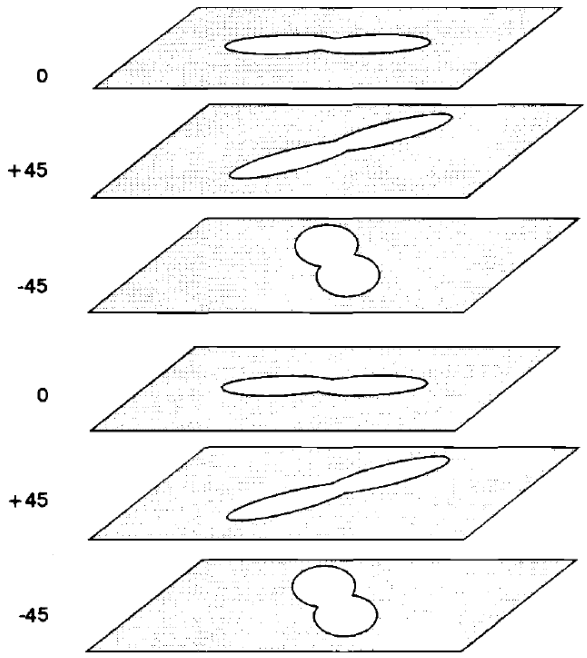

Figure 1.7: Delaminations shape and orientation [3].

Although all these damages in the laminate are present in the samples tested for this project, the delaminations influence in the ultimate load of the CAI test is the most significant damage, as it has been said by *Abrate, S.* [3]. Summarizing, compression failure will be caused by buckling and delamination growth. Initial matrix cracking and fiber breakage effects will be neglected in the finite elements models.

The interaction between the stability of a plate with delaminations and the growth of this delaminations can be explained with the simplification of a plate with a unique delamination like in Figure 1.8.

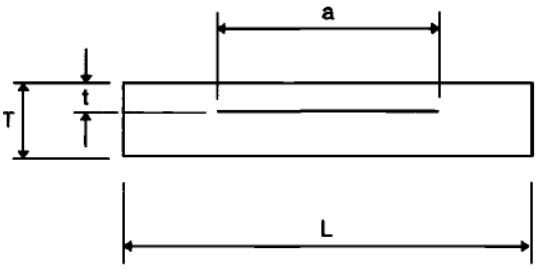

Figure 1.8: Sketch of a laminate with a delaminated area [3].

Depending on the global laminate stiffness and the local stiffness of the plies with delaminations, 3 different buckling modes can happen like in Figure 1.9. First, when the buckling load of the delaminated ply is much lower than the global buckling load of the laminate, the local buckling of this ply act alone. Secondly, in the opposite case where the global buckling load is much lower than the delaminated ply area, the buckling happens to all the laminate in the same direction. Finally, when the stiffness of the ply area delaminated and the global stiffness of the laminate are similar, both buckling (local and global) act at the same time but in different directions.

(a) Local buckling. (b) Global buckling. (c) Local-global buckling.

Figure 1.9: Buckling modes of a laminate with delaminations [3].

To sum up, these three modes may be developed in thin laminates. But, as the failure happens with a load larger than the laminate buckling load, the local mode becomes local-global mode eventually. This local-global mode is the most likely failure because of a delamination growth. Laminates with global buckling alone tend to fail due to maximum laminate strength are reached at some moment.

1.3 Description of the materials used

The samples used in all the tests of this project, have been extracted from a panel manufactured by the company *ClipCarbono (www.clipcarbono.com)* through pressure moulding process. The laminate is made of two different ply materials. One is an continuous unidirectional (UD) carbon fiber prepreg. The other one is a twill 2/2 weave (W) carbon fiber prepreg. Both with epoxy resin.

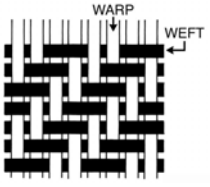

Figure 1.10: Example of a twill 2/2 weave fibers pattern.

The total thickness of the panel laminate is $2.132\,[mm]$ and it has 14 plies (2 woven and

12 unidirectional). The thickness of each ply has been computed as $t_{UD} = 0.144\ [mm]$ and $t_W = 0.202\ [mm]$ from a cross section of the laminate.

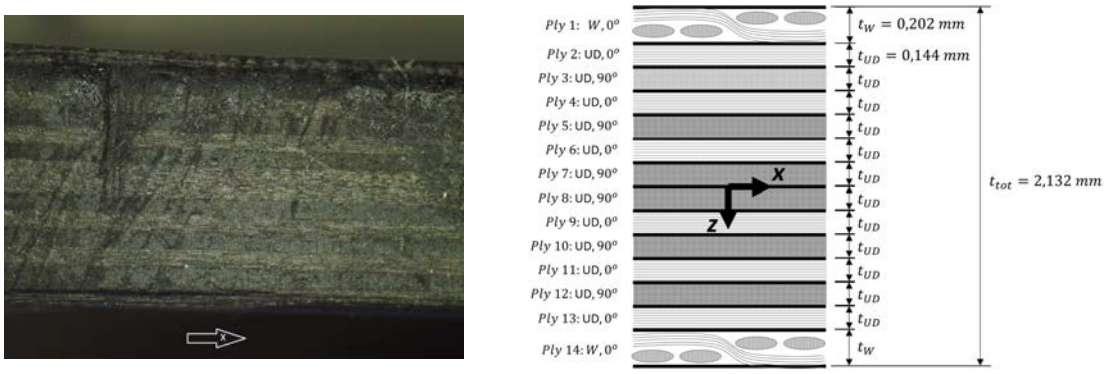

Figure 1.11: Panel plies layup.

The plies orientations and stacking follow the structure of an orthotropic laminate, which is at the same time a symmetrical and crossed-ply laminate. Its behavior is like an orthotropic lamina and has three planes of symmetry. The Tsai identification code of the laminate can be written as: $[0_W, 0_{UD}, 90_{UD}, 0_{UD}, 90_{UD}, 0_{UD}, 90_{UD}]_S$.

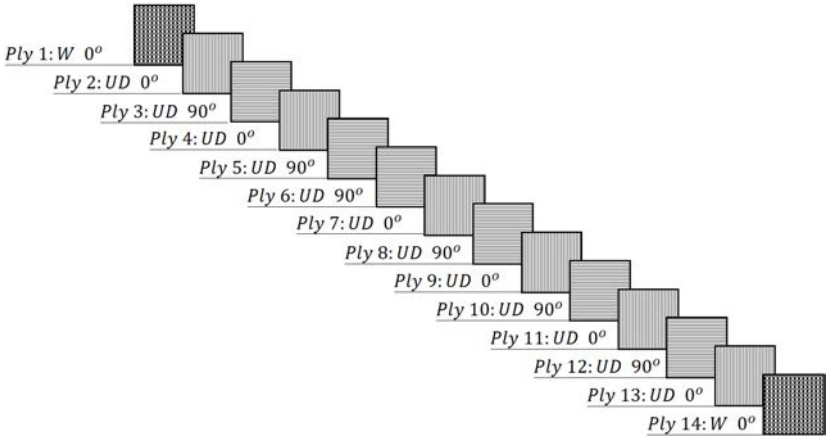

Figure 1.12: Laminate plies orientations.

As regards mechanical and physical properties of these two different plies, are not available. Nevertheless, some data from fibers and resin are available with which the mechanical properties of the plies will be computed in the next chapter. First, the filaments yarns which have been manufactured by the company TEIJIN CARBON EUROPE GMBH have the properties shown in Table 1.1.

Fiber Properties		
$E_{1,f}$	$[GPa]$	240
$\sigma_{f,F}$	$[MPa]$	4400
$\varepsilon_{f,F}$	$[\%]$	1.8
ρ_f	$[kg/m^3]$	1770
Yarns	$[-]$	$3K$

Table 1.1: Carbon fiber properties from TEIJIN CARBON EUROPE GMBH.

Finally, the prepreg layers and its resin are manufactured by the company SGL GROUP THE

CARBON COMPANY GMBH. The only data that can be extracted from them is the approximate value of the failure stress of an unidirectional laminate in the fiber direction, which is $2300\,[MPa]$.

1.4 Objectives

The main goal of this project is to compute the failure load of a thin composite laminated plate initially damaged under the CAI test by creating a numerical model with the commercial finite elements software Abaqus and validate it with experimental CAI tests results.

In order to fulfill this main goal, several milestones have to be achieved. The materials properties of the laminate plies have to be estimated. Besides, different experimental testing has to be done in order to create internal damage in the samples and, also, to characterize it. Finally, a finite elements model must be constructed with a laminate without initial damage, validate with experimental results and this should be the basis from which the model with initial damage is created.

Chapter 2

State of the Art

2.1 Introduction

The increase in the use of composite materials in the aerospace industry has accentuated the problem of damage caused by low-energy impacts on composite materials. As stated in the introduction section, these impacts may cause damages such as indentation, delamination, matrix cracking, fiber/matrix debonding and fiber breakage. Due to these damages, composites can exhibit a significant reduction in strength which has to be taken into account for a sufficient damage tolerant design. The strength loss due to impacts is experimentally analyzed with Compression-After-Impact (CAI) tests. The experimental approach concerns, first, an impact test on undamaged specimens at a controlled low energy usually carried out with a drop tower. Secondly, the damage is inspected by Non-Destructive-Inspection technology such as ultrasonic scanning. Finally, a CAI test is performed in order to check the residual strength of the composite plate with its internal damage.

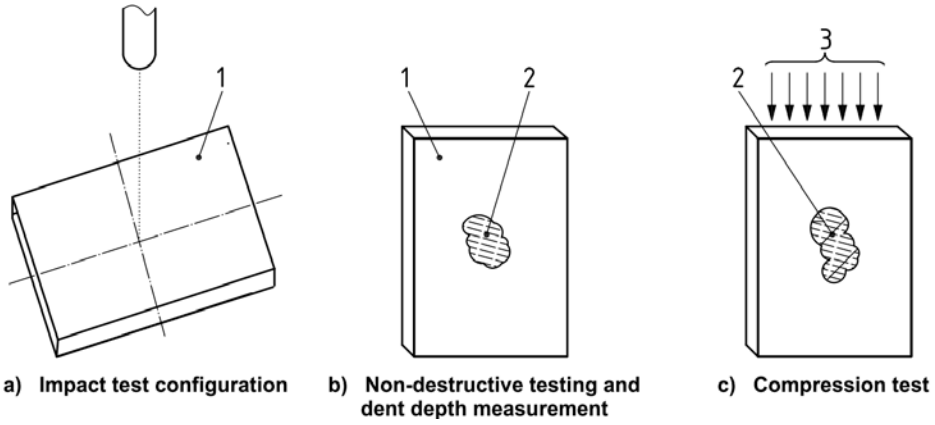

Figure 2.1: Principle of the compression-after-impact test [11].

A better understanding of the behavior of impacted composite laminates under compression loading is fundamental for the design and maintenance of more damage tolerant aerospace structures. As a consequence, there is a lot of experimental and numerical research available in open literature that is concerned with CAI testing. Lots of the experimental research has been carried out for thick laminates to measure the post-impact strengths of laminate plates. Some of them compare maufacturing methods suchs as autoclave and out-of-autoclave [12]. Also, the post-impact strengths have been studied for different fiber weave patterns ([13], [6] and [14]), the influence of the cross-ply stitching [15] and different ply orientations and staking sequence in laminates [16]. Several authors try to evaluate the influence of other parameters such as the

temperature [17], [18] and back pressure [19].

Besides the experimental research, other authors have tried to find numerical models which are capable to predict the CAI failure load and failure mechanisms for thick laminates, too. For example, *T. Ishikawa, S. Sugimoto et al.* [20] have carried out an experimental and numerical study of quasi-isotropic thick plates with two resin systems, CF/PEEK and CF/epoxy, using SACMA [21] and NASA CAI test methods combined with moiré topography and thermo-mechanical stress analysis measuring system. In this paper, they model a geometric idealization of the delaminated areas based in ultrasonic C-Scanning in order to predict the local buckling of these zones. *C. Soutis and P.T. Curtis* [22] develop a similar experimental and numerical study for thick laminates, too, with different ply stakings and resin system. Through ultrasonic C-scanning and X-ray shadow radio-graphs, they determined that the delaminated zones in the through-thickness direction was almost cylindrical and they assumed that it could be modeled as a notched plate. More over, to model the delamination growth, they used a cohesive zone model.

Research efforts have been done for thin-walled laminates, too, where global buckling typically occurs before failure can be observed in CAI testing. As a result, the failure mechanisms due to the impact damage interact with the global buckle. Therefore, some authors try to avoid buckling during experimental testing with modifications to the test device (cp. e.g. [23] and [24]) because geometric imperfections (i.e. mainly initial out-of-plane deformations) influence the CAI failure load of thin-walled composite plates with initial delaminations in CAI testing [25]. However, a lot of aerospace composite laminate panels are thin-walled and are potentially exposed to impact damages. For these panels under compression loads, the local failure mechanisms induced by impacts occur simultaneously to global buckling. As a consequence, global buckling interacts with the local failures typically induced by the damaged area. This interaction must be understood in order to design appropriately damage tolerant laminate panels. *H. Sekine, N. Hu and M.A. Kouchakzadeh* [26] have developed a numerical model for idealized elliptical delaminations where this global-local interaction has been evaluated.

Finite element models have been developed by several authors with different strategies and material models depending on the phenomena they were interested in investigate. For example, to model the initial delaminated zones in CAI tests, there are two main strategies, some authors try to create them manually through idealized geometries such as elliptical and circular shapes (cp. e.g. [27] and [28]), or even more realistic shapes according to the inspections made by NDT techniques [29]. Some others, instead of idealize this damaged areas, they try to compute the inter- and intralaminar damages by simulating the impact test. Then, they simulate the CAI test with all the damages already introduced in the model (cp. e.g. [30] and [31]). Continuum damage mechanics-based failure criteria, such as Maximum stresses, Hashin's, Puck's and Tsai-Wu (cp. e.g. [30] and [31]), have been used to model intralaminar failure. Regarding the delamination crack growth, also different models have been used such as Virtual Crack Closure Technique (VCCT) [27] and Cohesive Zone Models (CZM) with tie contacts [30] or cohesive elements [31].

2.2 Impact test

The aim of the impact test phase is to cause barely visible internal damage (BVID) in a composite laminated plate. Over the years different impact test apparatus have been used such as the gas gun, drop-weight and pendulum (Figure 2.2). Depending on the type of impact intended to test one of these apparatus have a better agreement with the real operation damage. For example, if the aim is to test the damage caused by flying debris during aircraft take-off and landing, the gas gun apparatus is the best option because it is suited for small projectiles with high-velocity. However, if the impact studied is more like an accidental tool drop on a composite structure, the drop-weight test fits better, because it can be simulated with a larger projectile at low-velocity. The pendulum test would be equivalent to the drop-weight test. Both, drop-weight and pendulum

tests, have to include a system to prevent multiple impacts after the impactor bounces back up.

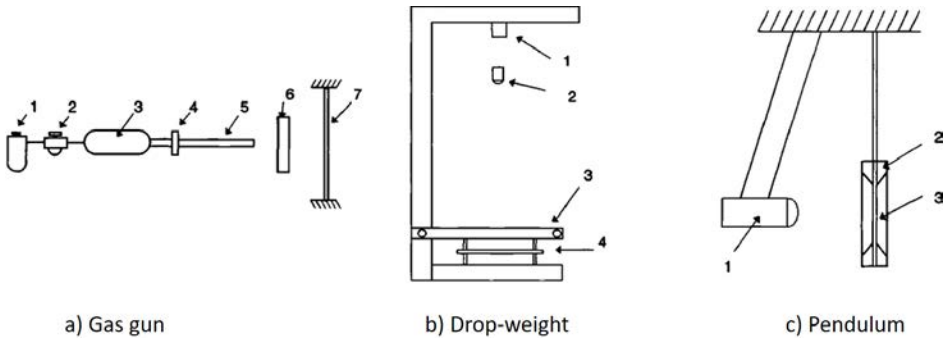

Figure 2.2: Apparatus used for impact test [3].

The CAI standards recommend to use for impact test phase a drop-weight tower like in Figure 2.3. This machine should have an hemispherical head impactor of $16 \pm 0.1\ [mm]$ in diameter and a suitable guide mechanism.

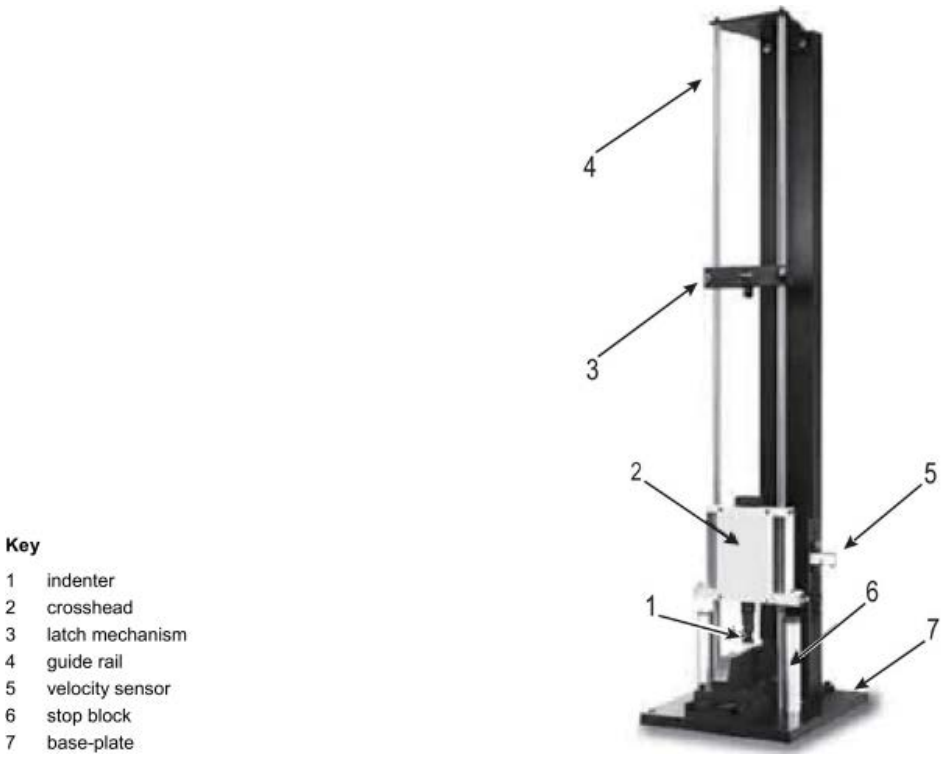

Figure 2.3: Instrumented drop-weight impact device with double guide rails [11].

Also, the specimen support fixture has a significant influence in the damage induced during the impact. The standards recommend to use a fixture like in Figure 2.4, where the specimen is fixed in its four corners by rubber-tipped clamps. Other fixtures more restrictive could induce a larger damage in the specimen for the same impact energy level. The recommended fixture should have a rectangular open window of $125 \pm 1\ [mm]$ in length and $75 \pm 1\ [mm]$ in width.

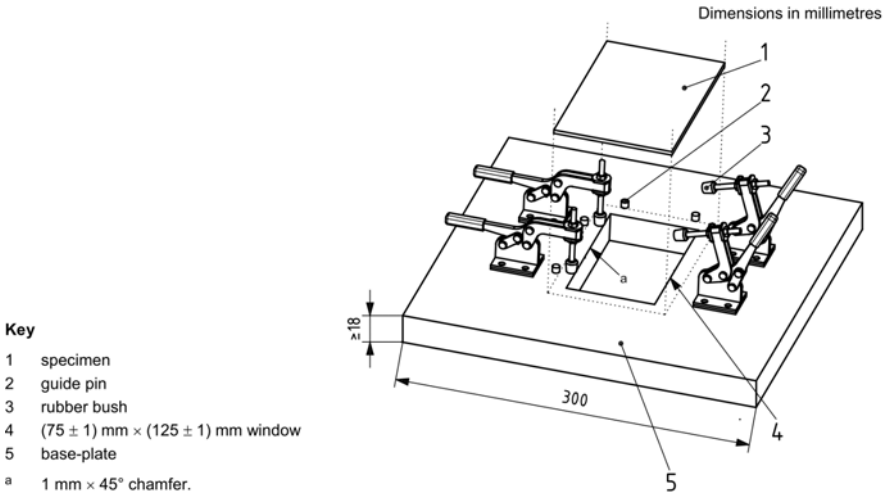

Figure 2.4: Example of a specimen support fixture [11].

2.3 Damage inspection methods

The damages caused by low energy impacts are most of the time BVID or even invisible without the assistant of special devices. Therefore, the standards recommend to use NDT techniques to detect the damaged areas, in particular ultrasonic C-scan. Nevertheless, other techniques are also possible such as X-ray radiography with penetrant system and pulse thermography system may be used too. X-ray radiography with penetrant is most suitable for detecting fiber breakage and matrix cracks in laminates. The typical damages observed in CAI tests are shown in Figure 2.5. All of them are valid damages for CAI test standards.

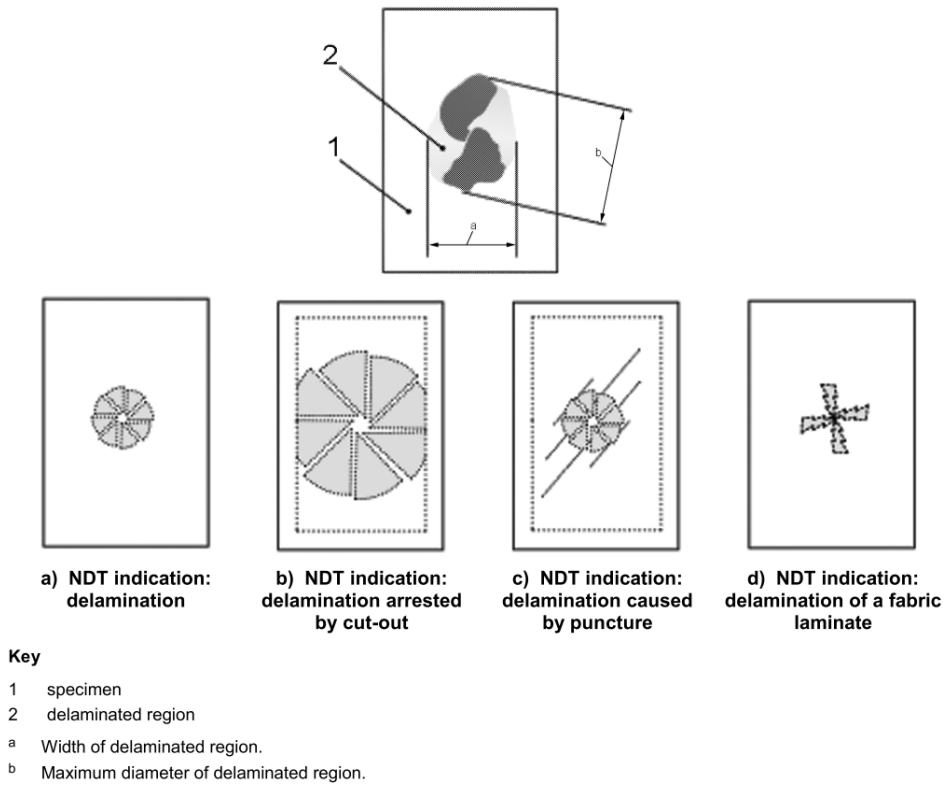

Figure 2.5: Example of a delamination shape (upper diagram) detected by ultrasonic C-scan and (lower four diagrams) typical damage patterns [11].

The ultrasonic C-scan allow to identify the depth and size of internal delaminations caused by impacts or fatigue loading. The principle on which it works is a very high frequency signal (up to 50 MHz) transmitted to the specimen by a transducer. The signal require a coupling medium between the transducer and the specimen such as water, because the signal can't travel through the air. When the signal sent from the transducer arrives to the back surface of the laminate or finds some defect, it is partially reflected and received in the transducer. From this reflected signal, can be measured the depth at which damages are located from the time it takes to get the transducer again. Also, the size of the damage projected on the surface at which the transducer is inspecting the specimen. This technique is very useful for aircraft inspections, but it can only detect the first damage. It is not posible to see anything behind (deeper) the first damage projection.

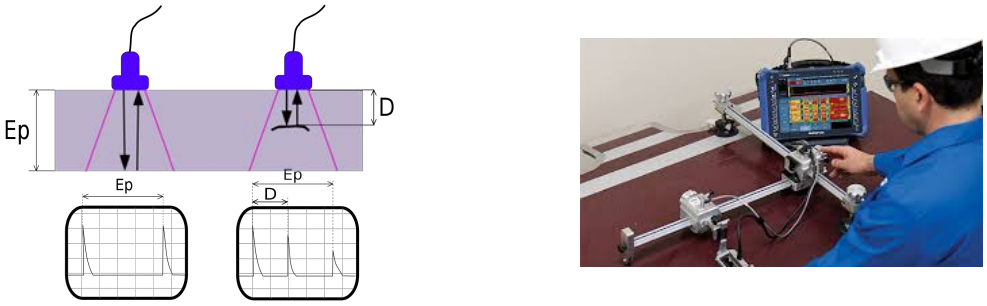

Figure 2.6: Example of ultrasonic C-scan principle and application.

Pulse thermography is also a non-destructive technique used to find defects in aircraft and aerospace components. This technique allows materials to be inspected very quickly for near-surface defects and bonding weaknesses. It can be applied over large areas without the need of direct contact with the component. In pulse thermography the material is heated up equally using a very short heat pulse where zones with defects have a different heat transference. Defects, bonding faults and corrosion can be observed using a thermographic camera on the surface.

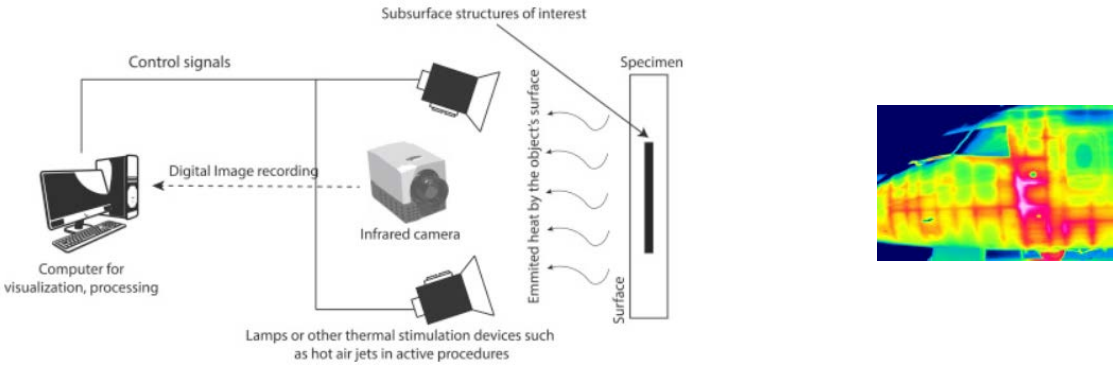

Figure 2.7: Example of pulsed thermography system configuration [32].

Finally, X-ray radiography is a technique able to deal with all different types of damages. For example, ultrasonic methods are suitable for examining delaminations, but cannot easily deal with vertically oriented cracks or multiple/stacked delaminations. X-ray radiography of damage generally consist of the penetration, with a liquid having a high X-ray absorption coefficient, of the cracked areas. This penetrant project shadows on the contact print which delineate the damaged regions. Based on this technology, X-ray Computed Tomography (CT) has been developed to get a three-dimensional representation of the complete damage in the specimen inspected. A CT image is the slice of the object scanned with a certain thickness. If an object has tomographic

imaging from multiple orientations, a three-dimensional/volume image can be obtained of the internal damage. This technique is very expensive and cannot be used in a field inspection.

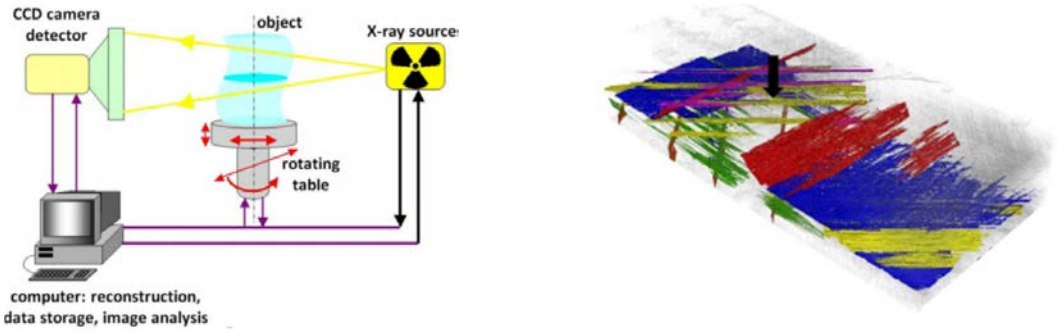

Figure 2.8: Example of X-ray Computed Tomography system (cp. [33] and [34]).

2.4 Compression-After-Impact test

There are different standards used in the aeronautical industry which describe the method to determine the low speed impact resistance characteristics of fiber reinforced plastics. These standards are: ISO 18352 [11], Airbus AITM 1-0010 [35], EN 6038 [36], ASTM D 7137 [37], Boeing BSS 7260 [38], DIN 65561 [39] and SACMA SRM 2R-94 [21]. Although the sample dimensions for both types of frame are the same, $150\,mm \times 100\,mm$. They can be classified in two groups regarding the type of frame used in the CAI test:

A. **Frame for ISO 18352 [11], Airbus AITM 1-0010 [35], EN 6038 [36]:** The specimen sides are restrained by knifes-edges. The upper and lower end of the specimen are clamped to the fixture. Therefore, it is considered as simply supported in the sides, and clamped in the lower and upper ends.

B. **Frame for ASTM D 7137 [37], Boeing BSS 7260 [38], DIN 65561 [39], SACMA SRM 2R-94 [21]:** The specimen sides are restrained by knife-edges. The fixture base and load plates are applied directly to the ends of the specimen. Therefore, it is considered the four sides as simply supported.

(a) Frame used by Airbus (INSTRON company) (b) Frame used by Boeing (Wyoming company)

Figure 2.9: Main CAI frames used in the aeronautical industry and for research.

In Figure 2.10, acceptable failure modes for CAI tests are shown, which can be combined with minor end crushing at a point along the compressively loaded edges of the specimen. If the end crushing is significant, the test won't be acceptable. Moreover, if global buckling or excessive bending occurs, the test is not valid for this standard.

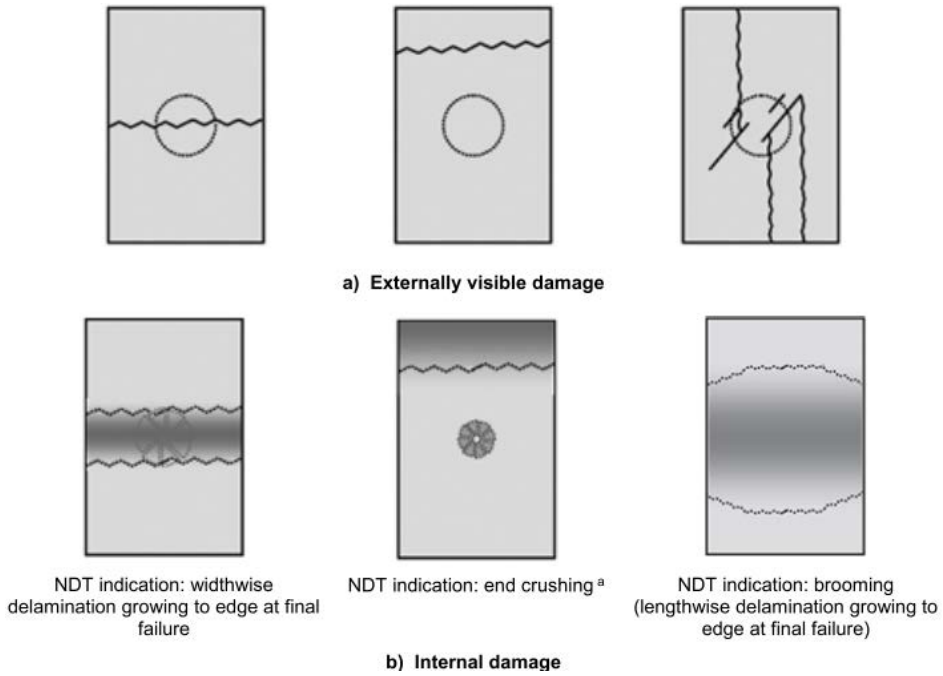

Figure 2.10: Examples of acceptable failure modes in compression-after-impact tests [11].

However, in thin laminates, global buckling occurs before the failure load. As a concequence, the stresses concentration induced by the upper clamp cause end crushing and it has a significant influence in the failure load. Therefore, in this project a modified frame developed by *M. Linke and J. A. García-Manrique* [40] is going to be used. The frame has some modifications of the by AIRBUS standard. Both frames are compared in Figure 2.11.

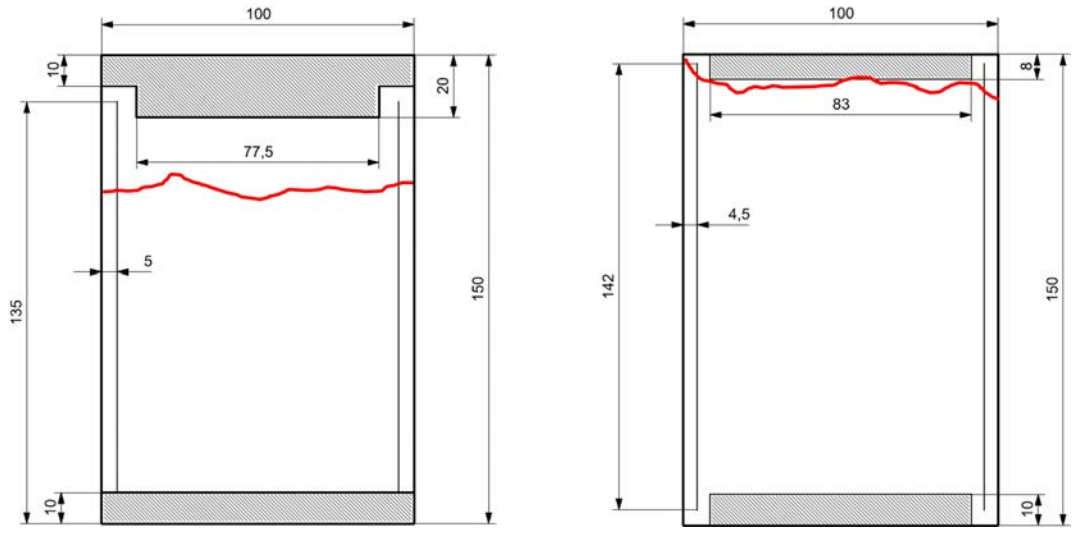

(a) HAW Hamburg CAI frame

(b) AIRBUS CAI frame

Figure 2.11: Specimen free window and constrains geometry for two different CAI frames.

As can be seen, this frame has lower free area and also tries to avoid the high stresses in the free edges of the upper corners. These high stresses in the standard frame are induced due to the post-buckling behavior when thin laminates are tested. Therefore, the rupture line is always located next to the top clamp, lowering the real failure load of the laminate. With the modified frame, the failure load is increased and the rupture line is more likely to be located far from the clamp.

Chapter 3

Theoretical framework

In this project some theoretical background is needed for the analytic and numerical computations carried out to create the finite element model of the CAI test. Therefore, in this chapter has been explained all the theoretical framework used in the next chapters. In particular, some background it is required to define the materials elastic and failure properties. The elastic properties definition of the plies laminate apply theoretical and semi-empirical micromechanic models and the Classical Laminate Theory (CLT). Regarding the strength of the plies, the Hashin's failure model for fiber reinforced materials is used in this project. Also, the delamination model used for the plies interfaces is explained. Moreover, due to the CAI test in this project is carried out with thin plates, the computations of the buckling load and the post-buckling behavior of plates is very important because the failure will happen after its buckling load. Finally, some background for the finite elements calculations is explained, such as the type of elements and computation solvers that have been used in this project.

3.1 Micromechanic models

The main goal of using the micromechanic models is to calculate the values of the elastic properties of orthotropic plies in its local axes. Not all the properties of the material are needed because in the numerical model will be assumed that the plies work in the plane stress state. The properties essentials for the plane stress state are the elastic modulus of the plies in the longitudinal and transverse direction (E_1 and E_2), also the in-plane poisson's ratio (ν_{12}) and the in-plane shear modulus (G_{12}). All the micromechanical models used in this section are extracted from the book *Principles of composite material mechanics* [41], which recommend analytic and semi-empirical models micromechanic depending on the reinforcement type and direction. These properties are calculated from the fiber and resin properties. Carbon fiber is a very anisotropic material, this is why is required the material properties in every direction ($E_{1,f}$, $E_{2,f}$, $\nu_{12,f}$, $G_{12,f}$). But the resin matrix is epoxy based and it is assumed as an isotropic material with elastic modulus E_m and poisson's ratio ν_m, where the shear modulus G_m is computed from them.

First, for unidirectional continuous fiber reinforced plies, the effective modulus in the fiber direction can be calculated with sufficient accuracy by the rule of mixtures:

$$E_1 = E_{1,f}\, V_f + E_m \left(1 - V_f\right) \tag{3.1}$$

Poisson's ratio of the UD lamina can be computed also by the rule of mixtures, although the result is not as precise as the elastic modulus in the fiber direction.

$$\nu_{12} = \nu_{12,f}\, V_f + \nu_m \left(1 - V_f\right) \tag{3.2}$$

The rule of mixture has not the sufficient accuracy to obtain the rest of the lamina properties.

Therefore, a semi-empirical Halpin-Tsai model is used instead:

$$\frac{M}{M_m} = \frac{1 + \xi\ \eta\ V_f}{1 - \eta\ V_f} \tag{3.3}$$

Where, η is:

$$\eta = \frac{\frac{M_f}{M_m} - 1}{\frac{M_f}{M_m} + \xi} \tag{3.4}$$

The parameter M is the elastic constant to compute and could be: E_2, G_{12} or v_{23}. Parameters M_f and M_m are the elastic constants of the fiber and matrix: $E_{2,f}$, $G_{12,f}$ or $v_{23,f}$ and E_m, G_m or v_m. The last parameter ξ is known as the curve fitting parameter which is also a measure of the degree of reinforcement of the matrix by the fibers. After several experiments were carried out, it was recommended to use $\xi = 2$ for E_2. Likewise, for G_{12} it was recommended to use $\xi = 1$ or $\xi = 1 + 40\ V_f^{10}$ if $V_f > 0.5$.

Secondly, for a woven ply there are different models to use. The Young's modulus in the 1 and 2 direction are assumed to be the same:

$$E_1 = E_2 = V_f \left(\frac{E_{1,f}}{2} + \frac{3\ E_m}{2} \right) + E_m \tag{3.5}$$

Now, for the in-plane shear modulus, the following formula is used:

$$G_{12} = E_m\ \frac{4\ V_f + 1}{3} \tag{3.6}$$

With this both properties already calculated, the poisson's ratio can be estimated too:

$$v_{12} = \frac{G_{12}}{E_1} \tag{3.7}$$

3.2 Classical Laminate Theory

The Classical Laminate Theory (based on books [41] and [42]) is an evolution from the classical theory of homogeneous isotropic plates. Using CLT, it is possible to analyze laminates with arbitrary plies orientations. This may have coupling effects between extensional, flexural and torsional deformations. This theory include in-plane loading due to shear and axial forces, but also bending and torsional moments. However, it is assumed that the laminate is in a state of plane stress and interlaminar stresses are neglected. Despite this limitations, this theory is able to predict correctly the stiffness and strength tendencies of a laminate. The hypothesis assumed for this theory are:

(a) Materials homogeneous and transversely isotropic.

(b) The in-plane strains ε_x, ε_y and γ_{xy}, are small compared with the unity (each ply responds to the lineal Hooke's law).

(c) The displacements u, v, and w are small compared to the plate thickness (ensure linearity). Tangential displacements u and v are linear functions of the z coordinate.

(d) The plate is an orthotropic laminate perfectly bonded together with an infinitesimal interfaces (continuum displacements through the thickness).

(e) The thickness of the plate, t, is constant and much smaller than the plate edges, a and b.

(f) The laminae are in a state of plane stress ($\sigma_z = 0$).

(g) The transverse normal strain ε_z is negligible.

(h) Any straight line normal to the laminate mid-surface remains straight. Therefore, transverse shear strains γ_{xz} and γ_{yz} are negligible. This is valid for pure bending or lengths greater than 10 times the laminate thickness.

(i) Transverse shear stresses τ_{xz} and τ_{yz} vanish on the plate surfaces defined by $z = \pm t/2$.

Some notation has to be introduced in order to formulate the CLT. First, the stacking numbering order is set from the top-down direction. Secondly, the position of each layer is measured from the middle surface of the laminate, where there is the plane $z = 0$. Finally, the orientation the laminated coordinate system is defined by the X, Y and Z directions. Likewise, the plies orientations are defined by 1 and 2 directions rotated an Φ_k angle from the X and Y directions of the laminate, and the 3 direction is coincident with the Z direction of the laminate. A scheme of this notations are shown in the following picture.

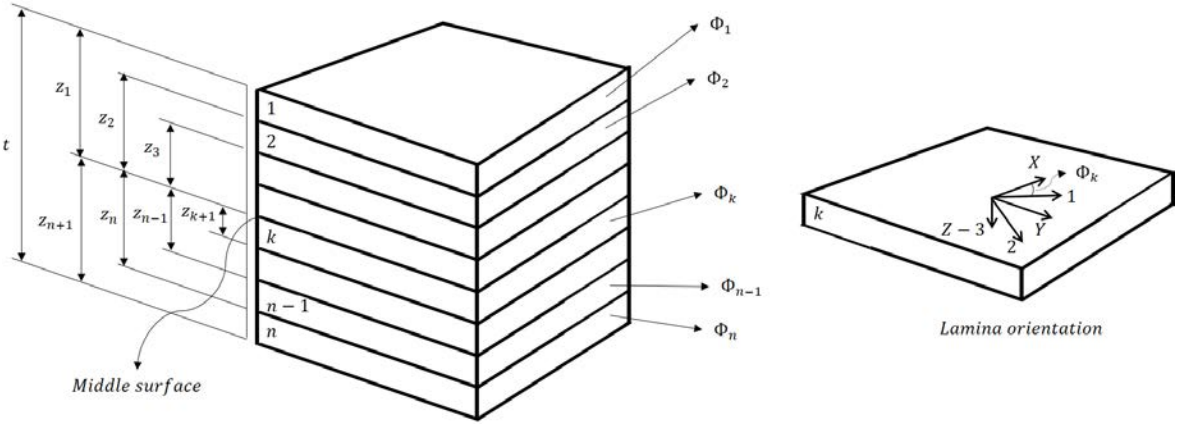

Figure 3.1: Stacking order formulation [42].

Furthermore, the relationship between the displacements and deformations is needed to be defined following the hypothesis assumed before. Assuming that the middle surface of the laminate is in the plane XOY of the global coordinate $OXYZ$. The displacements u, v, w are associated to the coordinates x, y, z respectively. The displacements associated to the middle surface are named as u^0, v^0, w^0. Due to the assumption $\varepsilon_z = 0$, the displacements in the z direction do not depend on the z coordinate:

$$w(x,y) = w^0(x,y) \tag{3.8}$$

Assuming that the section $ABCD$ from in Figure 3.2 has moved to the position $A'B'C'D'$. Because of the hypothesis that $\gamma_{xz} = 0$ and $\gamma_{yz} = 0$, the displacements can be formulated as :

$$u(x,y,z) = u^0(x,y) - z\,\sin\beta \tag{3.9}$$

Now, also with the assumption of small displacements, this approximation can be done:

$$\sin\beta \approx \tan\beta = \frac{\partial w^0}{\partial x} \tag{3.10}$$

Then, the final displacements formulation is:

$$u(x,y,z) = u^0(x,y) - z\,\frac{\partial w^0}{\partial x} \tag{3.11}$$

$$v(x,y,z) = v^0(x,y) - z\,\frac{\partial w^0}{\partial y} \tag{3.12}$$

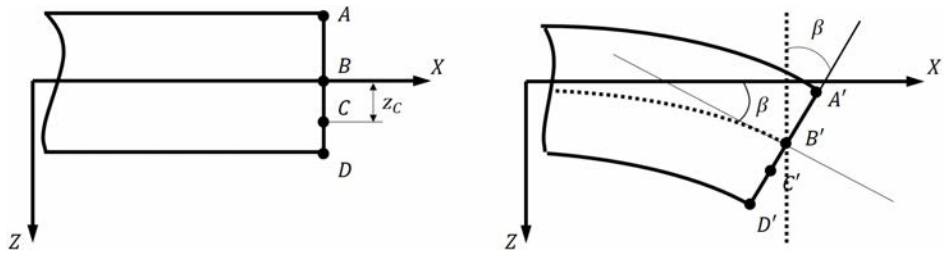

Figure 3.2: Coordinate system, in-plane forces and flexural and torsional momentum positive directions in a plate theory [42].

Now, with the Cauchy equations, the displacements can be related with the deformations:

$$\varepsilon_x = \frac{\partial u}{\partial x} = \varepsilon_x^0 - z\,\frac{\partial^2 w^0}{\partial x^2} = \varepsilon_x^0 + z\,K_x \tag{3.13}$$

$$\varepsilon_y = \frac{\partial v}{\partial y} = \varepsilon_y^0 - z\,\frac{\partial^2 w^0}{\partial y^2} = \varepsilon_y^0 + z\,K_y \tag{3.14}$$

$$\gamma_{xy} = \frac{\partial v}{\partial x} + \frac{\partial u}{\partial y} = \gamma_{xy}^0 - 2\,z\,\frac{\partial^2 w^0}{\partial x\,\partial y} = \gamma_{xy}^0 + z\,K_{xy} \tag{3.15}$$

In matrix structure is written as:

$$\begin{Bmatrix} \varepsilon_x \\ \varepsilon_y \\ \gamma_{xy} \end{Bmatrix} = \begin{Bmatrix} \varepsilon_x^0 \\ \varepsilon_y^0 \\ \gamma_{xy}^0 \end{Bmatrix} + z \begin{Bmatrix} K_x \\ K_y \\ K_{xy} \end{Bmatrix} \tag{3.16}$$

$$\{\overline{\varepsilon}\} = \left\{\varepsilon^0\right\} + z\,\{K\} \tag{3.17}$$

Where the first vector $\left\{\varepsilon^0\right\}$ are the deformations of the middle surface and the second vector $\{K\}$ are the middle surface curvatures.

$$\{K\} = \begin{Bmatrix} K_x \\ K_y \\ K_{xy} \end{Bmatrix} = \begin{Bmatrix} -\dfrac{\partial^2 w^0}{\partial x^2} \\ -\dfrac{\partial^2 w^0}{\partial y^2} \\ -2\,\dfrac{\partial^2 w^0}{\partial x\,\partial y} \end{Bmatrix} \tag{3.18}$$

Since the material coordinate system of each lamina forms an arbitrary angle respect to the laminate global coordinate system, the Hooke's law of every lamina has to be transformed to the laminate reference coordinate system:

$$\{\overline{\sigma}\} = \left[\overline{Q}\right]\left(\left\{\varepsilon^0\right\} + z\,\{K\}\right) \tag{3.19}$$

Where $[Q]$ is the stiffness matrix of an orthotropic lamina oriented in its local material coordinate system. For a specific layer inside the laminate, its matrix stiffness is written as $[Q]_k$.

$$[Q]_k = \begin{bmatrix} Q_{11} & Q_{12} & 0 \\ Q_{21} & Q_{22} & 0 \\ 0 & 0 & Q_{66} \end{bmatrix} = \begin{bmatrix} \dfrac{E_1}{1-\nu_{12}\,\nu_{21}} & \dfrac{\nu_{21}\,E_1}{1-\nu_{12}\,\nu_{21}} & 0 \\ \dfrac{\nu_{21}\,E_1}{1-\nu_{12}\,\nu_{21}} & \dfrac{E_2}{1-\nu_{12}\,\nu_{21}} & 0 \\ 0 & 0 & G_{12} \end{bmatrix} \tag{3.20}$$

Now, each layer stiffness matrix of the laminate has to be re-orientated from its local coordinate system to the global laminate coordinate system. The re-orientated matrix stiffness of each layer is named as $[\overline{Q}]_k$.

$$[\overline{Q}]_k = [T]_k^{-1}\,[Q]_k\,[R]\,[T]_k\,[R]^{-1} \tag{3.21}$$

Where the Reuter matrix $[R]$ and the rotational matrix $[T]_k$ are:

$$[T]_k = \begin{bmatrix} \cos^2\Phi_k & \sin^2\Phi_k & 2\,\sin\Phi_k\,\cos\Phi_k \\ \sin^2\Phi_k & \cos^2\Phi_k & -2\,\sin\Phi_k\,\cos\Phi_k \\ -\sin\Phi_k\,\cos\Phi_k & \sin\Phi_k\,\cos\Phi_k & \cos^2\Phi_k - \sin^2\Phi_k \end{bmatrix} \tag{3.22}$$

$$[R] = \begin{bmatrix} 1 & 0 & 0 \\ 0 & 1 & 0 \\ 0 & 0 & 2 \end{bmatrix} \tag{3.23}$$

The equilibrium equations of the CLT are calculated from the integrate through the thickness of the laminate. The in-plane forces and flexural and torsional momentum applied to the laminate are:

$$N_x = \int_{-t/2}^{t/2} \sigma_x\,dz \tag{3.24}$$

$$N_y = \int_{-t/2}^{t/2} \sigma_y\,dz \tag{3.25}$$

$$N_{xy} = \int_{-t/2}^{t/2} \tau_{xy}\,dz \tag{3.26}$$

$$M_x = \int_{-t/2}^{t/2} \sigma_x\,z\,dz \tag{3.27}$$

$$M_y = \int_{-t/2}^{t/2} \sigma_y\,z\,dz \tag{3.28}$$

$$M_{xy} = \int_{-t/2}^{t/2} \tau_{xy}\,z\,dz \tag{3.29}$$

Where N_x, N_y and N_{xy} are the forces per width length and M_x, M_y and M_{xy} are the moments per width length. The sign convention for this forces and moments are shown in the following picture:

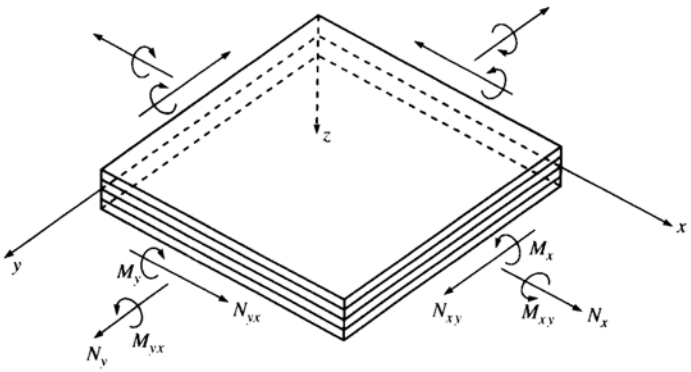

Figure 3.3: In-plane forces and flexural and torsional moments signs convention for plates [41].

Using the matrix notation:

$$\{N\} = \begin{Bmatrix} N_x \\ N_y \\ N_{xy} \end{Bmatrix} \tag{3.30}$$

$$\{M\} = \begin{Bmatrix} M_x \\ M_y \\ M_{xy} \end{Bmatrix} \tag{3.31}$$

So, considering that n is the number of laminae, the previous formula can be expressed as:

$$\{N\} = \int_{-t/2}^{t/2} \{\overline{\sigma}\}\, dz = \sum_{k=1}^{n} \int_{z_k}^{z_{k+1}} \{\overline{\sigma}\}\, dz = \sum_{k=1}^{n} \left[\overline{Q}\right]_k \left(\int_{z_k}^{z_{k+1}} \left\{\varepsilon^0\right\} dz + \int_{z_k}^{z_{k+1}} z\, \{K\}\, dz \right) \tag{3.32}$$

$$\{M\} = \int_{-t/2}^{t/2} \{\overline{\sigma}\}\, z\, dz = \sum_{k=1}^{n} \int_{z_k}^{z_{k+1}} \{\overline{\sigma}\}\, z\, dz = \sum_{k=1}^{n} \left[\overline{Q}\right]_k \left(\int_{z_k}^{z_{k+1}} \left\{\varepsilon^0\right\} z\, dz + \int_{z_k}^{z_{k+1}} z^2\, \{K\}\, dz \right) \tag{3.33}$$

These equations can be expressed as:

$$\{N\} = [A]\, \left\{\varepsilon^0\right\} + [B]\, \{K\} \tag{3.34}$$

$$\{M\} = [B]\, \left\{\varepsilon^0\right\} + [D]\, \{K\} \tag{3.35}$$

Where the matrix $[A]$, $[B]$ and $[D]$ define the stiffness matrix of the laminate:

$$A_{ij} = \sum_{k=1}^{n} \left[\left(\overline{Q}_{ij}\right)_k \int_{z_k}^{z_{k+1}} dz \right] = \sum_{k=1}^{n} \left[\left(\overline{Q}_{ij}\right)_k \left(z_{k+1} - z_k\right) \right] \tag{3.36}$$

$$B_{ij} = \sum_{k=1}^{n} \left[\left(\overline{Q}_{ij}\right)_k \int_{z_k}^{z_{k+1}} z\, dz \right] = \frac{1}{2} \sum_{k=1}^{n} \left[\left(\overline{Q}_{ij}\right)_k \left(z_{k+1}^2 - z_k^2\right) \right] \tag{3.37}$$

$$D_{ij} = \sum_{k=1}^{n} \left[\left(\overline{Q}_{ij}\right)_k \int_{z_k}^{z_{k+1}} z^2\, dz \right] = \frac{1}{3} \sum_{k=1}^{n} \left[\left(\overline{Q}_{ij}\right)_k \left(z_{k+1}^3 - z_k^3\right) \right] \tag{3.38}$$

Finally, the total stiffness matrix of the laminate is expressed as:

$$\begin{Bmatrix} \{N\} \\ \{M\} \end{Bmatrix} = \begin{bmatrix} [A] & [B] \\ [B] & [D] \end{bmatrix} \begin{Bmatrix} \left\{\varepsilon^0\right\} \\ \{K\} \end{Bmatrix} \tag{3.39}$$

Each one of the matrix has its elements in the following location:

$$[A] = \begin{bmatrix} A_{11} & A_{12} & A_{16} \\ A_{12} & A_{22} & A_{26} \\ A_{16} & A_{26} & A_{66} \end{bmatrix} \tag{3.40}$$

$$[B] = \begin{bmatrix} B_{11} & B_{12} & B_{16} \\ B_{12} & B_{22} & B_{26} \\ B_{16} & B_{26} & B_{66} \end{bmatrix} \tag{3.41}$$

$$[D] = \begin{bmatrix} D_{11} & D_{12} & D_{16} \\ D_{12} & D_{22} & D_{26} \\ D_{16} & D_{26} & D_{66} \end{bmatrix} \tag{3.42}$$

As discussed earlier, the laminate used in this project is classified as orthotropic laminate, and carry some particularities with it. First, the matrix $[B]$, which is responsible of the coupling between the in-plane deformations and curvatures, is null in all its elements. So all this couplings

are avoided. Also, some elements in the matrix $[A]$ and $[D]$ have some null elements. The null elements from matrix $[A]$ avoid the coupling between lineal and angular in-plane deformations. Null elements in $[D]$ matrix neglect the coupling between the bending and torsional deformations.

$$[A] = \begin{bmatrix} A_{11} & A_{12} & 0 \\ A_{12} & A_{22} & 0 \\ 0 & 0 & A_{66} \end{bmatrix} \tag{3.43}$$

$$[B] = \begin{bmatrix} 0 & 0 & 0 \\ 0 & 0 & 0 \\ 0 & 0 & 0 \end{bmatrix} \tag{3.44}$$

$$[D] = \begin{bmatrix} D_{11} & D_{12} & 0 \\ D_{12} & D_{22} & 0 \\ 0 & 0 & D_{66} \end{bmatrix} \tag{3.45}$$

Finally, to calculate the stresses in each ply in its local system require to calculate first the strain in the global system is calculated by:

$$\{\overline{\varepsilon}\}_i = \{\varepsilon^0\} + z_i \{K\} \tag{3.46}$$

Then, there are two paths to get the stresses and strains in each ply in the global and its local system. One path is:

$$\{\overline{\sigma}\}_i = \left[\overline{Q}\right]_i \{\overline{\varepsilon}\}_i \tag{3.47}$$

$$\{\sigma\}_i = [T]_i \{\overline{\sigma}\}_i \tag{3.48}$$

$$\{\varepsilon\}_i = [S]_i \{\sigma\}_i \tag{3.49}$$

The other path is:

$$\{\varepsilon\}_i = [R]\,[T]_i\,[R]^{-1}\,\{\overline{\varepsilon}\}_i \tag{3.50}$$

$$\{\sigma\}_i = [Q]_i \{\varepsilon\}_i \tag{3.51}$$

$$\{\overline{\sigma}\}_i = [T]_i^{-1} \{\sigma\}_i \tag{3.52}$$

Where $[S]$ is the flexibility matrix and the strain tensor in the global and local system is respectively:

$$\{\overline{\varepsilon}\}_i = \begin{Bmatrix} \varepsilon_x \\ \varepsilon_y \\ \gamma_{xy} \end{Bmatrix} \tag{3.53}$$

$$\{\varepsilon\}_i = \begin{Bmatrix} \varepsilon_1 \\ \varepsilon_2 \\ \gamma_{12} \end{Bmatrix} \tag{3.54}$$

Where the stress tensor in the global and local system is respectively:

$$\{\overline{\sigma}\}_i = \begin{Bmatrix} \sigma_x \\ \sigma_y \\ \tau_{xy} \end{Bmatrix} \tag{3.55}$$

$$\{\sigma\}_i = \begin{Bmatrix} \sigma_1 \\ \sigma_2 \\ \tau_{12} \end{Bmatrix} \tag{3.56}$$

3.3 Lamina failure criteria: Hashin

Lots of lamina failure criteria have been developed over the years for unidirectional fiber composites. The goal of these criteria is to determine the strength of an unidirectional composite or lamina in a state of combined stress, as well as the mode of failure. Moreover, all of them are based on linear elastic analysis and on the macromechanical point of view. It means that the detailed failure process is not studied. These principal failure criteria are: maximum stress, maximum strain, Tsai-Hill, Tsai-Wu, Hashin-Rotem and Hashin [43] criteria. All of them but the Tsai-Wu criterion are based on the plane stress state formulation for orthotropic materials. Tsai-Wu criterion is formulated for the whole tridimensional stress tensor but it has reduced forms for plane stress state.

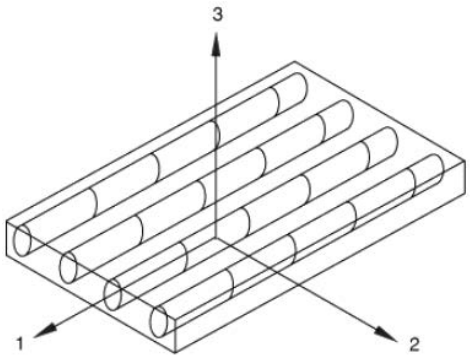

Figure 3.4: Unidirectional lamina sketch [44].

The principal strengths in a composite lamina are:

- X_t and X_c for tensile and compressive strength in the fiber direction respectively.
- Y_t and Y_c for tensile and compressive strength in the transverse direction respectively.
- S_L and S_T for in-plane and out-of-plane shear strengths respectively.

With the lamina failure criterion the failure mode can be identified and this is a very important tool to analyze a laminate. Likewise, an individual lamina mode failure does not means that the whole laminate has failed. The failure modes can be separated in the following classification:

- **Fiber Breakage (mode 1):** longitudinal stress (σ_1) or longitudinal strain (ε_1) dominates lamina failure.
- **Transverse Matrix Cracking (mode 2):** transverse stress (σ_2) or transverse strain (ε_2) dominates lamina failure.
- **Shear Matrix Cracking (mode 3):** shear stress (τ_{12}) or shear strain (γ_{12}) dominates lamina failure.

Depending on the interaction between the failure modes in the failure criterion definition, the lamina failure criteria can be classified as:

- **Limit criteria:** The maximum stress and maximum strain criteria belong to this group and they predict the failure and mode by comparing the lamina stresses or strains with the respective strengths. The failure modes have no influence between them. These are the most simple criteria and often overestimate the failure load of the lamina.

- **Interactive criteria:** The Tsai-Hill and Tsai-Wu criteria belong to this group and they predict the failure by using a single quadratic or higher order polynomial equation involving all stress or strain components. The failure of the lamina is assumed when the equation is satisfied and the failure mode is estimated indirectly by comparing the stress/strength ratios.

- **Separate mode criteria:** The Hashin-Rotem and Hashin criteria belong to this group and separate the matrix failure from the fiber failure. This group has a failure criterion in between the complete independent criteria and the complete interactive criteria type. There is some stress interaction but not with all the stress components like the interactive criteria.

In the following pictures all failure criteria are compared. Knowing that the one which fits better to the experimental results is the interactive Tsai-Wu criterion, the rest predict a failure load higher than the real in some stress state combination. The more unrealistic failure prediction, but the easiest, are the maximum stress and maximum strain criteria. Tsai-Hill, Hashin-Rotem and Hashin criteria are very close to the Tsai-Wu curve and the error is not very large. In the Abaqus software, only it is available the Hashin-Rotem and Hashin failure criteria for this kind of material. Therefore, Hashin failure criteria is the one that has been used in this project because is the most complete available. In future work would be very interesting to use other failure criteria like Tsai-Wu programming a subroutine.

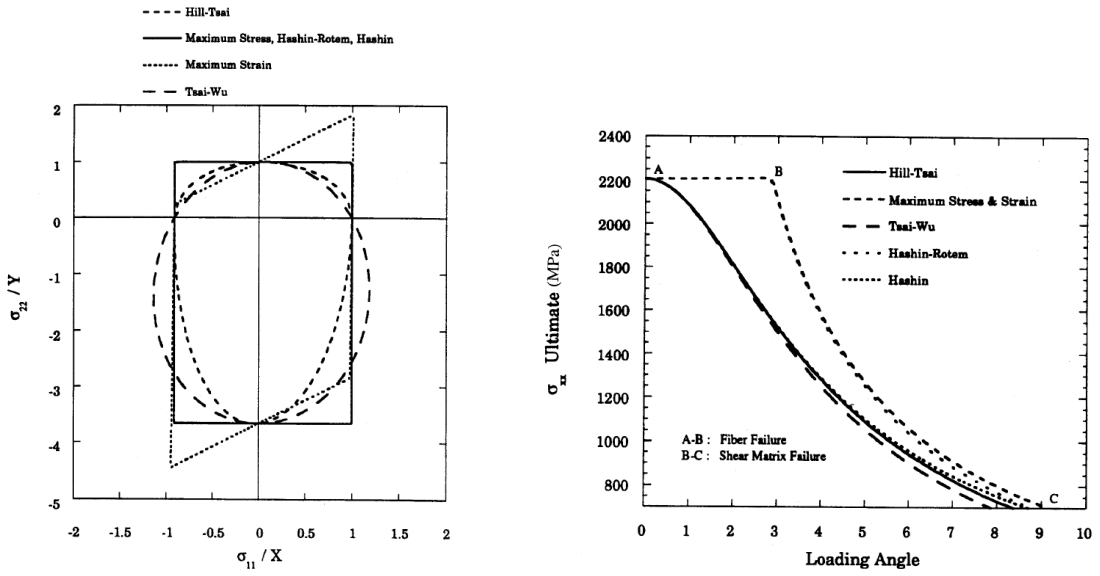

Figure 3.5: Failure criteria comparative [45].

Hashin damage model in Abaqus software, based on paper [43], has the capability to model anisotropic damage in fiber-reinforced materials without a large amount of plastic deformation before the damage initiation. The response of the undamaged material is assumed as linear elastic. Once the damage initiation criteria is reached, the damage evolution law is based on the energy dissipated during the damage process and linear material softening. This damage evolution is characterized by the degradation of the material stiffness. Four different failure modes are considered and the damage initiation following the Hashin failure criteria are:

- Fiber rupture in tension ($\hat{\sigma}_1 \geq 0$).

$$F_f^t = \left(\frac{\hat{\sigma}_1}{X_T}\right)^2 + \left(\frac{\hat{\tau}_{12}}{S_L}\right)^2 \tag{3.57}$$

- Fiber buckling and kinking in compression ($\hat{\sigma}_1 < 0$).

$$F_f^c = \left(\frac{\hat{\sigma}_1}{X_C}\right)^2 \tag{3.58}$$

- Matrix cracking under transverse tension and shearing ($\hat{\sigma}_2 \geq 0$).

$$F_m^t = \left(\frac{\hat{\sigma}_2}{Y_T}\right)^2 + \left(\frac{\hat{\tau}_{12}}{S_L}\right)^2 \tag{3.59}$$

- Matrix crushing under transverse compression and shearing ($\hat{\sigma}_2 < 0$).

$$F_m^c = \left(\frac{\hat{\sigma}_2}{S_T}\right)^2 + \left[\left(\frac{Y_C}{2\,S_T}\right)^2 - 1\right]\frac{\hat{\sigma}_2}{Y_C} + \left(\frac{\hat{\tau}_{12}}{S_L}\right)^2 \tag{3.60}$$

The effective stress used to evaluate the initiation criteria is computed from:

$$\{\hat{\sigma}\} = [M]\ \{\sigma\}\ , \tag{3.61}$$

where $\{\sigma\}$ is the true stress and $[M]$ is the damage operator:

$$[M] = \begin{bmatrix} \dfrac{1}{(1-d_f)} & 0 & 0 \\ 0 & \dfrac{1}{(1-d_m)} & 0 \\ 0 & 0 & \dfrac{1}{(1-d_s)} \end{bmatrix} \tag{3.62}$$

The internal damage variables d_f, d_m and d_s are calculated from the four failure modes explained before:

$$d_f = \begin{cases} d_f^t & if\ \hat{\sigma}_1 \geq 0 \\ d_f^c & if\ \hat{\sigma}_1 < 0 \end{cases} \tag{3.63}$$

$$d_m = \begin{cases} d_m^t & if\ \hat{\sigma}_2 \geq 0 \\ d_m^c & if\ \hat{\sigma}_2 < 0 \end{cases} \tag{3.64}$$

$$d_s = 1 - \left(1-d_f^t\right)\left(1-d_f^c\right)\left(1-d_m^t\right)\left(1-d_m^c\right) \tag{3.65}$$

When there is not damage initiated, the matrix $[M]$ is equal to the identity and materials respond to:

$$\{\hat{\sigma}\} = \{\sigma\} \tag{3.66}$$

However, when the damage start in at least one of the modes, the damage operator becomes more important in the damage initiation criteria for the other modes. The effective $\{\hat{\sigma}\}$ represents the real stress that is resisting the internal forces over the damaged area. During the post-damage initiation behavior based on energy dissipation, the material stiffness is reduced in the following form:

$$\{\sigma\} = [C_d]\ \{\varepsilon\} \tag{3.67}$$

$$[C_d] = \frac{1}{D}\begin{bmatrix} \left(1-d_f\right)E_1 & \left(1-d_f\right)\left(1-d_m\right)\nu_{21}E_1 & 0 \\ \left(1-d_f\right)\left(1-d_m\right)\nu_{12}E_2 & \left(1-d_m\right)E_2 & 0 \\ 0 & 0 & \left(1-d_s\right)GD \end{bmatrix}, \tag{3.68}$$

where $[C_d]$ is the damaged stiffness matrix of the material and $D = 1 - \left(1-d_f\right)\left(1-d_m\right)\nu_{12}\nu_{21}$. Damage evolution is modeled with equivalent displacements instead from strains because this reduce the mesh dependency of the model. The maximum displacements used in the damage

evolution model are calculated from a failure energy dissipation for each failure mode. This energies are for fiber traction failure mode G^c_{ft}, fiber compression failure mode G^c_{fc}, matrix traction failure mode G^c_{mt} and matrix compression failure mode G^c_{mc}. Each damage evolution follows the next curve, where unloading a partially damaged state is possible and at this point the stiffness is reduced and also the maximum stress achievable. Moreover, it is recommended to use a small viscous regularization to stabilize the solution, and this is set for each mode through the parameters η^c_{ft}, η^c_{fc}, η^c_{mt} and η^c_{mc}.

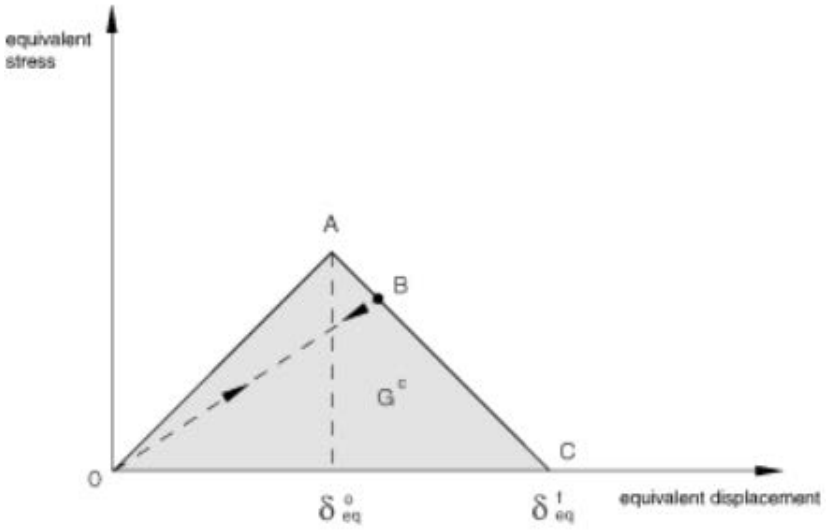

Figure 3.6: Linear damage evolution in Abaqus Hashin model [44].

This fiber-reinforced composite damage model must be used with elements with a plane stress formulation, which could be plane stress, conventional shell, continuum shell, and membrane elements.

In this project, conventional *S4R* and continuum shell *SC8R* elements have been used with plane stress formulation. Both use a reduced integration method to avoid the typical locking problems of the fully integrated elements. However, an hourglass control is need to be introduced to avoid the non-physical zero-energy deformation modes of the elements. The *S4R* elements are composed of four nodes with six degrees-of-freedom (DoF) per node, which are the three displacements (U_1, U_2, U_3) and the three rotations (UR_1, UR_2, UR_3). The thickness of conventional shell elements is defined internally by the section properties associated to these elements. On the other hand, continuum shell elements are composed of eight nodes with only three DoF allowed per node associated to the displacements (U_1, U_2, U_3). But they have a physical thickness from which is computed rotations of the elements by the displacements. In the following figure both elements are illustrated:

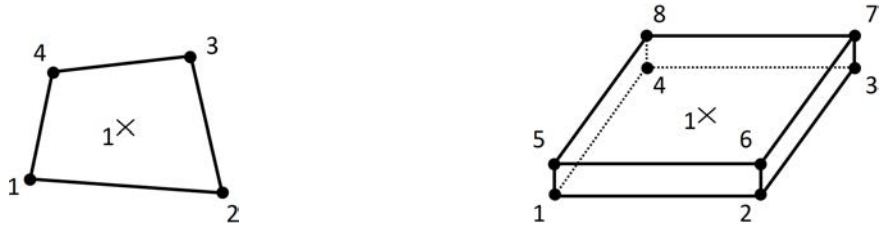

(a) Conventional shell element

(b) Continuum shell element

Figure 3.7: Shell element types used in the finite elements models of this project.

3.4 Interfaces delamination model

The interlaminar damage (delamination) is one of the most significant failure form in laminated composites when there is no reinforcement in the thickness direction. Therefore, analysis tools have been developed over the years to predict this complex failure [46]. One of them is the Virtual Crack Closure Technique (VCCT), from which significant information concerning the onset and delamination stability can be obtained with this tool. Nevertheless, it may require complex moving mesh techniques to advance the crack front and an initial delamination must be defined. Another technique is the use of cohesive elements placed at the interfaces between plies. Cohesive elements can overcome some of the difficulties of VCCT such as the capability of predict the onset and propagation of delamination without a previous crack location and propagation direction setting.

Abaqus finite elements code offers the possibility of modeling the behavior of interfaces in composite laminates with cohesive elements. There are different types of mechanical constitutive behavior to model these elements depending on the application and on the assumptions about deformation and stresses applicable to the problem. For very thin interfaces in composite laminates, the traction-separation-based modeling is the best suited. This model is derived from concepts of fracture mechanics like the amount of energy required to create new surfaces. The cohesive elements model the initial loading before the damage, the initiation of damage and, finally, the propagation of it leading to an eventual failure (delamination). The undamaged interface is described as linear elastic, and when the damage is initiated the stiffness under tensile and/or shear loading is degraded. Although the stiffness in the pure compression direction is not affected.

The cohesive elements are used in areas of the model where cracks are expected to develop and the delaminations are propagated only along the cohesive elements layers. Unlike other methods, cohesive elements do not need an initial crack to model the crack growth. The finite elements model of CAI test is a three-dimensional problem, so cohesive elements must be too. This means that they have three components of separation: one normal to the interface and two parallel to it. These three directions have a stress component associated.

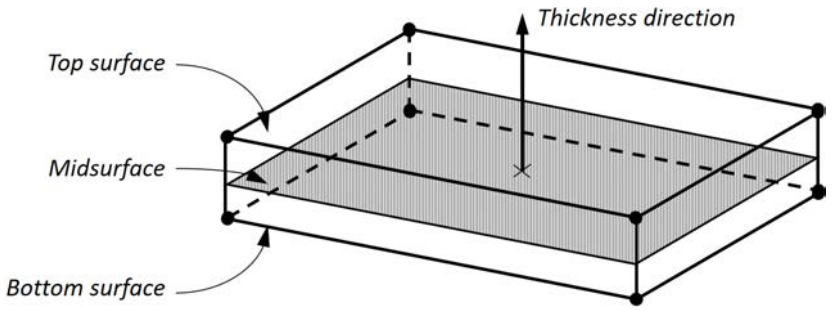

Figure 3.8: Spatial representation of a three-dimensional cohesive element [44].

Two different strategies are possible to include cohesive layers in a finite elements model with Abaqus code. The first is to use shared nodes at each surface of the cohesive element (top and bottom) with the the adjacent laminate plies. The second is to use tie constraints for connecting the surrounding elements of the laminate plies to the top and bottom surface of the cohesive elements. This last strategy is computationally worthy when the mesh required for the cohesive layer is much smaller that adjacent elements mesh of the plies. For the models developed in this project a relative small size of the plies mesh elements is required to model properly the intralaminar damage and local buckling of the initial damaged interfaces, therefore, is more computationally efficient to work with cohesive elements with shared nodes.

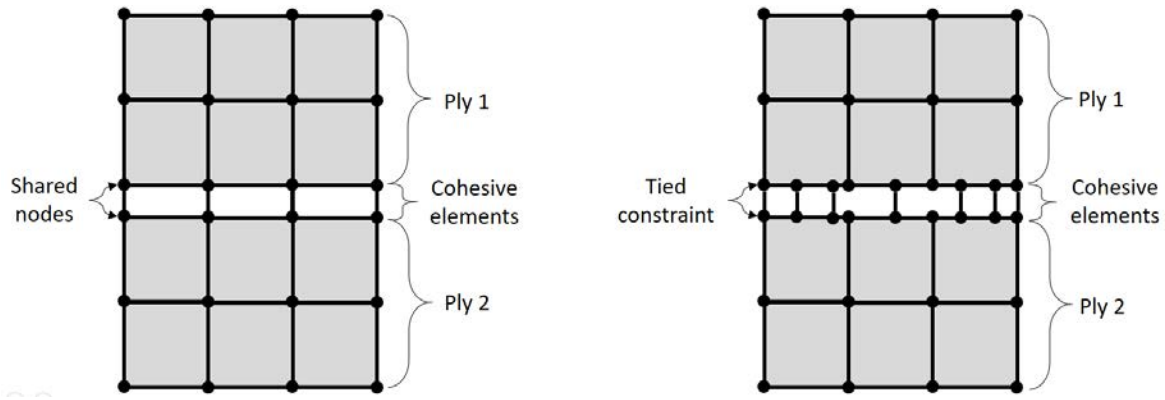

Figure 3.9: Cohesive elements modeling options [44].

The connectivity of these elements is the same as continuum elements. Nevertheless, they can be understood as being composed of two surfaces, top and bottom, separated by a thickness, where the relative motion between them along the thickness direction represents the opening and closing of the interface. Also, the relative motion of these surfaces in the plane normal to the thickness direction represent the transverse shear behavior of the elements. These elements do not generate stresses in a purely membrane response, i.e. stretching and shearing of the midsurface of the element.

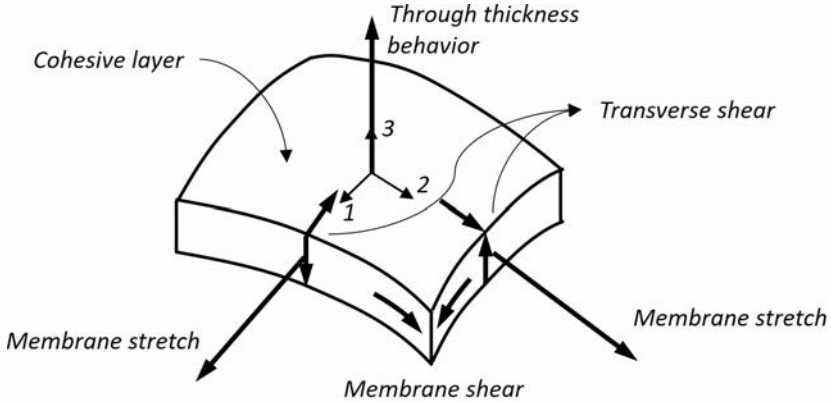

Figure 3.10: Deformation modes of a cohesive element [44].

Therefore, nominal traction stress vector, $\{t\}$, has three components in three-dimensional problems: the stress in the normal direction is represented by t_n and the shear stress in the local 1- and 2-directions are represented by t_s, t_t respectively. The separations that correspond to these directions are respectively δ_n, δ_s and δ_t. If the original thickness of the element is denoted by T_0, the nominal strains are:

$$\varepsilon_n = \frac{\delta_n}{T_0}, \ \varepsilon_s = \frac{\delta_s}{T_0}, \ \varepsilon_t = \frac{\delta_t}{T_0} \tag{3.69}$$

Then, the general elastic behavior is written as fully coupled between all the components:

$$\{t\} = \begin{Bmatrix} t_n \\ t_s \\ t_t \end{Bmatrix} = \begin{bmatrix} E_{nn} & E_{ns} & E_{nt} \\ E_{ns} & E_{ss} & E_{st} \\ E_{nt} & E_{st} & E_{tt} \end{bmatrix} \cdot \begin{Bmatrix} \varepsilon_n \\ \varepsilon_s \\ \varepsilon_t \end{Bmatrix} = [E]\{\varepsilon\} \tag{3.70}$$

However, the cohesive layer in this project is assumed that has an uncoupled traction-separation behavior:

$$[E] = \begin{bmatrix} E_{nn} & 0 & 0 \\ 0 & E_{ss} & 0 \\ 0 & 0 & E_{tt} \end{bmatrix} \tag{3.71}$$

As regards the damage initiation criteria, there are different possibilities, some based on stresses and others on strains. Also, both of them based on maximum and quadratic criteria. The damage initiation criteria assumed for this project is the Quadratic nominal stress criterion because the maximum criteria do not takes in account the interaction between stress components and overestimate the damage initiation load. The damage initiation for quadratic nominal criterion is determined by:

$$\left(\frac{\langle t_n \rangle}{t_n^0}\right)^2 + \left(\frac{t_s}{t_s^0}\right)^2 + \left(\frac{t_t}{t_t^0}\right)^2 = 1 \ , \tag{3.72}$$

where t_n^0, t_s^0 and t_t^0 are the peak values of the nominal stress when the deformation of the interface is purely in the normal or the first or second shear direction. The symbol $\langle\ \rangle$ used in the normal nominal stress, represents the Macaulay bracket which is interpreted as the pure compression stress does not initiate damage.

Once the damage initiation criteria is reached, the damage evolution is described by a material stiffness degradation or softening law which has a general framework similar to the one described in the fiber reinforced materials failure, Figure (reffig-hashindamageevolution. Nevertheless, many details are different. For describing the damage evolution, a new scalar variable is created, D, which evolves from 0 (no damage initiated) to 1 (delamination). This new variable modify the stress components predicted by the elastic traction-separation behavior for the undamaged material ($\bar{t}_n$, $\bar{t}_s$, $\bar{t}_t$):

$$\begin{aligned} t_n &= \begin{cases} (1-D)\ \bar{t}_n, & \bar{t}_n \geq 0 \\ \bar{t}_n \end{cases} \\ t_s &= (1-D)\ \bar{t}_s \\ t_t &= (1-D)\ \bar{t}_t \end{aligned} \tag{3.73}$$

The evolution of the damage under a combination of normal and shear deformation across the interface needs to introduce an effective displacement δ_m.

$$\delta_m = \sqrt{\langle \delta_n \rangle^2 + \delta_s^2 + \delta_t^2} \tag{3.74}$$

This mix of the deformation fields in the cohesive zone is named Mixed-Mode cohesive model [46]. In Abaqus code is possible to use three different measurements of mode mix: one based on tractions and two based on energies. They quantify differently the relative ratios of normal and shear deformations. In this project a mix mode definition based on energies is used. These energies are the work done by the tractions and their associated relative displacement (G_n, G_s and G_t).

$$\begin{aligned} G_n &= \int_0^{\delta_n^f} t_n \, d\delta_n \\ G_s &= \int_0^{\delta_s^f} t_s \, d\delta_s \quad , \\ G_t &= \int_0^{\delta_t^f} t_t \, d\delta_t \end{aligned} \tag{3.75}$$

The ratios used in the mix mode based on energies are determined in the next formulas, where the sum of all the energies is $G_T = G_n + G_s + G_t$. Because of only two of the three ratios defined before are independent, it is helpful to create a new energy quantity of the total work done by the

shear tractions and displacements $G_S = G_s + G_t$.:

$$m_1 = \frac{G_n}{G_T}$$
$$m_2 = \frac{G_s}{G_T} \tag{3.76}$$
$$m_3 = \frac{G_t}{G_T}$$

The damage evolution definition is set mainly by two components, one is specifying the energy dissipated to failure, G^C, or also defining the effective displacement at complete failure, δ_m^f. The energy release definitions or, also called, fracture energy criteria, most widely used are: the Power law and the Benzeggagh-Kenane (B-K) [47] fracture criterion. The Power law criterion determine the interaction of the individual (normal and two shear) modes to cause failure under mixed-mode conditions:

$$\left(\frac{G_n}{G_n^C}\right)^\alpha + \left(\frac{G_s}{G_s^C}\right)^\alpha + \left(\frac{G_t}{G_t^C}\right)^\alpha = 1\,, \tag{3.77}$$

where G_n^C, G_s^C and G_t^C are the normal and two shear fractures energies of individual modes, and α is the power exponent. Failure occurs when the above condition is satisfied, which means that the complete mixed-mode fracture energy $G^C = G_T$. The Power law formula can be rewritten in terms of the energy mixed ratios defined previously.

$$G^C = \frac{1}{\left[\left(\frac{G_n}{G_n^C}\right)^\alpha + \left(\frac{G_s}{G_s^C}\right)^\alpha + \left(\frac{G_t}{G_t^C}\right)^\alpha\right]^{1/\alpha}} \tag{3.78}$$

Benzeggagh-Kenane fracture energy criterion is defined by the fracture energies G_n^C and G_s^C, and by the material parameter η_{BK}:

$$G^C = G_n^C + \left(G_s^C - G_n^C\right)\left(\frac{G_S}{G_T}\right)^{\eta_{BK}} \tag{3.79}$$

These two fracture criteria has been compared to experimental mixed mode results where is concluded that for composite laminates with thermoplastic resins the power law with an exponent $\alpha = 1$ can reach a good approach. However, for epoxy based composites, is better to use B-K criterion as can be seen in the following picture. Therefore, for this project is used the B-K criterion.

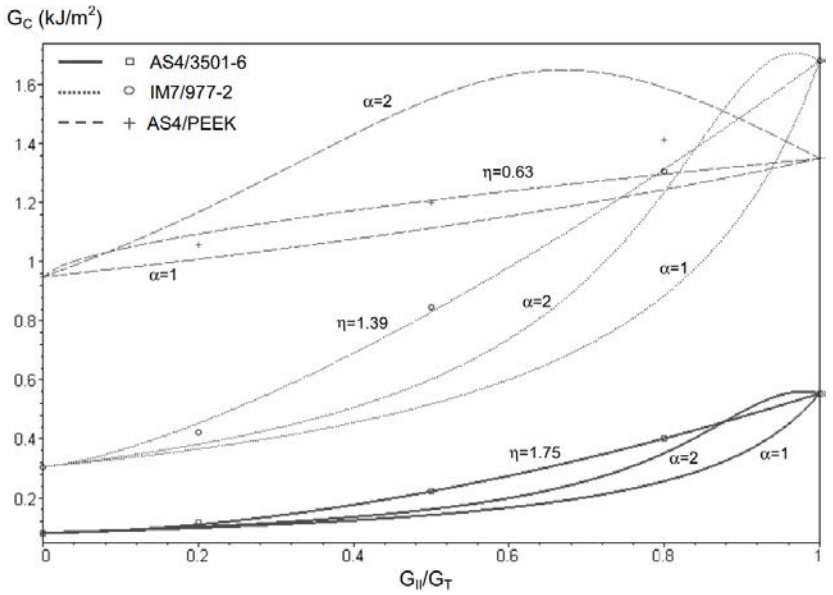

Figure 3.11: Mixed mode fracture energy toughness experimental and numerical comparative [46].

The second component of the damage evolution definition is the nature of the damage variable, D, which can be a linear or exponential softening law between the damage initiation and final failure. In this project a linear softening is used where δ_m^f is the failure displacement under mixed-mode conditions computed from the fracture energy G^C. The δ_m^0 is the displacement at the damage initiation under mixed-mode conditions, and δ_m^{max} refers to the maximum value of the effective displacement reached during the loading history:

$$D = \frac{\delta_m^f \left(\delta_m^{max} - \delta_m^0\right)}{\delta_m^{max} \left(\delta_m^f - \delta_m^0\right)} \tag{3.80}$$

For better understanding is shown the energy release and constitutive mechanical behavior with linear softening for separate modes in the following picture. Some points of interest are described in the picture such as the displacement at normal traction and shear traction damage initiation is named as δ_n^0, δ_s^0 and δ_t^0 respectively. Moreover, the displacement for final failure is named as δ_n^f, δ_s^f and δ_t^f for each fracture mode.

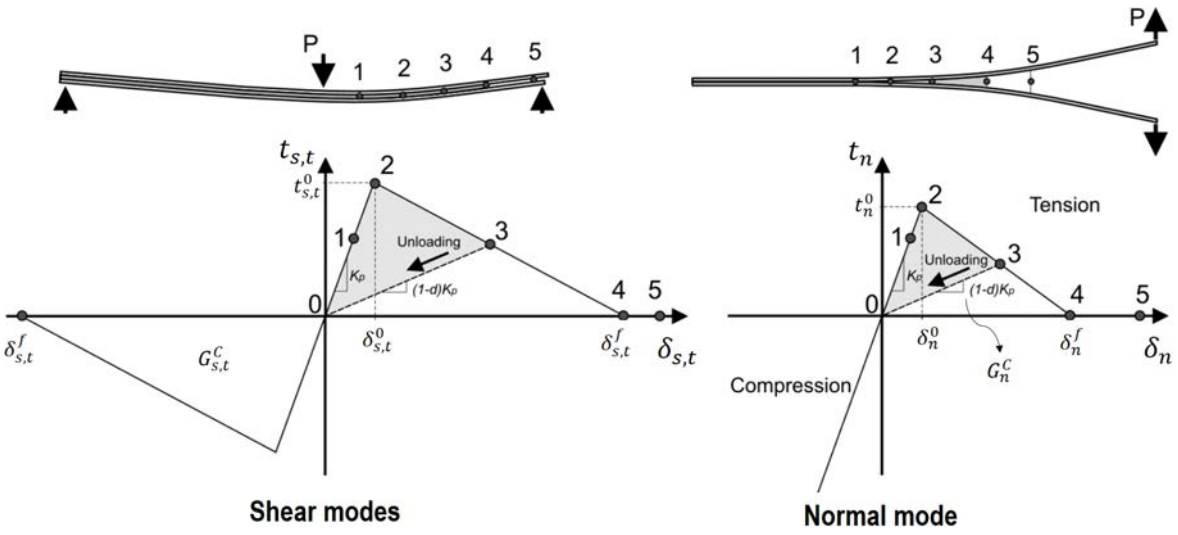

Figure 3.12: Pure mode constitutive equations [46].

Finally, the schematic representation of the dependence of damage initiation and evolution on the mixed-mode is shown for three different mixed-mode ratios in Figure 3.13. The vertical axis represent the tractions where τ^0 is the shear damage initiation computed from $\tau^0 = \sqrt{(t_s^0)^2 + (t_t^0)^2}$. The horizontal axes represent the normal and shear separations, δ_n and δ_S.

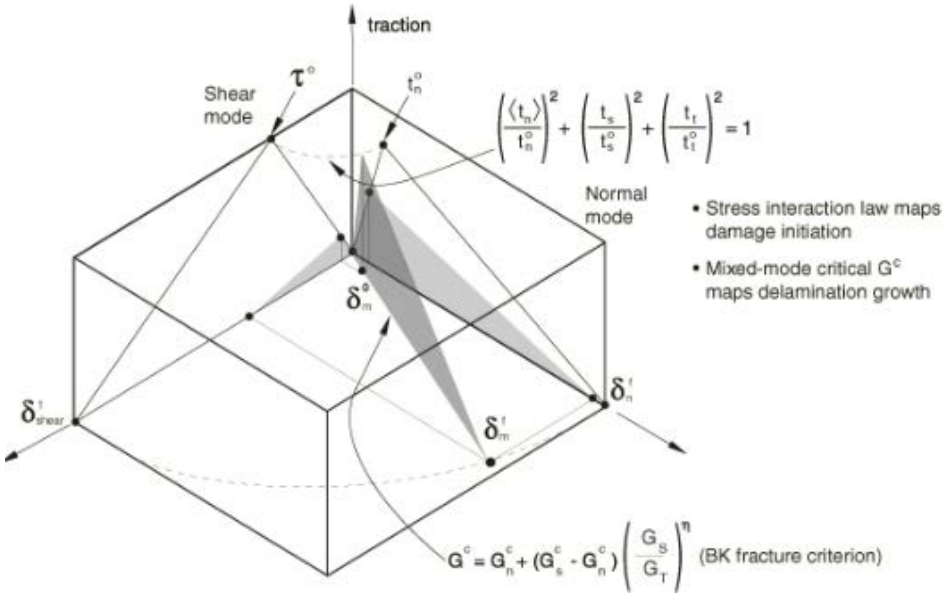

Figure 3.13: Illustration of mixed-mode response in cohesive elements with quadratic nominal stress damage inititation criterion, linear softening and Benzeggagh-Kenane fracture energy criterion [44].

In conclusion, this is the cohesive model used in the finite elements models developed for this project because with the proper parameters can reproduce the experimental results for a epoxy based composite laminate interface. Moreover, in finite element models is recommended to define a small viscous regularization to stabilize the solution through the parameter μ_{BK}.

3.5 Stability of elastic structures

Structural stability (based on books [48], [49] and [50]) has been a significant matter over time to predict earlier structural failures due to instabilities at lower loads than the materials strengths. An instability is defined as an equilibrium state or configuration of a structural element, structure or mechanical system which is unstable if any small disturbance of the system results in a sudden change in deformation mode or displacement value after which the system does not return to its original equilibrium state [49]. The concept of stability can be illustrated with a rigid body sitting in an axisymmetric paraboloid:

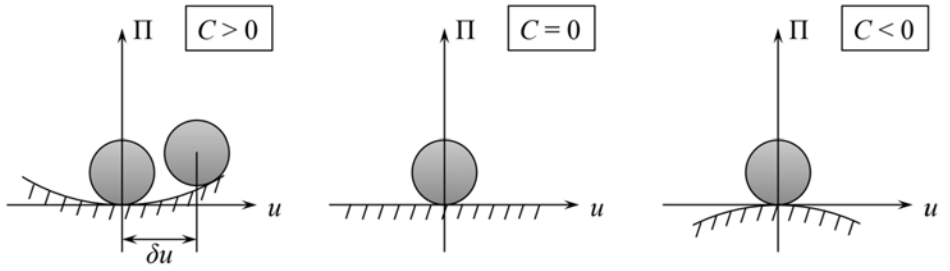

Figure 3.14: Illustration of stable, neutral and unstable equilibrium.

Where the total potential energy (Π) of these systems with a rigid body (internal elastic energy is null $U_b = 0$ and only exist potential energy V) is:

$$\Pi = U_b - V = V = m\,g\,h = C\,u^2 \tag{3.81}$$

This system is in equilibrium state since at the origin of the coordinate system ($u = 0$), the variation of the total potential energy $\partial\Pi$ is null:

$$\partial\Pi = 2\,C\,u\,\partial u = 0 \tag{3.82}$$

But, if the second derivative of the total potential energy is carried out depends on the sign of the constant C.

$$\partial^2\Pi = 2\,C\,(\partial u)^2 \tag{3.83}$$

Then, the relationship between the sign of this constant and the stability of the system determine if the system is a stable equilibrium ($C > 0$), neutral equilibrium ($C = 0$) or unstable equilibrium ($C < 0$).

$$\partial^2\Pi = \begin{cases} > 0 & Stable \\ = 0 & Neutral \\ < 0 & Unstable \end{cases} \tag{3.84}$$

3.5.1 Buckling and post-buckling behavior

In a structure or structural element, the buckling load (P_{cr}) is the point at which the current stable equilibrium changes from stable to unstable, and is simultaneously, the load at which the equilibrium state suddenly changes from previously stable configuration to another stable configuration with or without an accompanying large response (deformation or deflection). Therefore, the buckling load is the largest load for which stability of equilibrium of a structural element or structure exist in its original equilibrium configuration. Depending on the structure studied and boundary conditions, the buckling load and post-buckling behavior changes and at least four types of post-buckling behavior are possible. The buckling load is also known as the bifurcation point where two branches are possible to follow for the post-buckling behavior. Furthermore, for theoretically perfect structures, the bifurcation point is a sharp edge that divide very clearly the original configuration of the structure from the post-buckling configuration. But, all the structures have some level of imperfections in the geometry, applied loads and restraints. These imperfections lead to a smoother transition between the original configuration and the post-buckling behavior. In Figure 3.15 the four types of post-buckling behavior and the imperfection influence is shown with the load (P) versus deflection (w) diagrams:

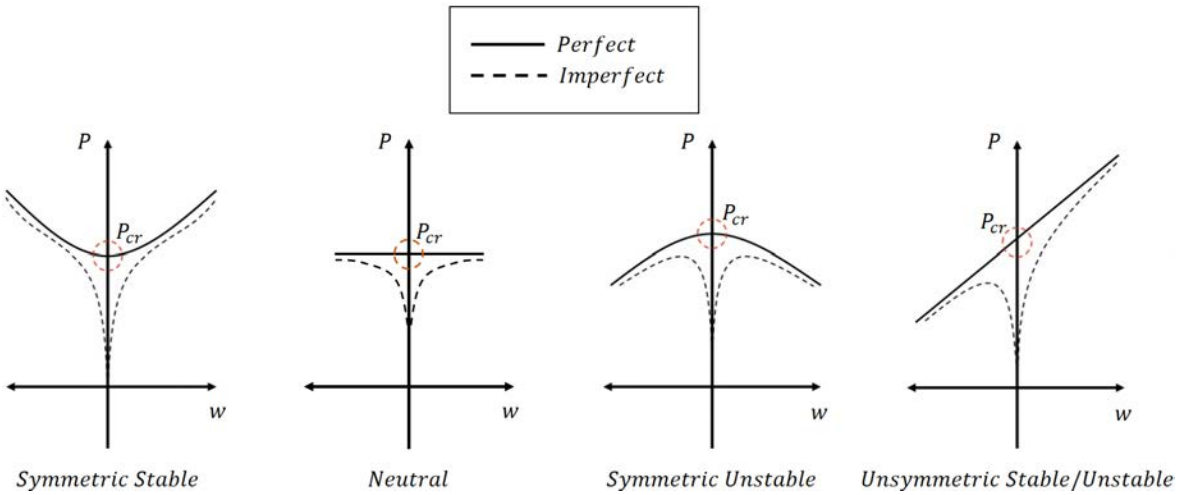

Figure 3.15: Types of post-buckling behavior for perfect and imperfect structure elements [49].

The main difference between the stable, neutral and unstable behavior is that the stable behavior can carry more load above the buckling load, the neutral behavior can carry at most the buckling load and the unstable cannot carry the buckling load. The most simple and typical examples of structure elements that reproduce the previous behaviors are columns, plates and cylindrical shells.

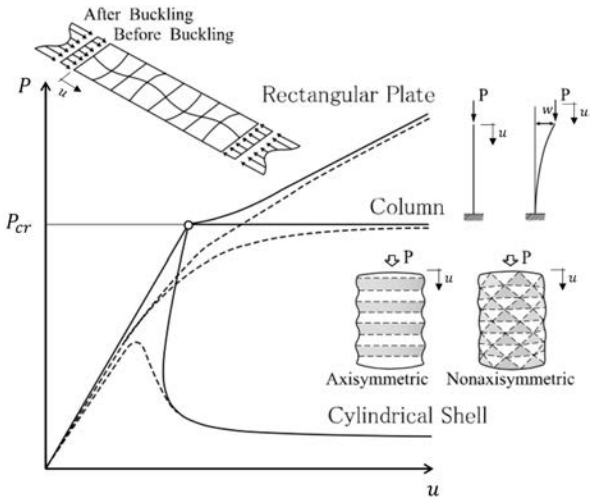

Figure 3.16: Example of post-buckling behavior of basic structure elements: columns, plates and cylindrical shells [51].

3.5.2 Buckling of simply supported isotropic plates under uniaxial compression

The buckling load in an isotropic plate under uniaxial load (N_x) with its four edges simply supported (4SS) can be computed analytically through the method of Ritz. This method use a test function with unknown parameters to define the deflection of the plate from the Navier solution. The test function must satisfy the boundary conditions in the four edges. Moreover, the origin of the coordinate system must be set in a corner of the plate, the largest edge in the x direction is named as a and the shortest edge in the y direction as b. Finally, an uniaxial load is applied distributed along the shorter edge in the compression direction of the longest edge.

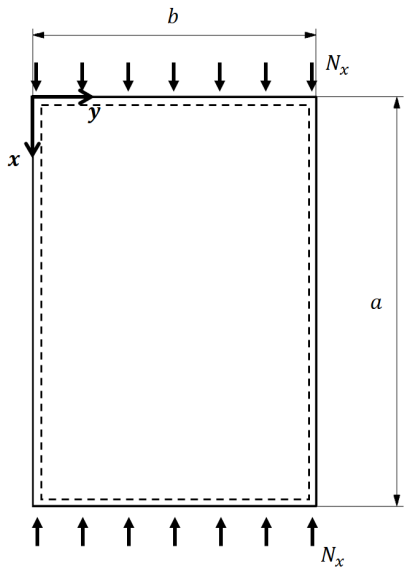

Figure 3.17: Dimensions 4SS theoretical plate under uni-axial load.

The test function $w(x,y)$ used that satisfies the 4SS plate boundary conditions is:

$$w(x,y) = \sum_{m}^{\infty}\sum_{n}^{\infty} w_{mn}\, \sin\left(\frac{m\,\pi\,x}{a}\right)\, \sin\left(\frac{n\,\pi\,y}{b}\right) \tag{3.85}$$

Where the parameters m and n are the number of semi-weaves in the x and y direction respectively, and the parameters w_{mn} are unknown. Ritz method minimize the total potential energy ($\Pi = U_b - V$), which is the difference between the internal energy U_b and external energy due to the external forces V, to solve the problem. Below is shown the general formula:

$$\frac{\partial \Pi}{\partial w_{mn}} = \frac{\partial\,(U_b - V)}{\partial w_{mn}} = 0 \tag{3.86}$$

The general form of this energies can be written as the integral of the deflection partial derivatives ($w_{,x}$, $w_{,y}$, $w_{,xx}$, $w_{,yy}$, $w_{,xy}$) and external forces (N_x, N_y, N_{xy}):

$$U_b = \frac{D}{2}\int_0^a\int_0^b \left[(w_{,xx}+w_{,yy})^2 - 2\,(1-\nu)\,\left(w_{,xx}\,w_{,yy} - w_{,xy}^2\right)\right] dy\,dx \tag{3.87}$$

$$V = \frac{1}{2}\int_0^a\int_0^b \left(N_x\,w_{,x}^2 + N_y\,w_{,y}^2 + 2\,N_{xy}\,w_{,x}\,w_{,y}\right)\,dy\,dx \tag{3.88}$$

Where the parameter $D = \frac{E\,t^3}{12\,(1-\nu^2)}$. These formulas can be simplified for this problem. First, there is only one type of load per edge length applied N_x. So, all other terms of the formula V are null. Second, due to the symmetry of the problem, the integral of the term $\left(w_{,xx}\,w_{,yy} - w_{,xy}^2\right)$ is null.

$$U_b = \frac{D}{2}\int_0^a\int_0^b (w_{,xx}+w_{,yy})^2\,dy\,dx \tag{3.89}$$

$$V = \frac{1}{2}\int_0^a\int_0^b N_x\,w_{,x}^2\,dy\,dx \tag{3.90}$$

Introducing the derivatives of $w_{,xx}$ and $w_{,yy}$ in Eq.(3.89):

$$\begin{aligned} U_b = \frac{D}{2}\int_0^a\int_0^b \Bigg[&\sum_{m}^{\infty}\sum_{n}^{\infty} w_{mn}\left(\frac{m\,\pi}{a}\right)^2 \sin\left(\frac{m\,\pi\,x}{a}\right)\sin\left(\frac{n\,\pi\,y}{b}\right) + \\ &+ \sum_{m}^{\infty}\sum_{n}^{\infty} w_{mn}\left(\frac{n\,\pi}{b}\right)^2 \sin\left(\frac{m\,\pi\,x}{a}\right)\sin\left(\frac{n\,\pi\,y}{b}\right)\Bigg]^2 dy\,dx \end{aligned} \tag{3.91}$$

Knowing that the integral of the cross terms product inside the sum are null, the solution of the integral from Eq.(3.91) is:

$$U_b = \frac{\pi^4\,D\,a\,b}{8}\sum_{m}^{\infty}\sum_{n}^{\infty} w_{mn}^2\left[\left(\frac{m}{a}\right)^2 + \left(\frac{n}{b}\right)^2\right]^2 \tag{3.92}$$

Now, it is going to be done the same process to V from Eq.(3.90). Introducing $N_x = N$ and the derivative $w_{,x}$:

$$V = \frac{1}{2}\int_0^a\int_0^b N\left[\sum_{m}^{\infty}\sum_{n}^{\infty} w_{mn}\,\frac{m\,\pi}{a}\,\cos\left(\frac{m\,\pi\,x}{a}\right)\sin\left(\frac{n\,\pi\,y}{b}\right)\right]^2 dy\,dx \tag{3.93}$$

As in the Eq.(3.92), the integral of the cross terms product inside the sum are null. Then, solution of the integral from Eq.(3.93) is:

$$V = \frac{\pi^2\,N\,b}{8\,a}\sum_{m}^{\infty}\sum_{n}^{\infty}\left(w_{mn}^2\,m^2\right) \tag{3.94}$$

Introducing the Eq.(3.92) and Eq.(3.94) in Eq.(3.86):

$$\frac{\pi^4 Dab}{4}\left\{w_{mn}\left[\left(\frac{m}{a}\right)^2+\left(\frac{n}{b}\right)^2\right]^2\right\}-\frac{\pi^2 N b}{4 a}\left(w_{mn}\, m^2\right)=0 \tag{3.95}$$

Solving this equation can be obtained the critical load per edge length:

$$N_{crit}=\frac{\pi^2 D\left(b^2 m^2+a^2 n^2\right)^2}{a^2 b^4 m^2} \tag{3.96}$$

In the equation above, it can be seen that there is no dependency on w_{mn}. Then, it is introduced the parameter $\alpha = a/b$. Also, the minimum load will be always when $n = 1$, but the m value that minimize the load depends on the value of α.

$$N_{cr}=\frac{\pi^2 D\left(m^2+\alpha^2\right)^2}{b^2 m^2 \alpha^2} \tag{3.97}$$

Buckling stress is computed by dividing N_{cr} by the plate thickness, and the parameter m determine the buckling mode and the semi-waves through the x direction of the post-buckling configuration:

$$\sigma_{cr}=\frac{N_{cr}}{t}=\frac{\pi^2 D\left(m^2+\alpha^2\right)^2}{t\, b^2 m^2 \alpha^2} \tag{3.98}$$

3.5.3 Buckling of simply supported composite laminate plates under uniaxial compression

For a given simply-supported flat composite laminate plate under uniaxial compression, an analogous procedure is carried out to compute the buckling stress and buckling mode. The general equation governing the buckling deflection in a rectangular flat orthotropic plate is the following differential equation based on book [52].

$$B_x\, w_{,xxxx}+2\, B_{xy}\, w_{,xxyy}+B_y\, w_{,yyyy}=N_x\, w_{,xx}+2\, N_{xy}\, w_{,xy}+N_y\, w_{,yy} \tag{3.99}$$

Where the coefficients B_x, B_{xy} y B_y are defined from the ABD-Matrix from Classical Laminate Theory:

$$\begin{cases} B_x = D_{11} \\ B_y = D_{22} \\ B_{xy} = D_{12}+2\, D_{66} \end{cases} \tag{3.100}$$

For the deflection of the plate from the Navier solution is set the same test function as the isotropic plate case because the boundary conditions are the same.

$$w(x,y)=\sum_m^\infty\sum_n^\infty w_{mn}\,\sin\left(\frac{m\,\pi\,x}{a}\right)\sin\left(\frac{n\,\pi\,y}{b}\right) \tag{3.101}$$

Including this test function inside the composite plate differential equation (3.99) and simplifying the differential equation for an uniaxial load N_x, the critical load $N_{x,cr}$ can be computed:

$$N_{x,cr}=\pi^2\left(\frac{n}{b}\right)^2\left[B_x\left(\frac{m\,b}{n\,a}\right)^2+2\,B_{xy}+B_y\left(\frac{n\,a}{m\,b}\right)^2\right] \tag{3.102}$$

In the equation above, it can be seen that the minimum load will be when $n = 1$. Then, it is introduced the parameter $\alpha = a/b$. The m value that minimize the load depends on the value of α and the stiffness components B_x, B_{xy} and B_y of the laminate.

$$\sigma_{cr}=\frac{N_{x,cr}}{t}=\frac{1}{t}\left(\frac{\pi}{b}\right)^2\left[B_x\left(\frac{m}{\alpha}\right)^2+2\,B_{xy}+B_y\left(\frac{\alpha}{m}\right)^2\right] \tag{3.103}$$

3.6 Finite elements analysis procedures

Depending on the problem to solve, a specific analysis procedure is needed to solve the finite elements model defined in Abaqus code. Four different analysis procedures already implemented in this software have been used to calculate the models of this project: Static stress analysis, Eigenvalue buckling analysis, Unstable collapse and postbuckling analysis and Explicit Dynamic analysis.

3.6.1 Static stress analysis procedure

First, the static stress analysis is an implicit method used when inertia effects can be neglected and it can be used with linear or nonlinear models. The nonlinear models can arise from lage-displacement effects, material nonlinearity, geometrical nonlinearity and/or boundary nonlnearity such as contact and friction. Nevertheless, this static procedure may have problems to find the equilibrium state if the stiffness of the material change sharply or during a fast damage evolution such as delamination growth. This leads to convergence problems.

3.6.2 Unstable collapse and post-buckling analysis procedure (Riks method)

The procedure for unstable collapse and post-buckling analysis is based on the Riks method. This method is generally used to predict unstable, geometrically nonlinear collapse of a structure. Also, it can include nonlinear materials and boundary conditions. In order to improve the stability of the model solution of the static stress analysis procedure, the Riks method use the load magnitude as an additional unknown and it solves simultaneously for loads and displacements. Therefore, a new quantity called arc length is used to measure the progress of the solution. The loading during a Riks computation is always proportional. This loading is based on the following equation:

$$P_{total} = P_0 + \lambda \left(P_{ref} - P_0 \right) , \tag{3.104}$$

where P_0 is a dead load, P_{ref} is a reference load vector, and λ is the load proportionality factor at each increment. Although this method skip the unstable problem due to the post-buckling bifurcation. It may have convergence problems when the delaminations growth through the cohesive layers because this is a dynamic event and this solver is not prepared for it.

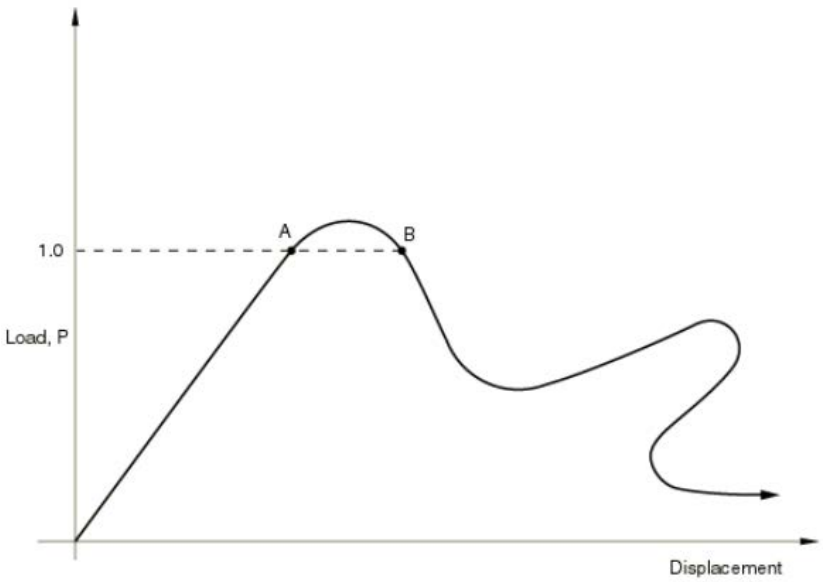

Figure 3.18: Proportional loading with unstable response [44].

3.6.3 Explicit dynamic analysis procedure

The explicit dynamic analysis is manly used for large models with relative short dynamic response time and for analysis with significant discontinuous events. It can also use consistent large-deformation theory and allow very general contact definitions. Moreover, it can be used to compute quasi-static analysis with fast failure development which is the case of the models developed in this project. The explicit dynamics analysis is based on the explicit integration rule along with the use of diagonal element mass matrices. The explicit central-difference integration rule is used to integrate the equations of motion:

$$\begin{cases} \dot{u}^N_{(i+\frac{1}{2})} = \dot{u}^N_{(i-\frac{1}{2})} + \dfrac{\Delta t_{(i+1)} + \Delta t_{(i)}}{2}\, \ddot{u}^N_{(i)} \\ u^N_{(i+1)} = u^N_{(i)} + \Delta t_{(i+1)}\, \dot{u}^N_{(i+\frac{1}{2})} \end{cases}, \tag{3.105}$$

where u^N is a degree-of-freedom, a displacement or rotations component, and the subscripts i refers to the increment number in an explicit dynamic step. The accelerations at the beginning of the increment is computed from the diagonal element mass matrix M^{NJ}, the vector of the applied loads P^J and the vector of the internal force I^J:

$$\ddot{u}^N_{(i)} = \left(M^{NJ}\right)^{-1} \left(P^J_{(i)} - I^J_{(i)}\right) \tag{3.106}$$

The time increment used in an explicit analysis must be smaller than the stability limit of the central-difference operator. Otherwise, the problem solution is unstable, which means that variable outputs oscillate with increasing amplitudes and the total energy balance change significantly. The maximum stable time increment is computed, generally, from the smallest element size and the highest wave speed in the model. The dilatation wave speed, c_d, in a element is computed as:

$$c_d = \sqrt{\frac{\hat{\lambda} + 2\,\hat{\mu}}{\rho}}\,, \tag{3.107}$$

where ρ is the density of the material and, $\hat{\lambda}$ and $\hat{\mu}$ are the effective Lam's constants which for isotropic materials are determined by:

$$\hat{\lambda} = \frac{E\,\nu}{(1+\nu)\,(1-2\,\nu)}\,, \tag{3.108}$$

$$\hat{\mu} = \frac{E}{2\,(1+\nu)}\,, \tag{3.109}$$

Therefore, the stability time increment can be estimated as:

$$\Delta t \leq min\left(L_e \sqrt{\frac{\rho}{\hat{\lambda} + 2\,\hat{\mu}}}\right), \tag{3.110}$$

where L_e is the characteristic length of the smallest element. For quasi-static problems, the computational cost can be significantly expensive because they are problems where a relative large simulation time is required and also relative small elements for a reliable mesh. Therefore, the incremental time step could be really small compared to the total simulation time. Different strategies are available to speed up the simulations and reduce the computational cost. For this project, the computational cost has been reduced by using mass scaling technique. This technique increase artificially the material density by a factor f^2 that reduces the number of increments required to fulfill the simulation time, n, to n/f. In other words, increase the incremental time step by a factor of f. The mass scaling can be defined directly by determining a mass scale factor or indirectly by determining a specific time increment step. However, a mass scaling factor is too high, can introduce errors such as the inertia forces dominate the model and change the solution.

3.6.4 Eigenvalue buckling analysis procedure

Finally, the eigenvalue buckling analysis procedure has been used in this project to compute the critical bifurcation load of the model. It is a linear perturbation model procedure and is also used to introduce the initial imperfection shape in the implicit and explicit post-buckling procedures. The eigenvalue buckling problem look for the loads for which the model stiffness matrix becomes singular:

$$K^{MN}\, v^{M} = 0\,, \tag{3.111}$$

where K^{MN} is the tangent stiffness matrix when the loads are applied and the v^{M} are the nontrivial displacements solutions. The applied loads can be pressures, concentrated forces, nonzero prescribed displacements and/or thermal loading. The buckling loads are computed relative to the base state of the structure and omit the material non-linearity, remaining the elastic properties. An incremental loading pattern Q^{N} is defined in the eigenvalue procedure scaled by the load multipliers λ_i. Therefore, the tangent stiffness matrix from the previous equation, is reformulated as:

$$\left(K_0^{MN} + \lambda_i\, K_\Delta^{MN}\right)\, v^{M} = 0\,, \tag{3.112}$$

where K_0^{MN} is the stiffness matrix corresponding to the base state and K_Δ^{MN} is the differential initial stress and load stiffness matrix due to the incremental loading pattern Q^{N}. The eigenvalues are represented by λ_i and the buckling mode shapes are represented by v_i^{M}. The superscripts M and N refers to degrees-of-freedom of the whole model and i refers to the buckling mode number. The matrices K_0^{MN} and K_Δ^{MN} are symmetrized because the eigenvalues and eigenvectors only can be extracted from symmetric matrices. The buckling load for each mode is computed from the product $\lambda_i\, Q^{N}$. There are two methods in Abaqus code to extract the eigenvalues, Lanczos and the subspace iteration. The Lanczos method is generally faster when a large number of eigenmodes is required. The subspace iteration eigensolver method is the default defined in Abaqus and is more efficient when few eigenmodes are required. Therefore, for this project in which only the first eigenmode (the most critical) is required, the subspace iteration eigensolver is used.

Chapter 4

Mechanical properties calculation of the composite panel

In this chapter, mechanical properties of the laminate plies have been estimated. Due to the composite panels manufacturer has not been able to provide this mechanical properties, a series of tensile tests, theoretical calculations and finite element model have been carried out to estimate values of stiffness and strength necessaries for modeling the CAI test.

4.1 Experiment Tensile test

The mechanical properties of the laminate plies have been estimated from the laminate global stiffness and strength. In order to achieve this goal, several tensile tests have been carried out following the standard *EN ISO 527-4 "Plastics - Determination of tensile properties - Part 4: Test conditions for isotropic and orthotropic fibre-reinforced plastic composites"* [53].

Figure 4.1: Tensile test set-up.

This is a standard developed for orthotropic materials, and can be used for composite laminates with different ply orientations and materials, as it is the case of the panel used in this project. The specimens tested have been cut following the recommended type 2 dimensions of the standard:

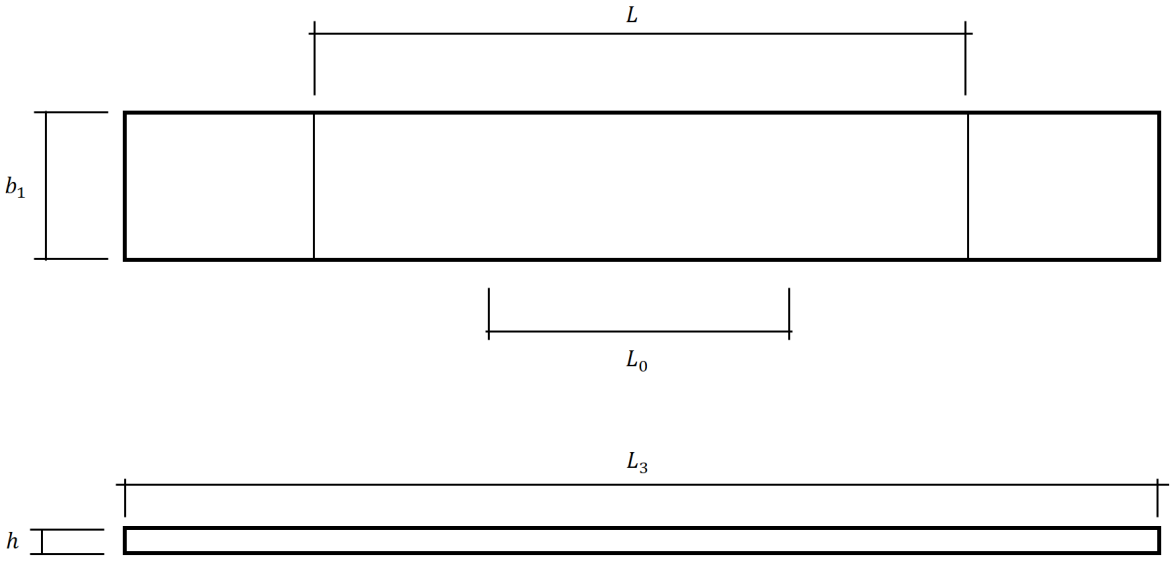

Figure 4.2: Scheme of the tensile test sample, type 2 at the EN ISO 527-4.

	Dimensions (mm)
Thickness, h	$2\ to\ 10$
Width, b_1	25 ± 0.5
Free length, L	150 ± 1
Measurement length, L_0	50 ± 1
Total length, L_3	≥ 250

Table 4.1: Recommended dimensions for Type 2 samples at the EN ISO 527-4.

A total of seven specimens have been cut by means of a water jet cutter. This is an industrial tool used to cut materials using very high-pressure jet of water and abrasive substance mixture.

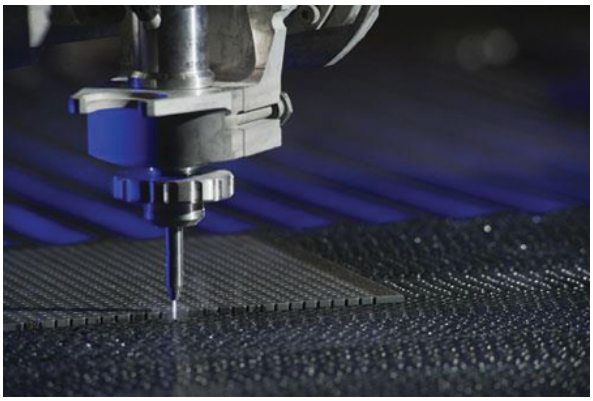

Figure 4.3: Water jet cutter example.

After cutting the specimens, the most relevant dimensions for the test calculations has been measured. The average values and standard deviations for each sample are shown in the following table:

	Thickness [mm]		Width [mm]	
Sample	Mean	s	Mean	s
P3-S01-T	2.14	0.015	23.72	0.08
P3-S02-T	2.13	0.011	22.53	0.38
P3-S03-T	2.14	0.04	23.34	0.05
P3-S04-T	2.10	0.03	23.35	0.05
P3-S05-T	2.12	0.03	23.34	0.19
P3-S06-T	2.12	0.02	24.67	0.03
P3-S07-T	2.15	0.03	24.76	0.02

Table 4.2: Dimensions measured for the tensile test samples.

The tests have been carried out with INSTRON 8802 testing machine. The strain has been measured with the *Advanced Video Extensometer AVE 2663-821*, which is a non-contacting extensometer capable of measure longitudinal and transverse deformations during the test.

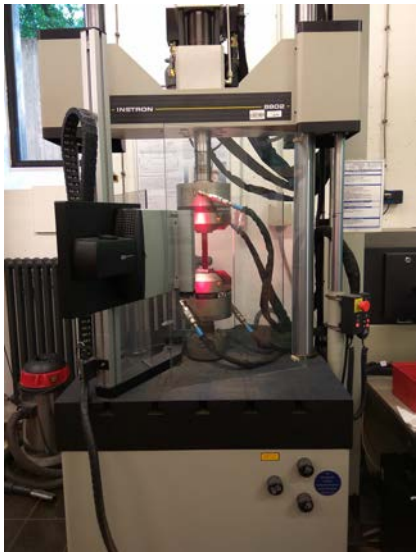

Figure 4.4: Tensile test set-up.

The experiment outputs are the force measured by the load cell of the testing machine and the strain deformation in the longitudinal and transverse direction measured by the video extensometer device. Due to the transverse strain measure has a lot of noise, no profitable information can be extracted. Therefore, the relevant results for this project are the evolution of the axial strain and the force at each time step. The results extracted from the transverse strain can be see in Appendix A:

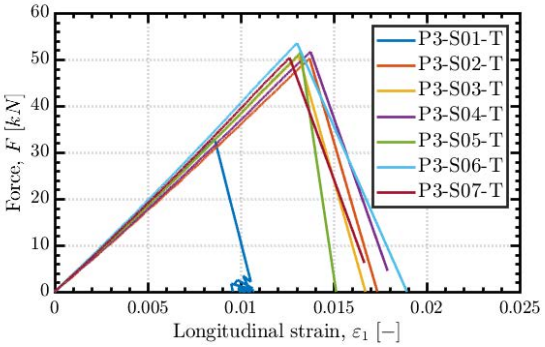

Figure 4.5: Tensile tests outputs.

From this data has been computed the failure stress (σ_F) and the elastic modulus E_{lam} in the load direction of the laminate for each sample. As the standard recommend, the stiffness of the laminate is computed by the following formula:

$$E_{lam} = \frac{\sigma'' - \sigma'}{\varepsilon'' - \varepsilon'} \tag{4.1}$$

Where σ' and ε' are the stress and strain in the longitudinal direction at strain $\varepsilon = 0.0005$. And σ'' and ε'' are the stress and strain in the longitudinal direction at strain $\varepsilon = 0.0025$. The stress σ is computed with the force measured by the testing machine and the sample section following the next formula:

$$\sigma = \frac{F}{b_1\, h} \tag{4.2}$$

Sample	$\sigma_F\ [MPa]$	$\varepsilon_{max}\ [-]$	$E_{lam}\ [GPa]$
P3-S01-T	646.2	0.00860	71.68
P3-S02-T	1047.2	0.01373	72.50
P3-S03-T	1017.0	0.01313	72.94
P3-S04-T	1052.0	0.01376	70.82
P3-S05-T	1040.4	0.01322	71.86
P3-S06-T	1021.1	0.01303	73.71
P3-S07-T	947.2	0.01263	69.35

Table 4.3: Results for the tensile test samples.

Averaged values have been estimated from the results of each sample. As can be seen in the Figure 4.5, the ultimate load of the sample P3-S01-T is much lower than the others. This is because the sample had an initial defect. Therefore, the ultimate load is not take in account at the average estimation, but the elastic modulus is useful. The final results are:

	Mean	s
$\sigma_F\ [MPa]$	1020.2	38.4
$\varepsilon_{max}\ [-]$	0.01325	$4.333 \cdot 10^{-4}$
$E_{lam}\ [GPa]$	71.84	1.44

Table 4.4: Average results for the tensile test.

Here, the picture of the damaged samples after the tests is shown.

Figure 4.6: Tensile test samples failure.

4.2 Micromechanic and CLT for mechanical properties set-up

The first approach to compute the elastic properties of each ply is made by the micromechanic point of view. With these results, the classical laminate theory is applied to check whether the whole laminate properties fit or not with the experimental results. Through this procedure, the properties that do not have a significant influence in the tensile test can be estimated by micromechanic models.

First of all, some basic data is needed to have a point to start with micromechanic models, such as the fibers Young's modulus, shear modulus and Poisson's ratio in the longitudinal and transverse direction. Due to carbon fibers have an anisotropic behavior, information about longitudinal and transverse directions is needed. However, the information given by the manufacturer was only in the fiber direction. Therefore, some research has been carried out to get the rest of properties that are typical in this material [41].

Carbon fiber properties	
$\rho_f\ [kg/m^3]$	1800
$E_{1,f}\ [GPa]$	230
$E_{2,f}\ [GPa]$	15
$\nu_{12,f}\ [-]$	0.3
$G_{12,f}\ [GPa]$	9
$\sigma_{F,f}\ [MPa]$	2400
$\varepsilon_{max,f}\ [-]$	0.018

Table 4.5: Carbon fiber properties.

The matrix is an epoxy resin which is an isotropic material. Therefore, only the Young's modulus and Poisson's ratio are needed to define the elastic mechancial behavior, because the shear modulus is computed from them with the following formula: $G = E/(2\cdot(1+\nu))$. All the resin data was not given by the manufacturer and was extracted from literature [41].

Epoxy resin properties	
$\rho_m\ [kg/m^3]$	1250
$E_m\ [GPa]$	3.8
$\nu_m\ [-]$	0.38
$G_m\ [GPa]$	1.38

Table 4.6: Epoxy resin properties.

From previous data in Tables 4.5 and 4.6 plus the fiber volume fraction of unidirectional $V_{f,UD}$ and woven $V_{f,W}$ plies, the micromechanic models can be computed. However, CLT calculations needs information about the laminate staking, plies orientation and thickness too.

Ply	Material	$t\ [mm]$	Φ [º]
1	Woven	0.202	0
2	UD	0.144	0
3	UD	0.144	90
4	UD	0.144	0
5	UD	0.144	90
6	UD	0.144	0
7	UD	0.144	90
8	UD	0.144	90
9	UD	0.144	0
10	UD	0.144	90
11	UD	0.144	0
12	UD	0.144	90
13	UD	0.144	0
14	Woven	0.202	0

Table 4.7: Laminate material, thickness and orientation.

Finally, using micromechanic models combined with CLT, several candidates has been evaluated changing the fiber volume fraction of the unidirectional and woven plies with a self-programmed code in MATLAB. The best fitting found with the experimental results has been for $V_{f,UD} = 0.58$ and $V_{f,W} = 0.55$, and these are the results:

Micromechanic models for unidirectional plies

- Young's modulus in the fiber direction.

$$E_1 = E_{1,f}\,V_f + E_m\,\left(1 - V_f\right) = 230 \cdot 0.58 + 3.8\,\left(1 - 0.58\right) = 135\,[GPa] \tag{4.3}$$

- In-plane poisson's ratio.

$$\nu_{12} = \nu_{12,f}\,V_f + \nu_m\,\left(1 - V_f\right) = 0.3 \cdot 0.58 + 0.38\,\left(1 - 0.58\right) = 0.334 \tag{4.4}$$

- Young's modulus in the transverse direction.

$$\begin{cases} \xi = 2 \\ \eta = \dfrac{\frac{E_{f,2}}{E_m} - 1}{\frac{E_{f,2}}{E_m} + \xi} = \dfrac{\frac{15}{3.8} - 1}{\frac{15}{3.8} + 2} = 0.4956 \\ E_2 = E_m\,\dfrac{1 + \xi\,\eta\,V_f}{1 - \eta\,V_f} = 3.8 \cdot \dfrac{1 + 2 \cdot 0.4956 \cdot 0.58}{1 - 0.4956 \cdot 0.58} = 8.40\,[GPa] \end{cases} \tag{4.5}$$

- In-plane shear modulus.

$$\begin{cases} \xi = 1 + 40\, V_f^{10} = 1 + 40 \cdot (0.58)^{10} = 1.1723 \\ \eta = \dfrac{\frac{G_{f,12}}{G_m} - 1}{\frac{G_{f,2}}{G_m} + \xi} = \dfrac{\frac{9}{1.38} - 1}{\frac{9}{1.38} + 1.1723} = 0.7177 \\ G_{12} = G_m \dfrac{1 + \xi\, \eta\, V_f}{1 - \eta\, V_f} = 1.38 \cdot \dfrac{1 + 1.1723 \cdot 0.7177 \cdot 0.58}{1 - 0.7177 \cdot 0.58} = 3.51\ [GPa] \end{cases} \tag{4.6}$$

Micromechanic models for woven plies

- Young's modulus in the fiber and transverse direction.

$$E_1 = E_2 = V_f \left(\frac{E_{1,f}}{2} + \frac{3\, E_m}{2} \right) + E_m = 0.55 \left(\frac{230}{2} + \frac{3 \cdot 3.8}{2} \right) + 3.8 = 70.18\ [GPa] \tag{4.7}$$

- In-plane shear modulus.

$$G_{12} = E_m \frac{4\, V_f + 1}{3} = 3.8 \frac{4 \cdot 0.55 + 1}{3} = 4.05\ [GPa] \tag{4.8}$$

- In-plane poisson's ratio.

$$\nu_{12} = \frac{G_{12}}{E_1} = \frac{4.05}{70.18} = 0.058 \tag{4.9}$$

Laminate stiffness computation with CLT

- Stiffness matrix of unidirectional plies oriented in its material coordinate system.

$$\nu_{21} = \frac{E_2}{E_1}\, \nu_{12} = \frac{8.4}{135} \cdot 0.334 = 0.0208 \tag{4.10}$$

$$\begin{aligned} [Q_{UD}] &= \begin{bmatrix} \frac{135}{1 - 0.334 \cdot 0.0208} & \frac{0.0208 \cdot 135}{1 - 0.334 \cdot 0.0208} & 0 \\ \frac{0.0208 \cdot 135}{1 - 0.334 \cdot 0.0208} & \frac{4.8}{1 - 0.334 \cdot 0.0208} & 0 \\ 0 & 0 & 3.51 \end{bmatrix} = \\ &= \begin{bmatrix} 135.94 & 2.82 & 0 \\ 2.82 & 8.46 & 0 \\ 0 & 0 & 3.51 \end{bmatrix} [GPa] \end{aligned} \tag{4.11}$$

- Stiffness matrix of woven plies oriented in its material coordinate system.

$$\nu_{21} = \frac{E_2}{E_1}\, \nu_{12} = \frac{70.18}{70.18} \cdot 0.058 = 0.058 \tag{4.12}$$

$$[Q_W] = \begin{bmatrix} \frac{135}{1-0.058\cdot 0.058} & \frac{0.058\cdot 135}{1-0.058\cdot 0.058} & 0 \\ \frac{0.058\cdot 135}{1-0.058\cdot 0.058} & \frac{4.8}{1-0.058\cdot 0.058} & 0 \\ 0 & 0 & 4.05 \end{bmatrix} = \\ = \begin{bmatrix} 70.42 & 4.07 & 0 \\ 4.07 & 70.42 & 0 \\ 0 & 0 & 4.05 \end{bmatrix} [GPa] \tag{4.13}$$

- Stiffness matrix of unidirectional plies oriented in the laminate global coordinate. system.

$$[\overline{Q}_{UD,0^o}] = \begin{bmatrix} 135.94 & 2.82 & 0 \\ 2.82 & 8.46 & 0 \\ 0 & 0 & 3.51 \end{bmatrix} [GPa] \tag{4.14}$$

$$[\overline{Q}_{UD,90^o}] = \begin{bmatrix} 8.46 & 2.82 & 0 \\ 2.82 & 135.94 & 0 \\ 0 & 0 & 3.51 \end{bmatrix} [GPa] \tag{4.15}$$

- Stiffness matrix of woven plies oriented in the laminate global coordinate system.

$$[\overline{Q}_W] = \begin{bmatrix} 70.42 & 4.07 & 0 \\ 4.07 & 70.42 & 0 \\ 0 & 0 & 4.05 \end{bmatrix} [GPa] \tag{4.16}$$

- Laminate stiffness matrices.

$$[A] = \begin{bmatrix} 153.21 & 6.52 & 0 \\ 6.52 & 153.21 & 0 \\ 0 & 0 & 7.71 \end{bmatrix} \cdot 10^6 \, [N/m] \tag{4.17}$$

$$[B] = \begin{bmatrix} 0 & 0 & 0 \\ 0 & 0 & 0 \\ 0 & 0 & 0 \end{bmatrix} [N] \tag{4.18}$$

$$[D] = \begin{bmatrix} 64.48 & 2.75 & 0 \\ 2.75 & 50.78 & 0 \\ 0 & 0 & 3.04 \end{bmatrix} [N\cdot m] \tag{4.19}$$

- Laminate elastic modulus in the x direction.

$$E_{1,Lam} = \frac{A_{11}}{t} = \frac{153.21\cdot 10^6}{2.132\cdot 10^{-3}} = 71.86 \, [GPa] \tag{4.20}$$

This value compared to the tensile test stiffness result ($71.84 \, [GPa]$) has a 0.03% of difference.

	$E_{1,Lam}$ $[GPa]$	Error $[\%]$
Experimental	71.84	-
CLT	71.86	0.03

Table 4.8: Experimental and CLT longitudinal stiffness comparative.

4.3 Tensile test finite element model

Finite elements models are created of the tensile test for two main reasons, one is to check the finite element model with elastic behavior of the laminate. The other reason is to estimate the strength properties of each ply material. Moreover, three three-dimensional models of tensile test has been created, one with conventional shell elements, other with continuum shell elements and the last one with continuum shell elements plus cohesive elements. Conventional shell elements have an elastic formulation based on CLT and they have no physical thickness in the model, it is a parameter of the section definition. However, to define interfaces for modeling CAI test delaminations, a layer-wise modeling is required and this only can be done by using continuum shell elements with a only one element per layer through-thickness direction. Continuum shell elements have a similar formulation to conventional shells but, they have a physical thickness. Finally, a model including the interfaces laminate plies has been created to evaluate the influence of these cohesive elements in the elastic behavior and failure load. All these types of elements are explained in Section 3.3 and Section 3.4.

When a model is created in Abaqus code, a consistent system of units has to be followed. The international system of units (SI) may be an option. However, there is a limitation in the Abaqus code which is that it has problems to create layers with a thickness smaller than 10^{-5} $[ud]$. If the SI is used, the thickness of the interfaces ($10^{-5} = 0.01 \cdot 10^{-3}$ $[m]$) is just one order of magnitude smaller than the thickness of the most thin ply ($0.144 \cdot 10^{-3}$ $[m]$). Therefore, the unit system used is the SI (mm) with length in mm and mass in $tonnes$, this way the thickness difference between laminate plies (0.144 $[mm]$) and interfaces (10^{-5} $[mm]$) is large enough.

Quantity	SI (mm)
Length	mm
Mass	t
Time	s
Force	N
Stress	MPa
Energy	mJ
Density	t/mm^3

Table 4.9: Unit system followed in finite elements models.

4.3.1 Geometry, boundary conditions and loads

The model geometry is based on the tensile test standard from in Figure 4.2 and Table 4.1, and only the zone between the test clamps is modeled.

Conventional shell model

For the model of conventional shell elements, the geometry is built from a planar rectangle with the dimensions shown in Figure 4.7. During the test, the fixtures constrain all the movements of

the specimen and, for conventional shell elements which have 6 DoF per node, 3 displacements (U_1, U_2 and U_3) and 3 rotations (UR_1, UR_2 and UR_3), the boundary conditions in both edges are also a clamped restrained. Although in one of the edges, in the axial direction U_1, a motion is prescribed instead of applying a force, because in this way the force distribution is more realistic along the specimen edges.

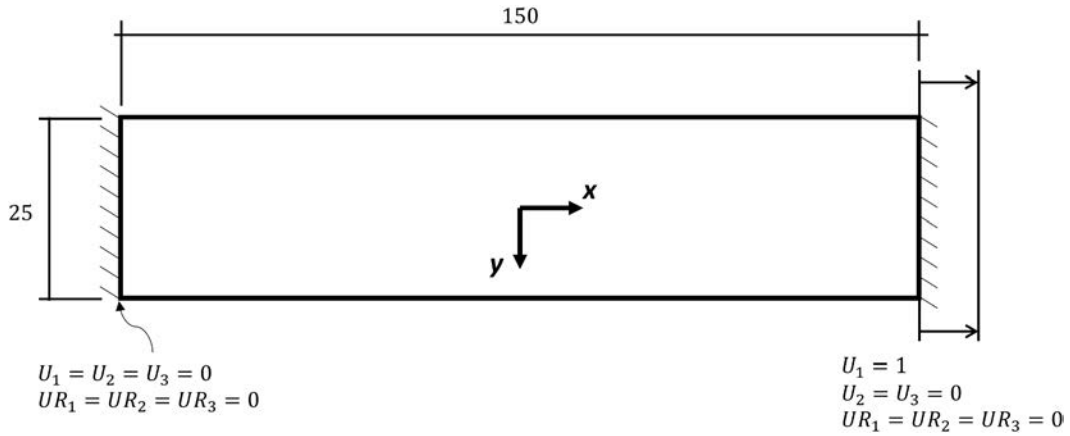

Figure 4.7: Geometry and boundary conditions of the conventional shell model (dimensions in mm).

In order to make easier the post-process of the results, a kinematic coupling constraint has been created between the displaced edge nodes and an artificial node created where all the boundary conditions of this edge are defined (Figure 4.8). This way, the reaction force of the laminate due to the prescribed displacement in the axial direction defined is saved during the calculations.

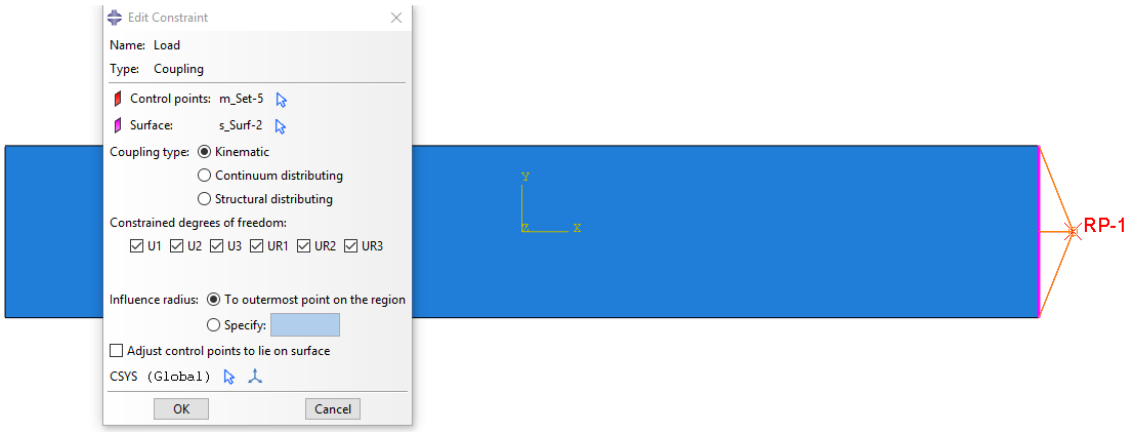

Figure 4.8: Coupling constraint in conventional shell model.

In Figure 4.9, the applied boundary conditions in the model are shown:

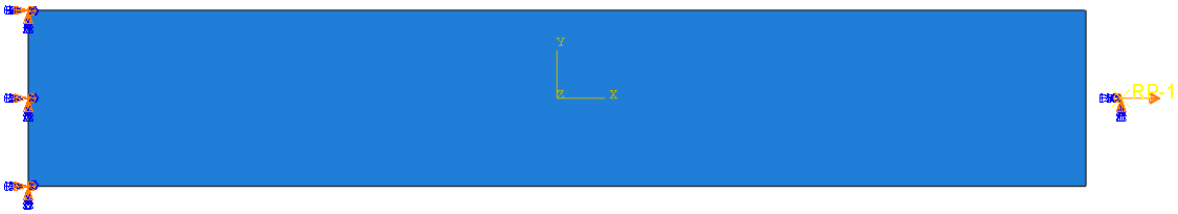

Figure 4.9: Boundary conditions applied in conventional shell model.

Continuum shell model

In the model with continuum shell elements, the geometry has to be able to model a layer-wise laminate. Therefore, the same geometric part as conventional shells is created but with a thickness of $2.132\,[mm]$. Then, this part has been cut by several horizontal planes until the 14 plies of the laminate are created. The thickness of each ply has to be in accordance with the respective ply of the laminate. Regarding the boundary conditions, they are not defined for continuum shell elements in the same way because they have only 3 DoF (U_1, U_2 and U_3). However, they are applied now to surfaces instead of edges and, if the displacements are restrained in all these surfaces, the rotations in the space are indirectly restrained too. So, at the end the boundary conditions applied are equivalent.

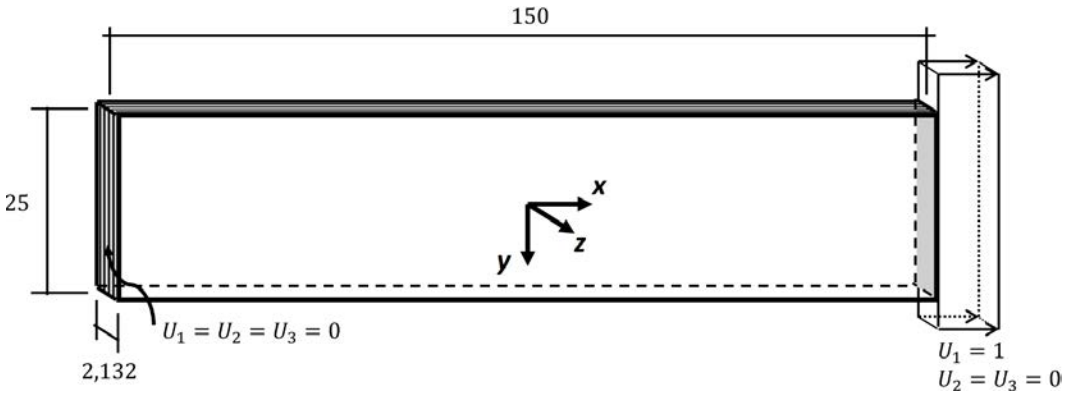

Figure 4.10: Geometry and boundary conditions of the continuum shell model (dimensions in mm).

Similarly to conventional shells, the surfaces with the prescribed displacement in the axial direction have been constrained to an artificial node through a kinematic coupling of the nodes of the surfaces.

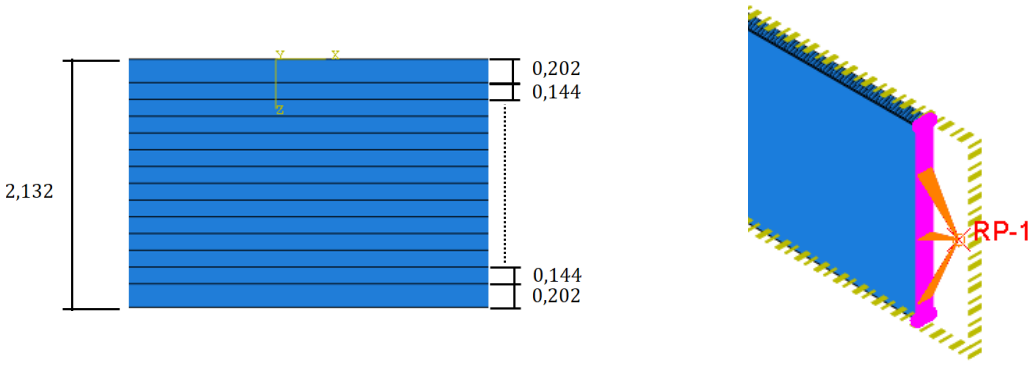

Figure 4.11: Geometry for continuum shells and coupling constraint (dimensions in mm).

Continuum shell and cohesive interfaces model

Finally, for this model with cohesive interfaces, the geometry is based on the previous model and is modified to include interfaces between plies. To create these interfaces, a cut has been done by an offset horizontal plane creating interfaces of thickness of 10^{-5} $[mm]$, which is the minimum value allowed by the software. The minimum value has been chosen because that will minimize the influence on the final results.

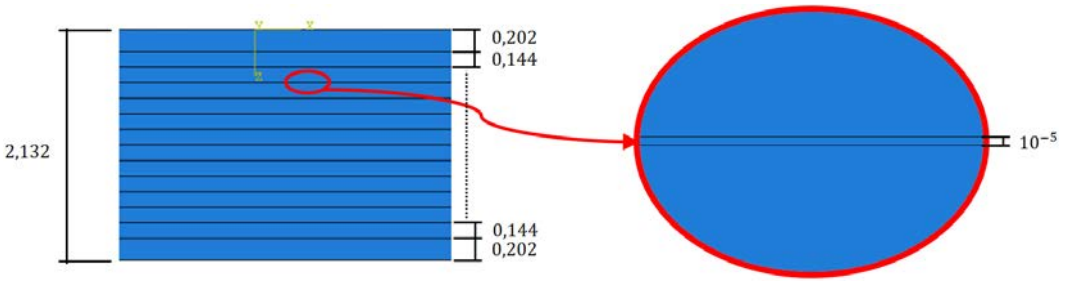

Figure 4.12: Plies and interfaces geometry (dimensions in mm).

4.3.2 Material models

Composite plies properties

Almost every elastic property required to define the elastic lamina material in Abaqus for the unidirectional and woven plies has been already obtained from the micromechanic and CLT models. The still missing data has been taken from similar materials. The final elastic properties definitions of the unidirectional and woven plies are:

	Units	UD	Woven
E_1	$[GPa]$	135	70.18
E_2	$[GPa]$	8.4	70.18
ν_{12}	$[-]$	0.334	0.058
G_{12}	$[GPa]$	3.51	4.05
G_{13}	$[GPa]$	3.51	3.18
G_{23}	$[GPa]$	2.68	3.18

Table 4.10: Elastic mechanical properties of the laminate plies.

As in Section 3.3 has been explained, to model the failure of each ply the Hashin criterion has been chosen ($\alpha = 1$) with an energy based damage evolution with linear softening.

	Units	UD	Woven
α	$[-]$	1	1
X_T	$[MPa]$	2300	1055
X_C	$[MPa]$	1450	676
Y_T	$[MPa]$	60	945
Y_C	$[MPa]$	200	614
S_T	$[MPa]$	70	63
S_L	$[MPa]$	65	63

Table 4.11: Hashin damage initiation definition of the laminate plies.

	Units	UD	Woven
G^C_{ft}	$[N/mm]$	14	14
G^C_{fc}	$[N/mm]$	14	14
G^C_{mt}	$[N/mm]$	0.2	14
G^C_{mc}	$[N/mm]$	7	14
η^C_{ft}	$[-]$	0.001	0.001
η^C_{fc}	$[-]$	0.005	0.005
η^C_{mt}	$[-]$	0.001	0.001
η^C_{mc}	$[-]$	0.005	0.005

Table 4.12: Hashin damage evolution definition of the laminate plies.

Cohesive material for modeling interfaces

As has been explained in Section 3.4, to model the interfaces with cohesive elements, a traction-separation law is chosen for the elastic behavior with a quadratic damage initiation criteria and a mixed mode B-K damage evolution with linear softening. All the data is taken from similar materials available in the literature. In a future work would be better to measure this properties for the laminate studied.

	Units	Value
E_{nn}	$[MPa/mm]$	1000000
E_{ss}	$[MPa/mm]$	1500000
E_{tt}	$[MPa/mm]$	1500000

Table 4.13: Elastic properties of the traction-separation law in cohesive elements.

	Units	Value
t^0_n	$[MPa]$	60
t^0_s	$[MPa]$	90
t^0_t	$[MPa]$	90

Table 4.14: Nominal stresses for damage initiation criterion in cohesive elements.

	Units	Value
η_{BK}	$[-]$	1
G^C_n	$[N/mm]$	0.25
G^C_s	$[N/mm]$	0.50
G^C_t	$[N/mm]$	0.50
μ_{BK}	$[-]$	0.001

Table 4.15: Fracture energies, exponent and viscous regularization parameter for damage evolution in cohesive elements.

4.3.3 Results and mesh dependency study

First, a mesh dependency study has been carried out with the model of conventional shell elements because the number of elements of the mesh is highly reduced and, therefore, there is a lower computational cost. The strategy followed has been to duplicate the number of nodes in x and y direction.

Nº Elements	Buckling stress $[MPa]$	Variation $[\%]$
150	1003.8	–
600	1008.7	0.49
2400	1009.2	0.05

Table 4.16: Mesh dependency analysis results for 2D tensile test.

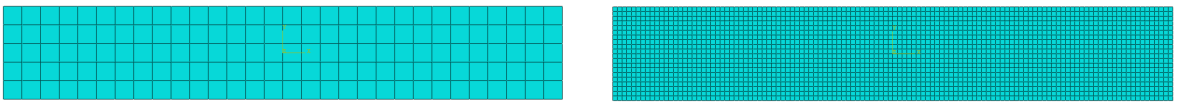

(a) 150 elements.

(b) 2400 elements.

Figure 4.13: Meshes used in the mesh dependency analysis.

With a mesh of 600 elements is assumed that the solution has converged and, if these elements size is used for the continuum shell models, the following results are obtained. They are also compared to the experimental average results:

Case	Buckling stress $[MPa]$	Variation $[\%]$
Experimental	1020.2	–
2D model	1008.7	1.13
3D model	1018.0	0.21

Table 4.17: Numerical and experimental results comparative for tensile test.

Finally, the results have shown that the finite element models models developed for the tensile test have been able to predict the failure stress of the experiment with an excellent precision.

Chapter 5

Experimental CAI tests

The experimental phases of the Compression-After-Impact tests, as it has been explained in Section 2, are composed of impact test, damage inspection and CAI test. In this project, a total of nine samples has been tested and named: P2-S11, P2-S12, P3-S01, P3-S02, P3-S03, P3-S04, P3-S05, P3-S06 and P3-S07. The samples have been cut by the same method the the tensile test samples and form two panels, called P2 and P3, with the same laminate. Therefore, in this chapter, all the experimental methods used and the results obtained are described.

5.1 Impact test

Although in CAI tests standards recommend to use a drop-tower apparatus to carry out this experiment with a specific specimen clamp system, the device available was an experimental pendulum system. Therefore, this last system is the one used for impact tests.

5.1.1 Pendulum system test

An experimental pendulum system for impact tests has been developed by the HAW University of Applied Science. The pendulum system was composed basically of three principal parts, an arm or beam with a cylindrical joint in the upper part and an assembly system to add masses to the lower edge. The second basic component is the frame where the samples were fixed. The third one, was a angular position sensor combined with a acquisition system which collect the position signal and time of the test at a determined frequency.

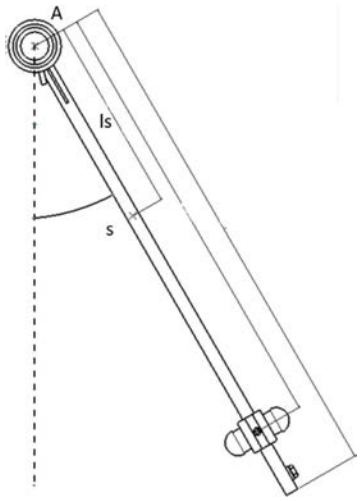

Figure 5.1: Pendulum impact system developed at HAW Hamburg University of Applied Science.

The pendulum has a stop pin to prevent more than one impact when it bounce back after the first impact. Moreover, the masses at the lower end can be tuned in order to get the proper impact energy level combined with the pendulum starting point height.

This pendulum system had a documentation associated written by students work based on free and forced oscillations of rotating pendulum (cp. e.g. [54]). At this documentation, all the masses from the pendulum mobile parts were measured and the distances to each center of masses. From this information, the mass moment of inertia J_A can be computed referenced to the point A respect from all the masses are rotating. In Figure 5.2, all the parts masses taken in account are defined:

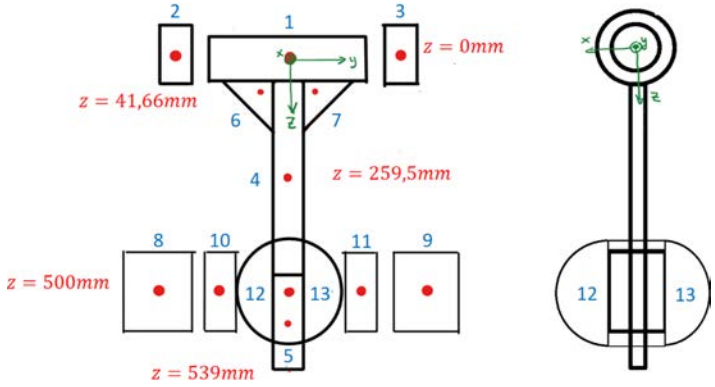

Figure 5.2: Pendulum center of masses for mass moment of inertia calculation.

The impact energy E_{imp} can be estimated from the mass moment of inertia $J_A = 0.383\ [kg \cdot m^2]$ combined with the angular velocity ω of the test:

$$E_{imp} = \frac{1}{2} J_A\ \omega^2\ , \tag{5.1}$$

where the angular velocity was computed from the numerical differentiation of the angular position $\phi(t)$ over time. The method used is known as symmetric difference quotient:

$$\omega(t_0) \approx \frac{\phi(t_0 + \Delta t) - \phi(t_0 - \Delta t)}{2\,\Delta t} \tag{5.2}$$

The samples fixture was formed by a rectangular window of $125\ [mm] \times 75\ [mm]$ where the samples were fully clamped along the four edges.

Figure 5.3: Pictures of the pendulum masses, indenter and sample clamp frame.

The sample clamp is much more restrictive than the recommended in the standards and the induced damages for a specific energy level may be larger. At the same time, the indenter has a diameter of $40\ [mm]$ instead of $16\ [mm]$ as recommended in the standards of Section 2.2.

5.1.2 Test results

The results from impact on the sample P2-S11 are presented in the following figure, where the angular position and angular velocity are represented over time. The differentiation of the angular position has a lot of noise and a filter has been applied to be able to get proper results:

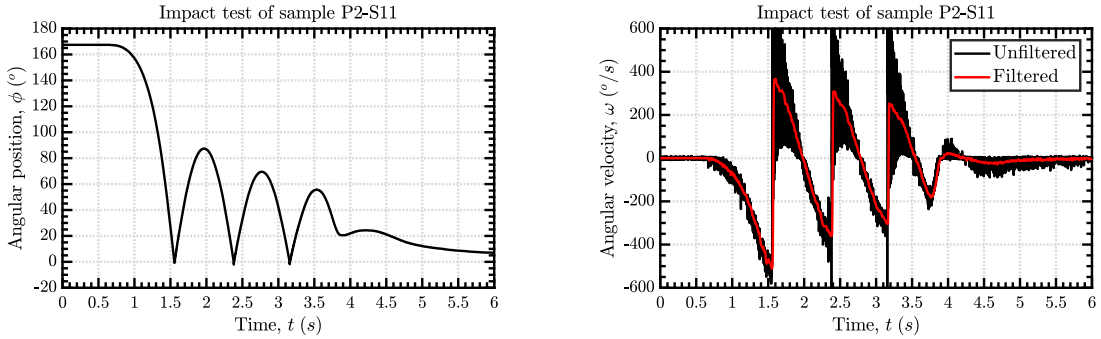

Figure 5.4: Example of angular position and velocity results for impact test of sample P2-S11.

The rest of impacts are shown in Appendix B. In the following graphs, all the impact energies and estimated damage energy absorbed by the laminates is shown.

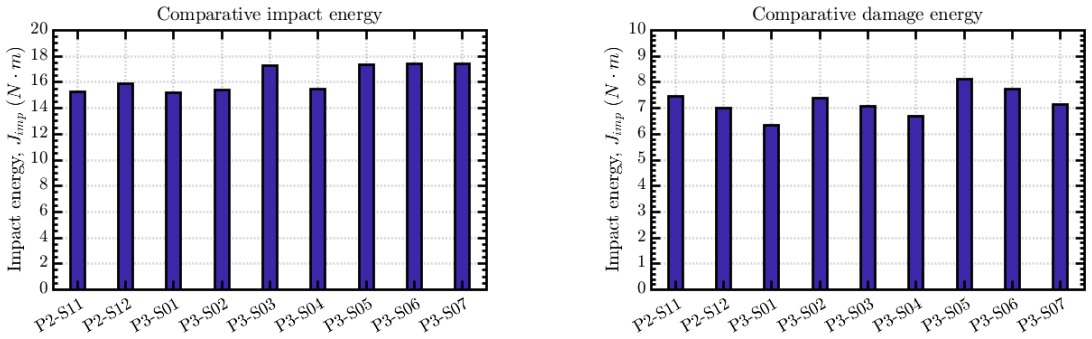

Figure 5.5: Summary impact test results.

Sample	Impact Energy $[J]$	Damage Energy $[J]$
P2-S11	15.29	7.45
P2-S12	15.91	7.00
P3-S01	15.20	6.34
P3-S02	15.37	7.40
P3-S03	17.26	7.04
P3-S04	15.48	6.67
P3-S05	17.37	8.12
P3-S06	17.41	7.71
P3-S07	17.40	7.12

Table 5.1: Impact tests result summary.

The impact energies are computed form the first peak of the angular velocity and it can be considered a reliable calculation. However, the estimation of the damage energy absorption cannot be fully trusted because it is computed from the lose of energy in the second peak and this lose is not only due to the damage absorption of the sample, it is also due to vibrations and frictions.

5.2 Ultrasonic C-scan inspection

In this project, the ultrasonic C-scanning has been employed for the damage detection and characterization of the impacted samples.

5.2.1 Ultrasonic scanning facility

The inspection system used in the HAW Hamburg University of Applied Science was composed of three subsystems such as the ultrasonic sensor, a numerical position control system and water pumping system. All these subsystems are controlled by a computer where all are connected to. Through this computer all the scanning inspection is controlled and also, all the data measured is collected. In Figure 5.6, the whole system can be seen:

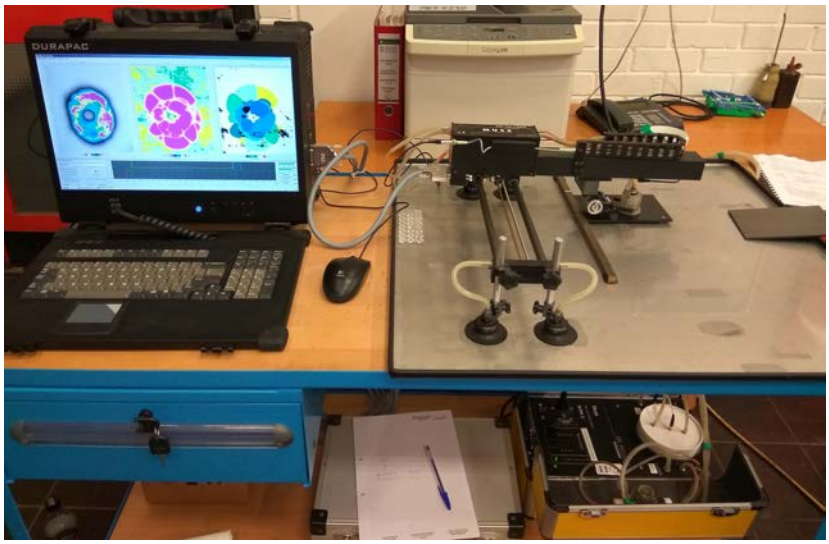

Figure 5.6: Ultrasonic C-scan system employed at the HAW University.

Between the sensor and the laminate to inspect has to be a coupling media, which is water in this case. This media allows to travel the ultrasonic waves between sensor and material to inspect. To be sure that there is water in between, the sensor is located inside a plastic cage connected to the water pumping system. This system inject water in the cage and absorb the excess of water and, this way always there is a film of water between the sensor and the laminate surface.

The set-up of the inspection is carried out in the computer where all the parameters required are defined. First, the parameters set-up of the sensor are defined in an undamaged zone. The aim of these parameters is that the software differentiates between an undamaged and damaged zone. This is done using the graph in Figure 5.7, which is the echo wave strength detected coming from the laminate versus the depth where the echo comes. This depth is computed from the time it takes for the signal to return to the sensor.

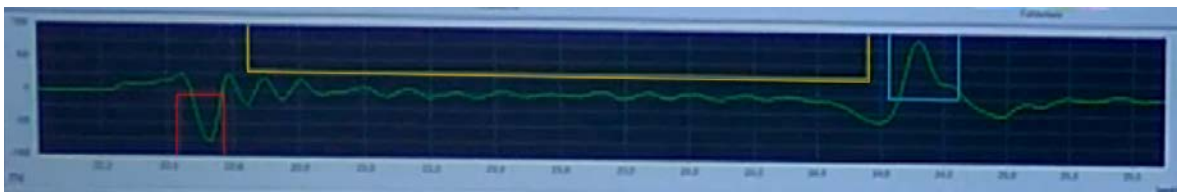

Figure 5.7: Graph for monitoring the echo signals received by the ultrasonic sensor.

The first peak from Figure 5.7 represents the echo from the upper surface of the laminate and it has to be found visually because there is a separation between the sensor and the upper surface of the laminate. This separation is due the sensor cage thickness and the water film in between. Also, the last peak has to be seen in this window, which is more or less at a distance form the first peak of the laminate thickness value. This last peak represents the bottom surface of the laminate. The parameters used to adjust this depth range are defined in Figure 5.8.

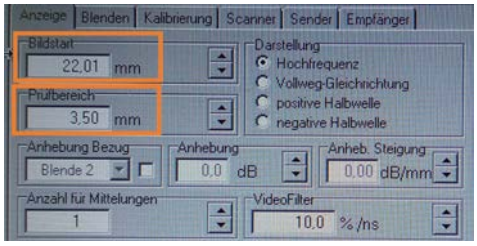

Figure 5.8: Signal through thickness range definition.

The red, blue and yellow areas from Figure 5.7 are defined in Figure 5.9a. These areas are where the software has to find the first peak (red rectangle), last peak (blue rectangle) and any intermediate peak caused by an internal damage (yellow rectangle). These rectangular areas have to be set visually by trying different undamaged zones of the laminate. The material sound speed has to be defined too (Figure 5.9b).

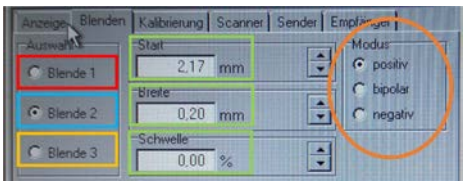

(a) Peaks detection zones definition.

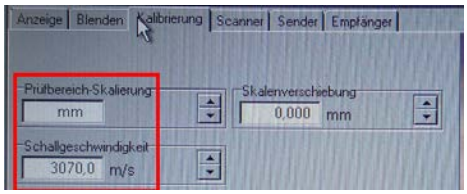

(b) Material sound speed definition.

Figure 5.9: Sensor parameters definition in software interface.

If the red and blue rectangles are too thin and far from the x-axis, information may be missed (cp. e.g. Figure 5.10a) when one of the peaks came out from these zones due vibrations during sensor movement or thickness changes in the laminate. Otherwise, if they are too wide and close to the x-axis, the information of the damages in the first and last interfaces may be missed. Moreover, the yellow area has to be close enough to capture the amplitude of the echo signals from internal damages but, not too close because a lot of noise is collected (Figure 5.10b).

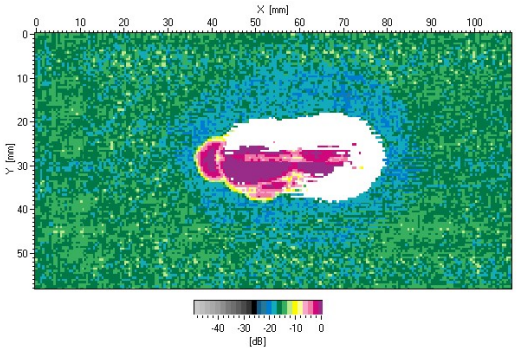

(a) Picture with missed information (white zones).

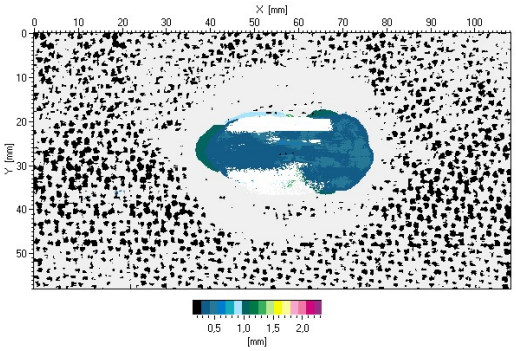

(b) Picture with noise (black dots).

Figure 5.10: Ultrasonic scans with bad set-up.

Finally, the area to inspect is defined in the parameters of Figure 5.11 and, the numerical position control system move the sensor through this area. Moreover, the sensor movement velocity and the distance traveled at each step in the x- and y-directions is also defined in the software interface. These last parameters are essential to get high-quality images of the damages. The higher the quality, the longer it will take. For initial fast results, a low-quality set-up is used with a velocity of 50% and steps in the x- and y-directions of $0.5\ [mm]$. Rather, for final high-quality results, a velocity of 30% and steps in the x- and y-directions of $0.1\ [mm]$ are set.

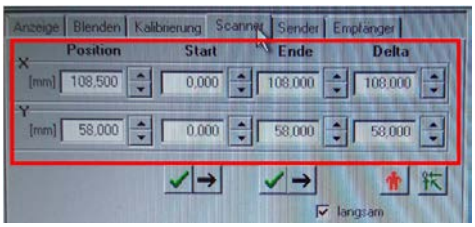

Figure 5.11: Rectangular area definition for numerical position control system.

From the ultrasonic C-scanning, the three pictures in Figure 5.12 are generate where different results are shown. In Figure 5.12a, the strength or intensity of the echo wave is plotted along the area inspected. The same results are shown in Figure 5.12a but, with the scale reversed. Finally, the picture with the most valuable information for this project is Figure 5.12c, because it shows where there is internal damage/delaminations and also the depth of it. Therefore, the shape and pattern through-thickness direction of the delaminations can be estimated form them.

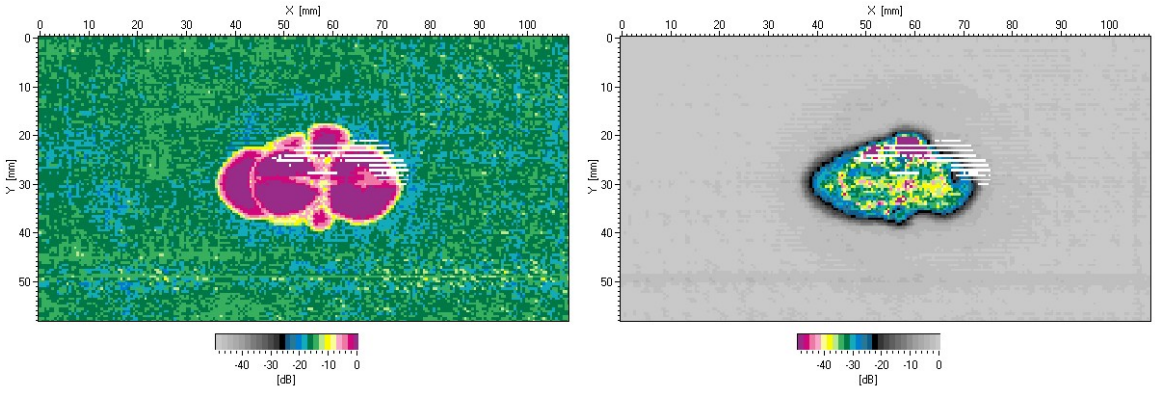

(a) Echo strength.

(b) Reversed echo strength.

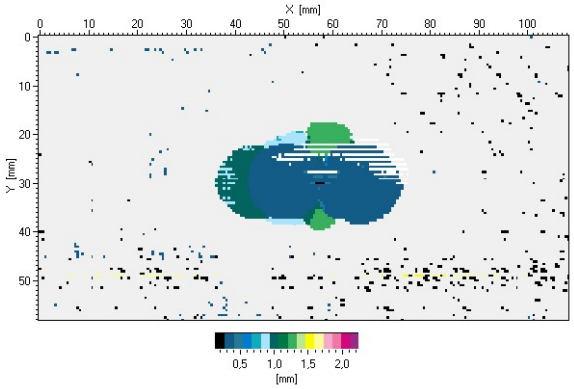

(c) Damage depth.

Figure 5.12: Pictures generate from ultrasonic C-scan inspection.

5.2.2 Pre- and post-impact scanning

Prior to impact tests, all the samples have been scanned to assure that they have no internal defects that may affect the CAI tests results. In Figure 5.13, an example of the scanning results for undamaged sample P3-S04 is shown where no damages or defects are observed. The rest of samples also present no defects or damages. In Appendix C can be seen the others inspections.

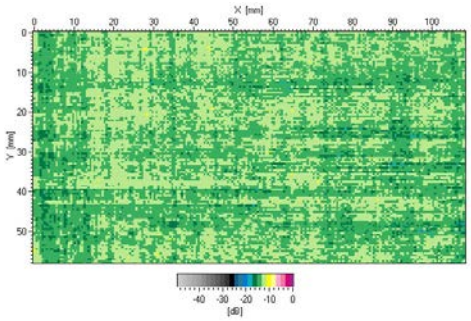

Figure 5.13: Pre-impact scan pictures of sample P3-S04.

After the impact test, a nomenclature for the sample faces has been set because is important to know which face has received the impact. Therefore, the impacted face has been named as *Back* and the opposite face as *Front* (Figure 5.14).

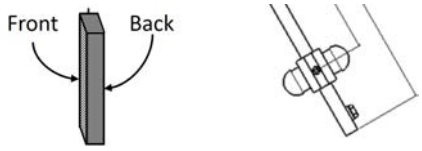

Figure 5.14: Samples faces name definition.

An initial series of inspections have been carried out of the whole area of the damaged samples, from the back face and with low-resolution results. These initial scanning have been used to have an idea of the total damaged area in every sample (Figure 5.15a). Then, from all these fast inspections, the size of the area of interest has been selected to carry out a detailed scan with high-resolution results (Figure 5.15b).

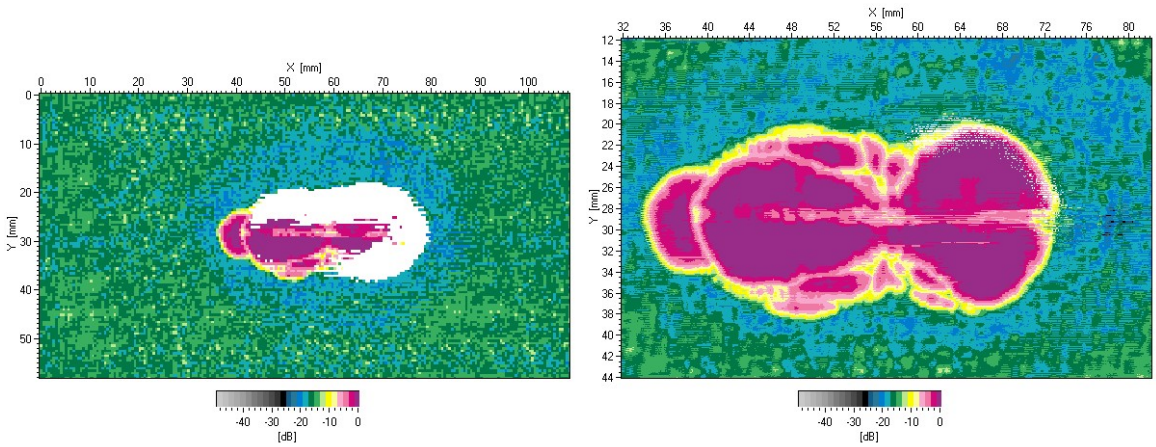

(a) Complete sample with low-resolution.

(b) Reduced area with high-resolution.

Figure 5.15: Preliminary front scanning of damaged sample P3-S02.

Once the detailed scanning has been done to all the samples from the front and back face, the color-scale used to define the depth levels has been homogenized (Figure 5.16).

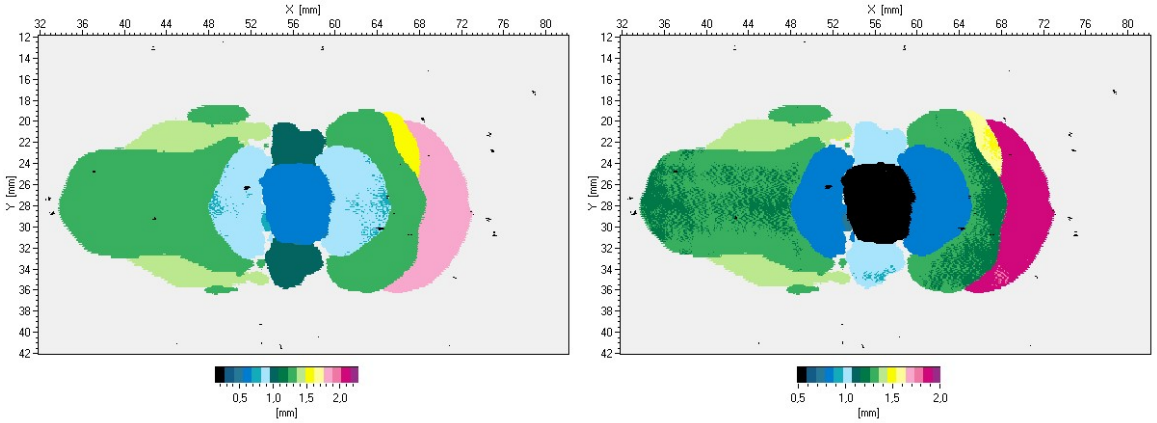

(a) Default color-scale. (b) Scaled color-scale.

Figure 5.16: Final post-process of back scanning of damaged sample P3-S02.

Finally, the identification of the damages to its corresponding laminate interfaces is carried out through the homogenized color-scale and detailed damage pictures combined with the histogram of the damage depths percentage per area scanned, like in Figure 5.17. In Appendix C, the rest of the ultrasonic C-scanning results are shown.

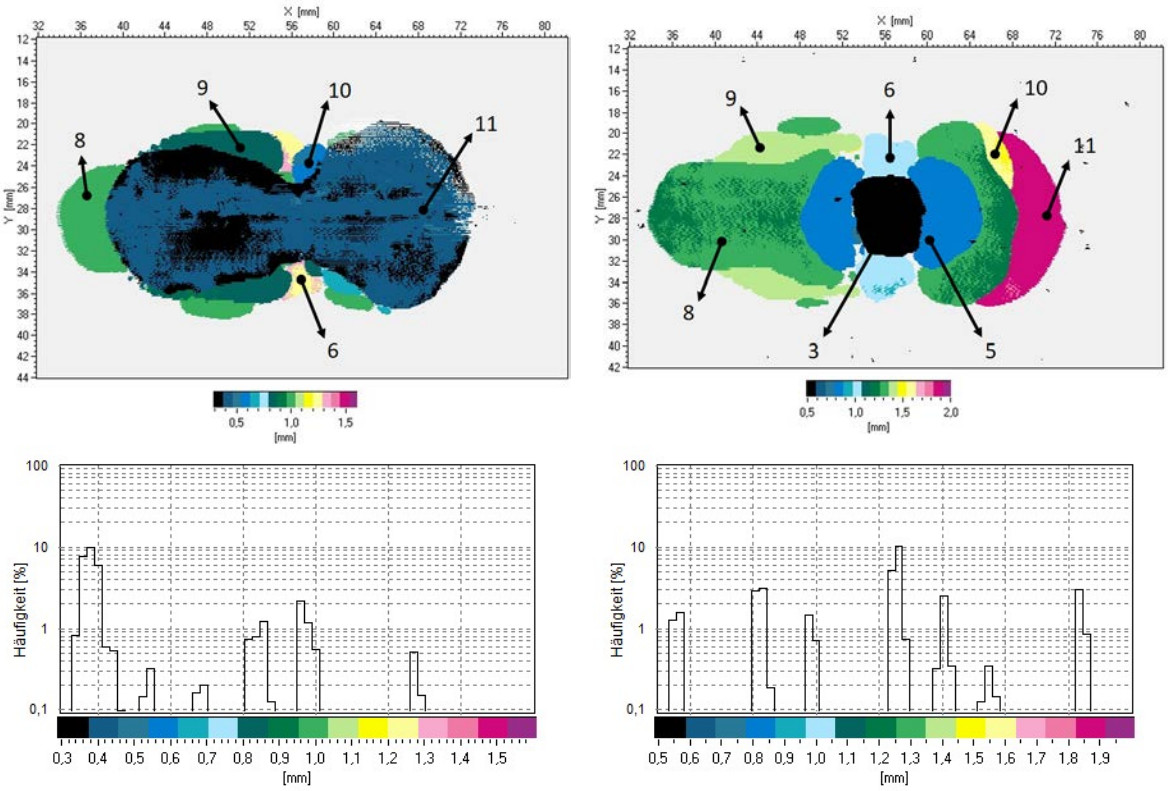

Figure 5.17: Damage interfaces identification in sample P3-S02.

This interface numbering is in accordance with the nomenclature defined in Figure 5.18. In agreement with some literature and with the delaminations observed in the ultrasonic scanning,

between layers with the same orientation (plies 7 and 8) there is no interfaces and, in consequence there can be no delaminations.

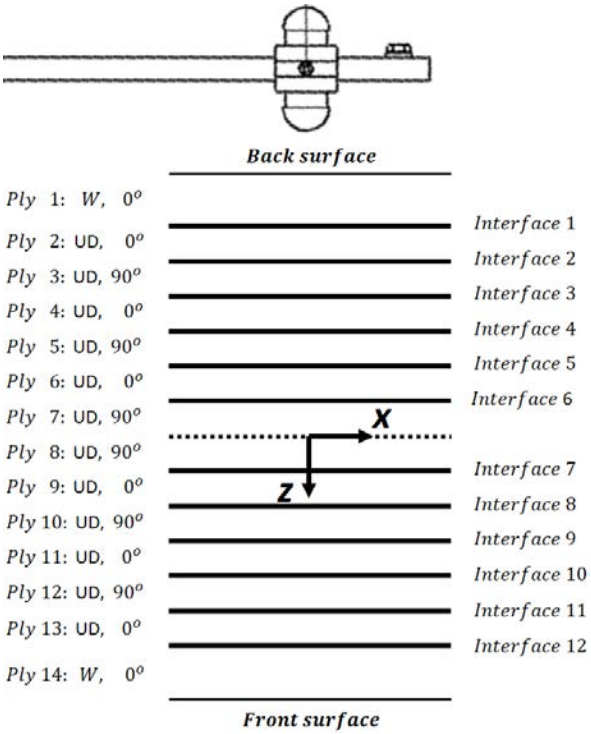

Figure 5.18: Interfaces numbering of laminates tested.

Although, a lot of information has been extracted from these inspections, the damage behind the first projections cannot be seen an this information is missing. This is why inspections have been carried out form both sides of the samples, to try to minimize this limitation.

5.2.3 Damage results summary

As a result of all the inspections carried out, all the projected areas of the delaminations have been compared to evaluate the size of the damaged area. As can be observed in Figure 5.19, the damage is located approximately at the same position and the area affected is quite similar.

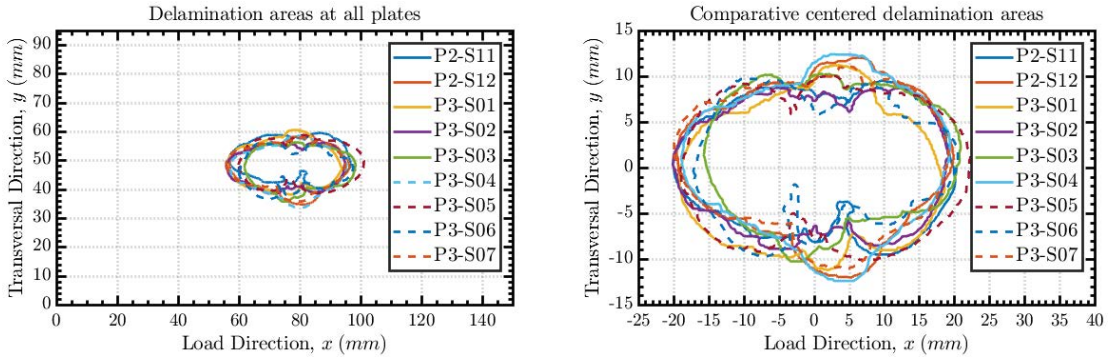

Figure 5.19: Comparative of global delamination shape.

Moreover, in Figure 5.20 and Table 5.2, the damaged area computed at each sample is represented. All the values are between $550\ [mm^2]$ and $670\ [mm^2]$, which are values much higher than the maximum established by the industry ($100\ [mm^]$) to start considering a repair.

In this project such a large damaged zone was the aim in order to see a more clear interaction between the local damage and the global buckling in thin plates under CAI test.

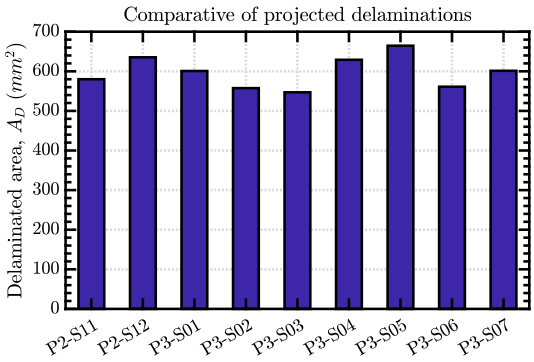

Figure 5.20: Comparative of total area delaminated projected.

Sample	Area damaged $[mm^2]$
P2-S11	580
P2-S12	635
P3-S01	601
P3-S02	557
P3-S03	547
P3-S04	629
P3-S05	665
P3-S06	561
P3-S07	601

Table 5.2: Projected delaminated area.

Finally, in a same bar plot, the delaminated areas with its respective impact and damage energy computed from the impact test have been compared. All the values are relative to its maximums in order to be capable of compare them in the same scale. However, in this comparative it is clear that despite the variation of area delaminated in the samples, there is not apparent relationship with the impact energies computed. The reason could be that the damage energy computed, as explained before, has uncontrolled phenomena additional to the energy absorption during the damaging process.

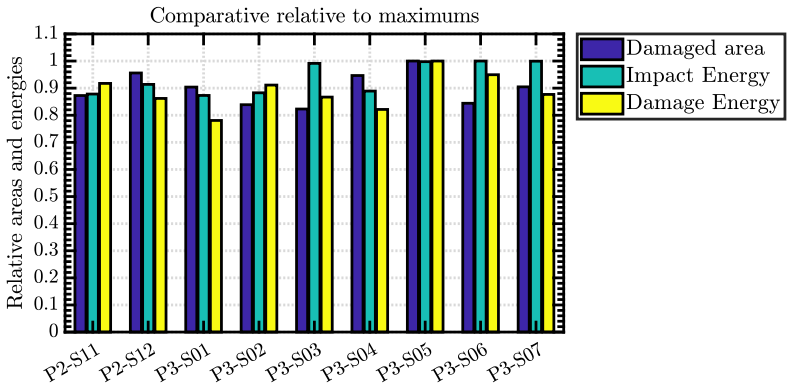

Figure 5.21: Comparative of the area delaminated with impact results relative to maximums.

5.3 Compression after impact test

The compression after impact test is carried out with the experimental frame developed in the HAW Hamburg University. Using an INSTRON testing machine of $100\ [kN]$ combined with the ARAMIS measuring system.

Figure 5.22: Test devices positioned for the experiment.

Materials, devices and preparations utilized in the test set-up are described in this chapter. As well as, the most relevant results are presented and discussed.

5.3.1 Test devices and procedure

In this section, the materials, devices and preparations used in the CAI experiments are described. This includes the load cell, measuring systems, samples preparation, and the post-process procedure with the ARAMIS software.

CAI frame test

As it has been said before, the experimental frame developed by the HAW Hamburg University has been used for the experiments. This frame is a modification based in the ISO 18352, Airbus AITM 1-0010 and EN 6038 standards.

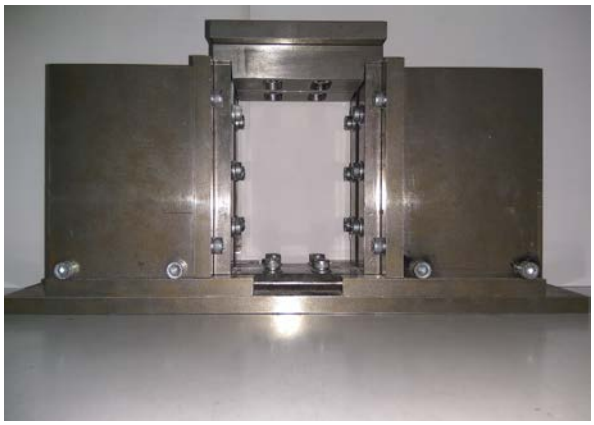

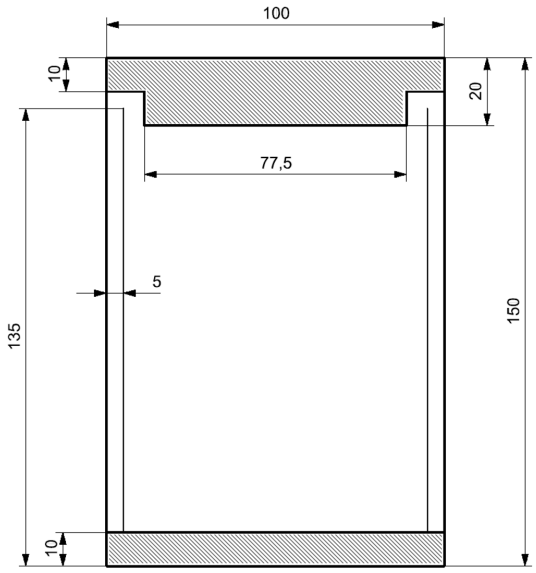

Figure 5.23: Experimental CAI frame from HAW Hamburg University.

The specimen sides are restrained by knifes-edges. And the upper and lower end of the specimen are clamped to the frame. Therefore, it is considered as simply supported in the laterals, and clamped in the lower and upper ends. Here a picture of it is shown, and also the main dimensions in a simplified scheme.

Measuring systems

The measuring devices used in the CAI tests are the INSTRON testing machine and the ARAMIS system. First, the evolution of the force with the time is obtained with the INSTRON testing machine. Also, the est machine is measuring the displacement along the load direction. But this measurement is not very accurate for small deformations. This is because it is not only measuring the displacement of the upper plate of the test frame, it is also measuring all the internal deformation of the machine. A complementary system is needed such as strain gauges, extensometers or deflectometers. These are the typical systems used for measure the displacements or deformations in one specific point and in one direction. ARAMIS measuring system (Gom mbH, Braunschweig, Germany) has been used for the experiments. A system with high accuracy capable of measure the displacements and deformations in all the visible window surface of the sample during the test.

Figure 5.24: ARAMIS adjustable – 3D Motion and Deformation Sensor.

ARAMIS is a non-contact and material-independent measuring system based on digital image correlation (DIC). The system performs high-precision measurements with a 3D image resolution in the submicrometer range, regardless of the specimen's geometry and temperature. There is no need for a time-consuming and expensive preparation. For statically or dynamically loaded specimens and components, ARAMIS provides accurate:

- 3D coordinates
- 3D displacements, velocities, accelerations
- Surface strain
- Material properties for simulation (Young's modulus etc.)
- Evaluations of 6 degrees of freedom (6 DoF)

This system needs an extra preparation of the samples, which is to coat the surface to be measured with white paint and spray it afterwards with graphite to get a pattern of small black dots over the white surface. This small dots are the points that the ARAMIS system are going to trace in order to compute the displacements and strains. Moreover, is convenient to mark some points of reference like the center of the free window of the plate, and four points more to mark the position of the X and Y axis.

Figure 5.25: Sample preparation with white coat and graphite spray.

During the coating, it is important to leave some space free in the edges to prevent that the coat get in contact with the frame fixtures. Also, the dots size and density has to be in accordance with the area to be measured. The products used are the following:

Figure 5.26: White coat and graphite spray products used in the sample preparation.

Post-process procedure in ARAMIS software

Once the experiment is finished, all the pictures taken by the cameras are collected. Then, some basic steps are necessary to get proper results. First, the area where the results are going to be shown has to be picked. With this area, the software create a mesh based in the sprayed dots.

Figure 5.27: Area selected and mesh of points created.

Following, the start point has to be chosen, where all the displacements are going to be computed from it. Finally, the coordinate system has to be set. This coordinate systems should be the same in all the samples to perform proper comparatives. Inside the coordinate system definition menu, the reference plane is set in the first place. Due to there is an imperfection in the plate because of the impact, is important to create this reference plane with three points far away from the impact point. The coordinate system used for all the results is in the middle of the free window of the plate with the following orientation:

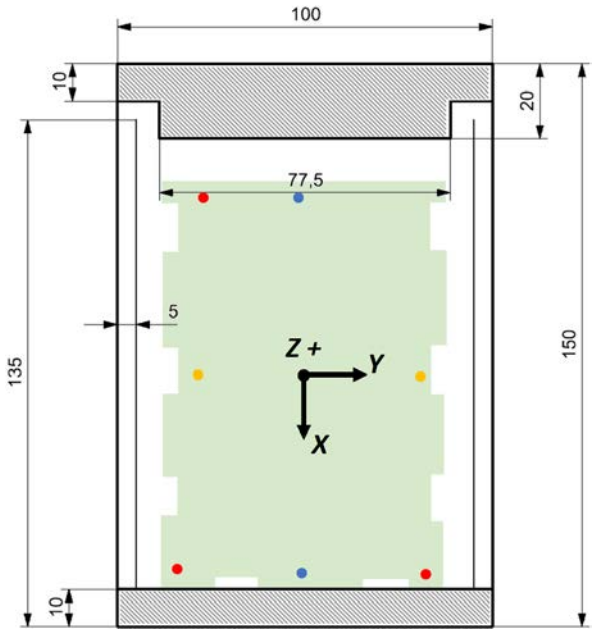

Figure 5.28: Test devices positioned for the experiment.

Red points in the previous picture are an example for the ones chosen for the reference plane creation. Blue points are for the X axis and the yellow points are for the Y axis.

5.3.2 Experimental results

The results shown here are the most significant to check if the experiment was working correctly and to compare with the finite elements model in next chapter. These results are the failure stress, shortening curves and out-of-plane displacements. Moreover, interesting results such as initial geometrical imperfections is possible to obtain with the ARAMIS system. However, the ARAMIS results of sample P3-S01 have no been saved due to a connection problem during the test.

	Length $[mm]$		Width $[mm]$		Thickness $[mm]$	
Samples	Mean	s	Mean	s	Mean	s
P2-S11	148.17	0.03	95.02	0.05	2.22	0.03
P2-S12	147.85	0.02	96.46	0.31	2.16	0.04
P3-S01	148.19	0.15	95.01	0.03	2.12	0.01
P3-S02	147.97	0.05	94.92	0.05	2.15	0.01
P3-S03	148.00	0.04	94.97	0.05	2.17	0.01
P3-S04	148.01	0.01	94.95	0.06	2.08	0.01
P3-S05	148.12	0.13	94.97	0.05	2.15	0.02
P3-S06	148.07	0.03	95.00	0.06	2.18	0.03
P3-S07	148.01	0.02	94.90	0.11	2.12	0.02

Table 5.3: Average results for the tensile test.

Failure plate stress

From the failure load registered by the testing machine, the CAI stress is computed for each sample dividing by its respective cross-section. Moreover, these failure stresses are compared to the undamaged plate failure stress $\sigma_{CAI}^{No\ Damage} = 271.8\ [MPa]$ with a standard deviation of $2.9\ [\%]$ from literature research study carried out with same materials and CAI testing device [40]. As can

be seen in the results, the failure stress reduction is for most of the cases lower than $5\,[\%]$, even P3-S01 and P3-S04 cannot be said that they have a strength reduction. Samples P2-S12 and P3-S03 are the only ones with a strength reduction larger than $10\,[\%]$. Further on, these failure stresses are discussed in more detail with the results presented along this section.

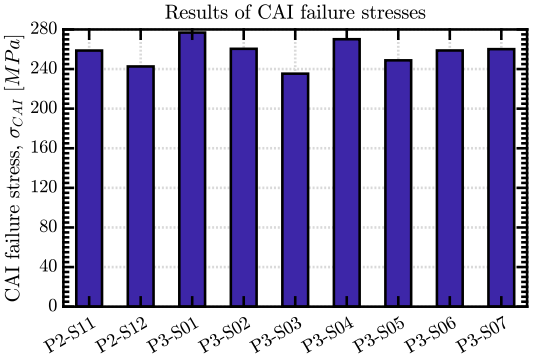

Figure 5.29: Comparative of CAI failure stresses of all samples.

Samples	Failure Load $[kN]$	Failure Stress $[MPa]$	Failure Stress loss $[\%]$
P2-S11	54.57	258.69	−4.82
P2-S12	50.55	242.62	−10.74
P3-S01	55.76	276.83	+1.85
P3-S02	53.15	260.44	−4.18
P3-S03	48.50	235.34	−13.41
P3-S04	53.35	270.13	−0.61
P3-S05	50.80	248.79	−8.47
P3-S06	53.59	258.76	−4.80
P3-S07	52.33	260.10	−4.30

Table 5.4: Average results for the tensile test.

Furthermore, the damaged area from inspection results has been compared to the CAI failure stress, both relative to its corresponding maximums values in order to be able to work in the same scale. It was expected that the size of the damaged area was inversely proportional to the CAI stress failure. Nevertheless, in Figure 5.30 apparently there is no relationship between the damaged area size and the CAI strength.

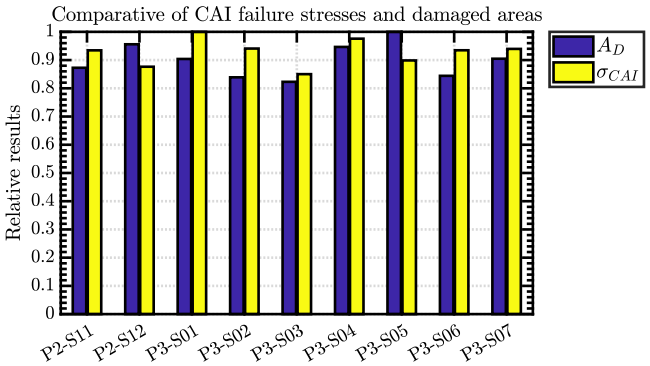

Figure 5.30: Comparative of relative CAI failure stresses of all samples and damaged areas.

Shortening curves

The shortening curves are a typical representation for problems with post-buckling behavior. In this experiments, with ARAMIS software interface for post-processing the results two points have been generated to get this shortening curve. These points are drawn in Figure 5.28 in blue color and it can be seen, they are in the most close position to the upper and lower clamps along the vertical center line. These points have been selected because the most close to the clamps they are, the least influence they have from the out-of-plane buckling displacement. However, as in Figure 5.31 can be seen, despite the proximity to the clamps, there are still two different paths followed by the post-buckling behavior due to the buckling direction of the plate. The samples P3-S03 and P3-S07 buckled in the back direction and the rest buckled in the front direction.

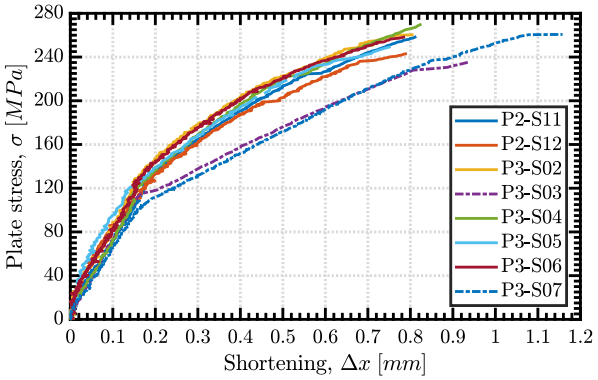

Figure 5.31: Experimental shortening curves measured.

The buckling direction influence on CAI shortening curves is explained in Figure 5.32 where the thickness of the laminate is the responsible of this change. For example,for samples buckled in the back direction have larger shortening at the failure load because the thickness add extra displacements in the loading direction when the plate buckles. The opposite occurs when the plate buckles in the front direction. Nevertheless, the reason why some tests buckle in one or the other direction cannot be still determined with only these results.

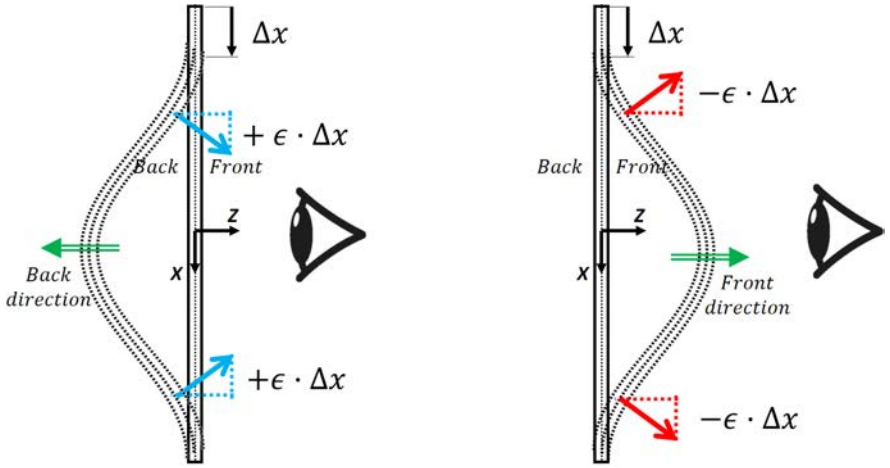

Figure 5.32: Post-buckling behavior of shortening curves depending on buckling direction.

Initial imperfection

In the ARAMIS software it is possible to measure the initial imperfection in the out-of-plane direction and this information is useful for creating the finite elements models. The initial geometric

imperfection of the plates can be extracted by measuring the Z position along the plate at the initial time step. Defining correctly the reference plane in the post-process software is very important. Therefore, when the coordinate system is defined at each test, the reference points must be taken far away from the impact position, ideally at the corners of the plate.

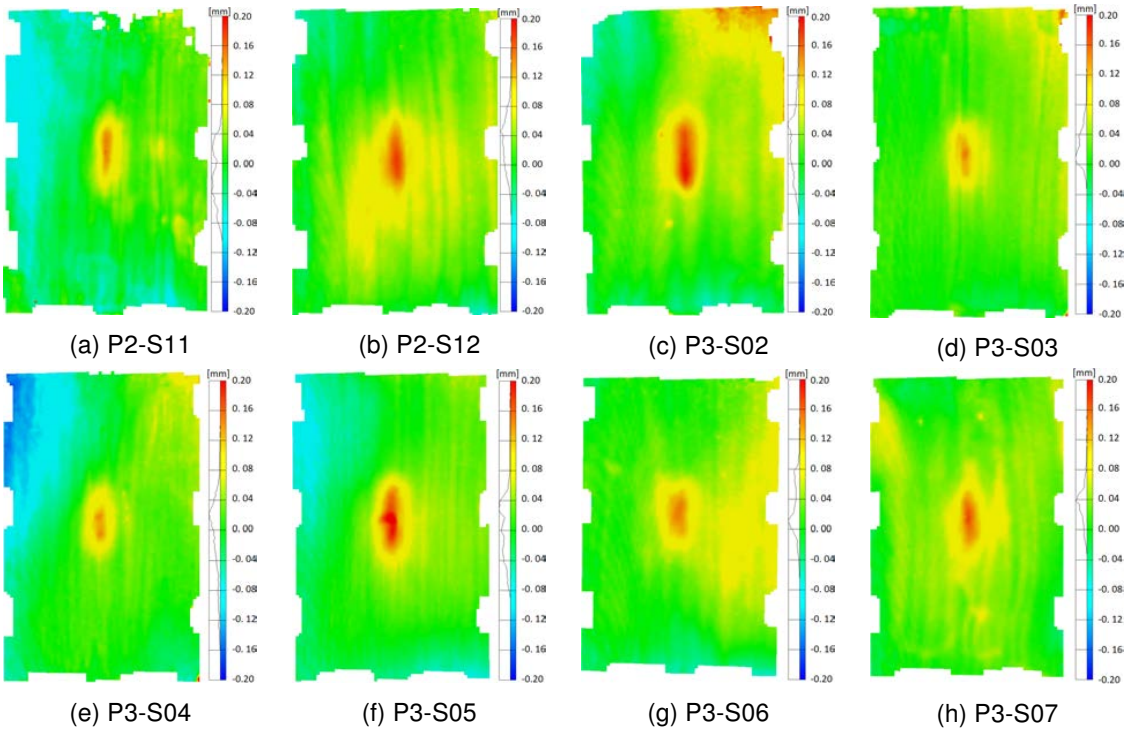

(a) P2-S11 (b) P2-S12 (c) P3-S02 (d) P3-S03

(e) P3-S04 (f) P3-S05 (g) P3-S06 (h) P3-S07

Figure 5.33: Contour plots of geometrical imperfection in samples tested.

As seen in the previous pictures, the impacts have caused an imperfection positive in the Z direction (front direction) at the center of the plates. It is also important to compare quantitatively the amount of imperfection in each plate. This has been done by defining a section perpendicular to the Y direction in the middle of the plate. The imperfection along the X direction are shown in Figure 5.34 where the maximum value is $w_0 = 0.25\ [mm]$ for the plate P3-S05. However, this is the largest imperfection, the rest are between $0.145\ [mm]$ and $0.175\ [mm]$. Plates P3-S03 and P3-S07 have the lowest imperfection levels.

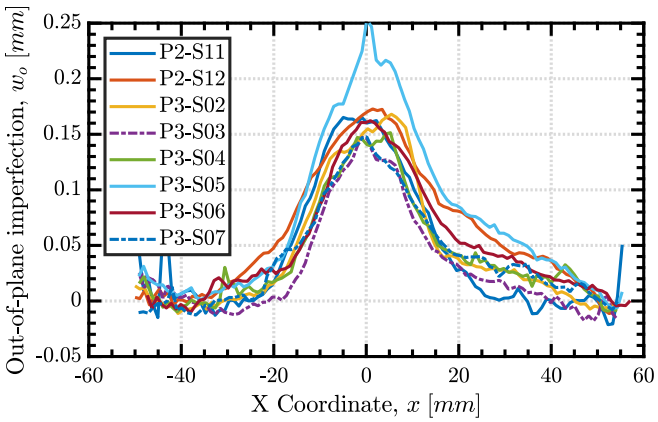

Figure 5.34: Summary of experimental geometric imperfections measured.

Out-of-plane displacements

The out-of-plane displacements measured by the ARAMIS system have been compared in all the samples tested for different load states. First, the beginning of buckling for an approximate stress of $100\,[MPa]$ has been studied. It corresponds to a point in the initial linear part of Figure 5.31.

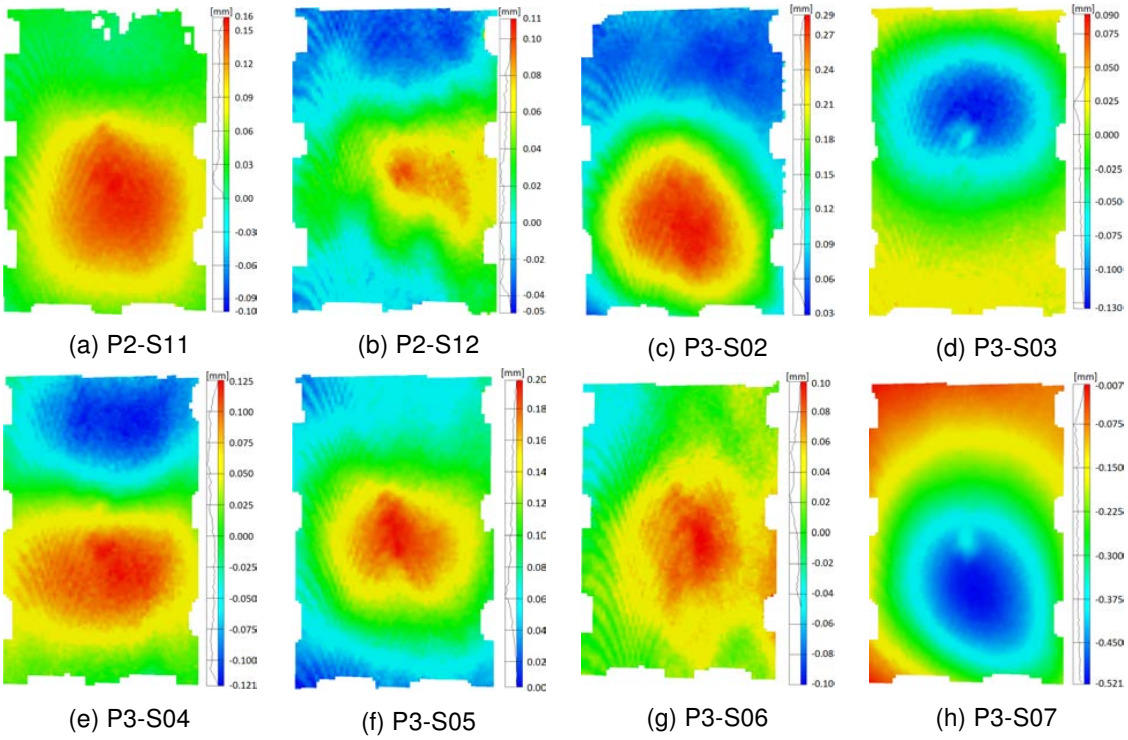

(a) P2-S11 (b) P2-S12 (c) P3-S02 (d) P3-S03

(e) P3-S04 (f) P3-S05 (g) P3-S06 (h) P3-S07

Figure 5.35: Contour plots of the beginning of buckling.

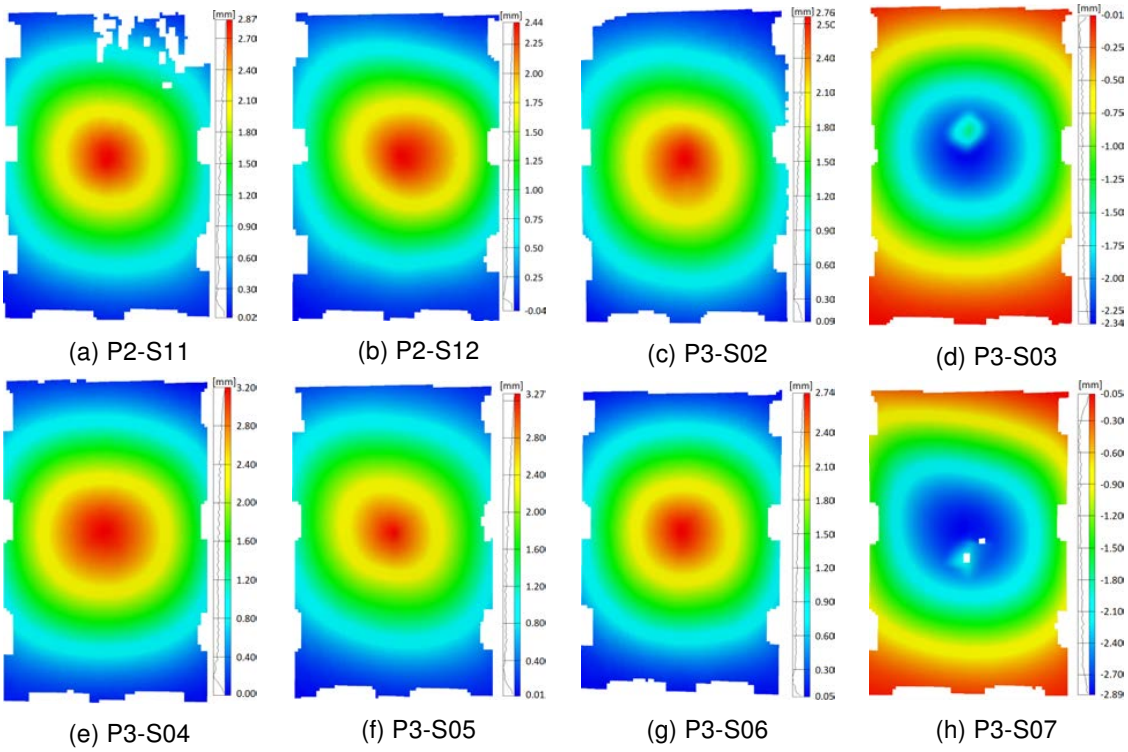

(a) P2-S11 (b) P2-S12 (c) P3-S02 (d) P3-S03

(e) P3-S04 (f) P3-S05 (g) P3-S06 (h) P3-S07

Figure 5.36: Contour plots of a stable buckling under $\sigma \approx 150\,[MPa]$.

In Figure 5.36, the samples are under a stress of $150\ [MPa]$ approximately when the stress of the plate is over the knee point of Figure 5.31 and the buckling behavior has been stabilized. In these results, the buckling direction of the samples P3-S03 and P3-S07 is different from the others and this is in agreement with the shortening results from Figure 5.31.

Now, the out-of-plane displacement is represented for the moment before failure occurs. The stresses corresponding to each sample are in Table 5.4.

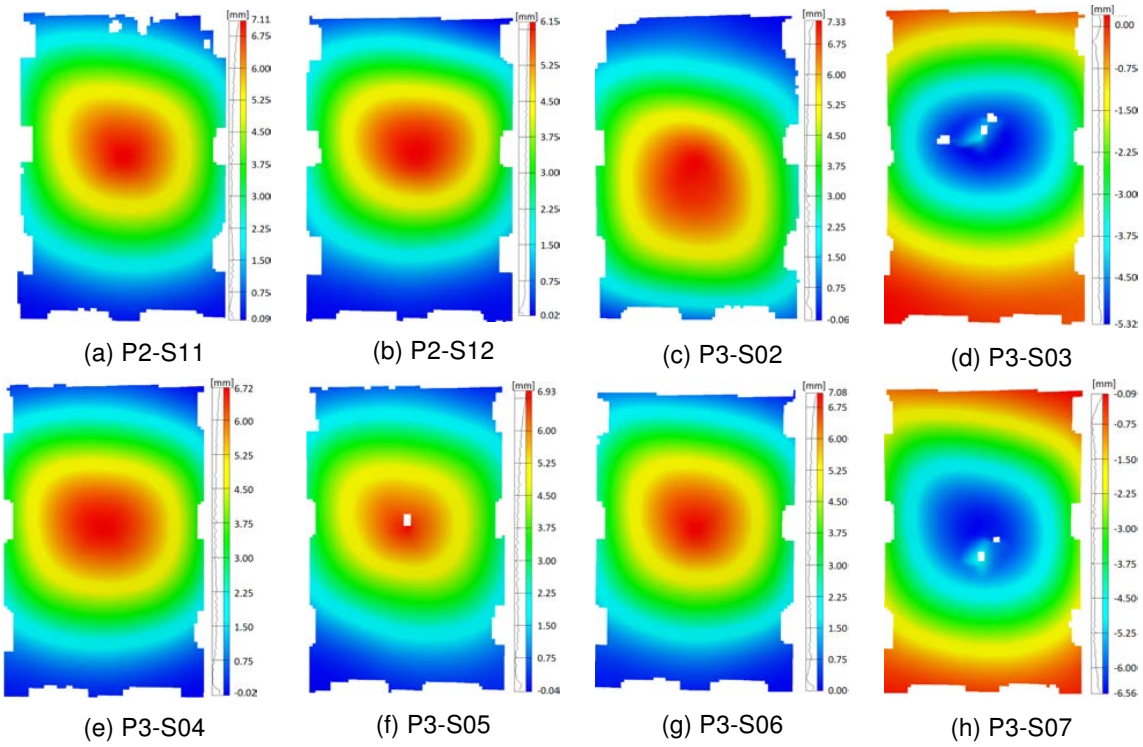

(a) P2-S11 (b) P2-S12 (c) P3-S02 (d) P3-S03

(e) P3-S04 (f) P3-S05 (g) P3-S06 (h) P3-S07

Figure 5.37: Contour plots of buckling at failure stress σ_{CAI}.

Finally, the out-of-plane displacements have been represented also along several vertical and horizontal sections defined in ARAMIS software. In Figure 5.38 and Figure 5.39, only the displacements along the two planes of symmetry are represented, the rest of results in other sections are included in Appendix D.

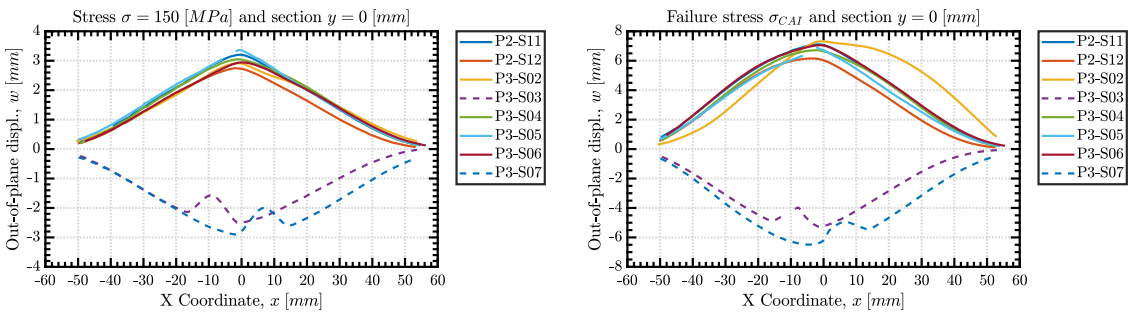

(a) Plate stress of $\sigma = 150\ [MPa]$. (b) Failure stress σ_{CAI}.

Figure 5.38: Out-of-plane displacements along $y = 0$ section.

According to the reference system defined in Figure 5.28, the load is applied at the upper edge, which corresponds to the coordinate $x = -60\ [mm]$ of Figure 5.38 and, the lower clamp is located at the coordinate $x = 60\ [mm]$. However, the curves cannot meet these coordinate

because the cameras cannot capture the areas very close to the frame fixtures. Despite this, in Figure 5.38a, it can be predicted that at the upper and lower edges are clamped. But, in Figure 5.38b, a strange behavior has been observed for sample P3-S02, because it seams that the lower edge has changed from a clamped to a simply support end. Despite this, all the others samples just before the failure have moved its maximums towards the upper edge. That may be caused due to friction phenomena in the lateral simply supported or, due to the upper clamped end has became to some constrain intermediate between a clamped and simply supported end. Moreover, for samples P3-S03 and P3-S07 with reversed buckling direction, local-buckling have been observed, which is also predicted in Figure 5.36. These local-buckling are situated at the circular lobes of the delaminations in the closest interface to the front surface, as the ones seen in Figure 5.17.

Figure 5.39 should have curves between $[-45, 45]\ mm$, but the range is also reduced due the same problem in the previous pictures, the cameras cannot see directly at the plates limits. In both, Figure 5.39a and Figure 5.39a, the limits of the curves represent lateral ends of the plates and a simply supported end can be predicted.

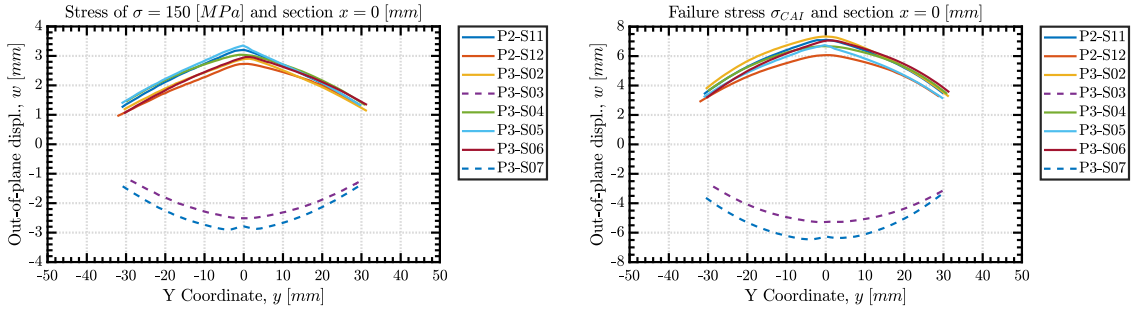

(a) Plate stress of $\sigma = 150\ [MPa]$.

(b) Failure stress σ_{CAI}.

Figure 5.39: Out-of-plane displacements along $x = 0$ section.

Ultimate load and rupture line

In the following pictures are presented the failed plates after the CAI tests.

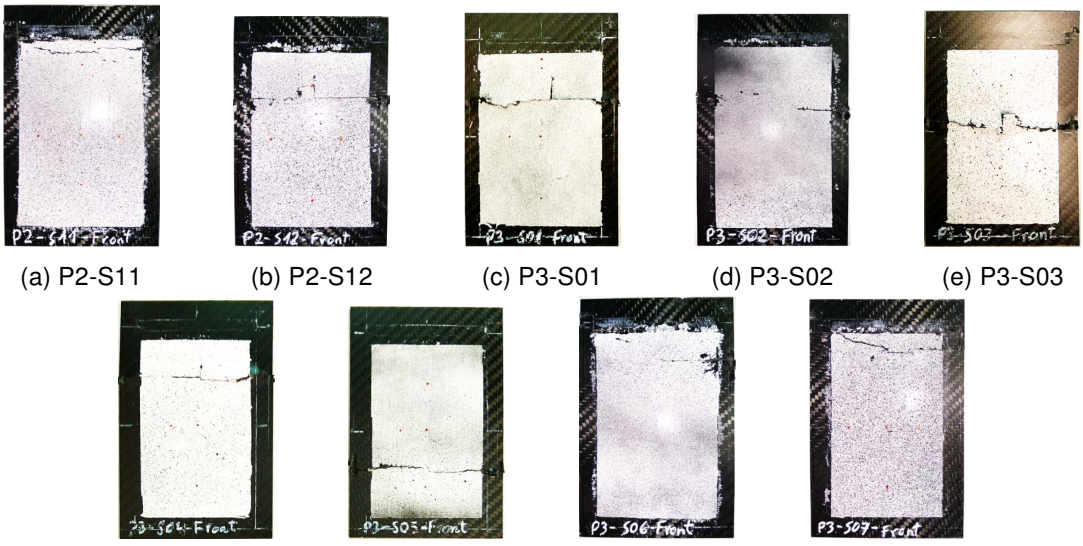

(a) P2-S11 (b) P2-S12 (c) P3-S01 (d) P3-S02 (e) P3-S03

(f) P3-S04 (g) P3-S05 (h) P3-S06 (i) P3-S07

Figure 5.40: Pictures of failed samples after CAI tests.

All ruptures lines positions obtained from previous pictures are measured from the lower edge (the upper edge cannot be trusted because of the compression displacement during the test) and it has been represented all together in Figure 5.41.

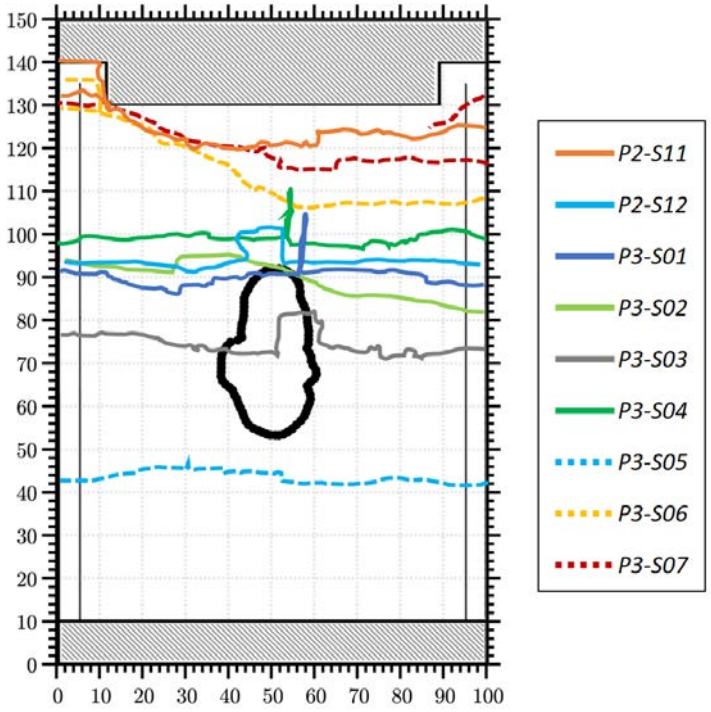

Figure 5.41: Rupture lines comparative over the one of the damage shape.

Buckling direction, imperfection and damaged area comparative

Finally, the rupture line, out-of-plane displacements at failure stress and delaminations observed in the ultrasonic C-scanning have been compared. Only four different cases are shown in here, the rest can be seen in Appendix D. First, the case of samples like P2-S11, P3-S06 and P3-S07 which seam that the failure has been influenced by the upper clamp (Figure 5.42).

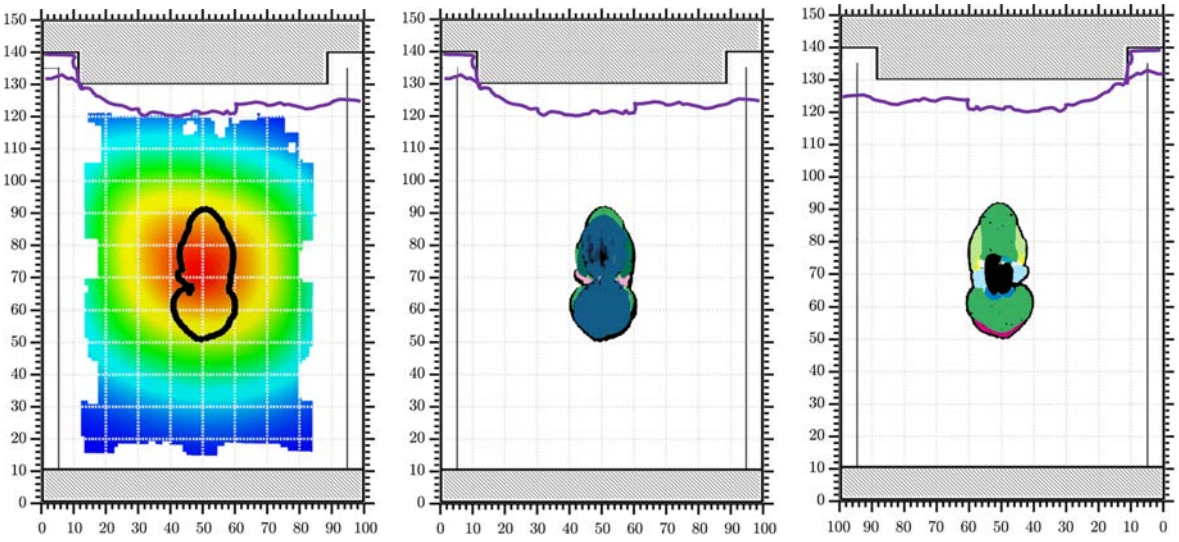

(a) Out-of-plane disp. (b) Front view delaminations (c) Back view delaminations

Figure 5.42: Rupture line, out-of-plane displacements and initial damage in sample P2-S11.

Secondly, samples such as P3-S01 and P3-S04 which seam that the local damage had no influence on the failure because it is the same as the undamaged plate and the rupture line is in the same position (Figure 5.43).

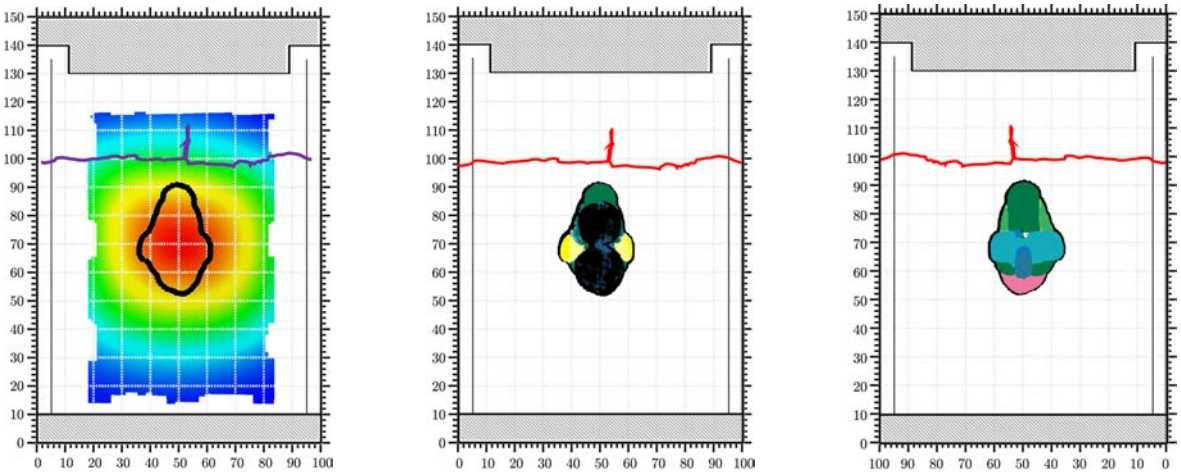

(a) Out-of-plane disp. (b) Front view delaminations (c) Back view delaminations

Figure 5.43: Rupture line, out-of-plane displacements and initial damage in sample P3-S04.

Third case are the samples like P2-S12 and P3-S05 which have the rupture line in the same position as the undamaged plate but the failure stress is slightly reduced. Sample P3-S02 could fit with them, but in the out-of-plane displacements plots along section paths has been observed that the lower clamp did something strange during the experiment and, as consequence, this test cannot be fully trusted.

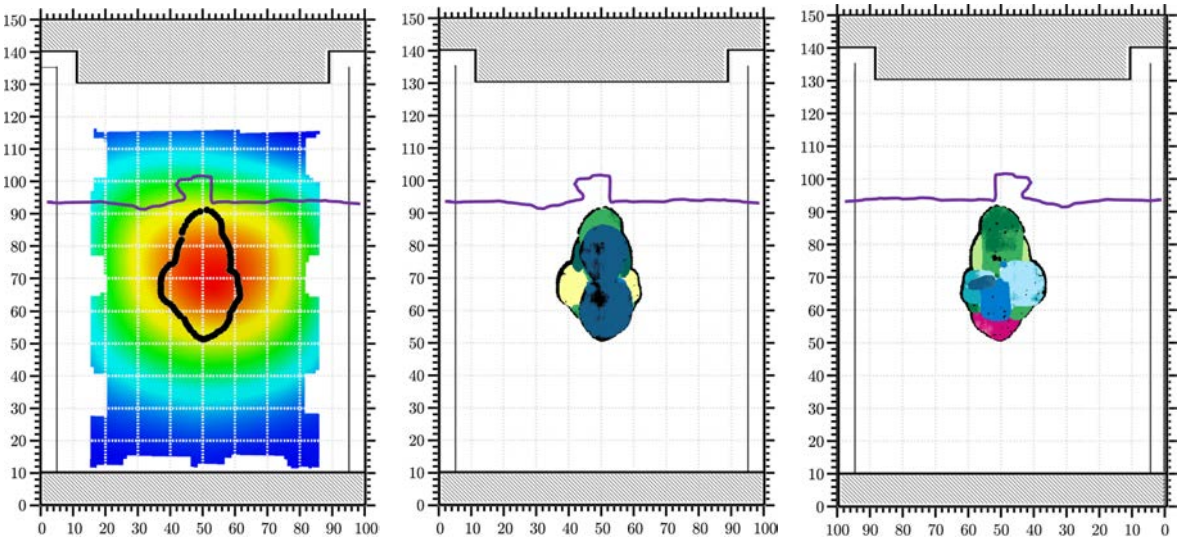

(a) Out-of-plane disp. (b) Front view delaminations (c) Back view delaminations

Figure 5.44: Rupture line, out-of-plane displacements and initial damage in sample P2-S12.

Finally, for sample P3-S03 with a reversed buckling direction was the test with the most reduced failure stress, approximately a $13.41\ [\%]$. The failure has been caused mainly because the interaction the global buckling with the local damage since the rupture line is located exactly at the middle.

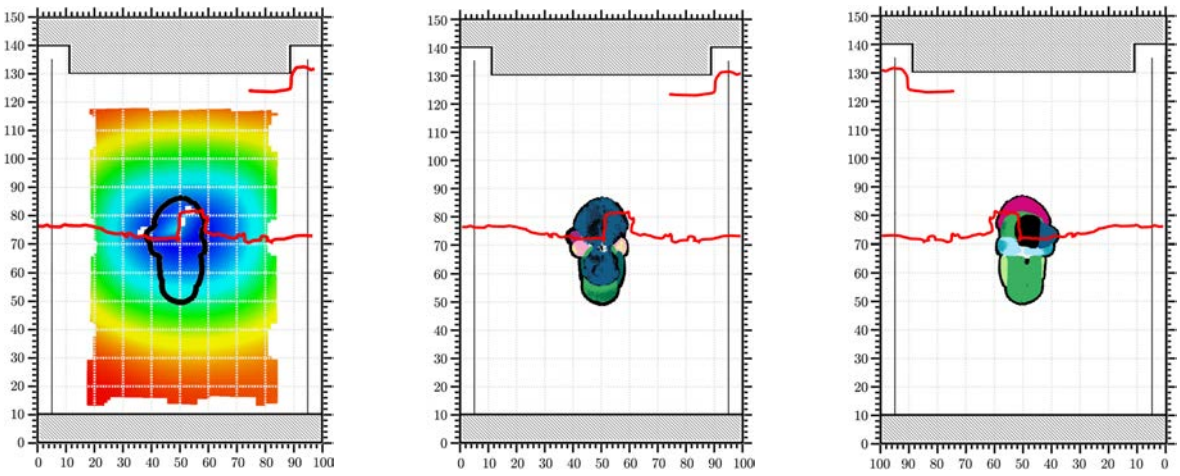

(a) Out-of-plane disp. (b) Front view delaminations (c) Back view delaminations

Figure 5.45: Rupture line, out-of-plane displacements and initial damage in sample P3-S03.

After all these results analysis, some insights have came up about the cause of the buckling direction and, that may be cause by the coupled influences of plate manufacturing imperfection, impact imperfection and internal damage patterns. Also, due to some samples have failed very close to the upper edge, maybe the fixture assembly was not carried out as good as necessary. This is why, could be interesting to modify the CAI frame in a manner that could be controlled the applied tightening torque to the fixtures in order to reduce the frame influence on the failure.

Chapter 6

CAI finite elements models

The finite elements models have been created step by step from the simplest to the most complex model using the Finite Elements code Abaqus (Dassault Systèmes SA, Paris, France). Basically, to check that the simulation set-up is correct and has physical sense. Starting with simulations of the linear buckling in a three-dimensional planar plate of aluminum, and ending with a three-dimensional layer wise composite laminated plate thickened including different non-linearity. These non-linearity included are of geometry, materials failure and cohesive elements for delaminations growth. At the end, three different models are proposed with all these phenomena, but with different initial damage modeling.

6.1 Models simplifications of geometry and boundary conditions

The plate geometry created for all models is a simplification of the free window during a CAI test. Two boundary conditions have been evaluated in the undamaged plate model creation, first a four edges simply supported case to be able to compare with the theoretical results from Chapter 3 of isotropic and laminate thin plates. In Figure 6.1, geometry modeled and boundary conditions used for each case are represented.

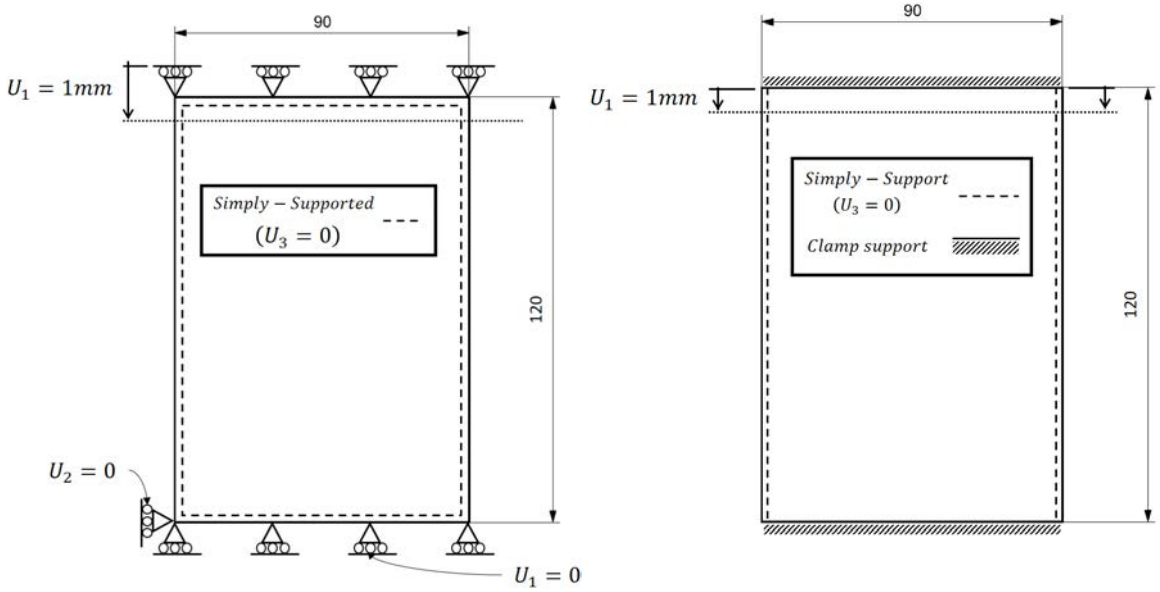

(a) 4SS boundary conditions.

(b) CAI boundary conditions.

Figure 6.1: Summary impact test results.

Where the dimensions of the plates are also shown in next table:

Plate geometry		
a	$[mm]$	120
b	$[mm]$	90
t	$[mm]$	2.132

Table 6.1: Plate dimensions of simplified geometry.

6.2 Undamaged plate modeling

First model of CAI test developed is for an undamaged plate. The modeling strategy followed is explained in this section, starting with a bi-dimensional geometry under linear buckling analysis and ending with a complete three-dimensional geometry with all non-linearity mentioned.

6.2.1 Linear buckling analysis

The linear buckling analysis is based on the theory explained in Section 3.6 and it is carried out for isotropic and orthotropic laminate 4SS plates and for orthotropic laminate plates under CAI test.

4SS isotropic bi-dimensional plate under uni-axial compression

This is the easiest model created in this project where the material of the plate is aluminum (Table 6.2) and the model is meshed with conventional shell elements.

Aluminum Mechanical Properties		
E	$[GPa]$	70
ν	$[-]$	0.33

Table 6.2: Aluminum elastic mechanical properties.

The value of theoretical critical buckling stress has been computed in Section 3.5.2 from Eq.3.98 for $m = 1$:

$$\sigma_{cr} = \frac{N_{cr}}{t} = \frac{\pi^2 D \left(m^2 + \alpha^2\right)^2}{t\, b^2\, m^2\, \alpha^2} \tag{6.1}$$

$$\sigma_{cr} = \frac{\pi^2 \cdot 62.12 \cdot \left(1^2 + \left(\frac{120}{90}\right)^2\right)^2}{(2.132 \cdot 10^{-3}) \cdot (90 \cdot 10^{-3})^2 \cdot 1^2 \cdot \left(\frac{120}{90}\right)^2} = 154.09\ [MPa]\,, \tag{6.2}$$

and $m = 2$:

$$\sigma_{cr} = \frac{\pi^2 \cdot 62.12 \cdot \left(2^2 + \left(\frac{120}{90}\right)^2\right)^2}{(2.132 \cdot 10^{-3}) \cdot (90 \cdot 10^{-3})^2 \cdot 2^2 \cdot \left(\frac{120}{90}\right)^2} = 166.66\ [MPa]\,, \tag{6.3}$$

where D is:

$$D = \frac{E\, t^3}{12\ (1 - \nu^2)} = \frac{70 \cdot 10^9 \cdot \left(2.132 \cdot 10^{-3}\right)^3}{12 \cdot (1 - 0.3^2)} = 62.12\ [N\, m] \tag{6.4}$$

Therefore, the critical buckling stress for the isotropic plate according to the theory is $\sigma_{cr} = 154.09\,[MPa]$ and it has only one semi-wave in the loading direction. Also, a mesh dependency study has been carried out of this model and compared to the theoretical results.

N° Elements	Buckling stress $[MPa]$	Variation $[\%]$
12	196.20	–
48	164.72	16.05
192	157.70	4.26
768	155.52	1.38
3072	154.76	0.49

Table 6.3: Mesh dependency analysis results for a bi-dimensional 4SS isotropic plate.

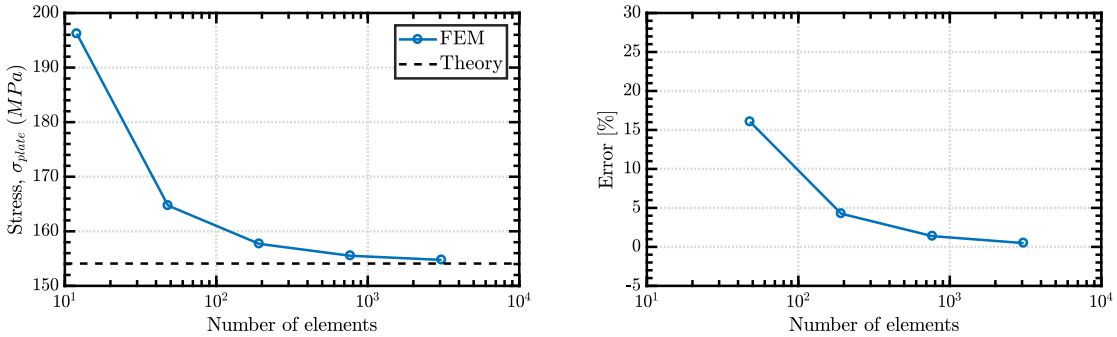

Figure 6.2: Mesh dependency study for a bi-dimensional 4SS isotropic plate.

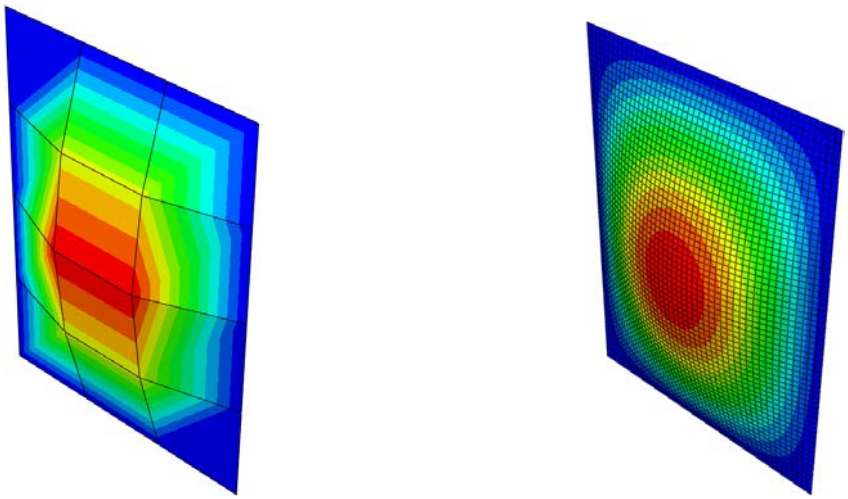

(a) 12 elements.

(b) 3072 elements.

Figure 6.3: Examples of buckling shapes for different number of elements in a bi-dimensional 4SS isotropic plate.

From these results, the linear buckling model has been checked with the theoretical results because the mesh dependency study shows that the results tends toward the theoretical value and, also the buckling shape with one semi-waves along the loading direction is in agreement with the finite element results.

4SS composite laminated bi-dimensional plate under uni-axial compression

Now, a similar procedure as for isotropic plate has been carried out for a composite laminated plate. The plies thickness, materials, stacking and orientation have been already explained in Table 4.7 and the orthotropic elastic properties of the plies materials have been defined in Table 4.10.

According to the theory developed to calculate buckling stress of orthotropic thin laminates in Section 3.5.3, the formula to calculate the critical buckling stress is Eq.3.103:

$$\sigma_{cr} = \frac{1}{t}\left(\frac{\pi}{b}\right)^2 \left[B_x \left(\frac{m}{\alpha}\right)^2 + 2\,B_{xy} + B_y \left(\frac{\alpha}{m}\right)^2\right], \tag{6.5}$$

for $m = 1$:

$$\sigma_{cr} = \frac{1}{2.132\cdot 10^{-3}}\left(\frac{\pi}{90\cdot 10^{-3}}\right)^2 \left[64.48\cdot\left(\frac{1}{\frac{120}{90}}\right)^2 + 2\cdot 8.83 + 50.78\cdot\left(\frac{\frac{120}{90}}{1}\right)^2\right] = 82.41\ [MPa], \tag{6.6}$$

and $m = 2$:

$$\sigma_{cr} = \frac{1}{2.132\cdot 10^{-3}}\left(\frac{\pi}{90\cdot 10^{-3}}\right)^2 \left[64.48\cdot\left(\frac{2}{\frac{120}{90}}\right)^2 + 2\cdot 8.83 + 50.78\cdot\left(\frac{\frac{120}{90}}{2}\right)^2\right] = 105.91\ [MPa], \tag{6.7}$$

where B_x, B_{xy} and B_y have been computed from the laminate bending and torsional stiffness calculated in Section 4.2 from Eq.4.19:

$$\begin{cases} B_x = D_{11} = 64.48\ [N\cdot m] \\ B_y = D_{22} = 50.78\ [N\cdot m] \\ B_{xy} = D_{12} + 2\,D_{66} = 2.75 + 2\cdot 3.04 = 8.83\ [N\cdot m] \end{cases} \tag{6.8}$$

Therefore, the critical buckling stress for the laminated plate according to the theory is $\sigma_{cr} = 82.41\ [MPa]$ and it has only one semi-wave in the loading direction. Also, a mesh dependency study has been carried out of this model and compared to the theoretical results.

N° Elements	Buckling stress $[MPa]$	Variation $[\%]$
12	102.56	–
48	86.25	15.90
192	82.70	4.11
768	81.78	1.12
3072	81.52	0.31

Table 6.4: Mesh dependency analysis results for a bi-dimensional 4SS laminated plate.

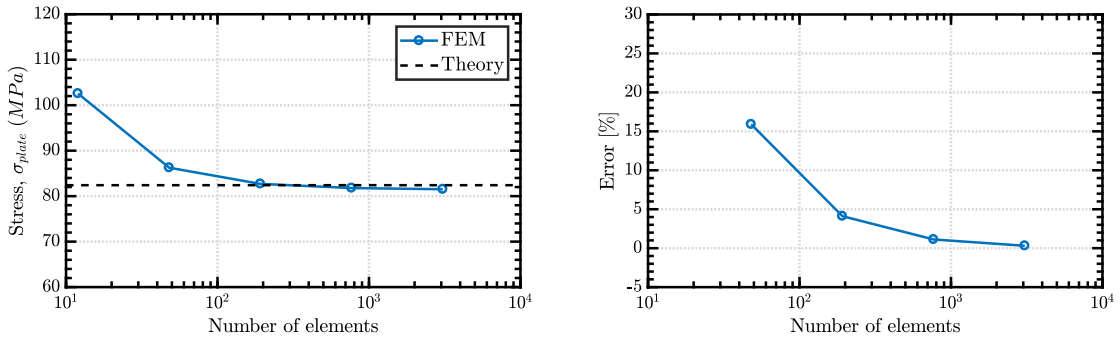

Figure 6.4: Mesh dependency study for a bi-dimensional 4SS laminated plate.

From these results, the linear buckling has been checked with the theoretical results because the mesh dependency study shows that the results tends toward the theoretical value and, also the buckling shape with one semi-waves along the loading direction is in agreement with the finite element results.

CAI test linear buckling with a bi-dimensional plate

Once the linear buckling analysis and laminate elastic properties set-up have been created successfully for a 4SS plate, next step has been to create the same analysis for a laminated plate under CAI test boundary conditions. This plate cannot be calculate so easily as the 4SS case, so only the finite elements results are represented and assumed that if the previous models have a good agreement with the theory, this will be also correct. The plate geometry and boundary conditions used are represented in Figure 6.1b, where the clamp support means that all the movements are constrain (U_1, U_2, U_3, UR_1, UR_2 and UR_3).

A mesh dependency study has been carried out with this model.

N° Elements	Buckling stress $[MPa]$	Variation $[\%]$
12	197.72	–
48	140.60	28.89
192	130.38	7.27
768	127.97	1.85
3072	126.65	1.03

Table 6.5: Mesh dependency results for a 2D laminated plate under CAI test boundary conditions.

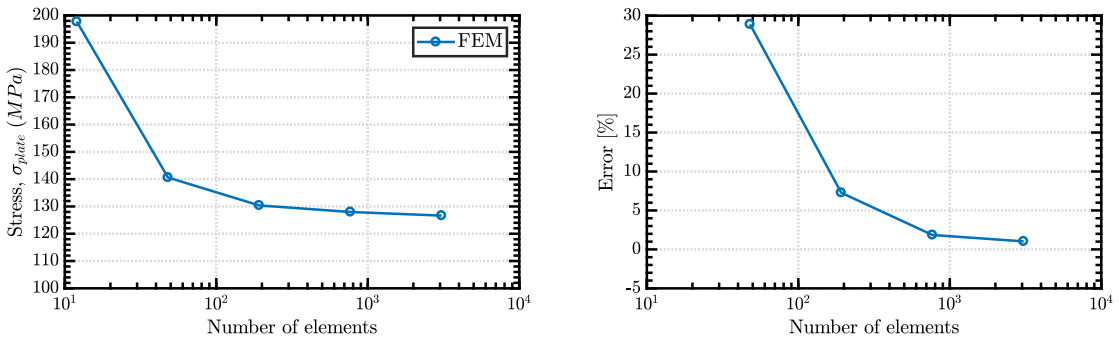

Figure 6.5: Mesh dependency study for a laminated plate under CAI test boundary conditions.

These results show that buckling stress converges to $\sigma_{cr} = 127\ [MPa]$ for the bi-dimensional CAI model. Also the buckling shape with one semi-waves along the loading direction and, as it was expected, the value of σ_{cr} larger than buckling stress for 4SS laminate buckling, due to the plate is more restrain.

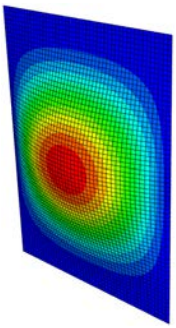

Figure 6.6: Buckling shape of first mode of the 2D laminated plate under CAI test boundary conditions.

CAI test linear buckling with a three-dimensional plate

Now, a layer-wise laminate three-dimensional model with cohesive interfaces has been created in order to check the plate buckling stress with the bi-dimensional model and, in consequence, verify the model. The plate dimensions are the same as before but, including the thickness of each layer of the laminate and interfaces as modeled for tensile test in Section 4.3. The mesh used continuum shell elements and cohesive elements, which formulation has been explained in Section 3.3 and Section 3.4. The element size in the plate plane is the same as used in previous model of 768 elements. The material used for the interfaces is defined in Table 4.13 and the boundary conditions for the clamp supports has to be modeled differently due to the continuum shell elements have only 3 DoF. Therefore, at clamp supports all displacements are restrain (U_1, U_2 and U_3) over the all area of the section, which is at the end an equivalent boundary conditions to the applied at the bi-dimensional problem.

Model	Buckling stress $[MPa]$	Variation $[\%]$
2D	127.97	–
3D	126.99	0.77

Table 6.6: Mesh dependency results for a 3D laminated plate under CAI test boundary conditions.

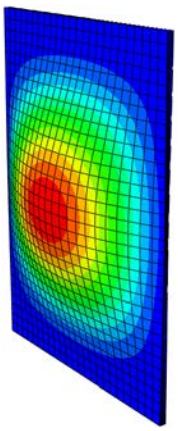

Figure 6.7: Buckling shape of first mode of the 3D laminated plate under CAI test boundary conditions.

The buckling shape and the buckling stress for three-dimensional model match with the results calculated in the bi-dimensional case. Therefore, the behavior of the three-dimensional model with interfaces has been validate.

6.2.2 Post-buckling analysis of the CAI test

Once the linear buckling analysis has been fully understood and controlled, the post-buckling analysis of the plate has been developed. The analysis procedure used for this simulations have been the implicit Riks method and the Explicit Dynamic procedure, both explained in Section 3.6. The post-buckling behavior in a plate has been explained in Section 3.5.1, where some key characteristics can be used to verify the post-buckling simulations. These characteristics are extracted from curves of load versus out-of-plane deflection (Figure 3.15) and shortening (Figure 3.16), where the curves present a smoother behavior when the imperfections increase and the knee points never overcome the linear buckling load.

In order to verify the post-buckling behavior of the laminated plate, in first instance the previous bi-dimensional model has been used with 768 elements but, including different levels of initial geometric imperfection and also the Hashin damage material model for unidirectional and woven plies defined in Table 4.11 and Table 4.12. The geometric imperfections have been introduced in the model by writing in the *Keyword* of the model that the imperfections has to be computed from the linear buckling shape displacements per node of the first mode and multiplied by a factor. This factor indirectly define the maximum initial imperfection of the geometry and the values used for this study are $0.01\,[mm]$, $0.02\,[mm]$, $0.1\,[mm]$ and $0.2\,[mm]$. The results for all these imperfection levels are represented in Figure 6.8

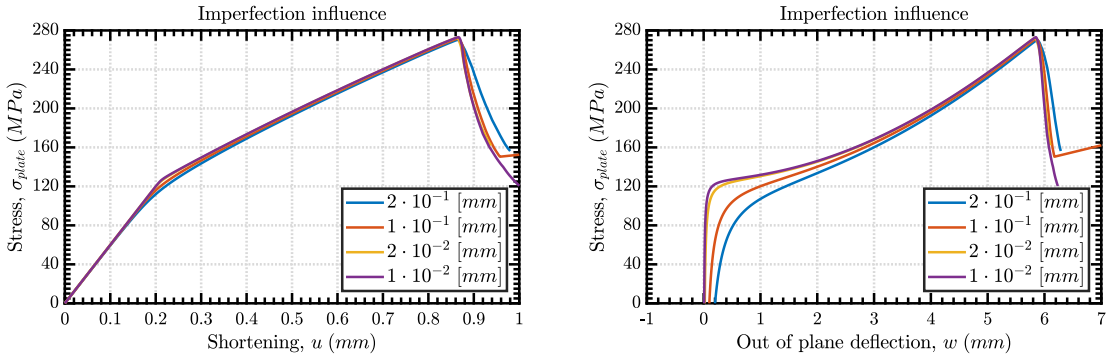

(a) Shortening curves.

(b) Out-of-plane deflection curves.

Figure 6.8: Imperfections levels study in a post-buckling 2D laminate model with 768 elements.

As shown in previous pictures, the post-buckling behavior is the expected. Moreover, an interesting result has been predicted too, which is that the failure load for different imperfection levels is barely affected as presented in Table 6.7, although there is a slightly drawdown of the failure load when the imperfection increases.

Imperfection	Failure stress $[MPa]$	$U_1\,[mm]$	$U_3\,[mm]$
$0.01\,[mm]$	273.14	0.867	5.85
$0.02\,[mm]$	272.44	0.863	5.84
$0.1\,[mm]$	271.68	0.865	5.86
$0.2\,[mm]$	270.33	0.865	5.87

Table 6.7: Imperfection influence in a 2D laminated plate under CAI boundary conditions.

At the same time, the mesh dependency of the failure stress has been also proven:

Nº Elements	Failure stress $[MPa]$	$U_1\,[mm]$	$U_3\,[mm]$
768	270.33	0.865	5.87
3072	268.86	0.859	5.84

Table 6.8: Mesh dependency results of a 2D laminated plate under CAI test boundary conditions with an initial geometric imperfection level of $0.2\,[mm]$.

If the whole curves that define the post-buckling behavior are checked, it is also observed that the simulation has converged already for a mesh with 768 elements.

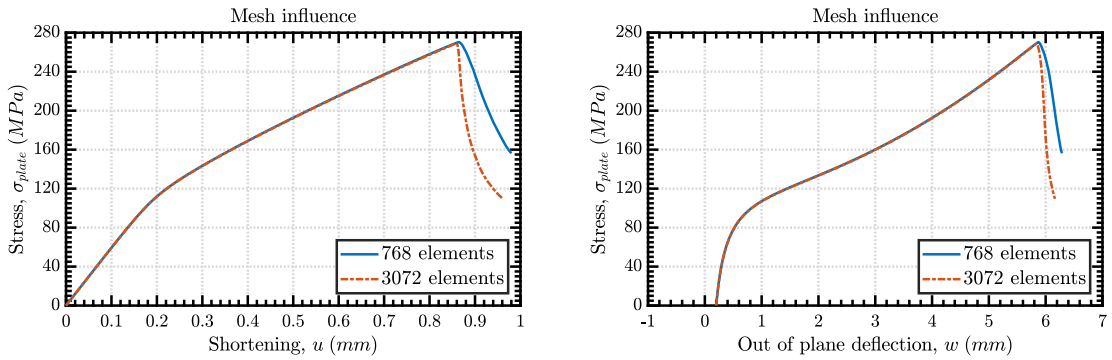

(a) Shortening curves.

(b) Out-of-plane deflection curves.

Figure 6.9: Post-buckling curves for 2D laminate model with 768 and 3072 elements and an imperfection level of $0.2\,[mm]$.

Some relevant post-buckling contour plots at the failure load are shown in next figures. First, the displacements at the failure stress have been represented at the mid-surface of the laminate:

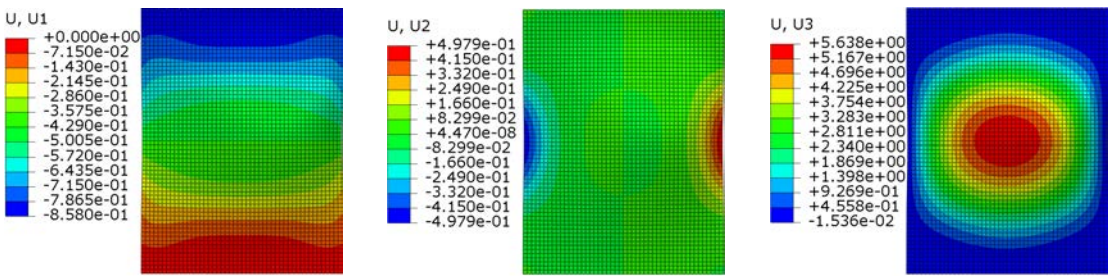

(a) Longitudinal (U_1).

(b) Transverse (U_2).

(c) Out-of-plane (U_3).

Figure 6.10: Displacements at failure stress for 2D laminate model with 3072 elements and an imperfection level of $0.2\,[mm]$.

Also, the Hashin damage initiation criterion for compression in the fiber direction of the critical plies in the laminate (ply 1 and 2) which are located at the concave and convex sides of the laminate. This failure mode has been represented over the others due to it is the mode that has the most decisive influence in the failure load of the plate. In the ply located on convex side, different zones have reach the damage initiation criterion of this mode such as close to the lower and upper edge and at the middle of the lateral sides. In the ply located on the concave side, the damage initiation criterion of this mode is widely extended along the middle horizontal line of the plate.

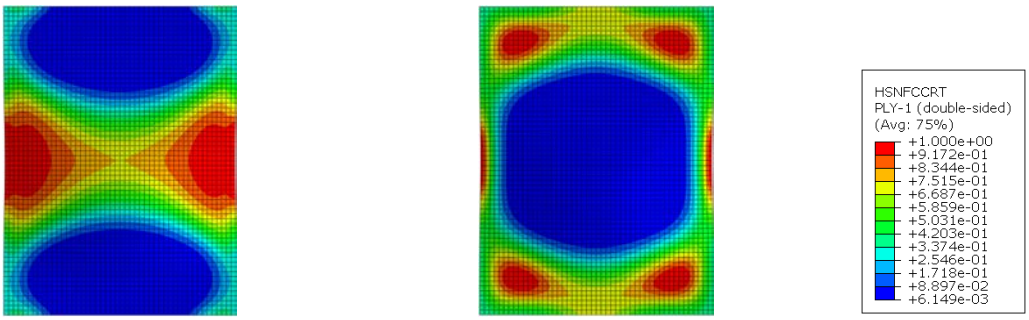

(a) Ply located on the concave side. (b) Ply located on the convex side.

Figure 6.11: Hashin fiber compression damage initiation criterion for 2D laminate model with 3072 elements and an imperfection level of $0.2\,[mm]$.

Although the failure of the plate appears that may occur at the top/bottom or at the middle of the plate, only is developed in the middle of the plate because the area that reach the damage initiation criterion is in every ply with fibers in the load direction and the upper and lower damage is only present in the ply of the convex side.

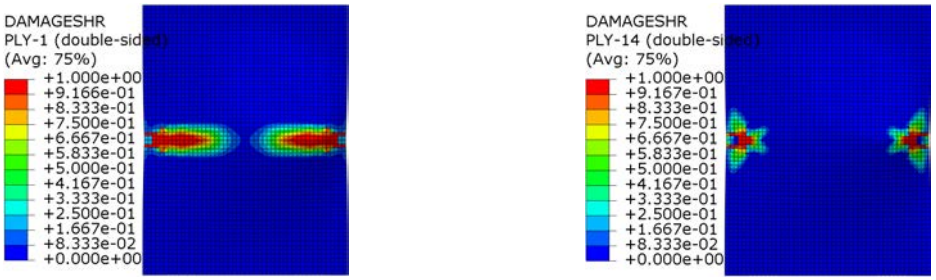

(a) Ply located on the concave side. (b) Ply located on the convex side.

Figure 6.12: Rupture line for 2D laminate model with 3072 elements and an imperfection level of $0.2\,[mm]$.

However, when a three-dimensional model is created including interfaces modeled with cohesive elements, the implicit Riks method is not capable to calculate this problem when the damage begins. This is because near to the failure load, the delaminations begin to growth suddenly and this is is a dynamic event where an implicit method cannot converge. Therefore, an explicit dynamic procedure is required because it does not need to find an equilibrium state in order to to converge. But, as explained in Section 3.6, the explicit computation for quasi-static problems, such as this problem, may have a very high computation cost. Therefore, a mass scaling technique has been applied to reduce it. This technique may introduce a non-realistic behavior if the mass scaling is increased excessively, where the inertia phenomena are not negligible. This is why, all the previous simulations carried out with the implicit method are necessary to check if the explicit results show the real behavior.

Also, the explicit dynamic procedure requires an initial geometric imperfection as the Riks method. Explicit simulations have been calculated with different levels of initial geometric imperfections and the maximum mass scaling factor that can be used without increasing too much the inertia phenomena has been studied. This study concluded that the greatest is the imperfection level, the largest mass scaling factor can be used. As a consequence, an initial geometric imperfection level of $0.2\,[mm]$ has been used for all the further models. In the following figure the implicit solution has been compared to explicit models with different mass scale factor:

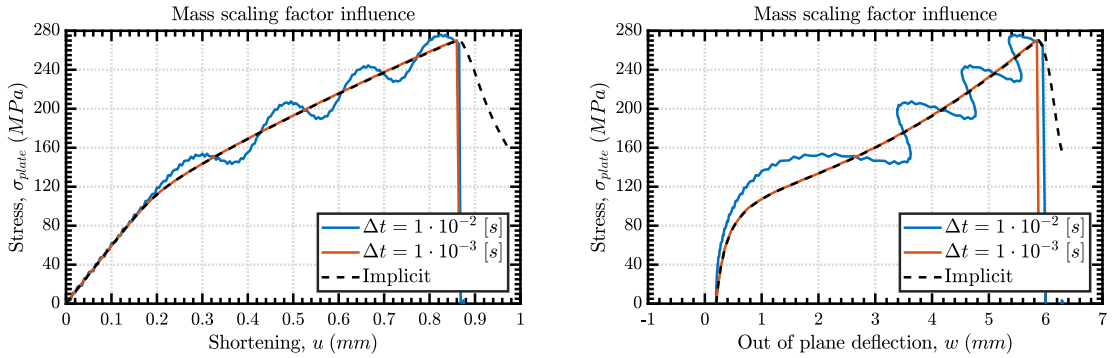

(a) Shortening curves.

(b) Out-of-plane deflection curves.

Figure 6.13: Mass scaling factor influence for 2D laminate model with 768 elements and an imperfection level of 0.2 $[mm]$.

In previous figure, the mass scaling factor, f, has been introduced indirectly by defining the time step desired. As a result of the study carried out for different time increment sizes ($\Delta t = 1 \cdot 10^{-2}, 8 \cdot 10^{-3}, 6 \cdot 10^{-3}$, ..., $1 \cdot 10^{-3}$ $[s]$), the maximum time increment that can be used is $\Delta t = 1 \cdot 10^{-3}$ $[s]$. From this value, the maximum mass scaling factor has been estimated through the minimum element size, L_e, and the maximum wave propagation velocity, c, in the materials.

$$c \approx \sqrt{\frac{E}{(1-\nu^2)\,\rho}} = \sqrt{\frac{135 \cdot 10^3}{(1-0.334^2) \cdot 1.6 \cdot 10^{-9}}} = 9.7452 \cdot 10^6 \; [mm/s] \tag{6.9}$$

$$\Delta t_{stable} \approx \frac{L_e}{c} = \frac{3}{9.7452 \cdot 10^6} = 3.08 \cdot 10^{-7} \; [s] \tag{6.10}$$

$$f \approx \sqrt{\frac{\Delta t}{\Delta t_{stable}}} = \sqrt{\frac{1 \cdot 10^{-3}}{3.08 \cdot 10^{-7}}} \approx 57 \tag{6.11}$$

Approximately, the mass scaling factor applied has been $f = 57$ and this information is useful for the 3D laminate model, because now, the smallest element length is defined by the thickness of the thinnest ply ($t_{UD} = 0.144$ $[mm]$) instead of the in-plane longitudes (3 $[mm]$). So, the time increment defined has to be reduced:

$$\Delta t_{stable} \approx \frac{L_e}{c} = \frac{0.144}{9.7452 \cdot 10^6} = 1.478 \cdot 10^{-8} \; [s] \tag{6.12}$$

$$\Delta t \approx f^2 \, \Delta t_{stable} = 57^2 \cdot 1.478 \cdot 10^{-8} = 4.80 \cdot 10^{-5} \; [s] \approx 5 \cdot 10^{-5} \; [s] \tag{6.13}$$

Therefore, for the 3D laminate explicit models, a time increment of $\Delta t = 5 \cdot 10^{-5}$ $[s]$ has been used. Although the interfaces thickness are much smaller than ply thickness, $t_I = 10^{-5}$ $[mm]$, they do not have an influence on the Δt_{stable}. The results for explicit post-buckling 3D laminate model have been compared to the results of the 2D model:

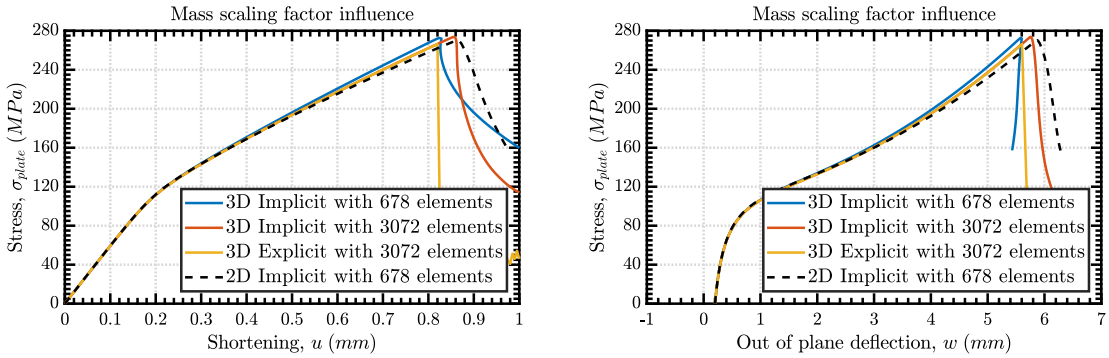

(a) Shortening curves.

(b) Out-of-plane deflection curves.

Figure 6.14: Undamaged 2D and 3D laminate model with an imperfection level of $0.2\ [mm]$.

Model	Failure stress $[MPa]$	$U_1\ [mm]$	$U_3\ [mm]$
2D implicit 768 elements	270.33	0.865	5.87
3D implicit 768 elements/ply	272.63	0.825	5.58
3D implicit 3072 elements/ply	273.71	0.856	5.75
3D explicit 3072 elements/ply	266.32	0.820	5.60

Table 6.9: Undamaged 2D and 3D laminate model results with an imperfection level of $0.2\ [mm]$.

From thee results, a small variation can be observed between the 2D and 3D model near to the failure behavior. These differences have been reduced by increasing the number of elements per ply in the 3D model. However, the computational time required has been increased considerably. As a result, the 3D model with a mesh of 3072 elements per ply and a time increment defined in the explicit analysis of $\Delta t = 5 \cdot 10^{-5}\ [s]$ is the final undamaged laminate model.

6.3 Damaged plate modeling

The point of departure for the different damages modeling has been the 3D model of the undamaged laminate developed until this point. In this section, how the initial damage has been modeled is explained and, also, the different strategies and simplifications of the damage used.

6.3.1 Initial damage modeling

In order to model the damage at the different laminate interfaces, different sections within each damaged interface have been defined, one as undamaged and tho other as damaged. The undamaged section has the cohesive material properties already defined in this project in Table 4.13, Table 4.13 and Table 4.13. However, for damaged sections, a degraded cohesive material based on the undamaged one has been used. This degraded material used has the same elastic properties as defined in Table 4.13, but the damage initiation criterion and the fracture energies have been drastically reduced. With these material configuration, the stiffness in the traction and shear direction is completely lost but, the stiffness in the compression direction remain as at the beginning. This way, the penetrations between layers are avoided and the plies are free to buckle in the other direction. The properties used for the damaged interfaces sections are:

	Units	Value
E_{nn}	$[MPa/mm]$	1000000
E_{ss}	$[MPa/mm]$	1500000
E_{tt}	$[MPa/mm]$	1500000

Table 6.10: Elastic properties of the traction-separation law in damaged cohesive elements.

	Units	Value
t_n^0	$[MPa]$	10^{-3}
t_s^0	$[MPa]$	10^{-3}
t_t^0	$[MPa]$	10^{-3}

Table 6.11: Nominal stresses for damage initiation criterion in cohesive damaged elements.

	Units	Value
η_{BK}	$[-]$	1
G_n^C	$[N/mm]$	10^{-6}
G_s^C	$[N/mm]$	10^{-6}
G_t^C	$[N/mm]$	10^{-6}
μ_{BK}	$[-]$	0.001

Table 6.12: Fracture energies, exponent and viscous regularization parameter for damage evolution in cohesive damaged elements.

Furthermore, as shown in Figure 5.32, the buckling may develop in two directions and the influence on the failure stress of it has been studied in the created initially damaged models. Two different shapes has been used to model the initial delaminated interfaces, one with a elliptical form based on the whole damaged area projected during ultrasonic C-scanning and, the other is a more realistic form of the damage shape at each interface.

6.3.2 Elliptical damage shape with cylindrical through-thickness pattern

The whole damaged area obtained during the ultrasonic C-scanning of each sample and represented in Figure 5.19, has been approximated to a ellipse of semi-major axis of $20\,[mm]$ and semi-minor axis of $13\,[mm]$.

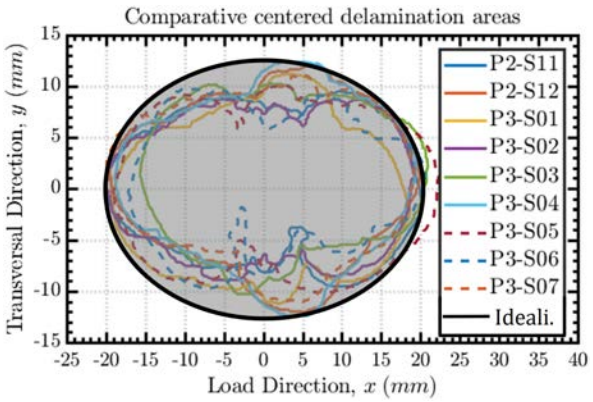

Figure 6.15: Whole projected damage idealization as a ellipse.

This elliptical damaged area has been introduced at each interface in the model of cylindrical through-thickness pattern as observed in next figures. As it has been mentioned in Section 5.2, between adjacent plies with the same orientation there is no physical interface and, therefore, there is no initial damage to model.

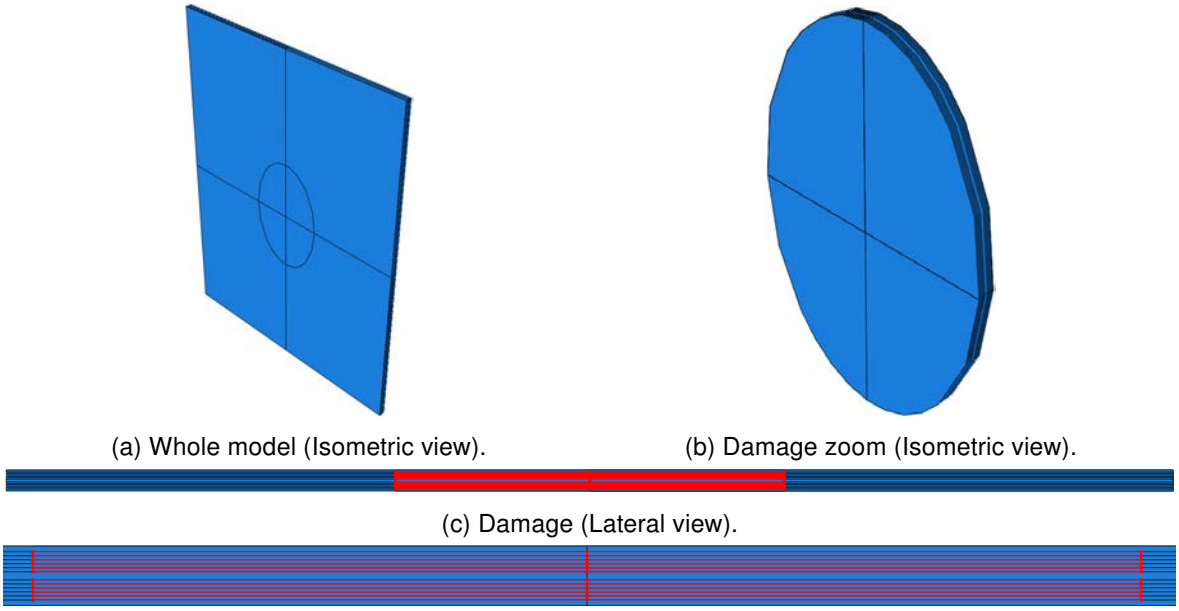

(a) Whole model (Isometric view).

(b) Damage zoom (Isometric view).

(c) Damage (Lateral view).

(d) Damage zoom (Lateral view).

Figure 6.16: Model of the elliptical delaminations and cylindrical pattern through-thickness.

In this model, it is not necessary to study the influence of the buckling direction due to the damage through-thickness direction is the same. The most relevant results for cylindrical damage are represented. First, it is studied the typical curves that show the post-buckling behavior and the failure stress of the plate:

Buckling direction	Failure stress $[MPa]$	U_1 $[mm]$	Failure stress reduction $[\%]$
Front/Back	178.86	0.505	32.84

Table 6.13: Results at failure load of models damaged with elliptical delaminations and cylindrical pattern.

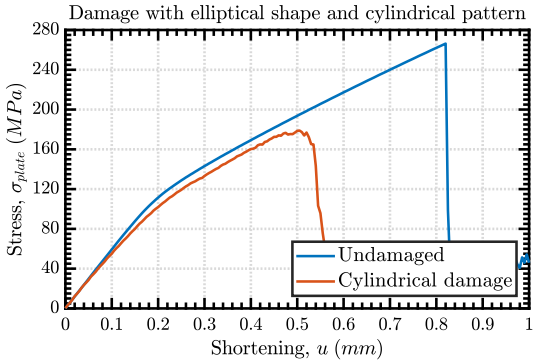

Figure 6.17: Shortening curve for damaged model with elliptical delaminations and cylindrical pattern.

Now, to figure out how the damage has been evolved the contour results of the out-of-plane

displacements, damage initiation criterion in the load direction for the critical plies, the local buckling evolution and the rupture line calculated.

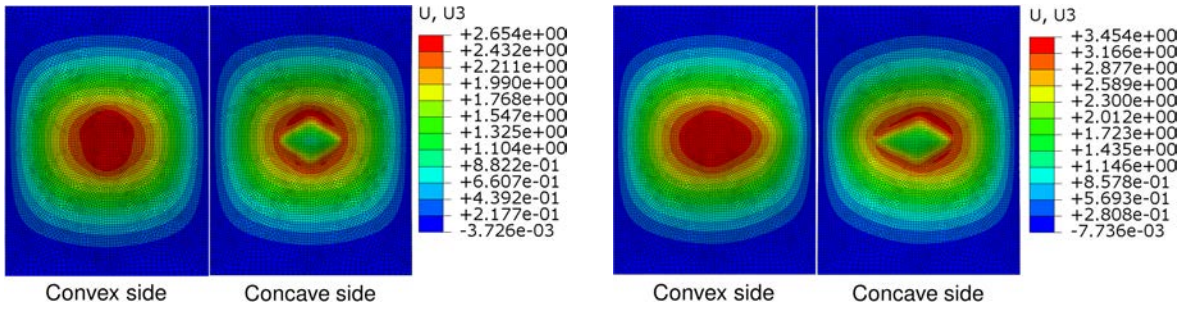

(a) Stress of $150\ [MPa]$. (b) Failure stress.

Figure 6.18: Out-of-plane displacements at model with elliptical delaminations and cylindrical pattern.

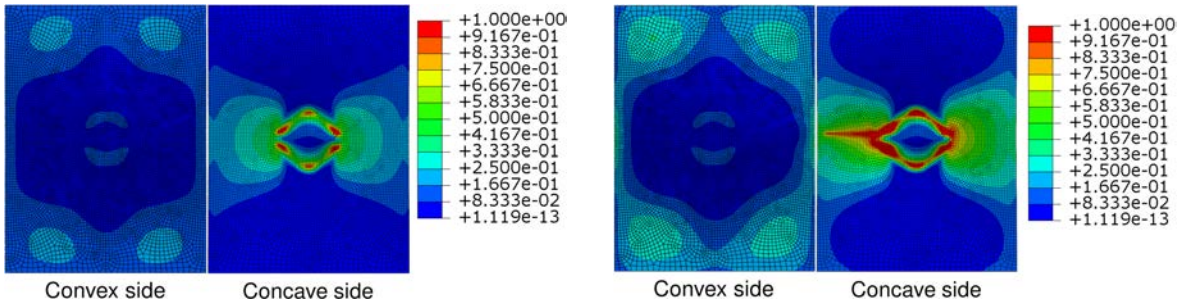

(a) Stress of $150\ [MPa]$. (b) Failure stress.

Figure 6.19: Hashin damage initiation criterion for fiber compression direction at model with elliptical delaminations and cylindrical pattern.

(a) Stress of $150\ [MPa]$. (b) Failure stress.

Figure 6.20: Delamination initiation criterion at model with elliptical delaminations and cylindrical pattern.

(a) Stress of $150\ [MPa]$.

(b) Failure stress.

Figure 6.21: Loca-global buckling interaction along load direction at model with elliptical delaminations and cylindrical pattern.

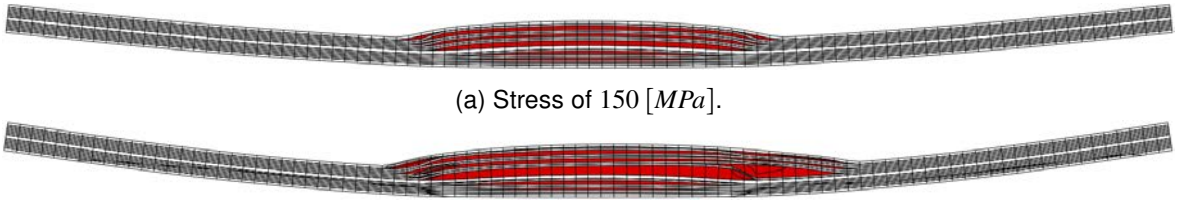

(a) Stress of $150\ [MPa]$.

(b) Failure stress.

Figure 6.22: Loca-global buckling interaction along transverse direction at model with elliptical delaminations and cylindrical pattern.

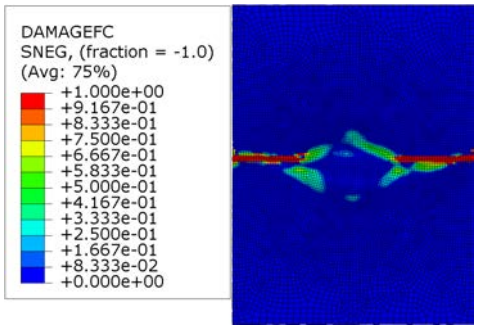

Figure 6.23: Rupture line at model with elliptical delaminations and cylindrical pattern.

Laminate failure stress has been significantly reduced because of the interaction of the global-local buckling during the simulation. The local buckling has caused a stress concentrated zone at the surrounding area which damaged the zone. This damage caused a loose of stiffness and, as a consequence, delaminations started to growth leading to the laminate failure.

6.3.3 Elliptical damage shape with conical through-thickness pattern

The conical pattern through-thickness variate the lengths of the maximum and minimum semi-axes from $20\ [mm]$ and $13\ [mm]$ to $5\ [mm]$ and $5\ [mm]$ respectively.

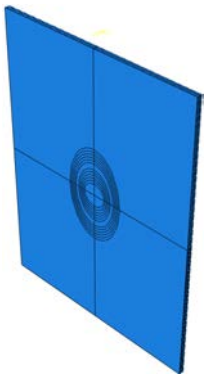

(a) Whole model (Isometric view).

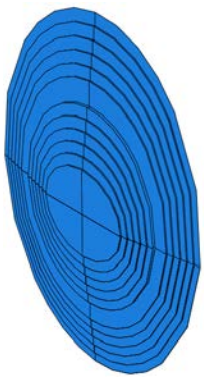

(b) Damage zoom (Isometric view).

(c) Damage (Lateral view).

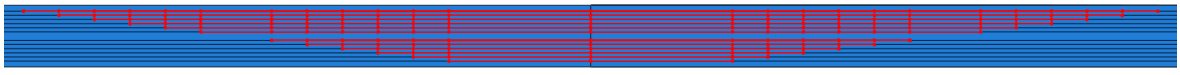

(d) Damage zoom (Lateral view).

Figure 6.24: Model of the elliptical delaminations and conical pattern through-thickness.

In this model, it is necessary to study the influence of the buckling direction due to the damage varies in the through-thickness direction. The most relevant results for conical damage are represented here. First, it is studied the typical curves for post-buckling behavior and the failure stress of the plate for both buckling directions and compared to the undamaged plate:

Buckling direction	Failure stress $[MPa]$	U_1 $[mm]$	Failure stress reduction $[\%]$
Front	195.08	0.530	26.75
Back	219.47	0.640	17.59

Table 6.14: Results at failure load of models damaged with elliptical delaminations and conical pattern.

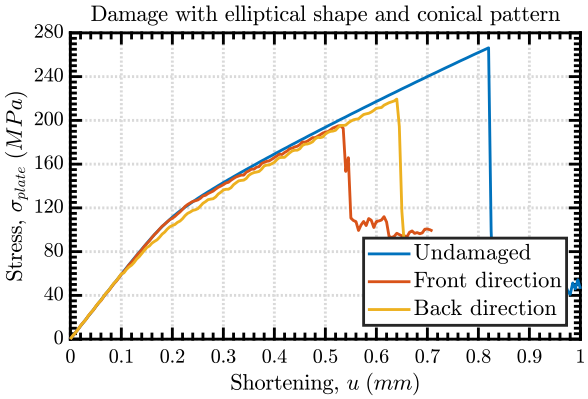

Figure 6.25: Shortening curves for damaged models with elliptical delaminations and conical pattern.

These results show a clear influence in the failure stress depending on the buckling direction for conical damage pattern. Now, the results for out-of-plane displacement, Hashin damage and delamination initiation criteria and local-global buckling interaction are represented in the following figures at both bucking directions.

Front buckling direction

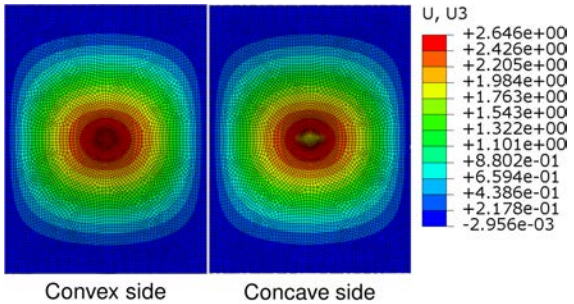

(a) Stress of 150 $[MPa]$.

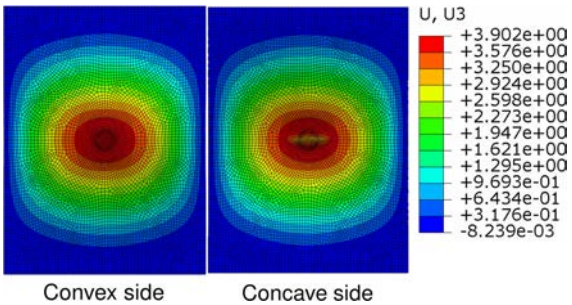

(b) Failure stress.

Figure 6.26: Out-of-plane displacements at model with elliptical delaminations, conical pattern and front buckling direction.

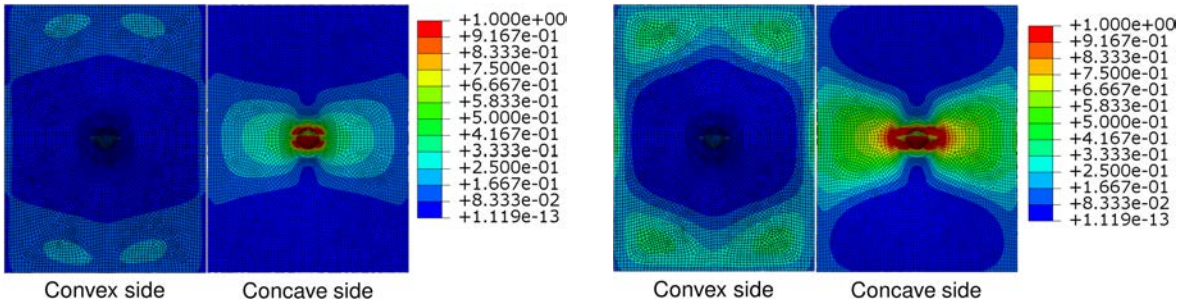

(a) Stress of $150\ [MPa]$. (b) Failure stress.

Figure 6.27: Hashin damage initiation criterion for fiber compression direction at model with elliptical delaminations, conical pattern and front buckling direction.

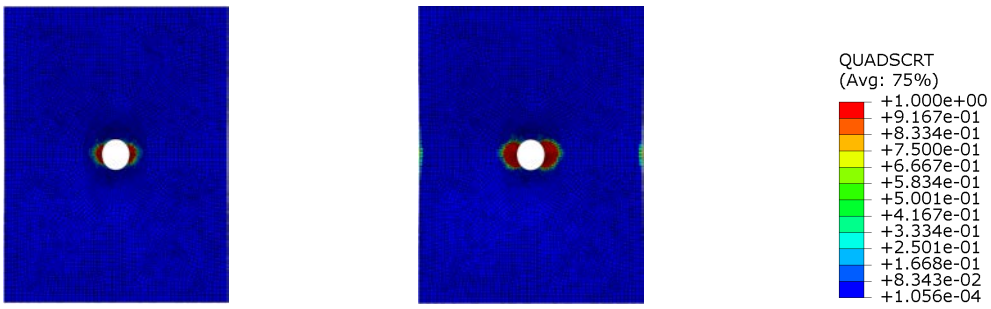

(a) Stress of $150\ [MPa]$. (b) Failure stress.

Figure 6.28: Delamination initation criterion at model with elliptical delaminations, conical pattern and front buckling direction.

(a) Stress of $150\ [MPa]$.

(b) Failure stress.

Figure 6.29: Local-global buckling interaction along load direction at model with elliptical delaminations, conical pattern and front buckling direction.

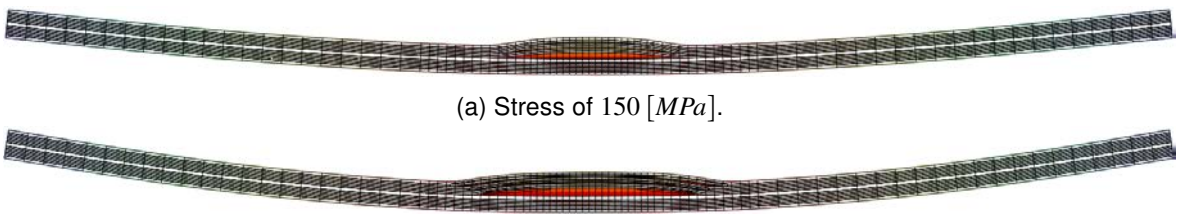

(a) Stress of $150\ [MPa]$.

(b) Failure stress.

Figure 6.30: Local-global buckling interaction along transverse direction at model with elliptical delaminations, conical pattern and front buckling direction.

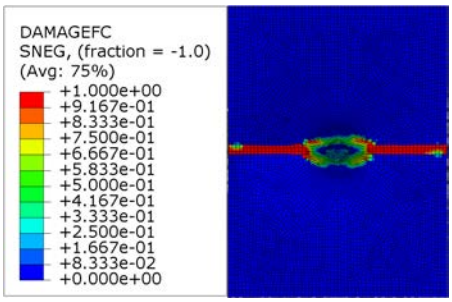

Figure 6.31: Rupture line at model with elliptical delaminations, conical pattern and front buckling direction.

During the simulation of the model with front buckling direction, the local buckling also occurs in the concave side of the laminate. Due to the initially delaminated areas close to the concave side are small, the local buckling provokes high strains at the vicinity and it has resulted in high stresses which initiate an early damage and delaminations growth.

Back buckling direction

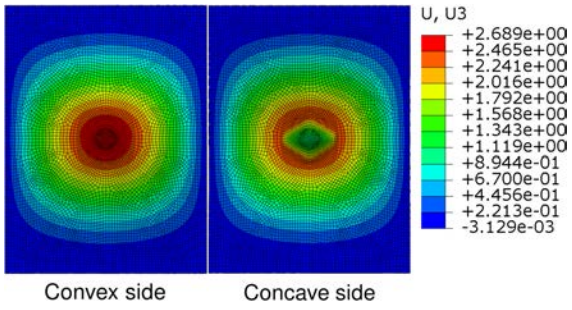

(a) Stress of $150\ [MPa]$.

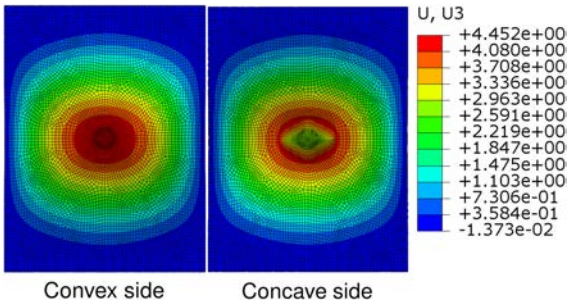

(b) Failure stress.

Figure 6.32: Out-of-plane displacements at model with elliptical delaminations, conical pattern and back buckling direction.

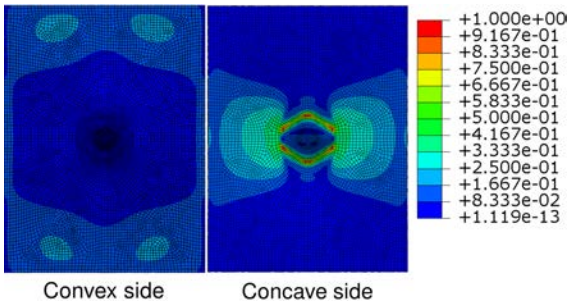

(a) Stress of $150\ [MPa]$.

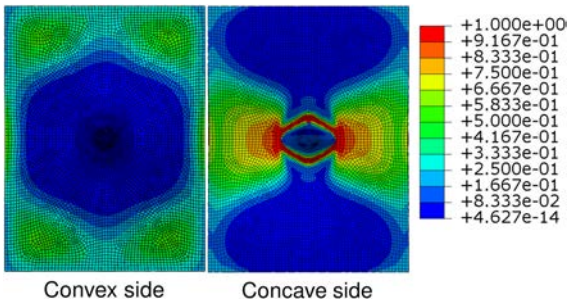

(b) Failure stress.

Figure 6.33: Hashin damage initiation criterion for fiber compression direction at model with elliptical delaminations, conical pattern and back buckling direction.

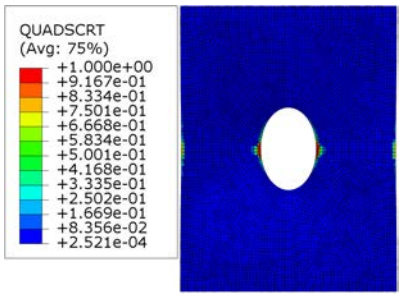

Figure 6.34: Delamination initiation criterion under failure stress at model with elliptical delaminations, conical pattern and back buckling direction.

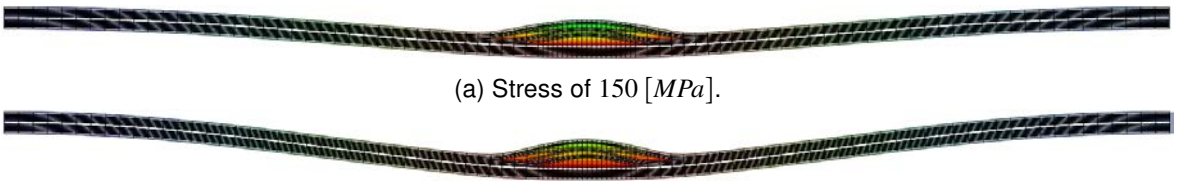

(a) Stress of $150\ [MPa]$.

(b) Failure stress.

Figure 6.35: Local-global buckling interaction along load direction at model with elliptical delaminations, conical pattern and back buckling direction.

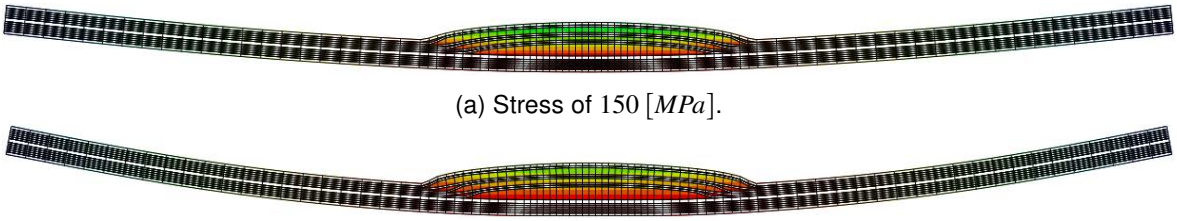

(a) Stress of $150\ [MPa]$.

(b) Failure stress.

Figure 6.36: Local-global buckling interaction along transverse direction at model with elliptical delaminations, conical pattern and back buckling direction.

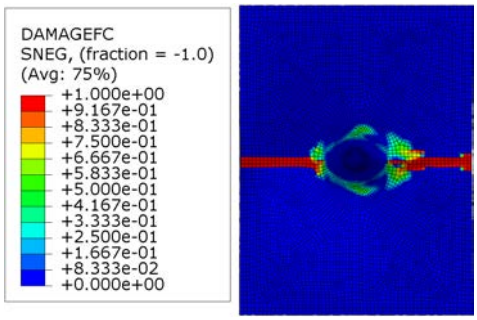

Figure 6.37: Rupture line at model with elliptical delaminations, conical pattern and back buckling direction.

During the simulation of the model with back buckling direction, the local buckling also occurs in the concave side of the laminate but, due to the initially delaminated areas close to the concave side now are the largest, the local buckling provokes no that high strains at the vicinity. Therefore, the damage is initiated earlier than the undamaged model but, the laminate can bear higher loads before the delaminations begin to growth.

6.3.4 Ultrasonic C-scanned damage shape and through-thickness pattern

Although a lot of information have been extracted from the ultrasonic scanning, some information is still missing when the delamination shapes are searched behind upper damages. Therefore, modeling the most realistic simulation, some assumptions have to be done. In this case, assumptions have been done in a conservative way where it is accept that the missing interfaces damage will have the same area than the upper damaged area visible. As defined in Figure 5.18, the interfaces are numbered from the impact side (back) and, according to all the inspections carried out from the back surface, the first damage seen was located at the third interface. So, the first and second interfaces have been modeled without initial damage. From this same inspection surface, damages until sixth interface have been easily observed and idealized:

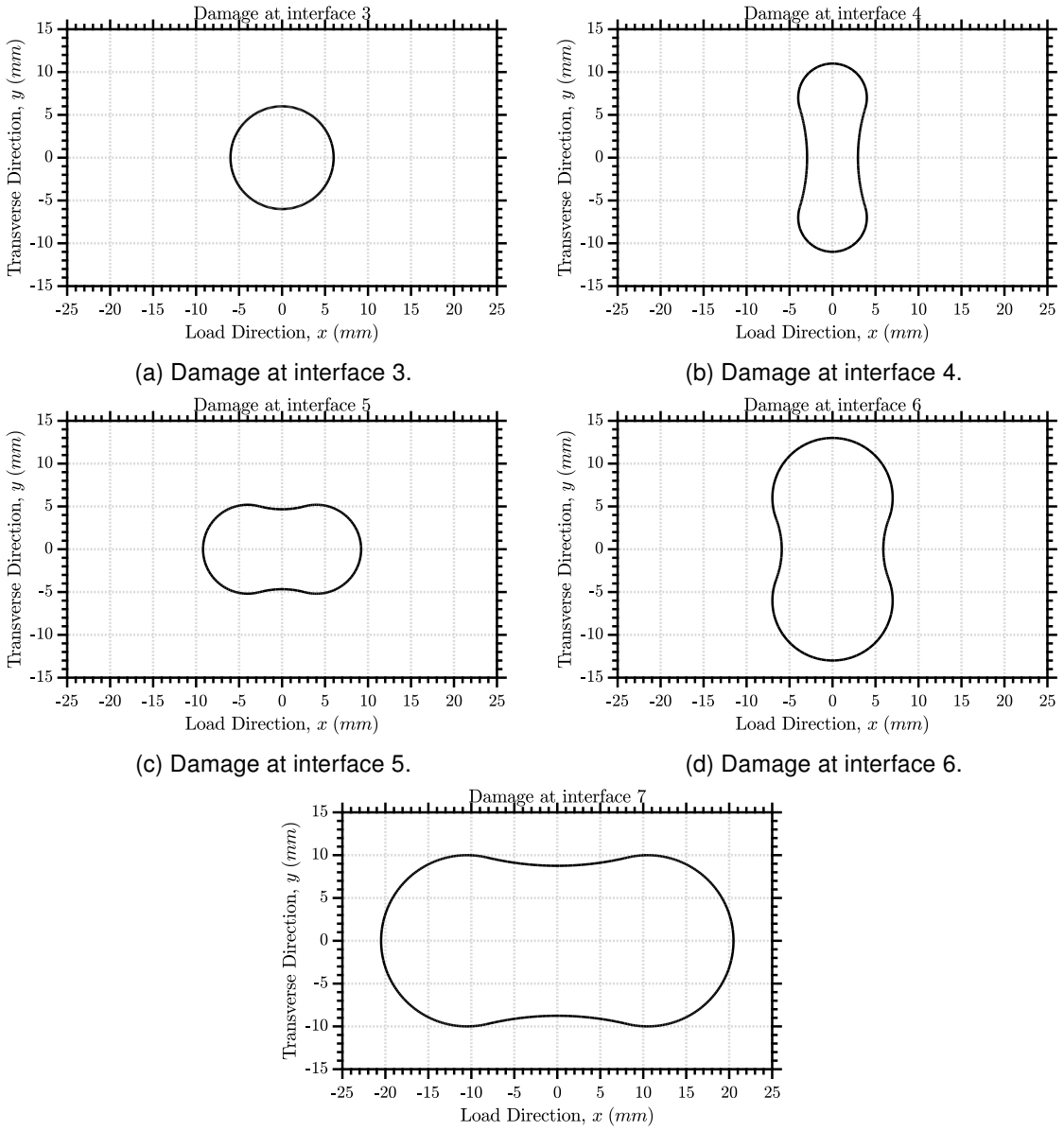

(a) Damage at interface 3.

(b) Damage at interface 4.

(c) Damage at interface 5.

(d) Damage at interface 6.

(e) Damage at interface 7.

Figure 6.38: Damage idealization of the ultrasonic C-scanning over back surface.

Due to the damage at seventh interface is the larges at the samples inspected, all damages behind cannot be seen from the back surface. Therefore, the damage idealization of the following interfaces is carried out from the scanning over the front surface. However, the only damage

clearly visible from this side is, apart from the damage at seventh interface, the damage of the eleventh interface. The information of the damage at the rest of interfaces between seventh and eleventh interfaces cannot be extracted with certainty. Therefore, it is assumed that all these interfaces have the same damage as the eleventh interface. Finally, due to some limitations of the ultrasonic system used in the project, some times the damages at the first interface of each side cannot be seen. From the back side it can be concluded that there is no damage in the first interface because there is no damage also in the second. However, the twelfth interface (first from the front surface) could be damaged. This is why has been assumed that the twelfth interface has the same damage as the eleventh.

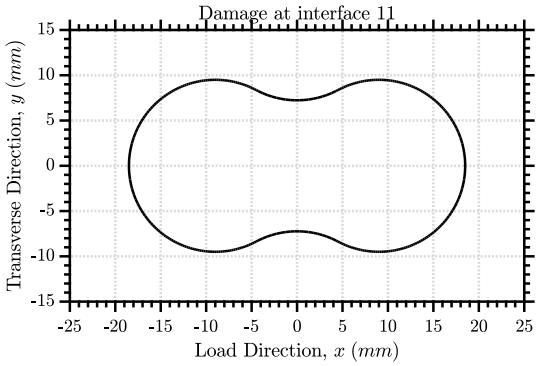

Figure 6.39: Damage idealization of 11 interface.

The model created with the ultrasonic scanned damage idealization is shown in the following figure with the initially delaminated zones defined before:

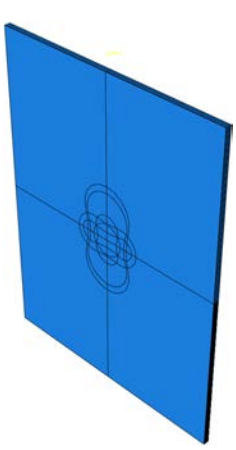

(a) Whole model (Isometric view).

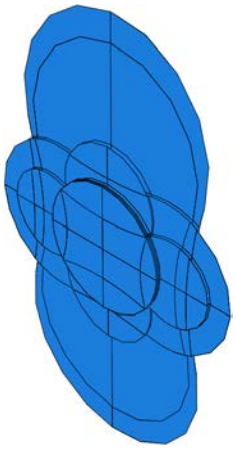

(b) Damage zoom (Isometric view).

(c) Damage (Lateral view).

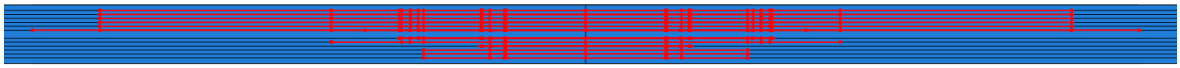

(d) Damage zoom (Lateral view).

Figure 6.40: Model of the ultrasonic C-scanned damage.

In this model, it is also necessary to study the influence of the buckling direction due to the damage varies in the through-thickness direction. The most relevant results are represented here. First, it is studied the typical curves for post-buckling behavior and the failure stress of the plate for both buckling directions and compared to the undamaged plate:

Buckling direction	Failure stress $[MPa]$	U_1 $[mm]$	Failure stress reduction $[\%]$
Front	259.58	0.800	2.53
Back	242.82	0.750	8.82

Table 6.15: Results at failure load of models with ultrasonic C-scanned damage.

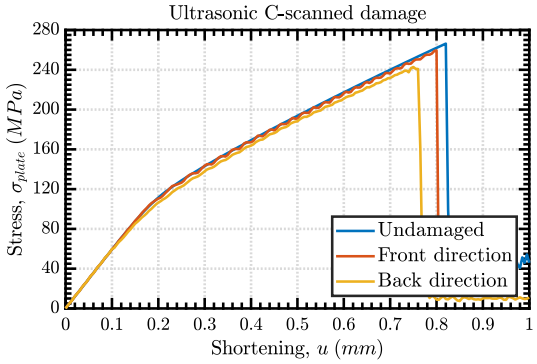

Figure 6.41: Shortening curve for laminate damaged according to ultrasonic C-scanning results.

These results show an influence in the failure stress depending on the buckling direction where the failure stress reduction is almost not appreciable for the front direction. Now, the results for out-of-plane displacement, Hashin damage and delamination initiation criteria and local-global buckling interaction are represented in the following figures at both bucking directions.

Front buckling direction

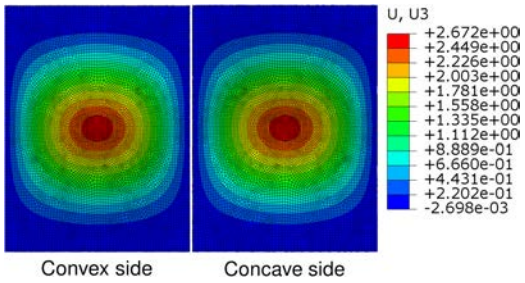

(a) Stress of 150 $[MPa]$.

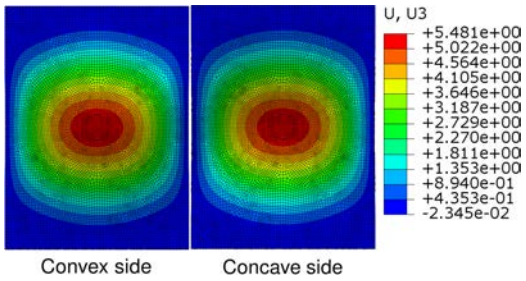

(b) Failure stress.

Figure 6.42: Out-of-plane displacements at model with ultrasonic scanned delaminations and front buckling direction.

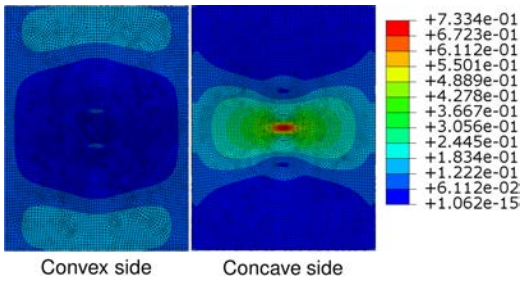

(a) Stress of 150 $[MPa]$.

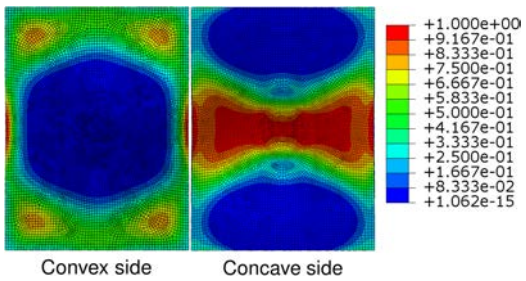

(b) Failure stress.

Figure 6.43: Hashin damage initiation criterion for fiber compression direction at model with ultrasonic scanned delaminations and front buckling direction.

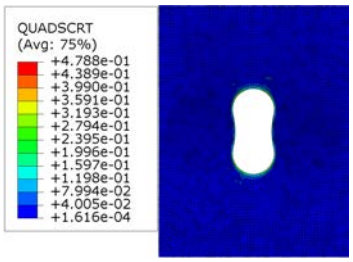

(a) Stress of $150\,[MPa]$.

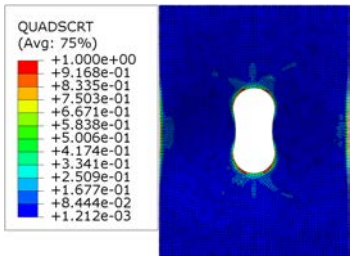

(b) Failure stress.

Figure 6.44: Delamination initiation criterion at model with ultrasonic scanned delaminations and front buckling direction.

(a) Stress of $150\,[MPa]$.

(b) Failure stress.

Figure 6.45: Local-global interaction along load direction at model with ultrasonic scanned delaminations and front buckling direction.

(a) Stress of $150\,[MPa]$.

(b) Failure stress.

Figure 6.46: Local-global interaction along transverse direction at model with ultrasonic scanned delaminations and front buckling direction.

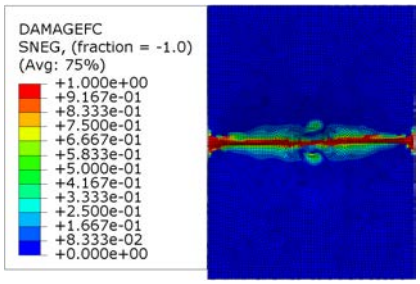

Figure 6.47: Rupture line at model with ultrasonic scanned delaminations and front buckling direction.

A very small reduction of the failure stress of the plate compared to the undamaged laminate has been observed. That was due to no local buckling was developed during the simulation at the concave side because of the small area delaminated and its position at the third interface. Therefore, the failure mechanism of the plate is mainly determined by the ply strengths at concave side as was the case of the undamaged model.

Back buckling direction

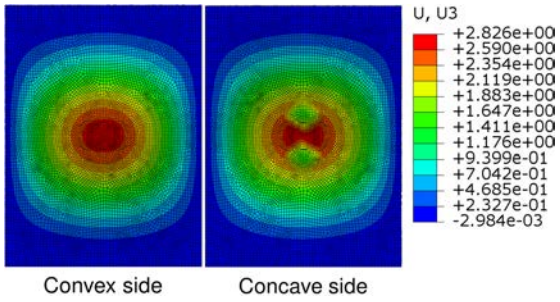

(a) Stress of $150\,[MPa]$.

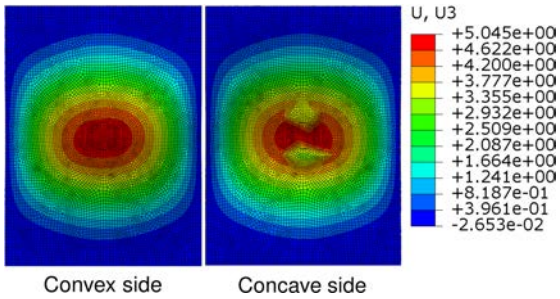

(b) Failure stress.

Figure 6.48: Out-of-plane displacements at model with ultrasonic scanned delaminations and back buckling direction.

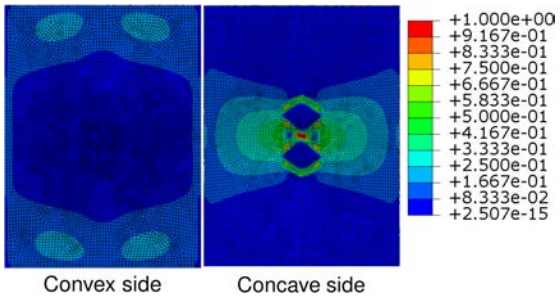

(a) Stress of $150\,[MPa]$.

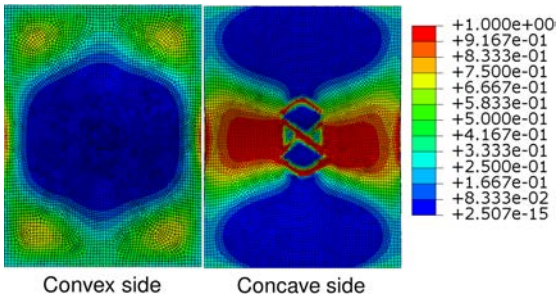

(b) Failure stress.

Figure 6.49: Hashin damage initiation criterion for fiber compression direction at model with ultrasonic scanned delaminations and back buckling direction.

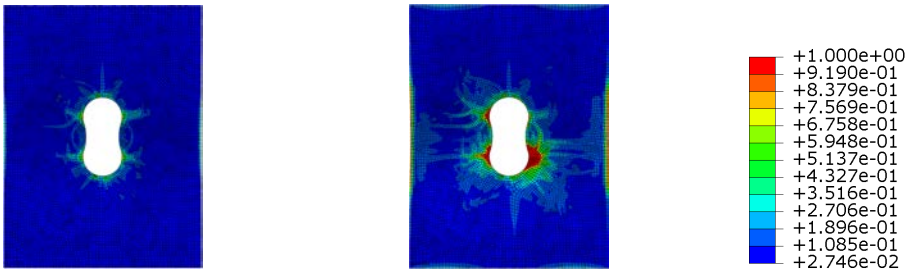

(a) Stress of $150\,[MPa]$. (b) Failure stress.

Figure 6.50: Delamination initiation criterion for fiber compression direction at model with ultrasonic scanned delaminations and back buckling direction.

(a) Stress of $150\,[MPa]$.

(b) Failure stress.

Figure 6.51: Local-global interaction along load direction at model with ultrasonic scanned delaminations and back buckling direction.

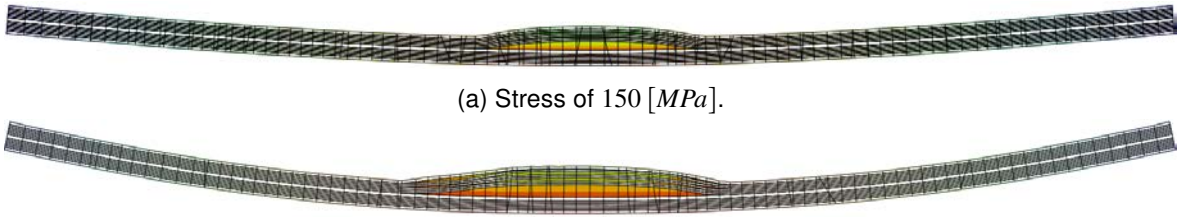

(a) Stress of $150\,[MPa]$.

(b) Failure stress.

Figure 6.52: Local-global interaction along transverse direction at model with ultrasonic scanned delaminations and back buckling direction.

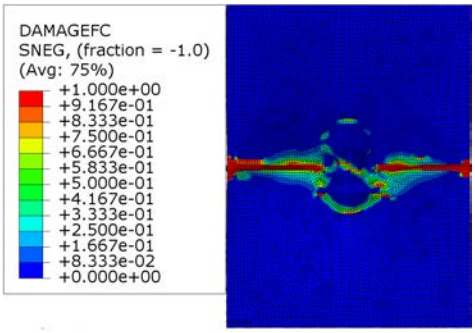

Figure 6.53: Rupture line at model with ultrasonic scanned delaminations and back buckling direction.

When the buckling of this idealized damage from the ultrasonic scanning has occurred in the back direction, local buckling has evolved during the simulation at the concave side. That has been due to the largest delaminated areas have been located near to the concave side of the post-buckling shape. As observed in the elliptical damage idealizations, when the local buckling occurs, the stresses increase at the surrounding area and the delaminations start to growth earlier and the failure stress of the plate is reduced.

6.3.5 Experimental and numerical results comparative

First, the failure stresses for the undamaged plate from the experiments in the literature and from the numerical model have been compared.

Case	Failure stress $[MPa]$	Exp.-Num. error $[\%]$
Experimental	271.80 ± 7.90	–
Undamaged model	266.32	-2.02

Table 6.16: Experimental and numerical results of undamaged laminate.

Now, for the damaged laminate, the two buckling directions observed have been differentiated in order to compare the results.

Case	Failure stress $[MPa]$	Exp.-Num. error $[\%]$
Experimental	258.94 ± 9.77	–
Elliptical and cylindrical	178.86	−30.90
Elliptical and conical	195.08	−24.63
Ultrasonic scanning ideal.	259.58	+0.29

Table 6.17: Experimental and numerical results of damaged laminate with front buckling direction.

Case	Failure stress $[MPa]$	Exp.-Num. error $[\%]$
Experimental	235.34	–
Elliptical and cylindrical	178.86	−24.00
Elliptical and conical	219.47	−6.74
Ultrasonic scanning ideal.	242.82	+3.18

Table 6.18: Experimental and numerical results of damaged laminate with back buckling direction.

Chapter 7

Project planning and budget

7.1 Planning

The milestones followed during this project have been classified in three groups: Office tasks, FEM tasks, and Experimental tasks. The office tasks have been related with literature research, thesis writing and presentation preparation. The FEM tasks have been described with all steps carried out to build the final CAI models with different damage idealization. Finally, the experimental tasks have grouped all the laboratory experiences carried out during the project. All these item have been disaggregated and represented in the Gantt diagram of Figure 7.1.

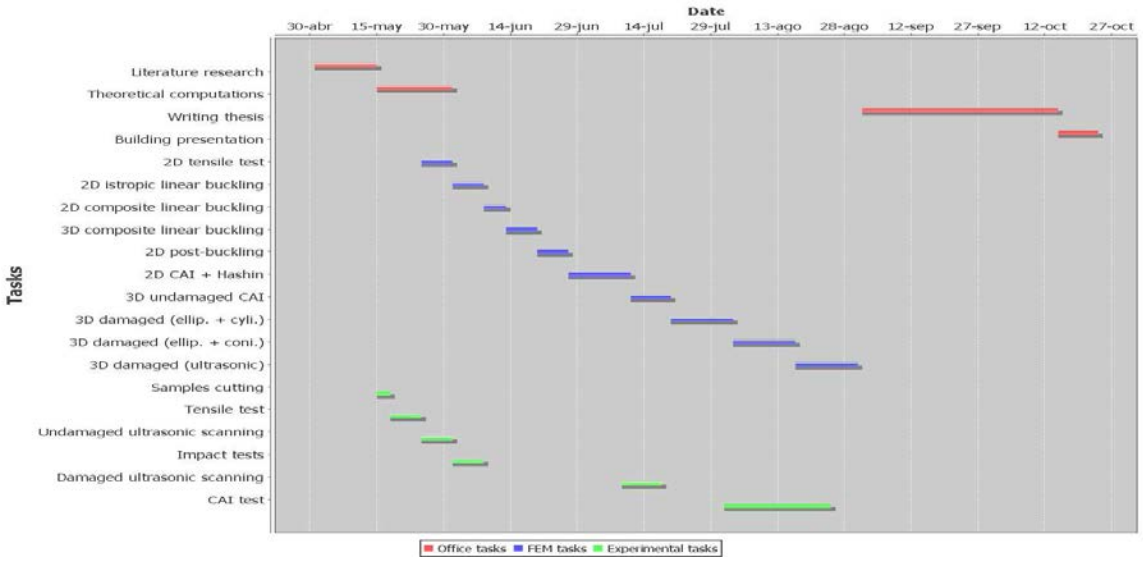

Figure 7.1: Gantt diagram.

7.2 Budget

In this section, the approximate costs of the resources used during the project have been described and classified as personal expenses, fungibles and equipment costs. All these costs have been estimated without taxes. Regarding the personnel costs, the project has had two supervisors, one at the HAW and the other at the UPV. Also, the salary estimation of the student developing this project has been based on an FPU contract for a doctorate student.

Personnel expenses			
Description	Time consumed (h)	Cost per hour (€/h)	Amount (€)
Supervisor 1	60	20	1,200
Supervisor 2	40	20	800
Researcher Assistant	800	6	4,800
Total: 6,800 €			

Table 7.1: Personnel expenses.

The fungibles used during the project have been summarized in next table:

Fungible costs	
Description	Amount (€)
Composite panel 400x500 cm	115
White paint ALL-GRUND KRAUTOL 750ml	20
GRAPHIT 33 spray 200ml	20
Painting utensils	10
Total: 165 €	

Table 7.2: Fungible costs.

Finally, most of the equipment used in this project are extremely expensive because they high-technology systems used for research and the aeronautical industry over a long period of time.

Value of equipment	
Description	Amount (€)
Testing machine INSTRON 8802	30,000
CAI frame	600
ARAMIS 3D measuring system	20,000
Advanced Video Extensometer AVE 2663-821	10,000
Ultrasonc C-scan system	100,000
Impact test system	1,000
Computer	2,000
Abaqus license	6,000

Table 7.3: Value of equipment.

Therefore, an amortization in ten years have been assumed and the costs have been calculated for a use of four months, which is the duration of the experimental part of the project.

Equipment costs	
Material	Amount (€)
Water jet tooling	20
Testing machine INSTRON 8802	1,000
CAI frame	20
ARAMIS 3D measuring software	700
Advanced Video Extensometer AVE 2663-821	350
Ultrasonic C-scan system	3,500
Impact test system	35
Computer	70
Abaqus research license	200
Total: 5,875 €	

Table 7.4: Equipment costs.

Finally, the total cost of the project has been estimated:

Total cost	
Description	Amount (€)
Personnel	6,800
Fungible	165
Equipment	5,875
Total: 12,840 €	

Table 7.5: Total cost.

Chapter 8

Conclusions and future work

The goals of this project have been successfully achieved. First, the finite element model of an undamaged laminate under CAI test has been calculated and it has demonstrate that is able to predict the failure load with outstanding precision compared with the experimental results. Secondly, the initially damaged laminate under CAI test has been created with different idealizations. These damage idealizations have shown the importance of studying the geometric imperfections influence that may determine the buckling direction when a thin laminate is tested. Moreover, it has been proved that depending on the buckling direction, different CAI strength may be obtained.

The models results have shown a large influence of the damage idealizations chosen over the final results. In this project, compared to the experimental results, the idealization based on the ultrasonic C-scanning at each interface has been able to predict the failure load with an acceptable accuracy.

Regarding the experimental phases of the project, they have been carried out with acceptable results. For example, the tensile test combined with the micromechanic models and CLT theory have worked for getting an acceptable plies mechanical properties, which it is demonstrated at the excellent models results. Also, impact energies measured have been quite similar which each other. Regarding the damaged areas inspected with the ultrasonic C-scanning system, they have been in quite agreement between all the samples. From CAI test, the results obtained have been considered as good enough for this project because they have shown the different geometric imperfections influence and the failure loads have had a low dispersion.

In future projects, a deeper investigation may be carry out. For instance, improving the impact test system regarding the way the sample is fixed and measuring more accurately the damage energy absorbed by the sample during the impact. Also, despite the damage idealization based on ultrasonic C-scanning has allowed a good agreement with experimental results, the use of X-ray 3D tomographic visualization could show the complete internal damage. This way, a more complete model which includes the real delaminated areas at each interface and also damages as matrix cracking and fiber breakage, which influence has been omitted in this project. The experimental CAI frame used may be also improved to have a better plate alignment and to control the force applied at the restrains. Finally, regarding the model set-up improvements, to get an even better agreement with the experiments, more accurate material properties would be needed to define the plies elastic behavior and damage models. Also, getting the proper cohesive interfaces properties for modeling better the delaminations in the model. It could be interesting to try other damage models for plies materials, such as the interactive Tsai-Wu criteria due to it is able to model the compression failure in composite laminates with very high accuracy.

Bibliography

[1] AIRBUS, “3rd Generation of Composite Materials for Airframe.” World Materials Forum, 2015.

[2] E. E. Herricks, D. Mayer, and S. Majumdar, “Foreign object debris characterization at a large international airport,” tech. rep., 2015.

[3] S. Abrate, *Impact on composite structures*. Cambridge university press, 2005.

[4] T.-W. Shyr and Y.-H. Pan, “Impact resistance and damage characteristics of composite laminates,” *Composite structures*, vol. 62, no. 2, pp. 193–203, 2003.

[5] S. Gholizadeh, “A review of non-destructive testing methods of composite materials,” *Procedia Structural Integrity*, vol. 1, pp. 50–57, 2016.

[6] X. Zhang, L. Hounslow, and M. Grassi, “Improvement of low-velocity impact and compression-after-impact performance by z-fibre pinning,” *Composites Science and Technology*, vol. 66, no. 15, pp. 2785–2794, 2006.

[7] R. Garcia, M. Linke, S. Neßlinger, and J. García-Manrique, “An infiltration strategy to repair carbon fiber reinforced polymer (cfrp) parts,” *Procedia Manufacturing*, vol. 13, pp. 380–387, 2017.

[8] M. Hautier, D. Lévêque, C. Huchette, and P. Olivier, “Investigation of composite repair method by liquid resin infiltration,” *Plastics, Rubber and Composites*, vol. 39, no. 3-5, pp. 200–207, 2010.

[9] Y. Yuan, M. Rong, M. Zhang, G. Yang, and J. Zhao, “Healing of fatigue crack in epoxy materials with epoxy/mercaptan system via manual infiltration.,” *Express Polymer Letters*, vol. 4, no. 10, 2010.

[10] M. Kempf, S. Schwaegele, A. Ferencz, and V. Altstaedt, “Effect of impact damage on the compression fatigue performance of glass and carbon fibre reinforced composites,” in *18th International Conference on Composite Materials, Jeju, Korea*, 2011.

[11] “Carbon-fibre-reinforced plastics — Determination of compression-after- impact properties at a specified impact-energy level.,” standard, International Organization for Standardization (ISO), Aug. 2009.

[12] A. T. Nettles and J. R. Jackson, “Compression after impact strength of out-of-autoclave processed laminates,” *Journal of Reinforced Plastics and Composites*, vol. 32, no. 24, pp. 1887–1894, 2013.

[13] N. Naik, M. Joglekar, H. Arya, S. Borade, and K. Ramakrishna, “Impact and compression after impact characteristics of plain weave fabric composites: effect of plate thickness,” *Advanced Composite Materials*, vol. 12, no. 4, pp. 261–280, 2004.

[14] M. Aktaş, H. E. Balcıoğlu, A. Aktaş, E. Türker, and M. E. Deniz, "Impact and post impact behavior of layer fabric composites," *Composite Structures*, vol. 94, no. 9, pp. 2809–2818, 2012.

[15] F. Aymerich and P. Priolo, "Characterization of fracture modes in stitched and unstitched cross-ply laminates subjected to low-velocity impact and compression after impact loading," *International Journal of Impact Engineering*, vol. 35, no. 7, pp. 591–608, 2008.

[16] Y. Liv, G. Guillamet, J. Costa, E. González, L. Marín, and J. Mayugo, "Experimental study into compression after impact strength of laminates with conventional and nonconventional ply orientations," *Composites Part B: Engineering*, vol. 126, pp. 133–142, 2017.

[17] M. Aktaş, R. Karakuzu, and Y. Arman, "Compression-after impact behavior of laminated composite plates subjected to low velocity impact in high temperatures," *Composite Structures*, vol. 89, no. 1, pp. 77–82, 2009.

[18] U. Khashaba and R. Othman, "Low-velocity impact of woven cfre composites under different temperature levels," *International Journal of Impact Engineering*, vol. 108, pp. 191–204, 2017.

[19] M. D. Kulkarni, R. Goel, and N. Naik, "Effect of back pressure on impact and compression-after-impact characteristics of composites," *Composite Structures*, vol. 93, no. 2, pp. 944–951, 2011.

[20] T. Ishikawa, S. Sugimoto, M. Matsushima, and Y. Hayashi, "Some experimental findings in compression-after-impact (cai) tests of cf/peek (apc-2) and conventional cf/epoxy flat plates," *Composites science and technology*, vol. 55, no. 4, pp. 349–363, 1995.

[21] "Recommended Test Method for COMPRESSION AFTER IMPACT PROPERTIES OF FIBER-RESIN COMPOSITES," standard, Suppliers of Advanced Composite Materials Association (SACMA), 1994.

[22] C. Soutis and P. Curtis, "Prediction of the post-impact compressive strength of cfrp laminated composites," *Composites Science and Technology*, vol. 56, no. 6, pp. 677–684, 1996.

[23] S. Sanchez-Saez, E. Barbero, R. Zaera, and C. Navarro, "Compression after impact of thin composite laminates," *Composites Science and Technology*, vol. 65, no. 13, pp. 1911–1919, 2005.

[24] M. Remacha, S. Sánchez-Sáez, B. López-Romano, and E. Barbero, "A new device for determining the compression after impact strength in thin laminates," *Composite Structures*, vol. 127, pp. 99–107, 2015.

[25] A. T. Rhead, R. Butler, and G. W. Hunt, "Compressive strength of composite laminates with delamination-induced interaction of panel and sublaminate buckling modes," *Composite Structures*, vol. 171, pp. 326–334, 2017.

[26] H. Sekine, N. Hu, and M. Kouchakzadeh, "Buckling analysis of elliptically delaminated composite laminates with consideration of partial closure of delamination," *Journal of Composite Materials*, vol. 34, no. 7, pp. 551–574, 2000.

[27] D. Bull, S. Spearing, and I. Sinclair, "Image-enhanced modelling of residual compressive after impact strength in laminated composites," *Composite Structures*, vol. 192, pp. 20–27, 2018.

[28] F. Esrail and C. Kassapoglou, “An efficient approach to determine compression after impact strength of quasi-isotropic composite laminates,” *Composites Science and Technology*, vol. 98, pp. 28–35, 2014.

[29] R. Craven, L. Iannucci, and R. Olsson, “Delamination buckling: A finite element study with realistic delamination shapes, multiple delaminations and fibre fracture cracks,” *Composites Part A: Applied Science and Manufacturing*, vol. 41, no. 5, pp. 684–692, 2010.

[30] W. Tan, B. G. Falzon, L. N. Chiu, and M. Price, “Predicting low velocity impact damage and compression-after-impact (cai) behaviour of composite laminates,” *Composites Part A: Applied Science and Manufacturing*, vol. 71, pp. 212–226, 2015.

[31] M. Abir, T. Tay, M. Ridha, and H. Lee, “Modelling damage growth in composites subjected to impact and compression after impact,” *Composite Structures*, vol. 168, pp. 13–25, 2017.

[32] C. Alvarez-Restrepo, H. Benitez-Restrepo, and L. Tobón, “Characterization of defects of pulsed thermography inspections by orthogonal polynomial decomposition,” *NDT & E International*, vol. 91, pp. 9–21, 2017.

[33] P. Pomarède, F. Meraghni, L. Peltier, S. Delalande, and N. F. Declercq, “Damage evaluation in woven glass reinforced polyamide 6.6/6 composites using ultrasound phase-shift analysis and x-ray tomography,” *Journal of Nondestructive Evaluation*, vol. 37, no. 1, p. 12, 2018.

[34] D. Bull, I. Sinclair, S. Spearing, and L. Helfen, “Composite laminate impact damage assessment by high resolution 3d x-ray tomography and laminography,” 2011.

[35] “Airbus Test Method - Fibre Reinforced Plastics - Determination of Compression Strength After Impact.,” standard, AIRBUS S.A.S, Oct. 2005.

[36] “Aerospace series - Fibre reinforced plastics - Test method - Determination of the compression strength after impact.,” standard, Aerospace and Defence Industries Association of Europe - Standardization (ASD-STAN), Nov. 2015.

[37] “Standard test method for compressive residual strength properties of damaged polymer matrix composite plates.,” standard, American Society for Testing and Materials (ASTM), Oct. 2005.

[38] “Advanced Composite Compression Test.,” standard, The Boeing Company, Seattle, WA, 1988.

[39] “Luft- und Raumfahrt. Faserverstärkte Kunststoffe. Prüfung von multidirektionalen Laminaten. Bestimmung der Druckfestigkeit nach Schlagbeanspruchung.,” standard, Deutsches Institut für Normung, 1989.

[40] M. Linke and J. García-Manrique, “Contribution to reduce the influence of the free sliding edge on compression-after-impact testing of thin-walled undamaged composites plates,” *Materials*, vol. 11, no. 9, p. 1708, 2018.

[41] R. F. Gibson, *Principles of composite material mechanics*. CRC press, 2011.

[42] E. Giner and J. Albelda, “Análisis y diseño de materiales compuestos,” *Universitat Politècnica de València*, 2001.

[43] Z. Hashin, “Failure criteria for unidirectional fiber composites,” *Journal of applied mechanics*, vol. 47, no. 2, pp. 329–334, 1980.

[44] C. ABAQUS, “Analysis User’s Manual, Version 6.14,” 2014.

[45] C. Sun, “Comparative evaluation of failure analysis methods for composite laminates (No. DOT/FAA/AR-95/109).,” tech. rep., 1996.

[46] P. P. Camanho and C. G. Dávila, “Mixed-mode decohesion finite elements for the simulation of delamination in composite materials,” 2002.

[47] M. L. Benzeggagh and M. Kenane, “Measurement of mixed-mode delamination fracture toughness of unidirectional glass/epoxy composites with mixed-mode bending apparatus,” *Composites science and technology*, vol. 56, no. 4, pp. 439–449, 1996.

[48] S. Timoshenko, *Theory of elastic stability 2e*. Tata McGraw-Hill Education, 1970.

[49] R. M. Jones, *Buckling of bars, plates, and shells*. Bull Ridge Corporation, 2006.

[50] L. Cedolin *et al.*, *Stability of structures: elastic, inelastic, fracture and damage theories*. World Scientific, 2010.

[51] T. Kobayashi and Y. Mihara, “Postbuckling analyses of elastic cylindrical shells under axial compression,” in *ASME 2009 Pressure Vessels and Piping Conference*, pp. 745–754, American Society of Mechanical Engineers, 2009.

[52] J. N. Reddy, *Mechanics of laminated composite plates and shells: theory and analysis*. CRC press, 2004.

[53] E. ISO, “527-4. Plastics-Determination of tensile properties-Part 4: Test conditions for isotropic and orthotropic fibre-reinforced plastic composites,” *International Organization for Standardization (ISO), Geneva, Switzerland*, 1997.

[54] P. Dobrinski, G. Krakau, and A. Vogel, *Physik für Ingenieure*. Teubner, 1970.

[55] T. Hasiotis, E. Badogiannis, and N. G. Tsouvalis, “Application of ultrasonic c-scan techniques for tracing defects in laminated composite materials,” *Strojniški vestnik-Journal of Mechanical Engineering*, vol. 57, no. 3, pp. 192–203, 2011.

[56] F. Aymerich and W. Staszewski, “Impact damage detection in composite laminates using nonlinear acoustics,” *Composites Part A: Applied Science and Manufacturing*, vol. 41, no. 9, pp. 1084–1092, 2010.

[57] H. Öry and H. Reimerdes, “Faserverbundwerkstoffe,” *Vorlesung an der RWTH, Aachen*, 1989.

[58] “CRAG TEST METHODS FOR TEE EASURE NT OF TEE ENGWTERING ROPEIS OF FIBRE RzINORCED PLASTICS,” standard, Royal Aerospace Establishment, Feb. 1988.

[59] M. De Freitas and L. Reis, “Failure mechanisms on composite specimens subjected to compression after impact,” *Composite Structures*, vol. 42, no. 4, pp. 365–373, 1998.

[60] O. Khondker, I. Herszberg, and H. Hamada, “Measurements and prediction of the compression-after-impact strength of glass knitted textile composites,” *Composites Part A: Applied Science and Manufacturing*, vol. 35, no. 2, pp. 145–157, 2004.

Appendices

A Tensile test results

Pictures of the tensile tests outputs:

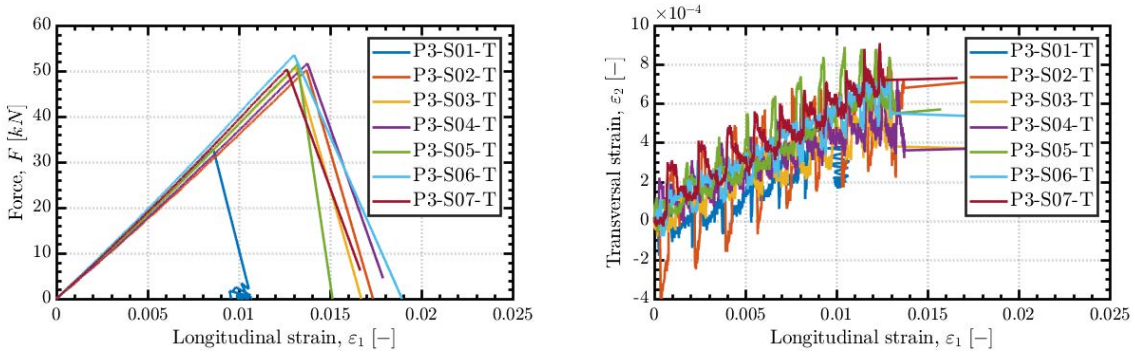

Figure 8.1: Tensile tests outputs.

Pictures of damaged samples after the tests.

Figure 8.2: Tensile test samples failure.

B Impact test results

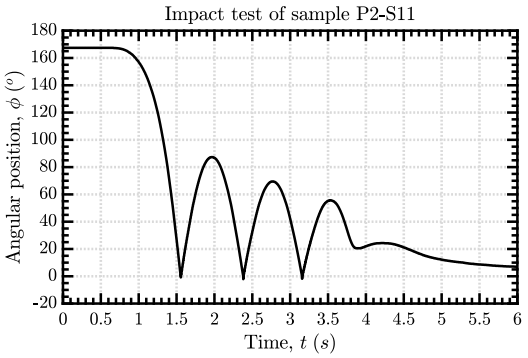

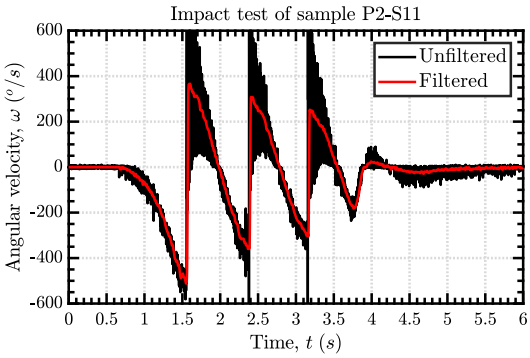

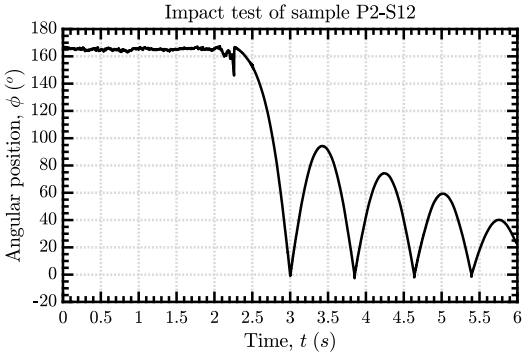

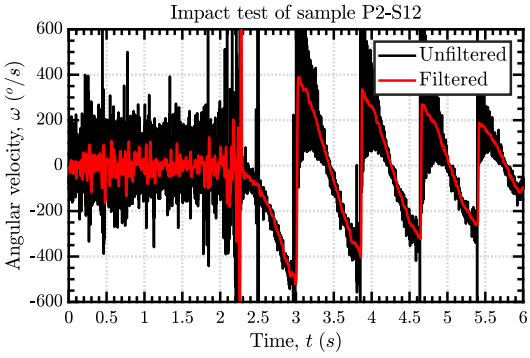

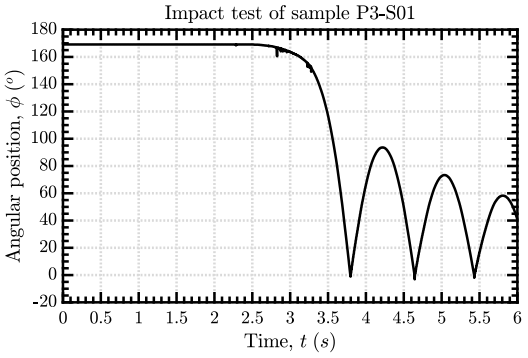

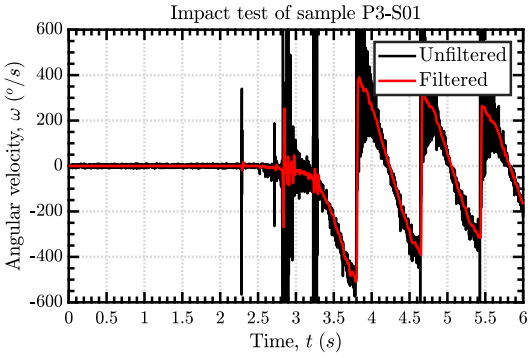

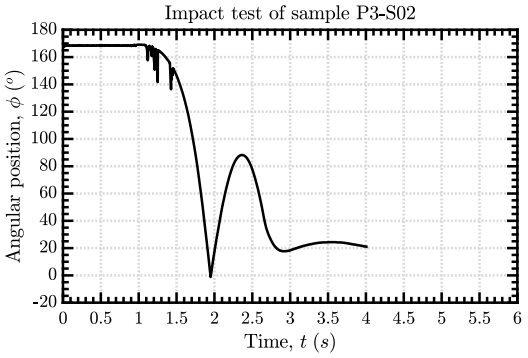

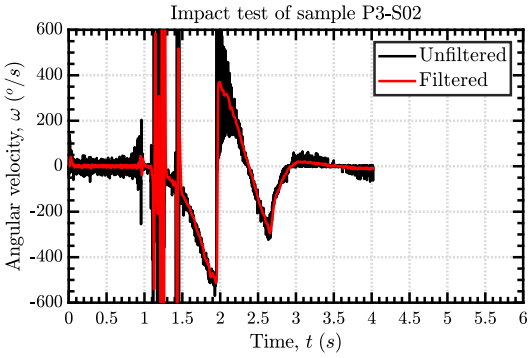

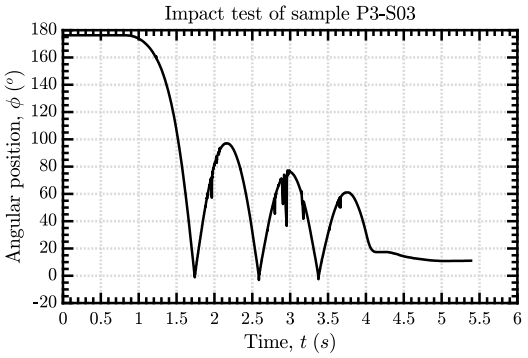

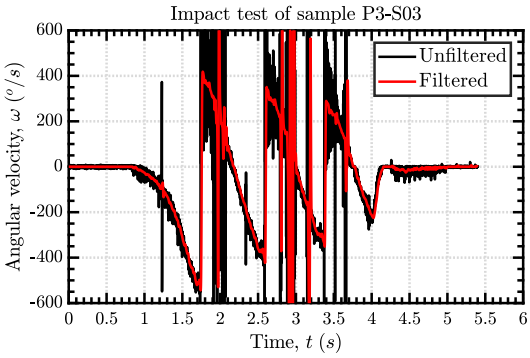

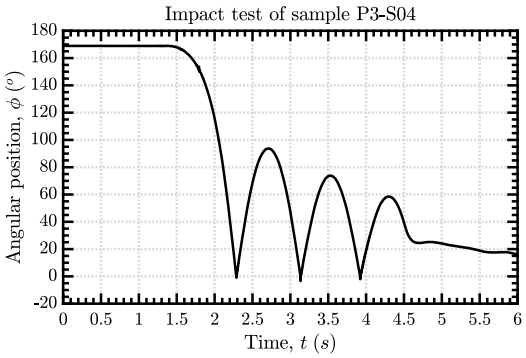
Impact test of sample P3-S04
Angular position, ϕ (^{o})
Time, t (s)

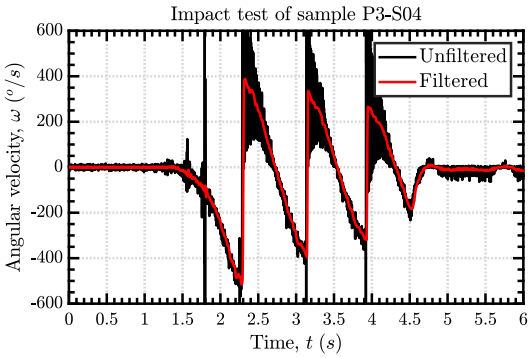
Impact test of sample P3-S04
Unfiltered
Filtered
Angular velocity, ω ($^o/s$)
Time, t (s)

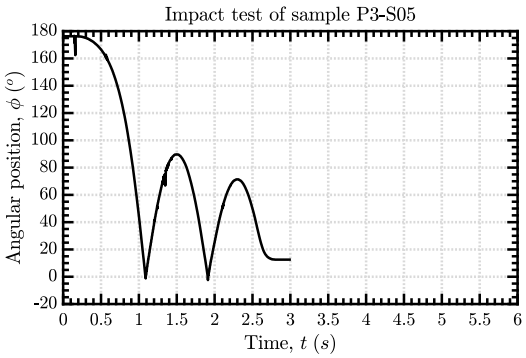
Impact test of sample P3-S05
Angular position, ϕ (^{o})
Time, t (s)

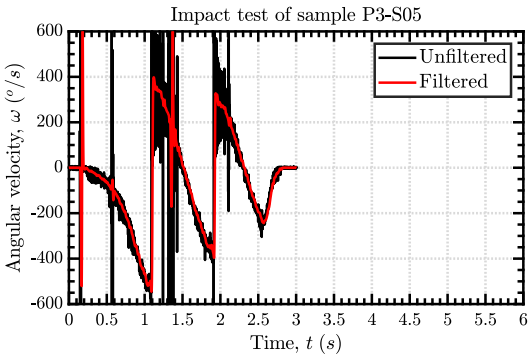
Impact test of sample P3-S05
Unfiltered
Filtered
Angular velocity, ω ($^o/s$)
Time, t (s)

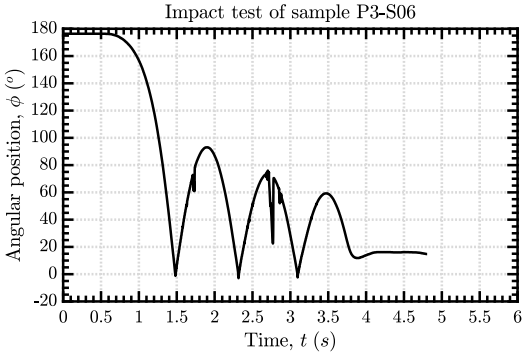
Impact test of sample P3-S06
Angular position, ϕ (^{o})
Time, t (s)

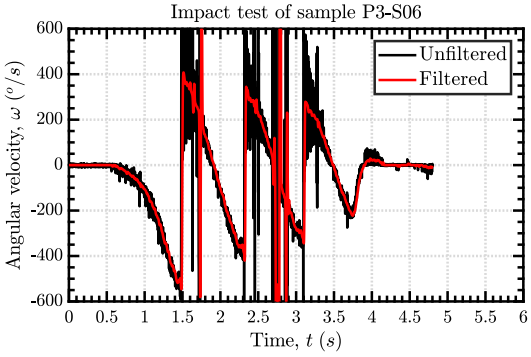
Impact test of sample P3-S06
Unfiltered
Filtered
Angular velocity, ω ($^o/s$)
Time, t (s)

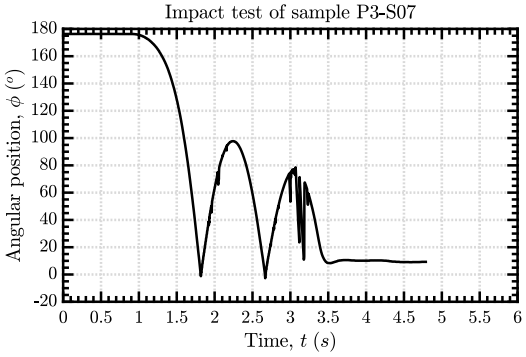
Impact test of sample P3-S07
Angular position, ϕ (^{o})
Time, t (s)

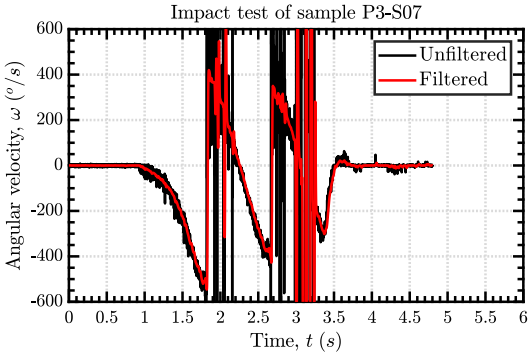
Impact test of sample P3-S07
Unfiltered
Filtered
Angular velocity, ω ($^o/s$)
Time, t (s)

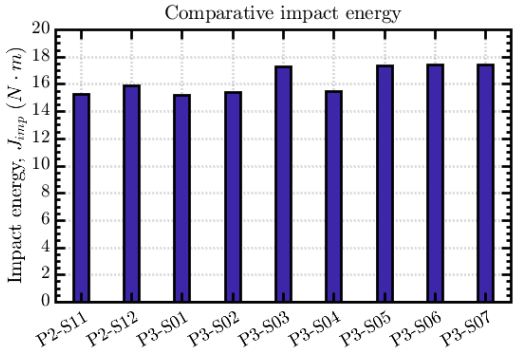
Comparative impact energy
Impact energy, J_{imp} ($N \cdot m$)
P2-S11
P2-S12
P3-S01
P3-S02
P3-S03
P3-S04
P3-S05
P3-S06
P3-S07

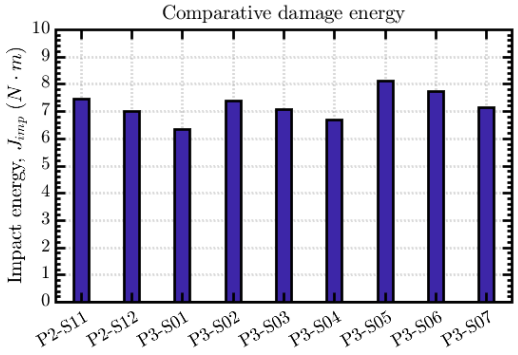
Comparative damage energy
Impact energy, J_{imp} ($N \cdot m$)
P2-S11
P2-S12
P3-S01
P3-S02
P3-S03
P3-S04
P3-S05
P3-S06
P3-S07

C Ultrasonic C-scan inspection

C.1 Scanning results summary

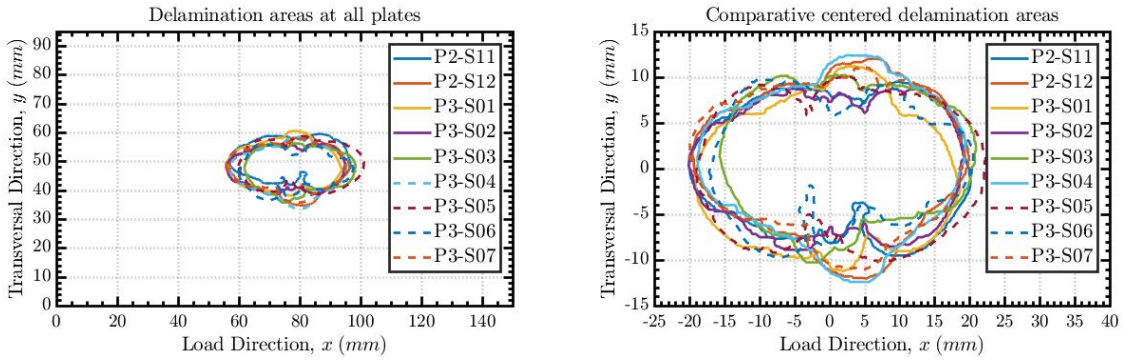

Figure 8.3: Comparative of global delamination shape.

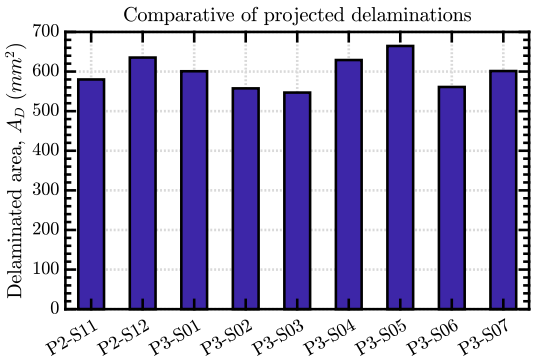

Figure 8.4: Comparative of total area delaminated projected.

C.2 Inspection of pre-impacted samples

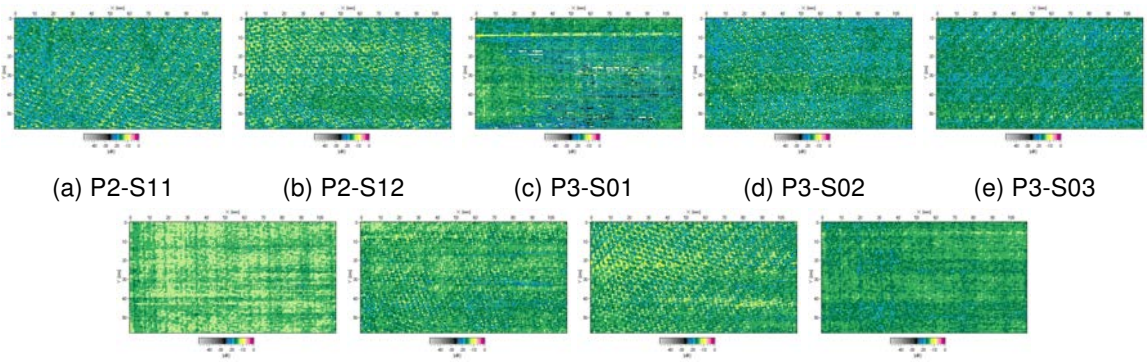

(a) P2-S11 (b) P2-S12 (c) P3-S01 (d) P3-S02 (e) P3-S03

(f) P3-S04 (g) P3-S05 (h) P3-S06 (i) P3-S07

Figure 8.5: Ultrasonic scanning of pre-impacted samples.

C.3 Inspection of post-impacted samples

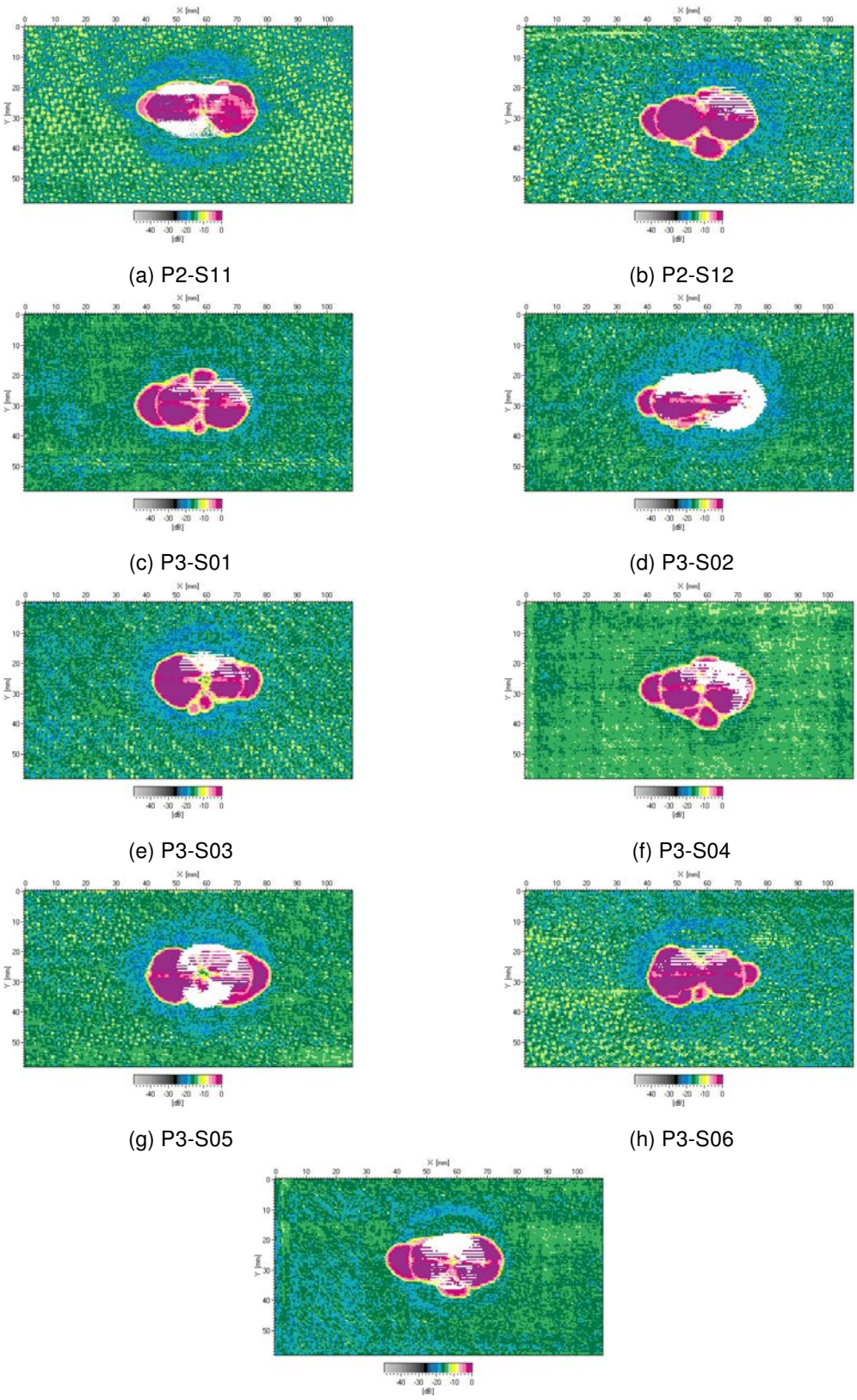

(a) P2-S11

(b) P2-S12

(c) P3-S01

(d) P3-S02

(e) P3-S03

(f) P3-S04

(g) P3-S05

(h) P3-S06

(i) P3-S07

Figure 8.6: Ultrasonic scanning of post-impacted samples.

C.4 Detailed damage depth pictures from front and back surfaces

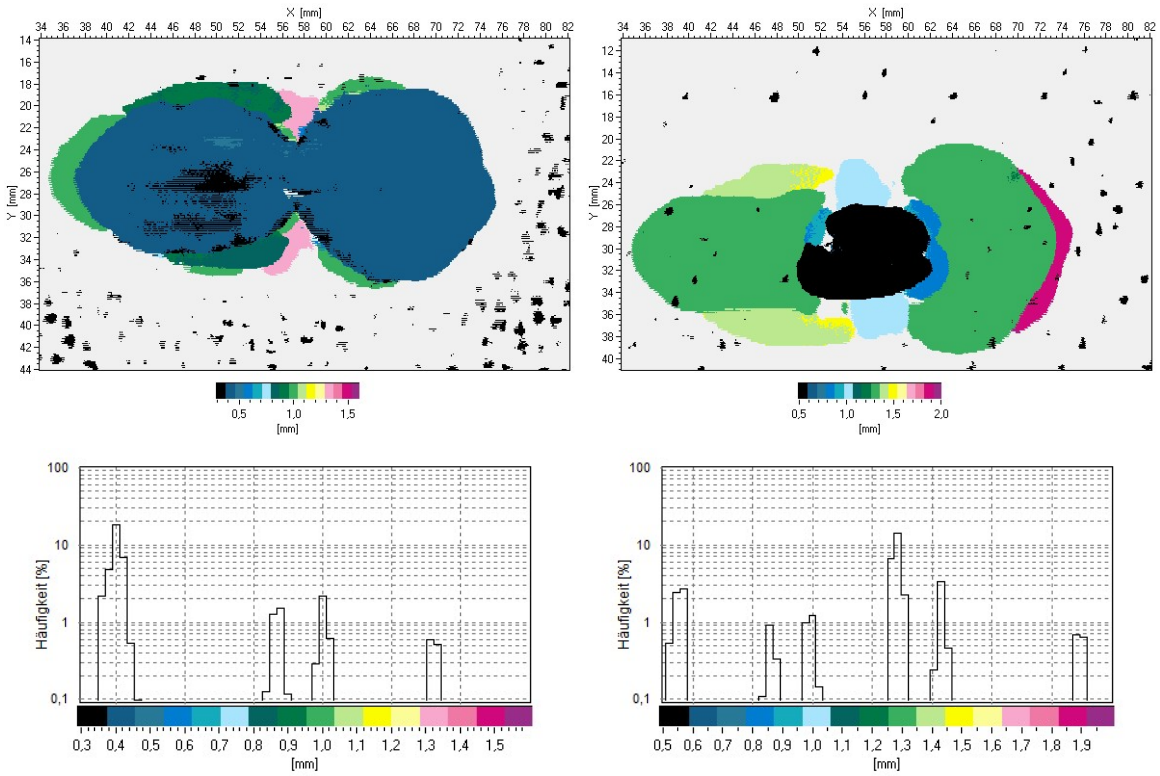

Figure 8.7: Post-impact detailed scan pictures of sample P2-S11.

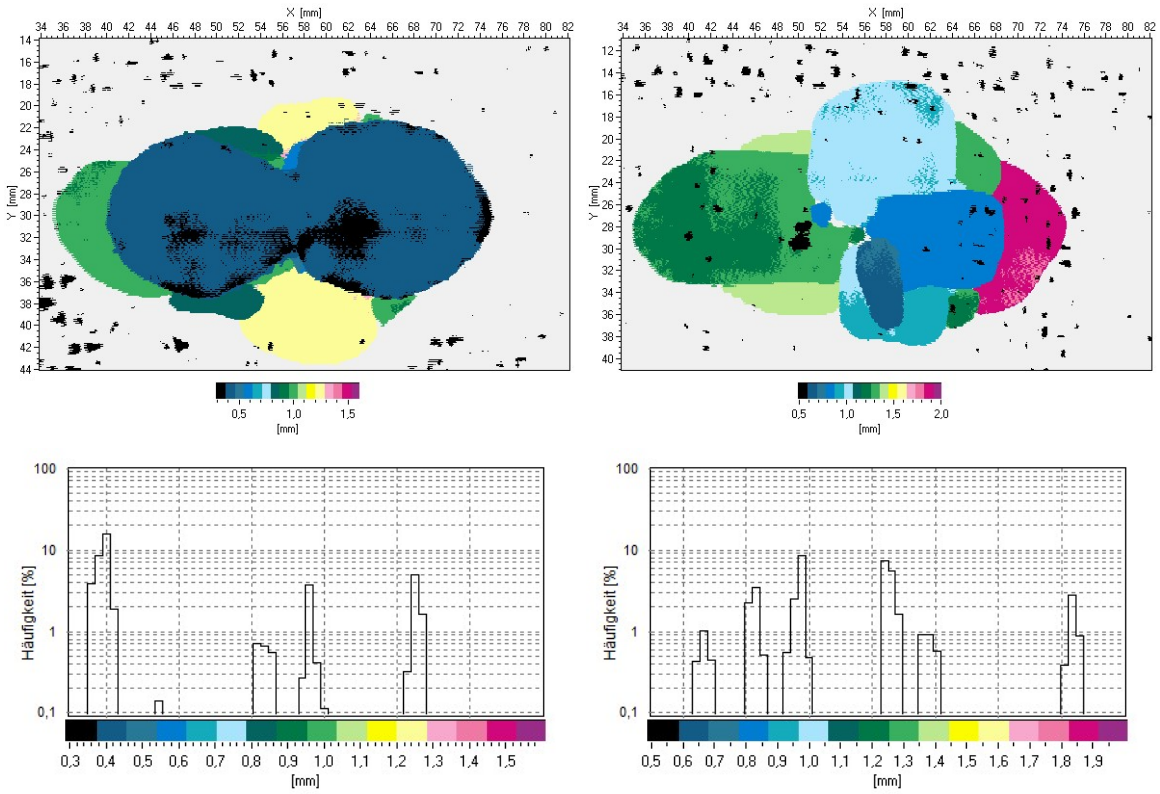

Figure 8.8: Post-impact detailed scan pictures of sample P2-S12.

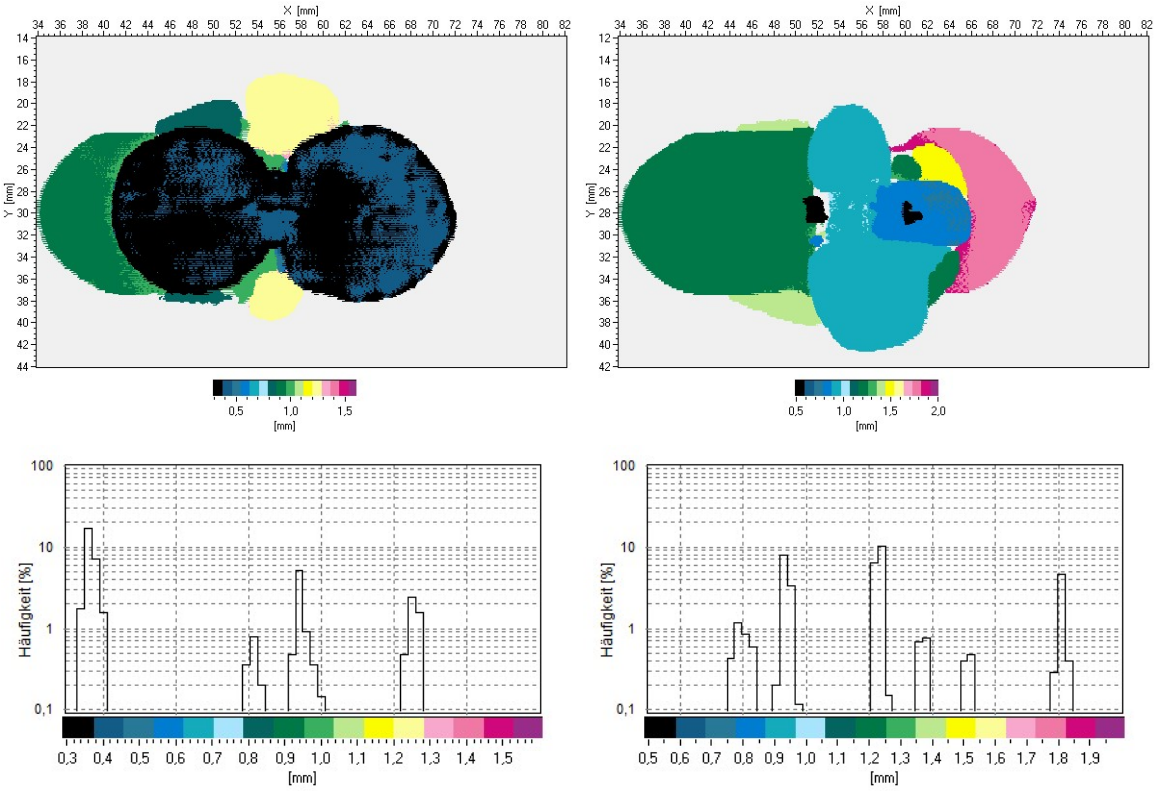

Figure 8.9: Post-impact detailed scan pictures of sample P3-S01.

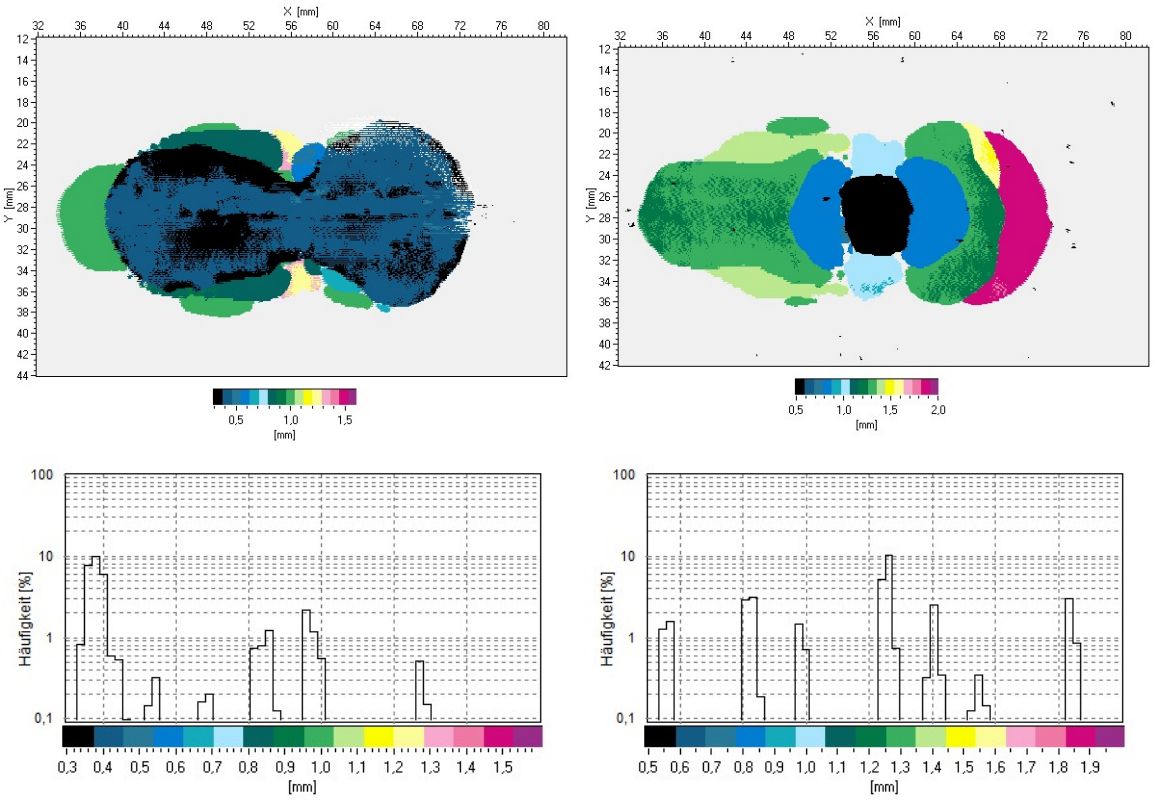

Figure 8.10: Post-impact detailed scan pictures of sample P3-S02.

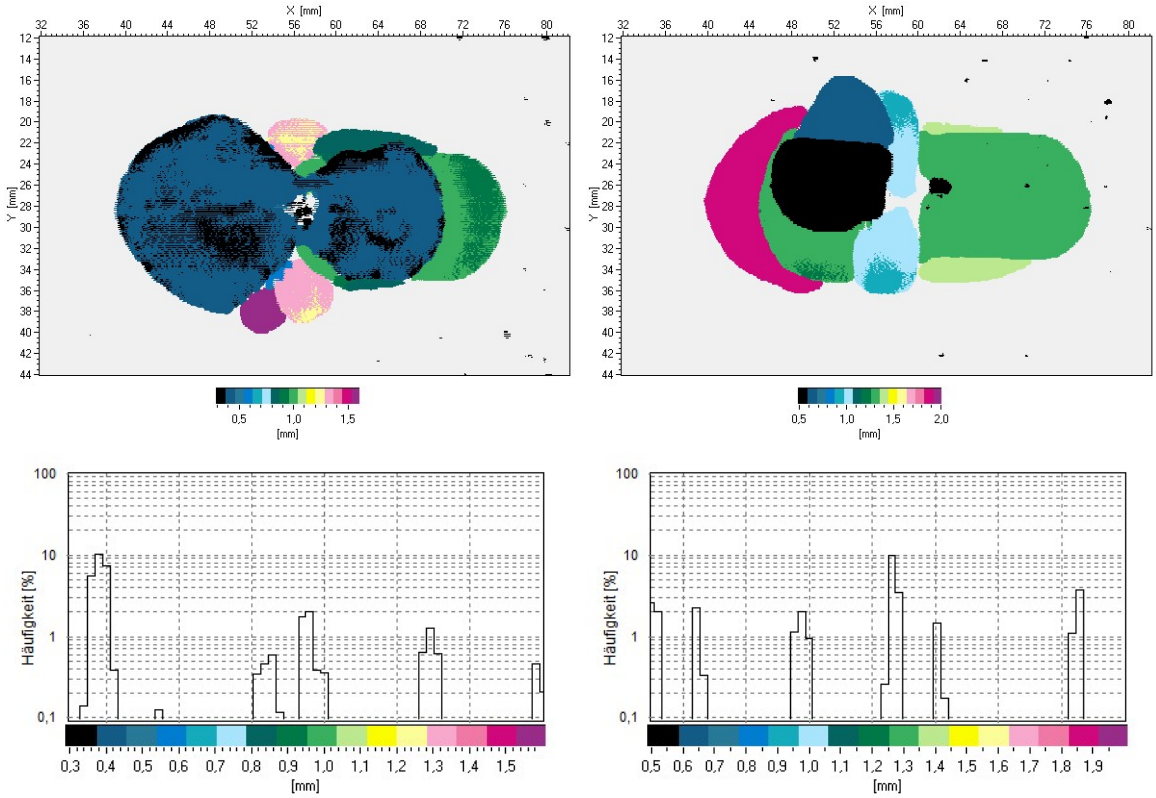

Figure 8.11: Post-impact detailed scan pictures of sample P3-S03.

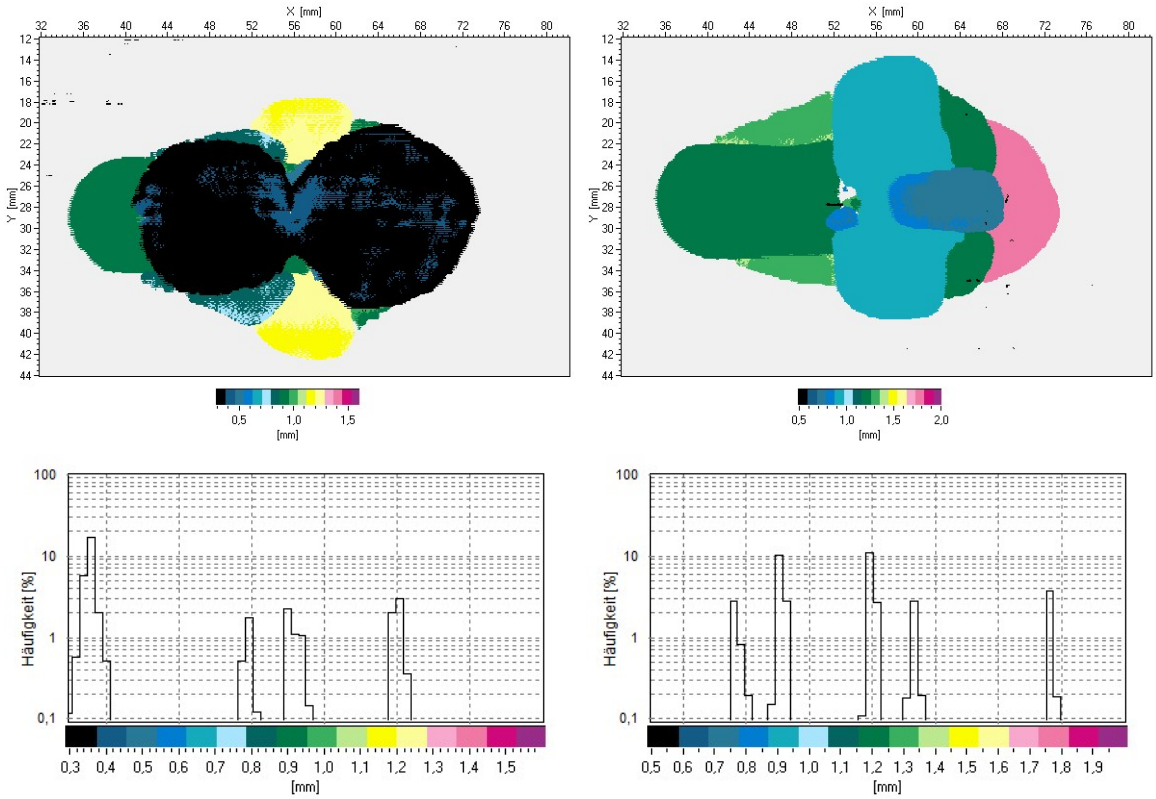

Figure 8.12: Post-impact detailed scan pictures of sample P3-S04.

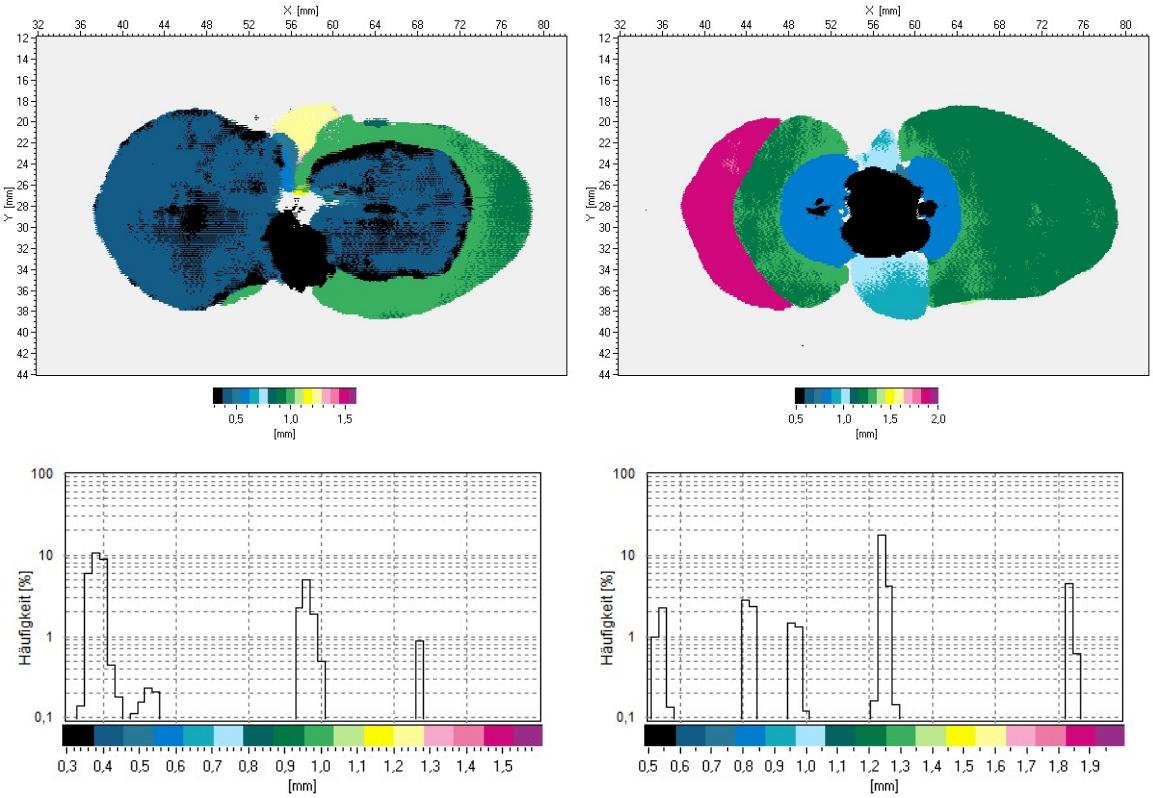

Figure 8.13: Post-impact detailed scan pictures of sample P3-S05.

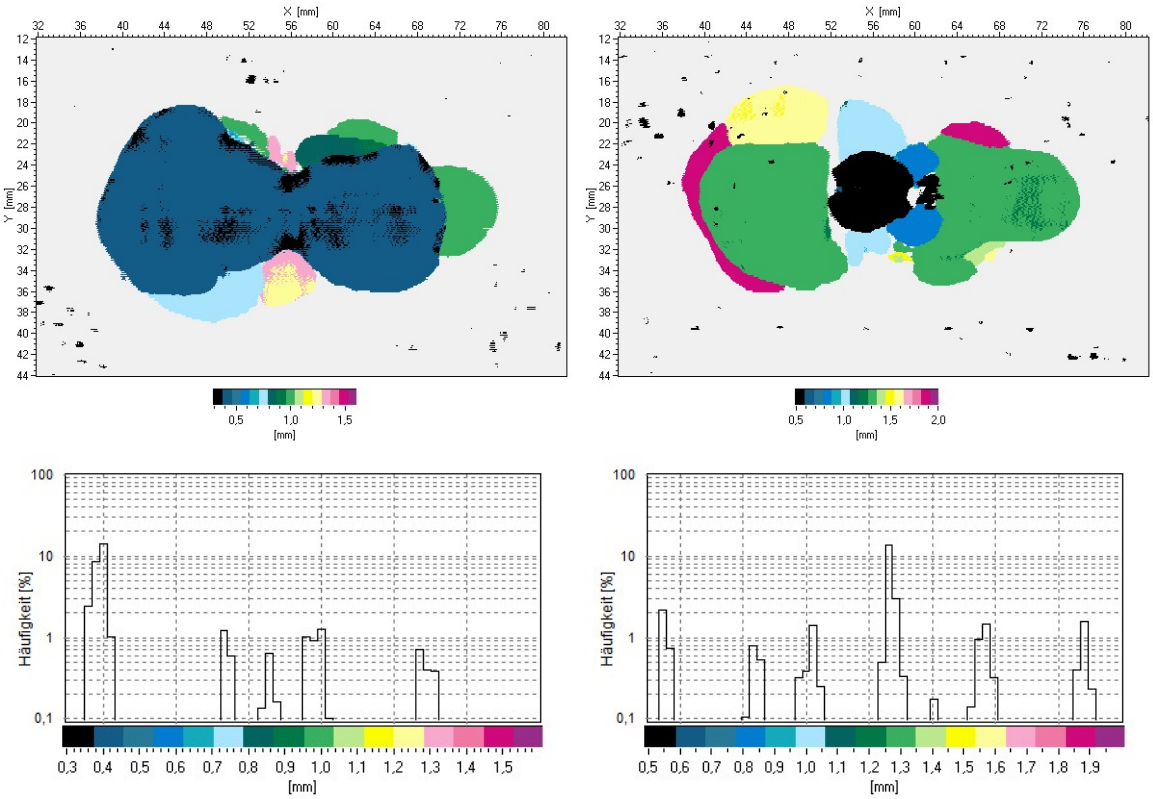

Figure 8.14: Post-impact detailed scan pictures of sample P3-S06.

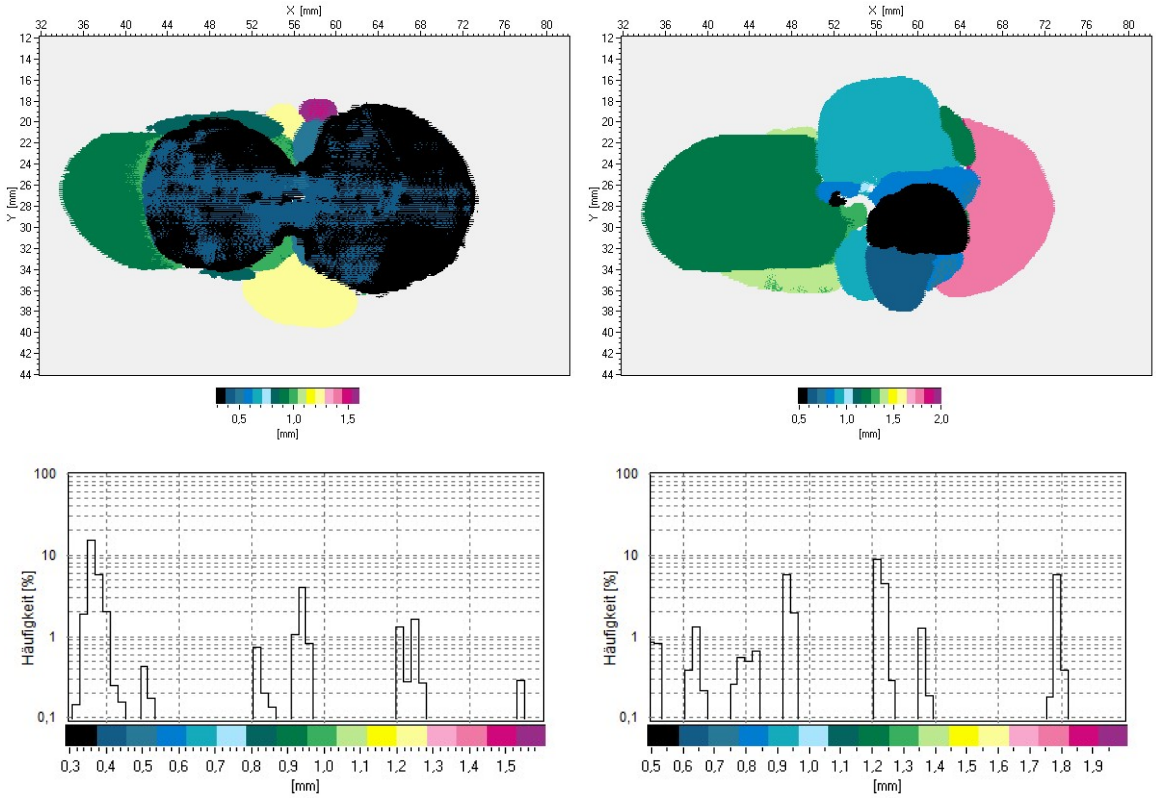

Figure 8.15: Post-impact detailed scan pictures of sample P3-S07.

D Compression-After-Impact test

D.1 Failure plate stress

Samples	Fail. Load $[kN]$	Fail. Stress $[MPa]$
P2-S11	54.57	258.79
P2-S12	50.55	243.17
P3-S01	55.76	276.30
P3-S02	53.15	260.43
P3-S03	48.50	235.33
P3-S04	53.35	270.13
P3-S05	50.80	249.36
P3-S06	53.59	258.48
P3-S07	52.33	260.72

Table 8.1: Average results for the tensile test.

D.2 Initial imperfection

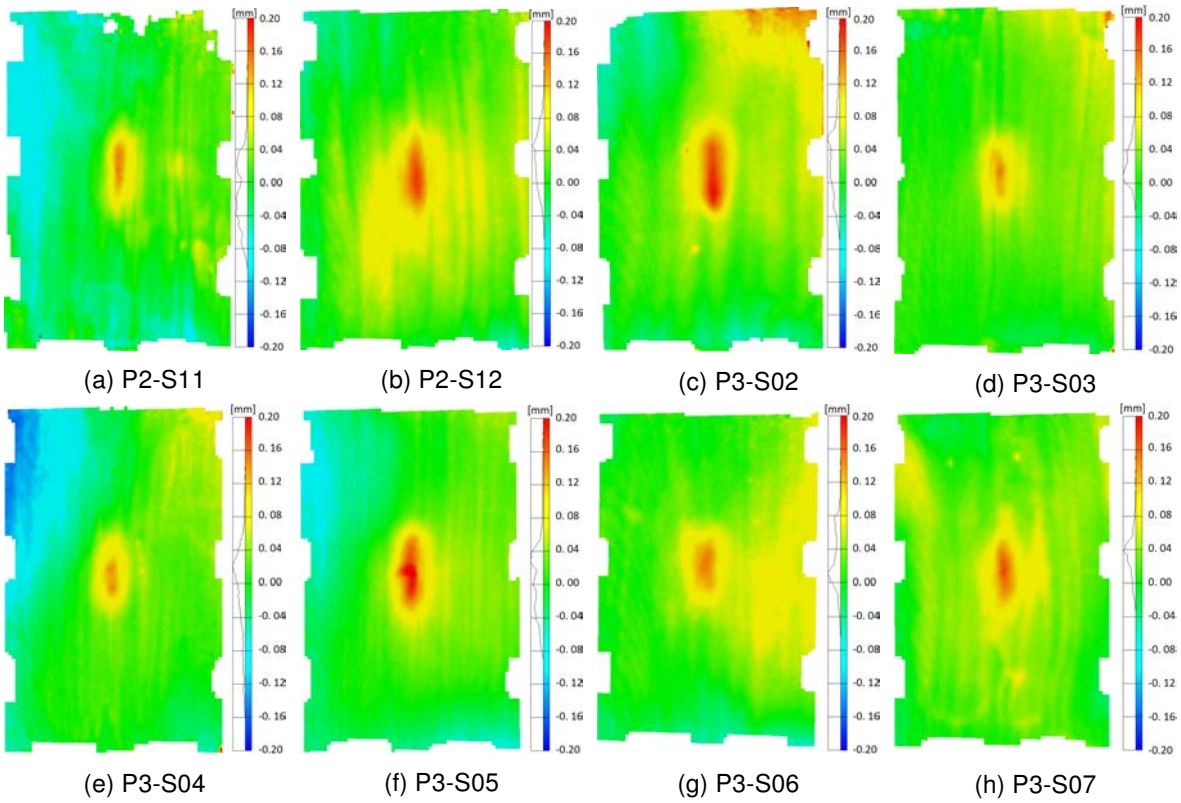

(a) P2-S11 (b) P2-S12 (c) P3-S02 (d) P3-S03

(e) P3-S04 (f) P3-S05 (g) P3-S06 (h) P3-S07

Figure 8.16: Post-impact detailed scan pictures of sample P3-S07.

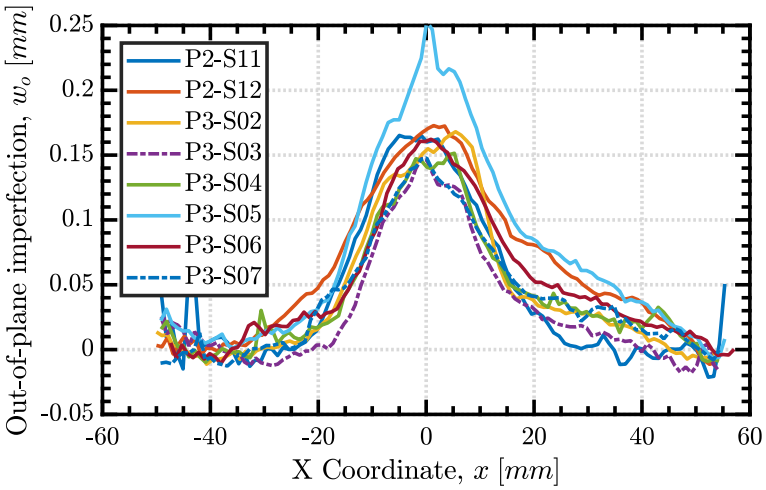

Figure 8.17: Experimental imperfections measured.

D.3 Out-of-plane deflection

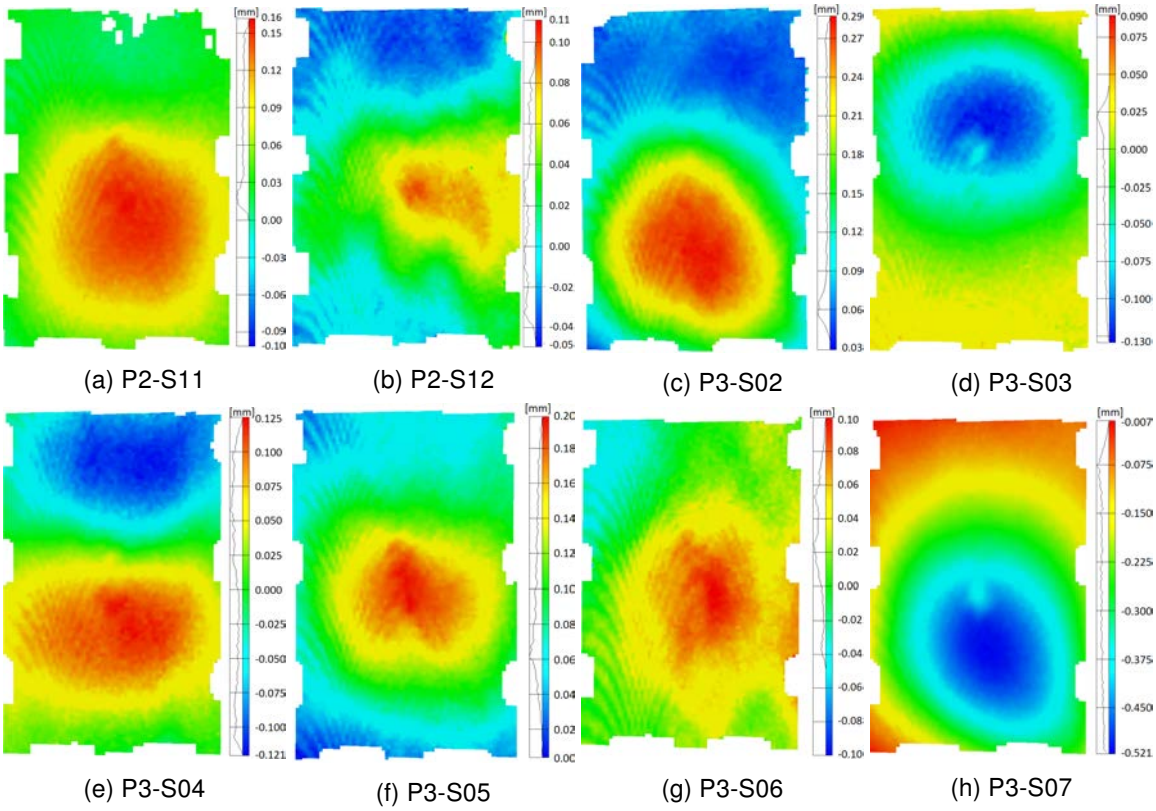

(a) P2-S11 (b) P2-S12 (c) P3-S02 (d) P3-S03

(e) P3-S04 (f) P3-S05 (g) P3-S06 (h) P3-S07

Figure 8.18: Contour plots of the beginning of buckling.

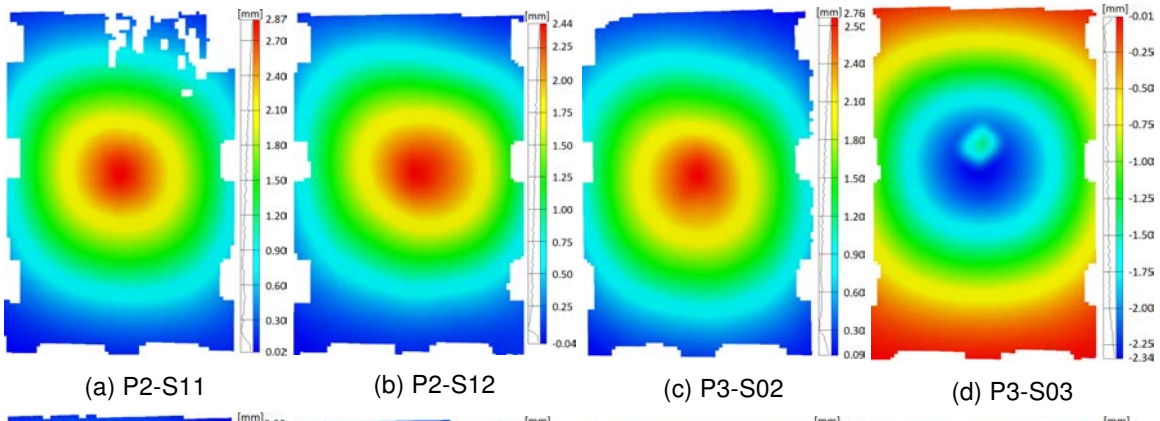

(a) P2-S11 (b) P2-S12 (c) P3-S02 (d) P3-S03

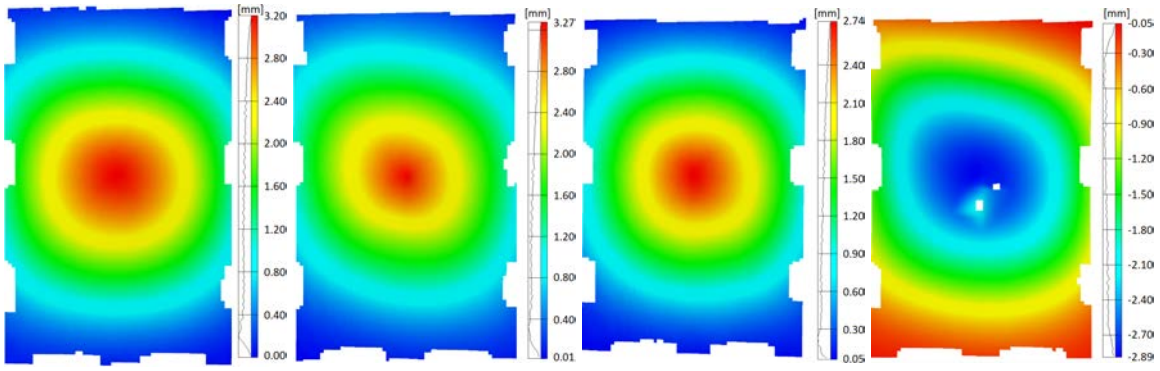

(e) P3-S04 (f) P3-S05 (g) P3-S06 (h) P3-S07

Figure 8.19: Contour plots of a stable buckling under $\sigma \approx 150\ [MPa]$.

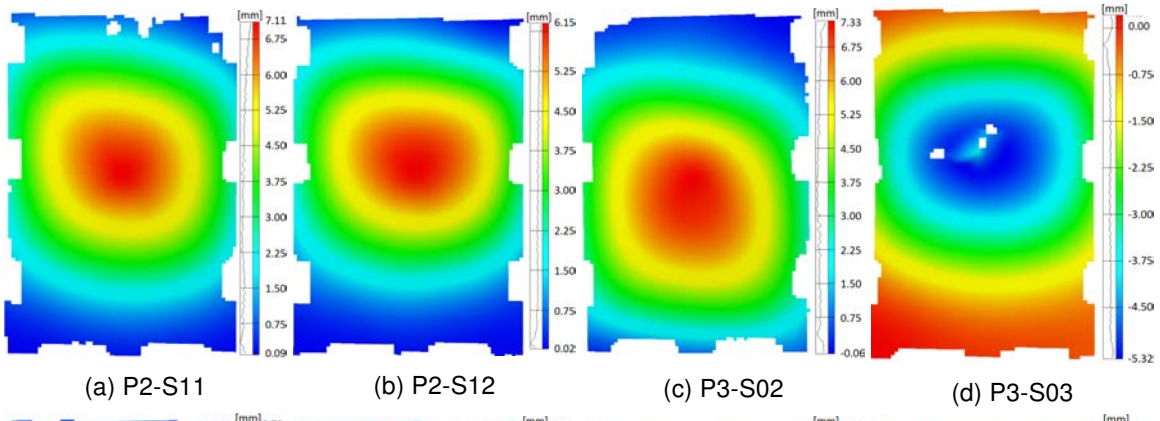

(a) P2-S11 (b) P2-S12 (c) P3-S02 (d) P3-S03

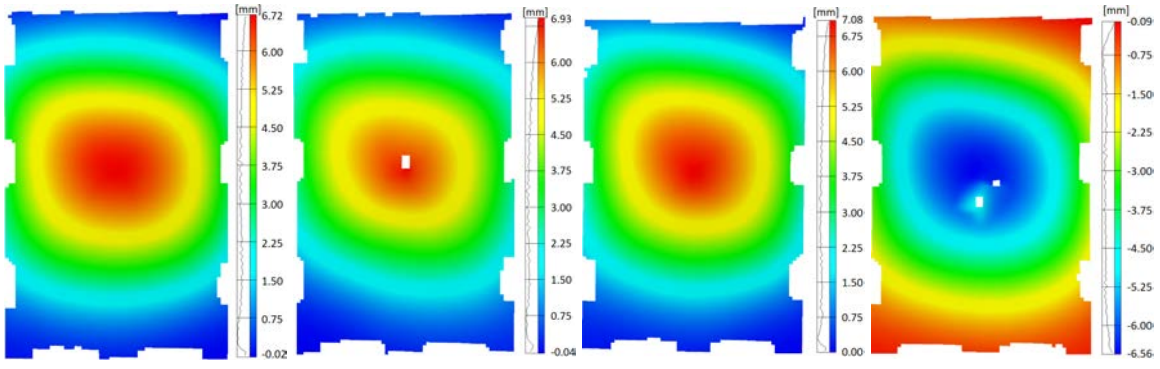

(e) P3-S04 (f) P3-S05 (g) P3-S06 (h) P3-S07

Figure 8.20: Contour plots of buckling at failure stress σ_{CAI}.

D.4 Shortening curves

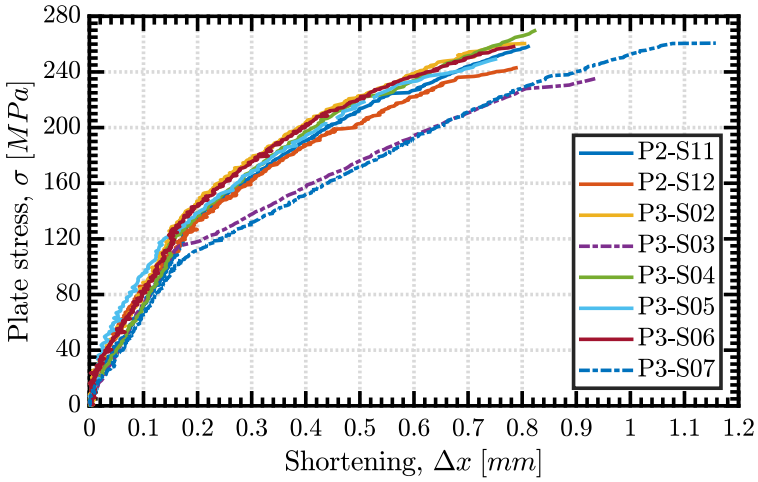

Figure 8.21: Experimental shortening curves measured.

D.5 Out-of-plane displacements along section paths

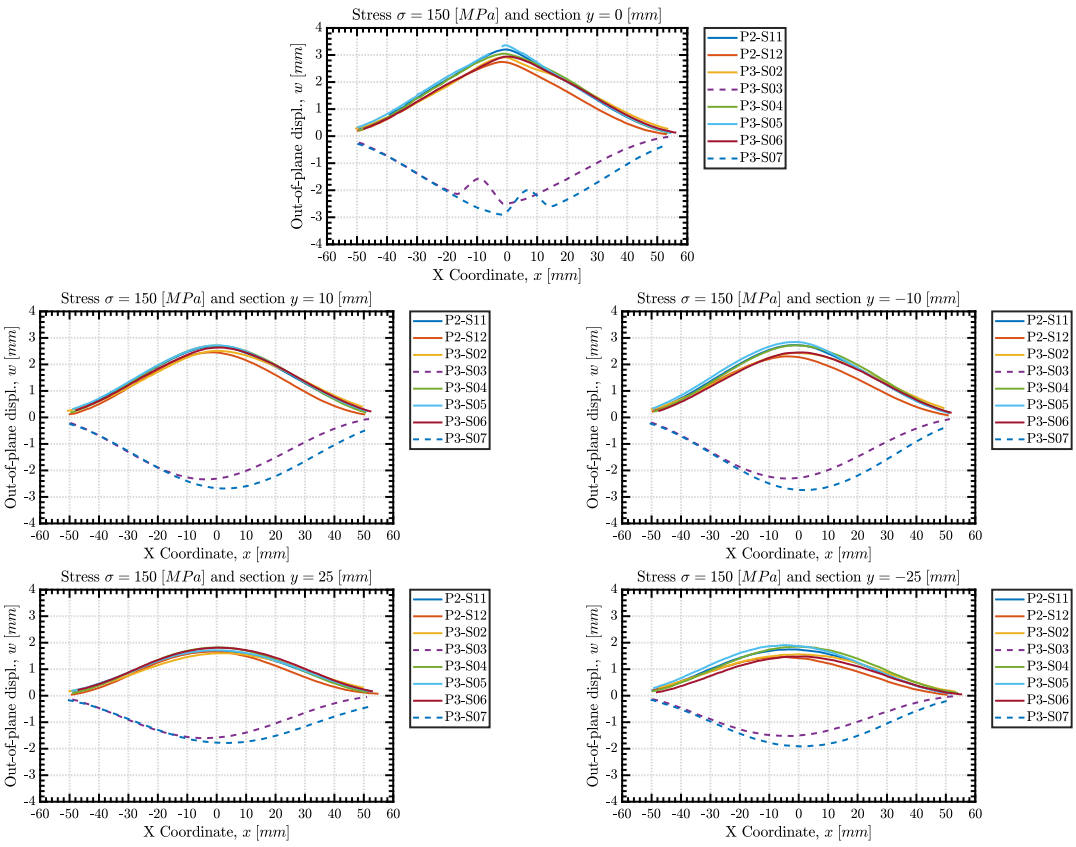

Figure 8.22: Out-of-plane displacements for $\sigma = 150$ $[MPa]$ along Y sections.

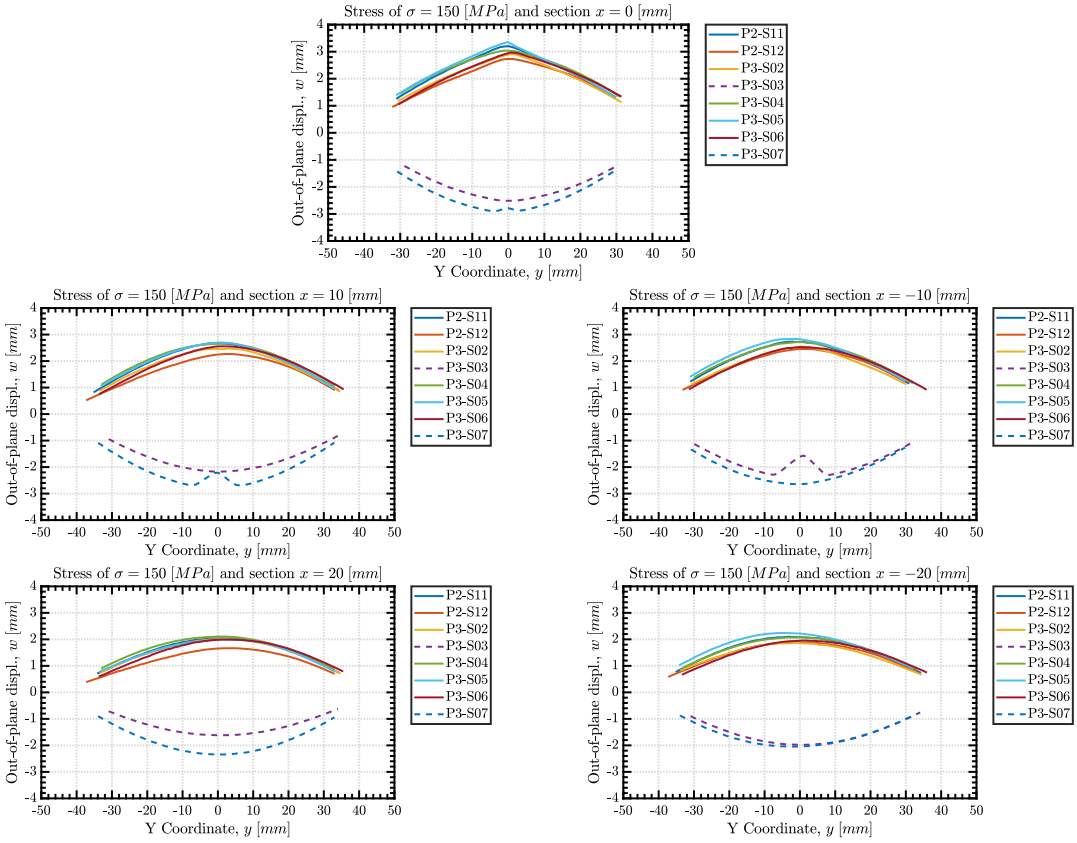

Figure 8.23: Out-of-plane displacements for $\sigma = 150\ [MPa]$ along X sections.

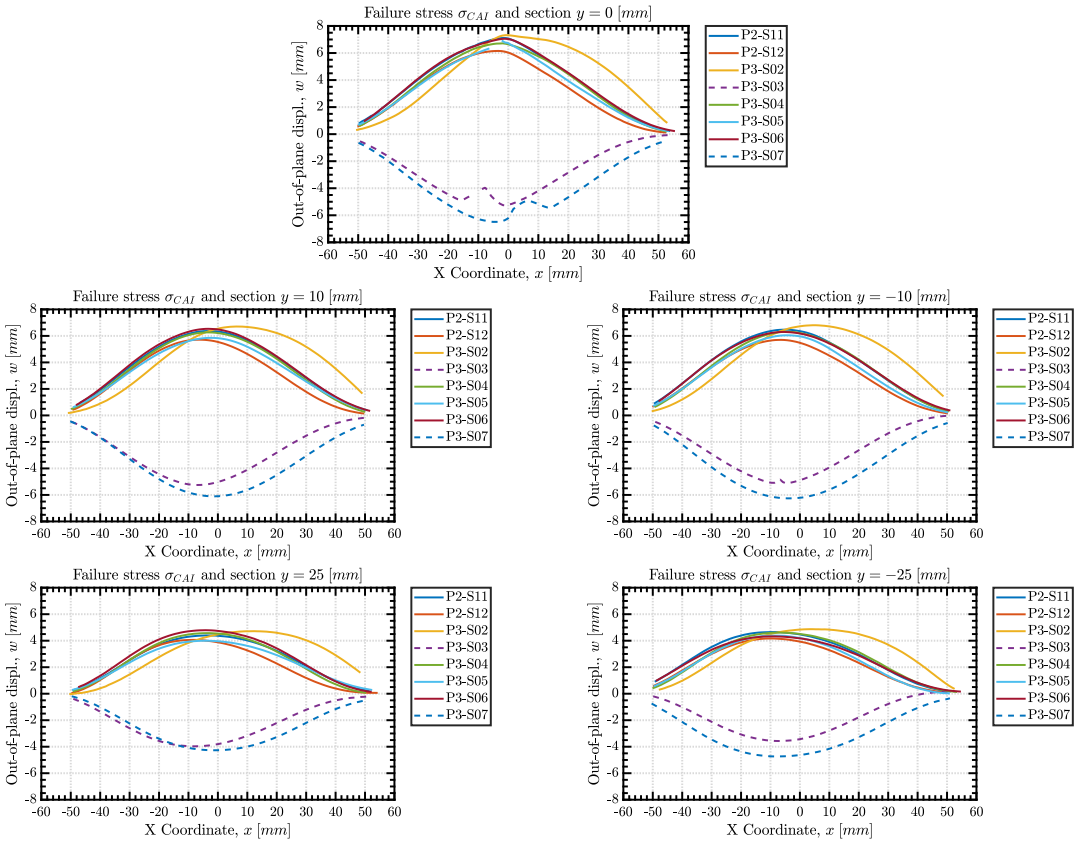

Figure 8.24: Out-of-plane displacements for failure stress σ_{CAI} along Y sections.

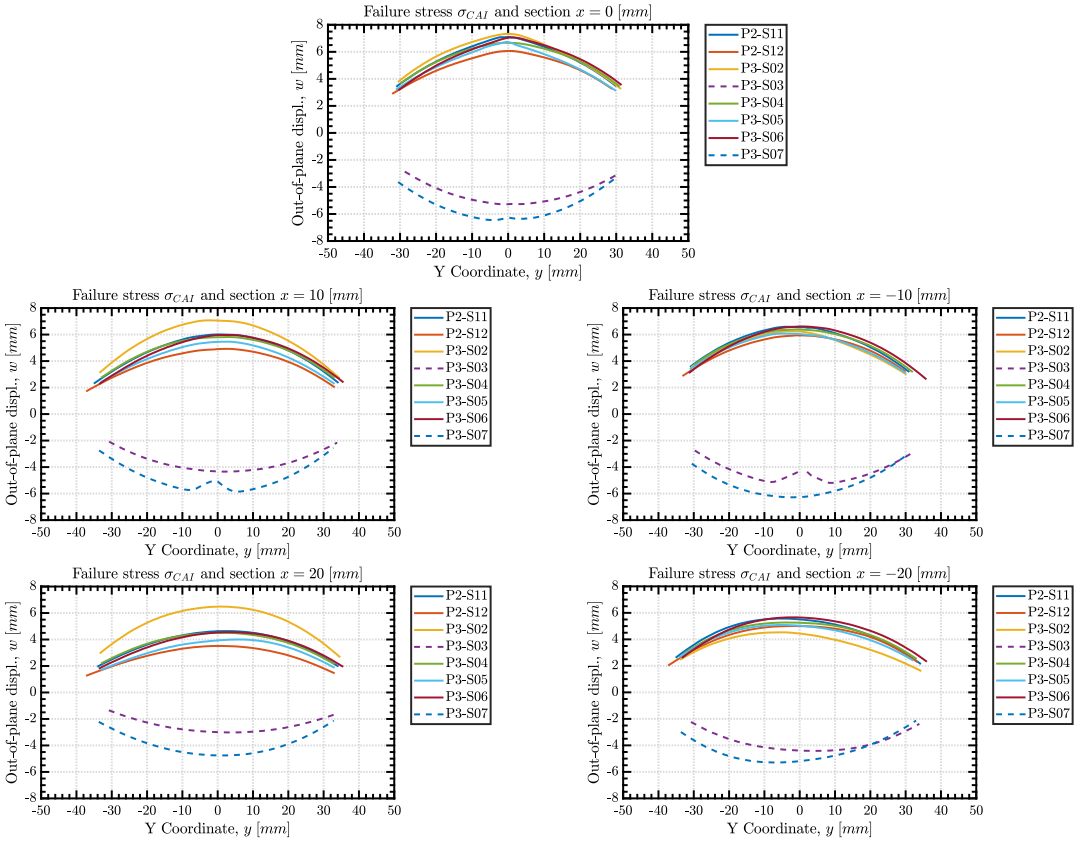

Figure 8.25: Out-of-plane displacements for failure stress σ_{CAI} along X sections.

D.6 Rupture line

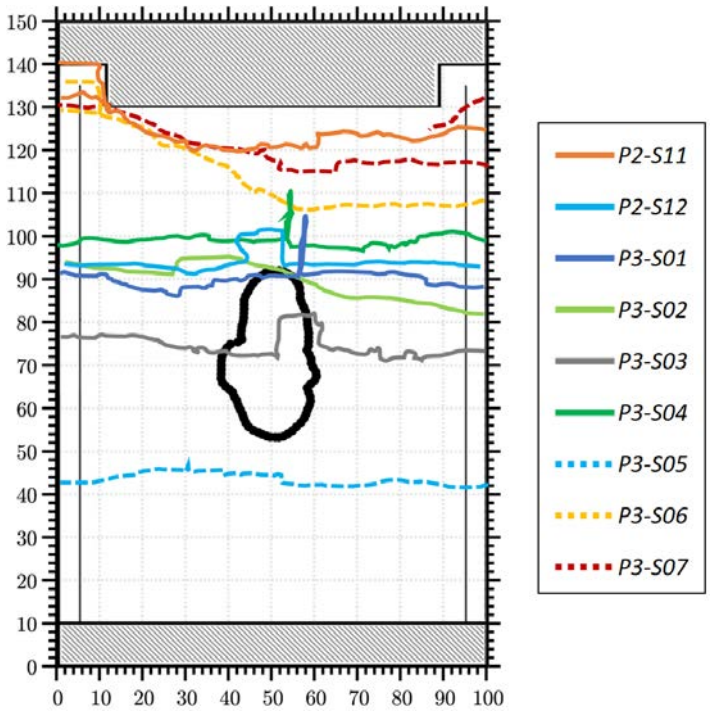

Figure 8.26: Rupture lines comparative over the delaminated shape of one of the samples.

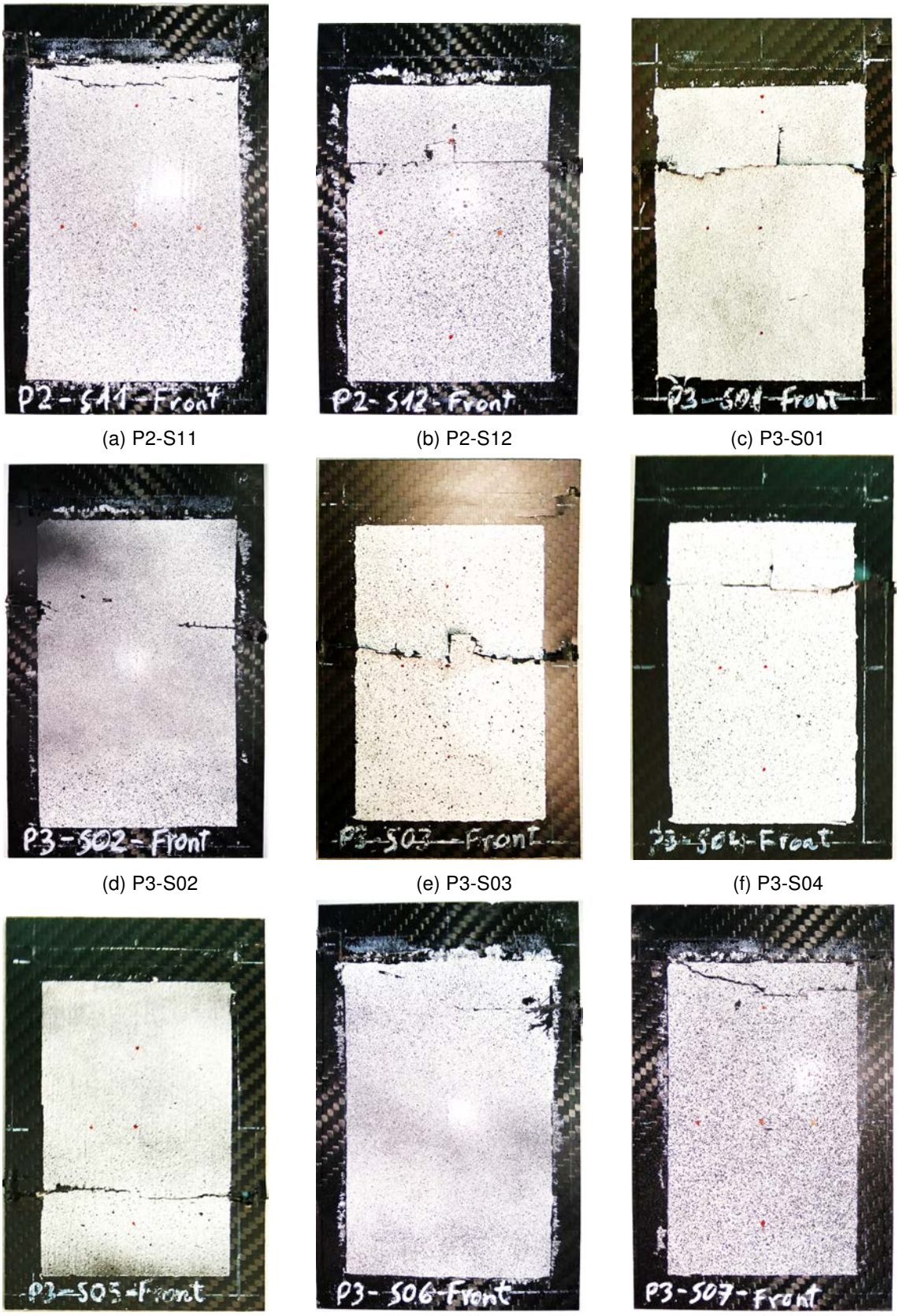

(a) P2-S11 (b) P2-S12 (c) P3-S01

(d) P3-S02 (e) P3-S03 (f) P3-S04

(g) P3-S05 (h) P3-S06 (i) P3-S07

Figure 8.27: Post-impact detailed scan pictures of sample P3-S07.

Comparative of buckling direction, rupture line and delaminated area

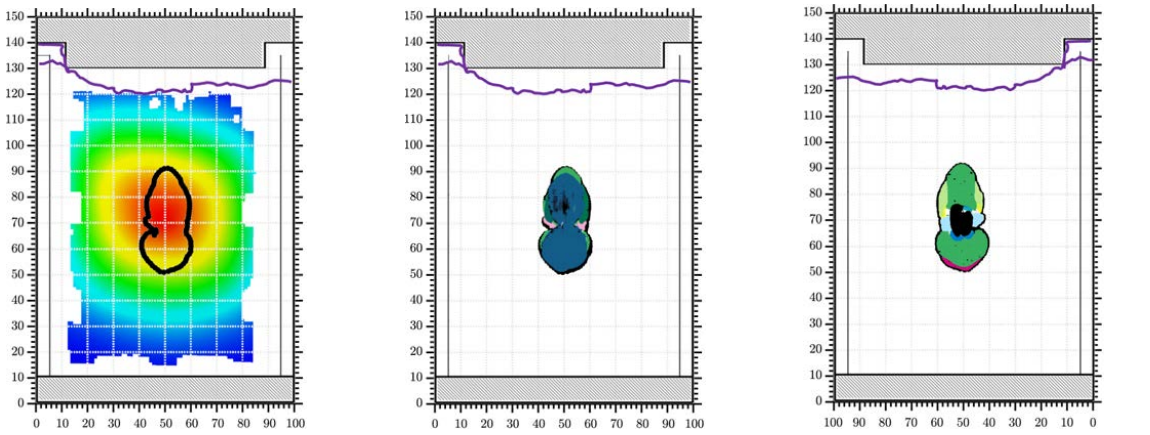

(a) Out-of-plane disp. (b) Front view delaminations (c) Back view delaminations

Figure 8.28: Rupture line, out-of-plane displacements and initial damage in sample P2-S11.

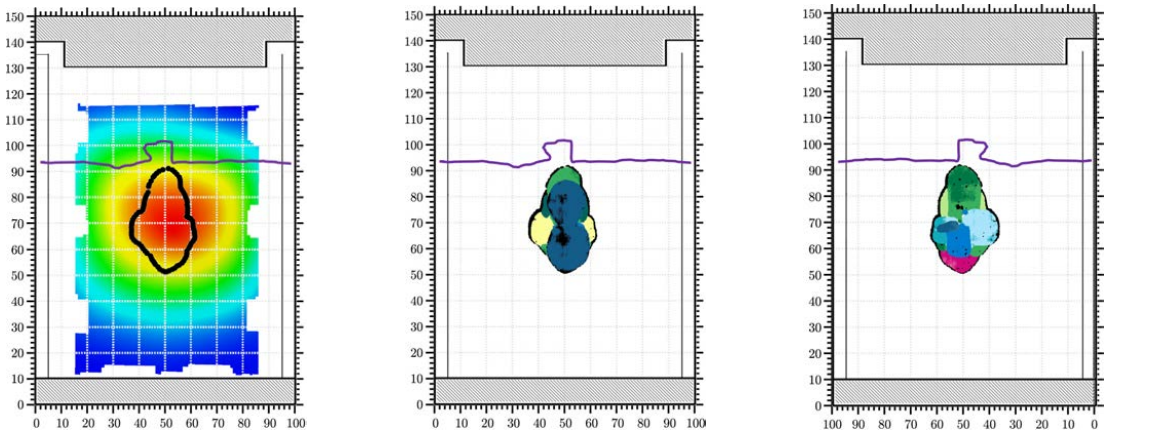

(a) Out-of-plane disp. (b) Front view delaminations (c) Back view delaminations

Figure 8.29: Rupture line, out-of-plane displacements and initial damage in sample P2-S12.

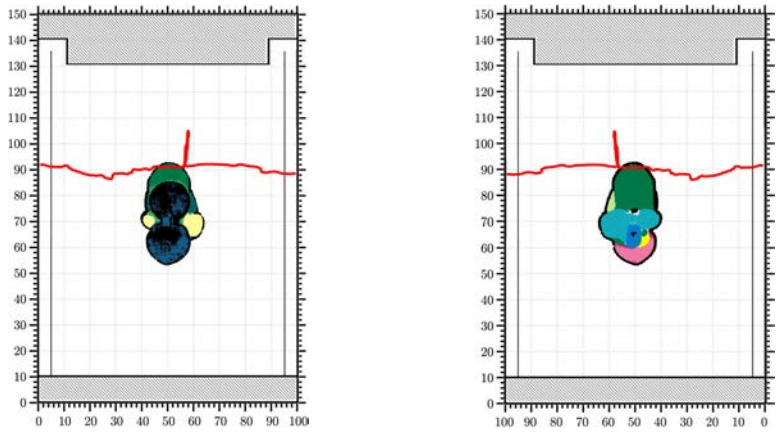

(a) Front view delaminations (b) Back view delaminations

Figure 8.30: Rupture line and initial damage in sample P3-S01.

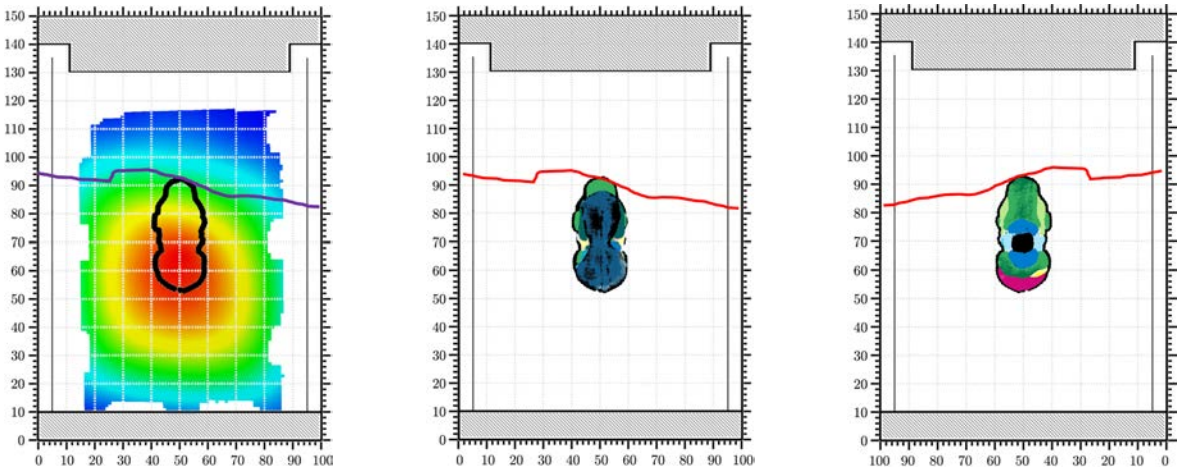

(a) Out-of-plane disp. (b) Front view delaminations (c) Back view delaminations

Figure 8.31: Rupture line, out-of-plane displacements and initial damage in sample P3-S02.

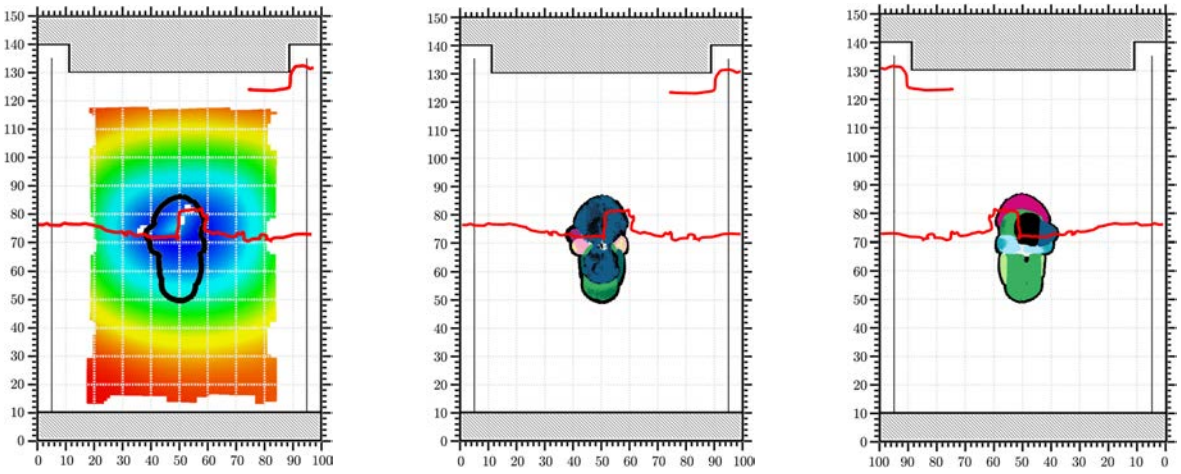

(a) Out-of-plane disp. (b) Front view delaminations (c) Back view delaminations

Figure 8.32: Rupture line, out-of-plane displacements and initial damage in sample P3-S03.

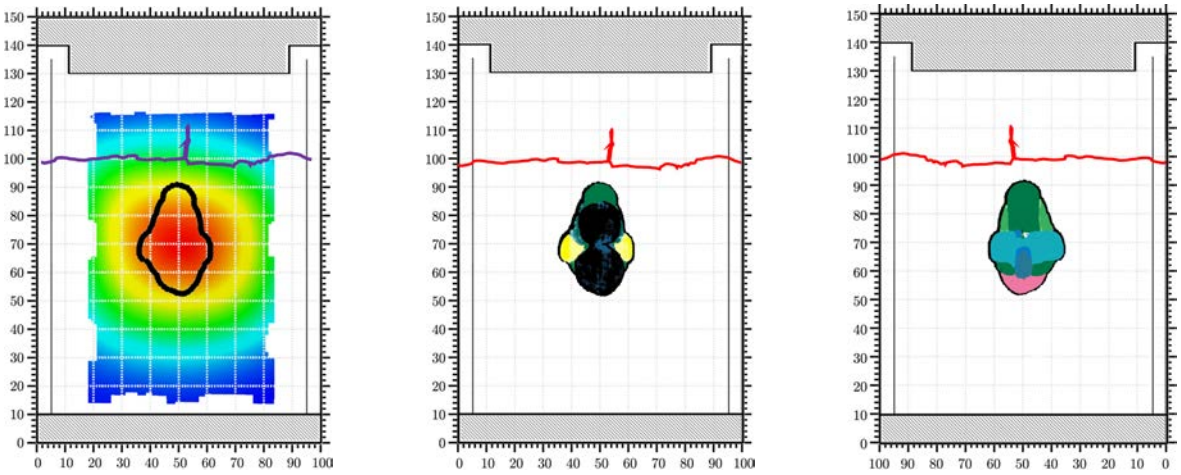

(a) Out-of-plane disp. (b) Front view delaminations (c) Back view delaminations

Figure 8.33: Rupture line, out-of-plane displacements and initial damage in sample P3-S04.

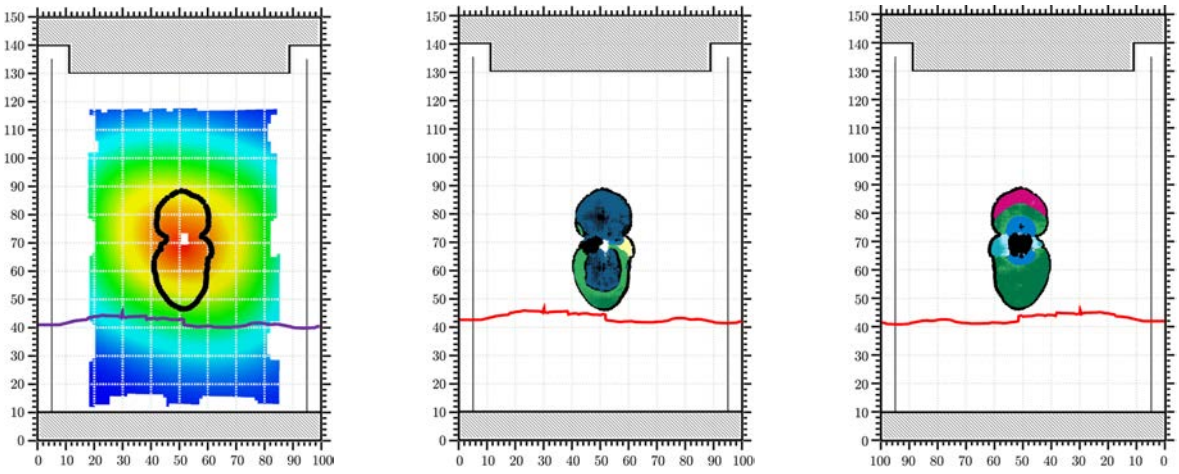

(a) Out-of-plane disp. (b) Front view delaminations (c) Back view delaminations

Figure 8.34: Rupture line, out-of-plane displacements and initial damage in sample P3-S05.

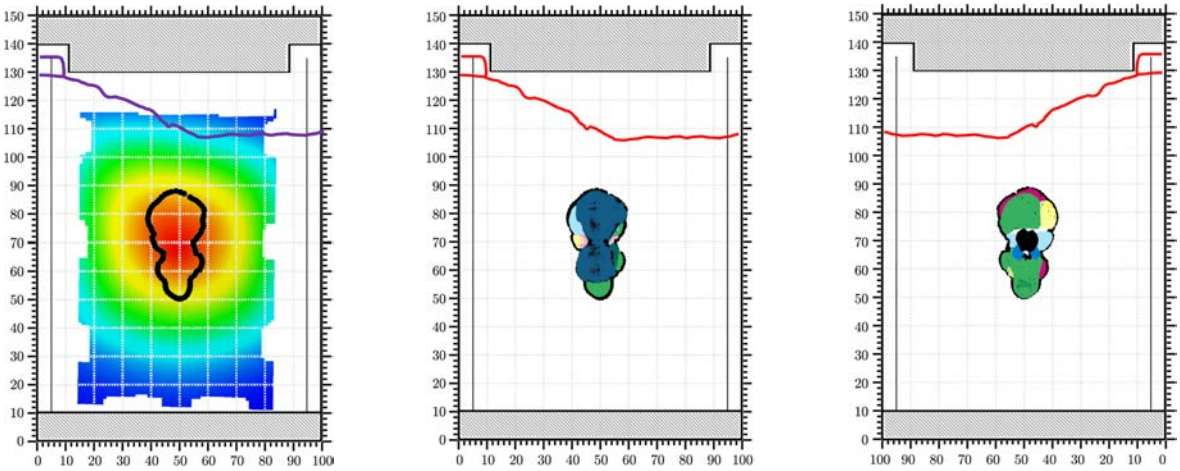

(a) Out-of-plane disp. (b) Front view delaminations (c) Back view delaminations

Figure 8.35: Rupture line, out-of-plane displacements and initial damage in sample P3-S06.

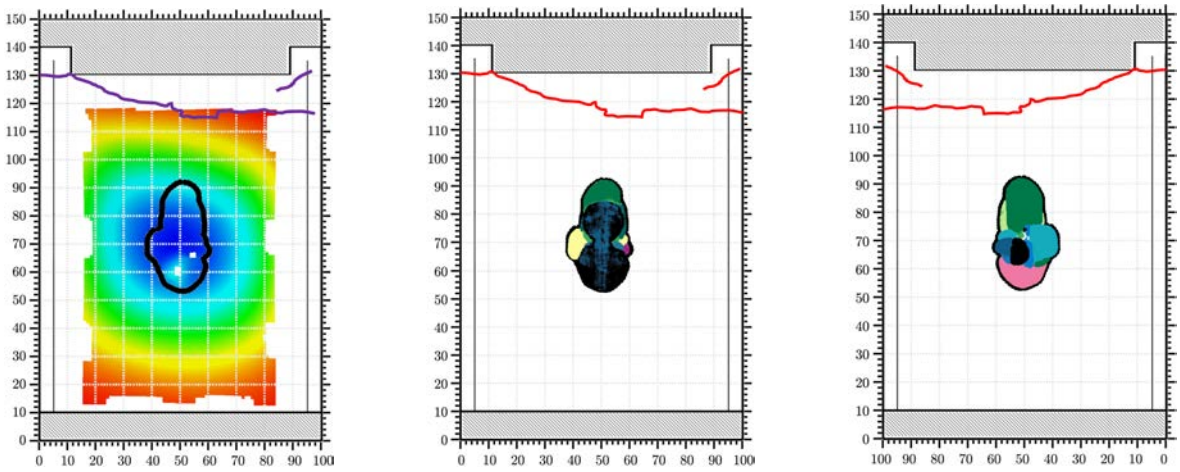

(a) Out-of-plane disp. (b) Front view delaminations (c) Back view delaminations

Figure 8.36: Rupture line, out-of-plane displacements and initial damage in sample P3-S07.